UNIVERSITÀ DEGLI STUDI DI NAPOLI
FEDERICO II

DOCTORAL THESIS

Development of Methodologies for the Aerodynamic Design and Optimization of New Regional Turboprop Aircraft

Author:
Pierluigi DELLA VECCHIA

Supervisor:
Prof. Luigi DE LUCA

Co-Supervisor:
Prof. Fabrizio NICOLOSI

A thesis submitted in fulfillment of the requirements for the degree of Doctor of Philosophy

in the

Doctor of Philosophy School in Aerospace, Naval and Quality Engineering

April 2, 2013

Declaration of Authorship

I, Pierluigi Della Vecchia, declare that this thesis titled, 'Development of Methodologies for the Aerodynamic Design and Optimization of New Regional Turboprop Aircraft' and the work presented in it are my own. I confirm that:

- This work was done wholly or mainly while in candidature for a research degree at this University.
- Where any part of this thesis has previously been submitted for a degree or any other qualification at this University or any other institution, this has been clearly stated.
- Where I have consulted the published work of others, this is always clearly attributed.
- Where I have quoted from the work of others, the source is always given. With the exception of such quotations, this thesis is entirely my own work.
- I have acknowledged all main sources of help.
- Where the thesis is based on work done by myself jointly with others, I have made clear exactly what was done by others and what I have contributed myself.

This PhD thesis has been defended in a public dissertation on May, 3rd 2013 under the judgment of a specialized commission composed by:

- Prof. Giorgio Guglieri, Department of Mechanical and Aerospace Engineering, Politecnico di Torino;
- Prof. Giulio Avanzini, Department of Innovation Engineering, Università del Salento;
- Prof. Salvatore Miranda, Department of Industrial Engineering, Università degli Studi di Napoli "Federico II".

Signed: _____

Date: _____

"Rem tene, verba sequentur..."

Marcus Porcius Cato (Tusculum, 234 a.C. - 149 a.C.), *Orationes*

UNIVERSITÀ DEGLI STUDI DI NAPOLI
FEDERICO II

University of Naples FEDERICO II

Abstract

Faculty of Aerospace Engineering
Doctor of Philosophy School in Aerospace, Naval and Quality Engineering

Doctor of Philosophy

Development of Methodologies for the Aerodynamic Design and Optimization of New Regional Turboprop Aircraft

by Pierluigi Della Vecchia

The Development of Methodologies for the Aerodynamic Design and Optimization of New Regional Turboprop Aircraft is presented proposing innovative procedures and tools to improve the aerodynamic of this aircraft category. Nowadays the increase in oil price, the huge growth of air transport traffic and the increasing attention to the aircraft environmental footprint led to considerable interest of specialists in new configurations of regional transport aircraft. Airlines and aircraft industries forecast in the next twenty years about 12000 turboprop aircraft will be delivered. Of these aircraft about 7000 will replace the older turboprop which reach their product life-cycle, while the remaining amount of about 6000 aircraft will be new turboprop aircrafts to satisfy market needs. The 61% of new turboprop delivered expected to be under 70 seats category (20% under 50 seats and 41% of 70 seats), while the new 90+ seat segment is a strong percentage of the total, i.e. the 39%. For these reasons this work aims to provide some guidelines in the aerodynamic design of future regional turboprop aircraft with about 90 or more passengers. Currently there are no configurations on the market of this type, so a typical 70 passengers turboprop aircraft is taken as reference starting point to put in evidence those aircraft components which particularly affects the "aerodynamic", especially in terms of aerodynamic drag. Particular emphasis is posed on aircraft performance, to highlight how a more accurate aerodynamic design can improve aircraft performance and so give aerodynamic guidelines in the design of new turboprop aircraft configurations. Research work can be divided into three main topics: *i)* airfoil design and optimization,

ii) aircraft components design and optimization and *iii)* vertical tail design. Airfoil design and optimization is a typical aeronautic topic, which involves several aspects such as parameterization techniques, optimization algorithms and aerodynamic solvers. These aspects have been analyzed and put together into a user friendly code which allows to design and optimize a generic airfoil geometry choosing *i)* the parameterization technique, *ii)* the optimization algorithm and *iii)* the aerodynamic solver. Constraints and multi-objective optimization have been performed, highlighting the crucial features in the design and optimization of a regional turboprop airfoil. The second topic aims to provide an optimization procedure for several aircraft components, fast to use also in a preliminary design phase. By coupling non uniform rational b-spline (NURBS) and a panel code aerodynamic solver, the geometry of a regional turboprop nose, wing-fuselage junction and undercarriage vane have been optimized to reduce aircraft aerodynamic drag. Particular emphasis has been also posed on the winglet design, highlighting how an accurate design can give an improvement in the whole regional aircraft flight envelope. The last topic involves the design of vertical tail plane for turboprop aircraft. This is a crucial topic for all twin-engine commuter aircraft because of all the ground performance are strictly related to the minimum control speed (V_{MC}) which mainly depends from the engine failure speed (V_{EF}), clearly related to vertical tail design. As a matter of fact both Part 23 and Part 25 of the aircraft regulations relates the certification speeds (especially for ground performance) to the V_{MC}; the lower will be the last, the better will be the performance. Moreover a performance improvement also means the commercial success of an aircraft, given the capability to be more competitive in several scenarios respect to competitors. In this research work, using a Navier-Stokes aerodynamic solver, a new method named VeDSC (Vertical tail Design Stability and Control) to design a vertical tail and a rudder has been carried out. More than 300 Navier-Stokes runs have been performed to accomplish with the objective. Particular care has been posed to the software set-up and several test-cases have been performed to validate the methodology. Finally the new method has been applied to several turboprop and twin-engine commuter aircraft and compared to typical semi-empirical methodologies to highlight the capabilities and reliability.

Acknowledgements

A PhD research work needs to sustain of many, many people! I am greatly indebted to a lot of people that, in a way or another, helped me to realize this work.

First of all I want express my gratitude to Prof. Fabrizio Nicolosi for offering me this great opportunity. I still remember, just graduated, the day I asked whether you had some work for me at the Department. You told me something about wing-fuselage aerodynamic optimization on a turboprop... and I immediately immersed myself in this subject so obscure for me. Thanks again for your support, inspiration, experiences and passion for the "flight vehicle" that you always gave me during these years. It was never doing research for the sake of doing research.

Thanks to Prof. Agostino De Marco, everyday "source of inspiration" technicals (and none). You really extended my curiosity to worlds unknown to me until then. Thanks again for the patience and the understanding during the days of training until late at night.

Thanks to Danilo, Elia, Gennaro and Salvatore (in rigorous alphabetical order) who have helped me during the years to carried out this work, not only for the immense technical support, but also for making our group a pleasant and exciting place to work, despite the not easy condition.

Last but not the least, my greatest gratidute goes to my family and to Maria for being there, at any time.

Pierluigi Della Vecchia

Contents

List of Figures

List of Tables

Abbreviations

AEO	**A**ll **E**ngine **O**perative
AOT	**A**irfoil **O**ptimization **T**ool
CAD	**C**omputer **A**ided **D**esign
CFD	**C**omputetional **F**luid **D**ynamic
CPU	**C**entral **P**rocessing **U**nit
DII	**D**ipartimento di **I**ngegneria **I**ndustriale
DNO	**D**irect **N**umerical **O**ptimization
EASA	**E**uropean **A**viation **S**afety **A**gency
ESDU	**E**ngineering **S**cience **D**ata **U**nit
FAR	**F**ederal **A**viation **R**egulations
FEM	**F**inite **E**lement **M**ethod
GB	**G**radient **B**ased
GA	**G**enetic **A**lgorithm
ID	**I**nverse **D**esign
MATLab	**M**atrix **L**aboratory (a MathWorks software)
N-S	**N**avier **S**tokes
NACA	**N**ational **A**dvisory **C**ommittee for **A**eronautics
NASA	**N**ational **A**eronautics and **S**pace **A**dministration
NURBS	**N**on **U**niform **R**ational **B**-**S**pline
OEI	**O**ne **E**ngine **I**noperative
SCoPE	**S**istema **Co**perativo **P**er **E**laborazioni Scientifiche Multidisciplinari
USAF DATCOM	**U**nited **S**tates **A**ir **F**orce **D**ata **C**ompendium
VeDSC	**Ve**rtical tail **D**esign **S**tability and **C**ontrol

Symbols

A	aspect ratio
AR	aspect ratio
C_D	3-D Drag coefficient
C_L	3-D Lift coefficient
$C_{\mathcal{L}}$	3-D Rolling moment coefficient
C_M	3-D Pitching moment coefficient
C_N	3-D Yawing moment coefficient
C_Y	3-D Sideforce coefficient
C_d	2-d Drag coefficient
C_f	friction coefficient
C_l	2-d Lift coefficient
C_m	2-d Pitching moment coefficient
C_p	pressure coefficient
P_0	maximum shaft horsepower
R/C	rate of climb
S	wing surface
S_H	horizontal tailplane surface
S_V	vertical tailplane surface
S_{TO}	take-off distance
S_{LAN}	landing distance
SHP	shaft horsepower
V_{EF}	engine failure speed
V_{MC}	minimum control speed
V_{TAS}	true airspeed

$2r$	fuselage diameter at vertical tail aerodynamic center
b	wing span
b_H	horizontal tailplane span
b_V	vertical tailplane span
b_{v1}	vertical tailplane span extended on fuselage centerline
c	wing chord
$cant_w$	winglet cant angle
c_{mac}	mean aerodynamic chord
c_v	vertical tailplane chord
d_f	fuselage diameter
e	oswald factor
e_w	wing induced drag factor
h_w	winglet height
r_w	winglet radius
r_f	fuselage half equivalent diameter
toe_w	winglet toe angle
z_w	wing position

Δ_w	winglet sweep angle
Λ	wing and tailplane sweep angle
α	angle of attack
β	angle of sideslip
ϵ_w	winglet twist angle
η_p	propeller efficiency
θ	fuselage upsweep angle
λ	taper ratio
λ_w	winglet taper ratio

To my Family and my Love...

Chapter 1

Introduction

1.1 Turboprop and Regional Aircraft Market

Nowadays the increase in oil price, the huge growth of air transport traffic and the increasing attention to the aircraft environmental footprint led to considerable interest of specialists in new configurations of regional aircraft. The independent society *Forecast International, Inc.*[1] in a study named *The Market for Regional Transport Aircraft* [1], highlights that 4198 regional aircraft will be built from 2011 through 2020. The Connecticut-based research firm estimates the value of this production at 130 billion in constant 2011 US dollars. The forecast includes both jet-powered and turboprop-powered regional aircraft, with jets accounting for just over 60 percent of the total unit production. The Forecast International study indicates that Bombardier, Embraer, and ATR will be the leaders among regional aircraft manufacturers during the 2011-2020 period. Bombardier, with a product line that includes jets and turboprops, is expected to build 1278 regional aircraft during the timeframe, representing a 30.4 percent share of the market. Embraer specializes in jets, and the study predicts that the Brazilian company will produce 992 regional jets for a 23.6 percent market share. Turboprop manufacturer ATR is expected to build 668 aircraft, representing a 15.9 percent share.

Bombardier Commercial Aircraft Vice President Marketing Philippe Poutissou during the RAA Annual Convention [2] has expressed optimism about the future and he sees strong demand for this size aircraft in the market in the next two decades. *Bombardier Aerospace Commercial Aircraft Market Forecast* in its study *Commercial Aircraft Market Forecast 2012-2031* [3] identifies the crucial points of the regional market growth in the following:

- Economic Trends

[1] Forecast International, Inc. http://www.forecastinternational.com is a leading provider of Market Intelligence and Analysis in the areas of aerospace, defense, power systems and military electronics. Based in Newtown, Conn., USA, Forecast International specializes in long-range industry forecasts and market assessments used by strategic planners, marketing professionals, military organizations, and governments worldwide.

- Oil Price
- Airline Industry Trends

which are strongly interdependent.

1.1.1 Economic Trends

Bombardier Company points out that the world's recovery from the 2008 financial crisis began in 2009 and has continued, at varying paces and with varying degrees of success into 2012. Growth in gross domestic product (GDP) has reflected this variation, reaching 4.1% in 2010 and 2.7% in 2011(see Fig. 1.1). The recovery has slowed due to continuing economic concerns, notably the Euro-zone crisis, high and volatile oil prices and China's ability to sustain its comparatively rapid growth. Also the economic recovery is taking longer than expected in mature markets, while growth in emerging economies has returned to pre-crisis rates [3]. The crucial aspects of the Economic Trends influence on the transport aircraft market is clearly visible in Fig. 1.2,where the demand for air travel, and with it the health of the world's airline industry, depends heavily on the strength of the economy. New aircraft orders are

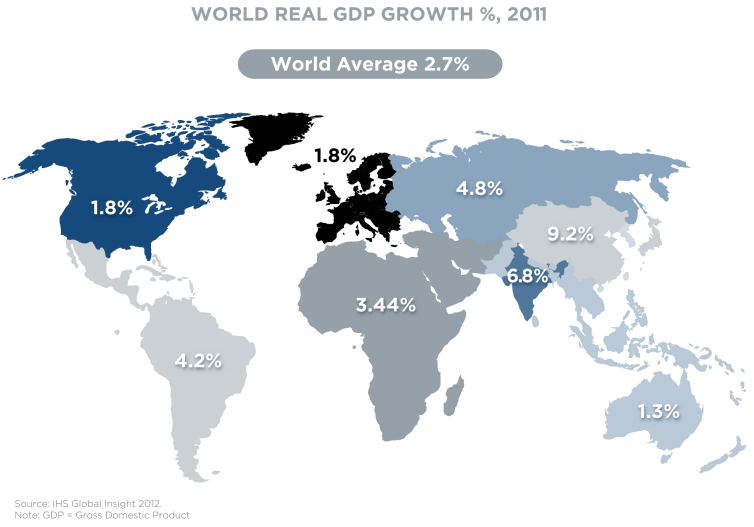

FIGURE 1.1: World real GDP growth %, 2011 [3]

(encompassing 20 - 220 seats) more than quadrupled from 2009 to 2011. Net orders rose to 2381 units in 2011, up from the 2010 tally of 1414 units, which itself more than doubled the 2009 pace of 556 aircraft orders [3]. *Commercial Aircraft Market Forecast* anticipates total demand for new aircraft in the 20 to 149-seat segments to be evenly divided between mature and emerging markets. Although starting from much smaller baselines (and assuming proportionate growth in aviation infrastructure), demand for new aircraft is expected to be particularly strong in emerging markets, such as China, Asia/Pacific (including

India) and Latin America. Europe, Africa, and the Middle East are expected to require somewhat fewer aircraft during the period and North American forecast demand remains unchanged. Moreover the propensity for the air travel is strongly dependent from the population growth and urbanization, as highlighted in [3].

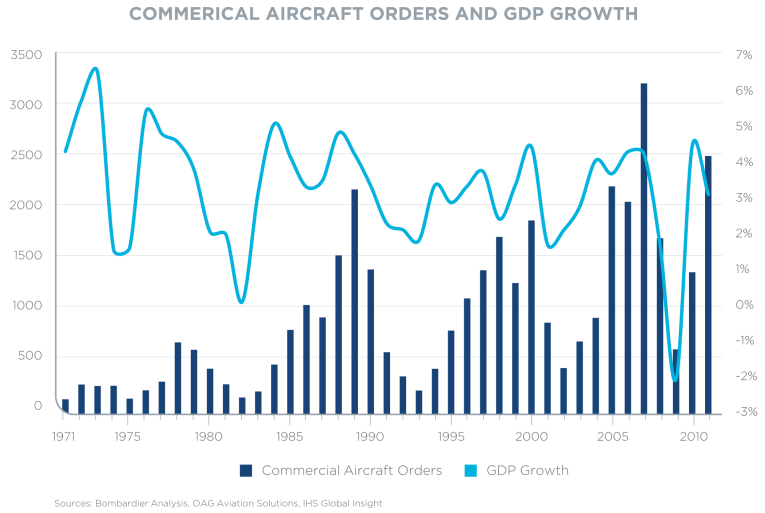

FIGURE 1.2: Commercial Aircraft orders and GDP growth [3]

1.1.2 Oil Price

Bombardier Aerospace Commercial Aircraft Market Forecast [3] again puts in evidence that the outlook for consistently high oil prices and continued oil price volatility presents some of the biggest challenges for the world airline industry. According to IATA[2], jet fuel, which closely tracks the price of crude oil represents airlines' largest single expense, now is amounting to 34% of operating costs on average. With this large and growing influence, oil prices and oil price volatility are major determinants of the size and other make-up of the commercial aircraft fleet of the future. Looking at Fig. 1.3 from an average price of $80 a barrel in 2010, oil prices rose by $20 to $100 per barrel in 2011. In the final months of the year, the prices spiked higher, and continued upwards by 8% in the first five months of 2012. Although peak prices have not reached the $147 per barrel experienced in July 2008, neither have they retreated to the December 2008 low of less than $35 per barrel. With 2011 average oil prices 25% higher than 2010, the main aircraft industries anticipate that prices will remain above $100 per barrel through 2012 and, indeed, throughout the 20-year forecast period.

[2]The International Air Transport Association (IATA) http://www.iata.org is the trade association for the world's airlines, representing some 240 airlines or 84% of total air traffic.

Looking ahead, EIA[3] in its *International Energy Outlook 2011* [4] said that in the reference case (see Fig. 1.3), world oil prices will be $95 per barrel in 2015, increasing slowly to $126 per barrel in 2030[4]. Whatever the oil price outlook, the leading companies highlight that in the next twenty years the arrival of new aircraft incorporating technological advantages that deliver direct operating cost reductions will accelerate the retirement of older, less fuel-efficient aircraft types.

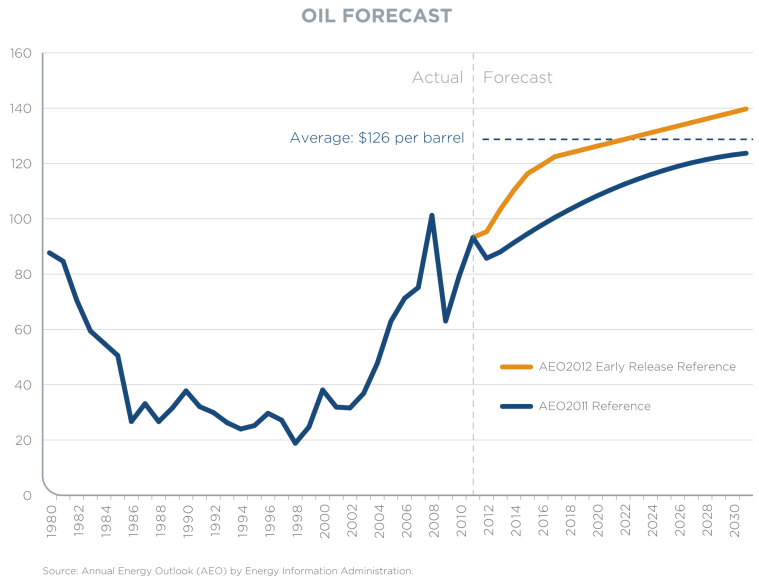

FIGURE 1.3: Oil Price forecast [3]

1.1.3 Airline Industry Trends

Although moving in a difficult international economic scenario, the demand for air transportation remained strong through 2011 to 2012. Again IATA reported that total passenger demand increased 5.9% in 2011 with a 4.8% expected in 2012. Global airline revenues have increased throughout the period of economic recovery, from a low of $476 billion in 2009, to $547 billion in 2010, and to $597 billion in 2011, representing a 9.3% year-over-year increase. According to IATA, global airline profitability improved significantly, from a net loss of $4.6 billion in 2009 to total net profits of $15.8billion in 2010, before declining to $7.9 billion in 2011, as shown in Tab. 1.1. As it can be

[3]Energy Information Administration (EIA) http://www.eia.gov it the Official Energy Statistics from the U.S. Government.

[4]The reference case represents EIA's current best judgement regarding exploration and development costs and accessibility of oil resources outside the United States. It also assumes that OPEC producers will choose to maintain their share of the market and will schedule investments in incremental production capacity so that OPEC's conventional oil production represents about 42 percent of the world's total liquids production.

TABLE 1.1: Airline Industry net profits (Billions U.S. dollars)

Region	2007	2008	2009	2010	2011	2012F
World	12.9	-16.0	-4.6	15.8	7.9	3.0
North America	3.7	-9.6	-2.7	4.1	1.3	1.4
Europe	6.4	0.0	-4.3	1.9	0.5	-1.1
Asia/Pacific	3.0	-4.7	2.6	8.0	4.9	2.0
Middle East	-0.1	-0.3	-0.6	0.9	1.0	0.4
Latin America	0.1	-1.4	-1.5	0.9	0.3	0.4
Africa	-0.2	-0.1	-0.1	0.1	0.0	-0.1

Source: International Air Transportation Association (IATA), June 2012.

seen in Tab. 1.1 regionally, Asia Pacific is expected to perform best, indicating profitability of $2.0 billion. North America airline profitability is expected to be $1.4 billion, Middle East $0.4 billion and Latin America $0.4 billion. Airlines in Europe and Africa are expected to incur new losses of $1.1 billion and $0.1billion, respectively. In summary, the economic recovery is continuing and demand for air transportation also continues to increase with it, subject to the challenges posed by slow growth in global gross domestic product and high oil prices. In the face of these challenges, airlines have shown creativity and consistency, in addressing their expenses a scenario in which operating a modern, highly fuel-efficient aircraft fleet remains the single most important strategy for business viability and long-term success [3].

U.S. Bureau of Transportation Statistics[5] reported in Ref. [5] three different business models in the passenger segment of airline industry: *(i) Mainline* or *Network carriers*, *(ii) Regional carriers* and *(iii) Low-cost carriers*. *Mainline carriers* are characterized by fleets of 100-plus seat aircraft serving multiple cities and countries through hub-and-spoke networks. *Regional carriers* typically operate smaller aircraft, such as regional jets and turboprops with fewer than 100 seats, on short and medium-haul routes and *Low-cost carriers* typically operate aircraft from 70 to 200 seats on point-to-point service connecting secondary airports. As it can be seen in Fig. 1.4, the profitability of the Low-cost and Regional carriers was present also during the crisis period, whereas the Mainline carriers have suffered most severely this period due to the cost pressures, notably high fuel prices, and relentless competition.

Another not negligible aspect to be considered is the aircraft retirement. This aspect is mainly linked to the product life-cycle, international and local noise and emission regulations and fees. With regards to the current fleet of 20 to 149 seat commercial passenger aircraft, Bombardier [3] anticipates that 60% will retire by 2031. Looking in more detail, Bombardier expects the fewest retirements in the 60 to 99 seat segment, and the most 70% of today's

[5]The Bureau of Transportation Statistics (BTS) http://www.rita.dot.gov/bts/ is a U.S. Government statistical agency.

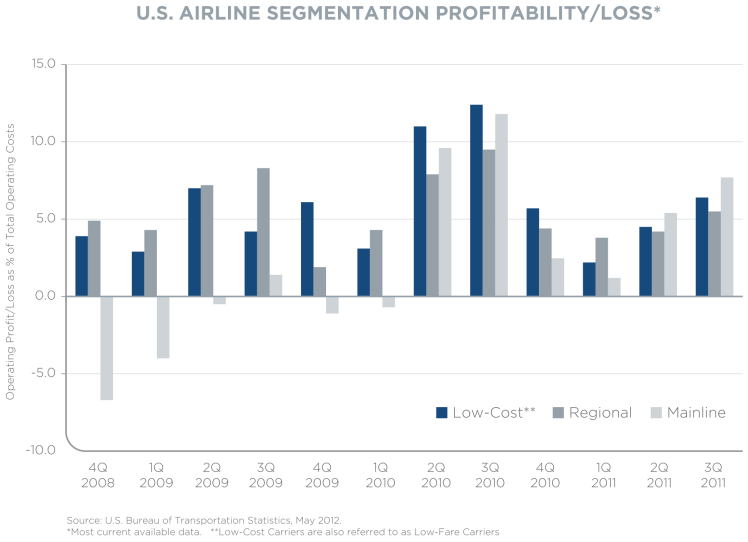

FIGURE 1.4: U.S. Airline segmentation profitability/loss [3]

fleet in the 20 to 59 seat segment. These aircraft will be retired due to their comparatively higher per-seat operating costs and high fuel costs.

1.1.4 Regional Market Forecast

Keeping in mind all the aspects analysed, the final forecasts on which all the specialists are almost completely agree are summarized in Tab. 1.2 [3]. Bombardier Commercial Aircraft Market Forecast believes that in the 2012 - 2031 period will be a delivery of 12800 new 20 to 149 seat aircraft, including of approximately 7000 aircraft retirements. The overall fleet growth will be 52%, representing an annual growth rate of 2.1%. As it can be seen in Tab. 1.2, 6900 new aircraft are expected in the 100 to 149 seat category, 5600 in the 60 to 99 and only 300 in the 20 to 59 category.

TABLE 1.2: Fleet growth forecast

World	2011 Fleet	Deliveries	Retirements	2031 Fleet
20 to 59 seat	3600	300	2700	1200
60 to 99 seat	2500	5600	1300	6800
100 to 149 seat	5100	6900	3000	9000
TOTAL	11200	12800	7000	17000

Source: Bombardier Forecasts

While the 6900 new aircraft in the 100 to 149 seat category will be expected to be all jet powered, the remaining approximately 5900 new aircraft of the 20 to 99 categories will be divided between turboprop and jet powered.

Both Bombardier and ATR companies agree on the number of the new turboprop aircraft deliveries in the next two decades, and it is around 3000 new turboprops.

As highlighted by the *ATR* Senior Vice President of Operations, Luigi Lombardi, during EWADE 2011 conference, the airlines will need about 3000 new turboprops in the next 20 years [6] with a value of 70 billion dollars. The 42% of the new turboprop deliveries expected to be 70 seats. The new 90+ seat segment is a strong percentage of the total, i.e. the 39% as shown in Fig. 1.5.[6]

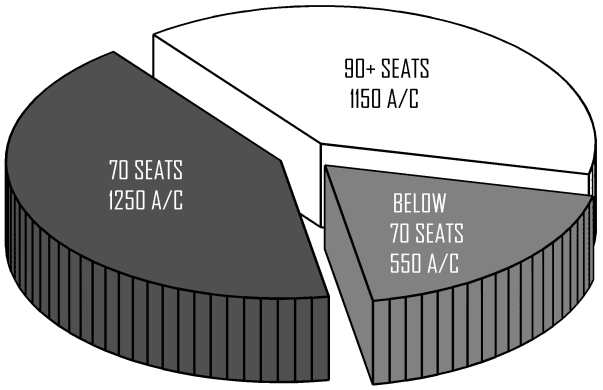

FIGURE 1.5: Long term demand for Large Turboprop, ATR Forecast, March 2010 [6]

The main competitors of the turboprop markets (ATR and Bombardier) agree on the fact that the smaller segment market is only a part of the largest seat segment. However they have different vision on the opportunities to invest on this category, due to the capability of ATR to maintain in production the ATR42 aircraft thanks to the strong commonality with the ATR-72. ATR forecasts that in next twenty years about 550 new 30 to 50 seat aircraft will be delivered [6], with a growth in the next ten years than following by a little drop. As it can be seen in Fig. 1.6, the growth rate is expected increase until the 2030 for 61+ seat segment. This segment is one of the most dynamic in commercial aviation, as growth will be driven largely by the evolving relationship between mainline and regional carriers. Since on short range lengths turboprop aircraft are more economical to operate than jets, modern turboprops are a natural hedging tool for air carriers against high and volatile fuel prices. High speed turboprops are now used by many airlines to replace 50 seat regional jets on short haul routes, with little or no increase in block time or reduction in passenger comfort. Moreover environmental issues and increasing

[6] ATR Assumptions are: 1) Regional Passenger Traffic Growth Average 20-Year: 7.0% 2) Fuel Price: 90$ per Barrel average 10 years (2010-2019); 110$ 2 nd decade (2020-2029); 3) Next Generation RJ Technology impact taken into account; 4) Forecast not constrained by Scope Clause

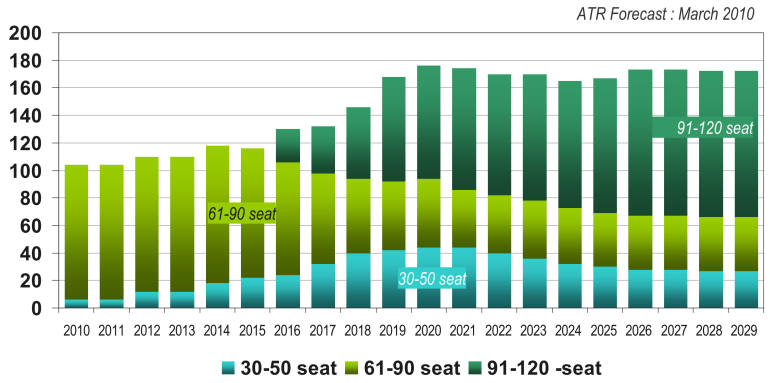

FIGURE 1.6: Turboprop Forecast,Delivery Stream (2010-2029) [6]

environmental regulations will mainly stimulate research and activities on application of new technologies in the new aircraft design, especially new turboprop design. On the basis of all these considerations the airline industry

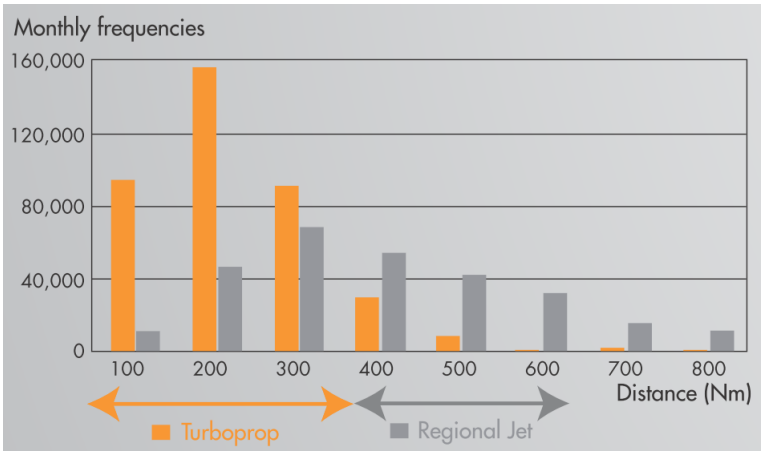

FIGURE 1.7: Turboprop and Regional jet typical range. *Source: ATR Forecast*

has already started to move towards the purchase of larger, more efficient regional aircraft, whether jets or turboprops. Once again ATR and Bombardier, the only two commercial turboprop manufacturers left, agree, saying they are focusing on the larger turboprops with both saying if a 90-seater were in production today, the airlines would buy it. That seems to belie the prejudice against turboprops that Embraer says is redolent among mainlines. ATR forecast[7] said that *"they have initiated a market and technology evaluation*

[7]Brochure: Regional market outlook, Turboprop perspective 2010-2029, ATR Marketing Department. http://www.atraircraft.com/media/downloads/Regional%20Market%20Outlook%202010-2029.pdf

process to study the feasibility of the ATR Next generation large Turboprop aircraft". The main goals of this aircraft category should be:

- *Respond to increased demand and growing traffic on turboprop connections*
- *Reduce seat-mile costs*
- *Compete on short-haul connections with similar sized Regional Jets.*

Again ATR notices that *"Airlines have clearly identified the respective environments for regional jet and turboprop, recognizing the respective advantages and the fact that the turboprop is the most profitable way to operate short-haul sectors"* as shown in Fig. 1.7. Luigi Lombardi in Ref. [6] adds that turboprop and regional jet must have a complementary role, however highlighting that the 75% of the sectors below 400 nautical miles range today is operated by turbopropellers.

1.2 Turboprop Aircraft Configuration

The need to develop regional turboprop transport aircraft is tied to particular needs of both passengers and airlines. First of all, a generic regional turboprop aircraft has to be faster than conventional transport means as trains, cars or ships and it has to be relatively cheap. Looking at aircraft performance, a turboprop aircraft has a short take-off and landing distance (sometimes on semi prepared runways) and a cruise airspeed not higher than 350 knots. From a deeper airlines point of view, this aircraft has to meet the requirements of low operative and maintenance costs, it is cheaper than an equivalent regional jet and above all it has a lower fuel consumption saving money and pollution. Passengers want to have a reliable aircraft, competitive in terms of costs, with low noise emission and, also on this aircraft category a good comfort. Aircraft industries were deeply involved in the design of new regional turboprop aircraft during the seventies and eighties in conjunction with the oil crisis. During these years several turboprop aircraft were designed and produced worldwide, increasing the competition stimulation. Until the early nineties more than ten aircraft industries built turboprop aircraft with a fairly good success. In a paper named *Learning, Technical Progress and Competitiveness in The Commuter Aircraft Industry: An Analysis of Embraer*, Frischtak [7] in the 1992 argued that the *"market has become more crowded, with a greater degree*

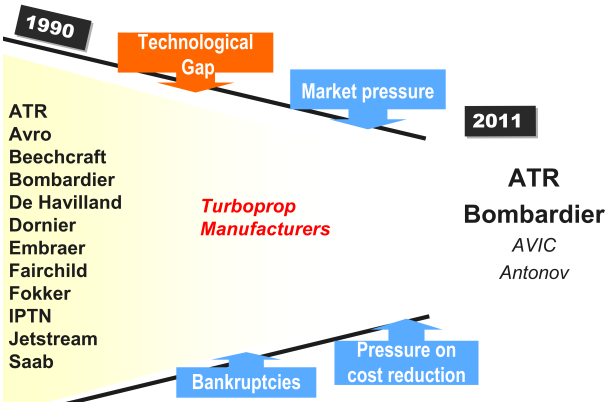

FIGURE 1.8: Regional Turboprop Industry Consolidation. *Source: ATR Forecast* [6]

of product overlap"[8]. Unfortunately as Frischtak [7] foresaw, many companies were destined to disappear or to modify the product and nowadays only four regional turboprop aviation industry are present on the market, whose leaders are ATR and Bombardier(see also Fig. 1.8). ATR has in the market ATR42 and ATR-72, whereas Bombardier the Dash8 Q-400. ATR-72 and Bombardier Dash8 Q-400 shown in Fig. 1.9 will be considered as reference in the description of a typical turboprop aircraft configuration.

1.2.1 Typical Turboprop Characteristics

Nowadays large turbo-propeller aircraft (with about 70 seat) has a maximum take-off weight W_{TO} of about 23-28 tons with a an empty weight W_E slightly higher than 50% of the W_{TO} (about 13-17 tons). Table 1.3 summarizes the main characteristics of the two reference aircraft shown in Fig. 1.9. As it has been said before, the reference turboprop aircraft are the ATR-72 and the Bombardier Dash8-Q400. Both the aircrafts have a straight tapered High-wing configuration with a surface about 60 - 70 m^2 and span about 27-30 meters, which means an aspect ratio around 12. The main reason to have a high-wing configuration is to have an easy cabin access and a better aircraft clearance. Moreover from the consideration to guarantee possible take-off from not prepared runways the low-wing configuration is penalized due to possible

[8]Frischtak in Ref. [7] in the 1992 said: "*The commuter aircraft industry has undergone major changes in the last decade or so, Both technological and market forces have converged to make the survival of incumbent firms more difficult. On the one hand, increased aircraft size and complexity have led to an escalation of development costs; on the other, the market has become more crowded, with a greater degree of product overlap. At the same time, firms are being pushed to develop and offer not one, but families of aircraft characterized by substantial communality to enable a reduction in users' operational costs. As a result, producers are under competitive stress and many have posted losses. Those linked to or in any way supported by Government funds are claiming large infusions of capital to sustain their market position*"

(a) ATR-72-600 (b) DASH8 Q-400

FIGURE 1.9: ATR-72 and DASH8-Q400 aircraft

ingestion for the engine and high possibility for the propeller to not work in optimal conditions. The tail surfaces have similar geometrical characteristics both in terms of configuration and dimensions. T-tail configuration has been adopted for both the aircraft, with ratio between tail plain and wing surface very close about 0.20 (see Tab. 1.3) both for the horizontal and vertical tail. Also the fuselage length and fuselage fineness ratio are comparable for both the aircrafts, between 10 and 12. From a structural point of view the airframe structures are made of high strength aluminum alloy. This choice is primary due to reliability and low maintenance and construction costs. ATR-72 has a high wing monoplane and a fail-safe fuselage built of light aluminum alloy. The ATR in Ref. [8] declared composite materials percentage almost high and around the 20% of the W_E. Figure 1.10 shows the ATR-72 composite materials distribution (divided into carbon fibres, fibreglass and kevlar fibres). In the last years ATR increased the use of composite materials extending to the entire tail planes. Bombardier declared the use of composite panels on radome, nose equipment bay, wing-fuselage fairings, tail-cone , dorsal fin and horizontal stabilizer leading edge. Steel structural alloy are used in the landing gear for both the aircraft. From all the above-mentioned considerations it

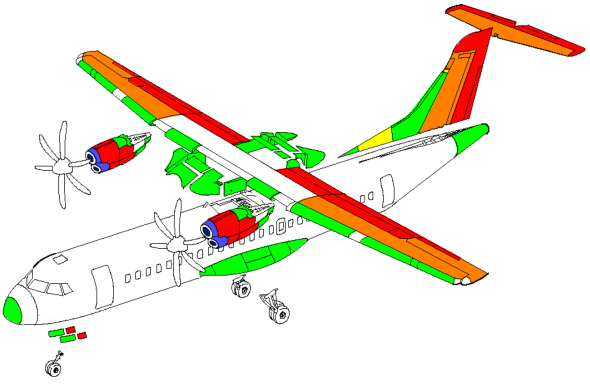

FIGURE 1.10: ATR-72-500/600 Composite Materials. *Source: ATR Forecast* [8]

TABLE 1.3: Large turboprop aircraft main characteristics

	ATR-72	Dash8-Q400
Crew	2+2	2+2
Passengers	70	78
$W_{TO}(kg)$	23000	27995
$W_E(kg)$	12850	17148
Fuselage length (m)	27.17	32.81
Fineness ratio $\frac{l}{d}$	10.10	12.20
Wing		
$S(m^2)$	61.00	63.08
$b(m)$	27.05	28.42
AR	12.0	12.1
root airfoil $\frac{t}{c}$	18%	18%
tip airfoil $\frac{t}{c}$	13%	12%
Horizontal tail		
$S_H(m^2)$	12.00	14.56
$b_H(m)$	8.10	7.85
AR_H	4.4	4.3
$\frac{S_H}{S}$	0.20	0.23
V_H	1.13	1.96
Vertical tail		
$S_V(m^2)$	12.00	14.13
$b_V(m)$	4.34	4.28
AR_V	1.57	1.30
$\frac{S_V}{S}$	0.20	0.22
V_V	0.10	0.13
Performance		
Cruise Speed $(knots)$	276	350
Service Ceiling (m)	7620	6250
Range (km)	2666	2400
Rate of Climb (ft/min)	1847	-
Take-off distance (m)	1223	1350

Source: Jane's. All World's Aircraft 2008-2009.

possible to identify the main features of large turboprop aircraft (referred to the nowadays market leaders aircraft):

- High-wing
- T-tail
- Slender fuselage
- Engine wing mounted
- Easy cabin accessibility both for passengers and baggage
- Reliable, low maintenance and construction costs structure
- Advanced system instrumentations, glass-cockpit and Fly-by-wire
- Cabin comfort.

As highlighted in Sec.1.1 market needs of new turboprop aircraft, preferably a new design conception, more reliable, environment friendly, with low noise emission and with low maintenance and operative costs. All the considerations made regarding economics and configurations aspects involving a turboprop aircraft. It is quite evident that an aircraft of this category in order to satisfy all these requirements must have a very accurate design. In particular, the aerodynamic design of these aircraft involves many aspects that must be assessed and addressed very thoroughly in the design phase. A very important feature of the aerodynamic design is the aerodynamic drag. For these reasons in the following Sec.1.3 the aerodynamic drag breakdown of typical large turboprop aircraft is addressed to better understand which are the main drag sources and which the influence of drag reduction on the aircraft performance.

1.3 Turboprop Drag and Performance

1.3.1 Drag Breakdown

Figure 1.11 shows the reference geometry of a large turboprop aircraft, the ATR-72. Table 1.4 summarizes the main characteristics used to carried out the aerodynamic drag breakdown of this aircraft. The aircraft zero lift drag coefficient has been calculated according with methodologies proposed by Roskam [9] and Raymer [10]. In Ref. [9, 10] the total drag coefficient of an aircraft is assumed as sum of the zero lift drag coefficient and the induced drag coefficient. This assumption is made when the approximation of a parabolic drag polar is considered in order to estimate the drag coefficient for lower incidence such as cruise and climb, that is until the lift coefficient becomes greater than 1. Parabolic drag coefficient has been assumed as shown in Eq. 1.1, where AR is the aspect ratio of the wing and e is the Oswald factor of the complete aircraft.

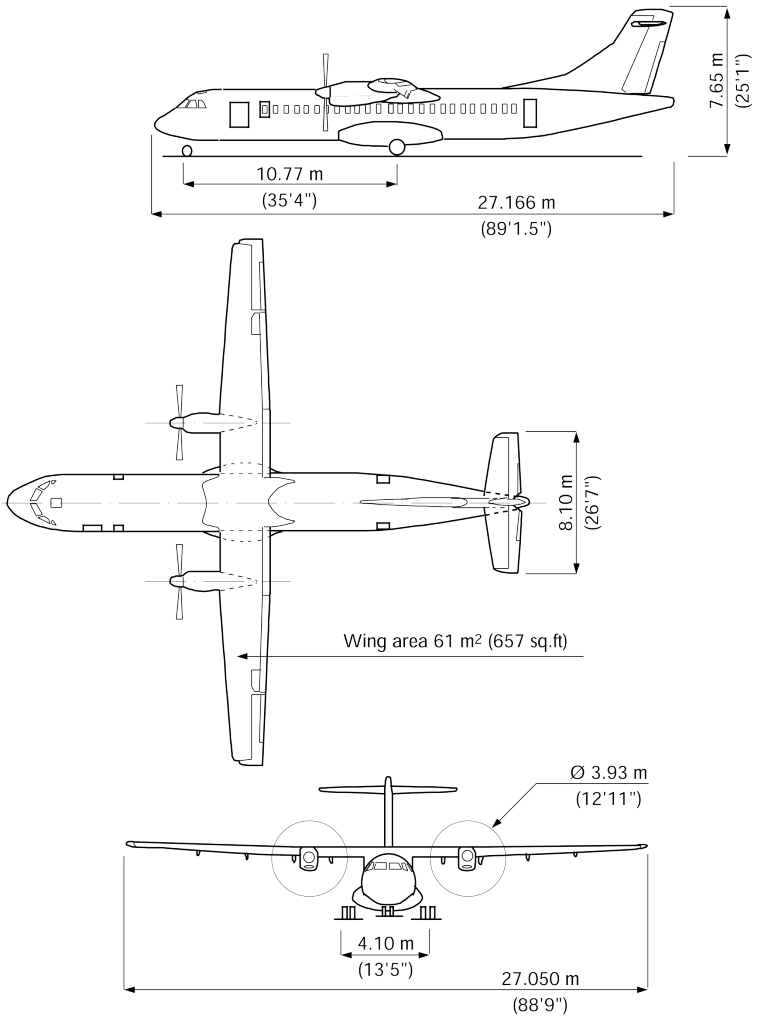

FIGURE 1.11: ATR-72 3-View. Courtesy of ATR

$$C_D = C_{D_0} + \frac{C_L^2}{\pi ARe} \tag{1.1}$$

According to the procedure of Ref. [9] and [10] the total zero lift drag coefficient is equal to 0.0306 [9]. Figures 1.12 and 1.13 show the drag breakdown of the aircraft zero lift drag coefficient. The main drag sources are related to the skin friction drag coefficient of the aircraft components equal about to 64% (Fuselage, Wing, Nacelles and Tail planes). The remaining 36% is attributable to drag sources difficult to estimate, such as Wing-Body, Wing-Nacelle and Tail planes interferences, wind-shield geometry, fuselage and nacelles base

[9]Main assumption are: Mach number M=0.43, Reynolds number Re=11.5e6, transition fixed at 10% of all lifting surfaces, wing and fuselage are in treated metal alloy, tail planes are in composite material, wind-shield is with flat windows with protruding, gaps are in flap, ailerons, elevator and rudder.

drag, excrescences, cooling and gaps. By summing the contributions related to the main aircraft components it is possible to see that the 35% of the total C_{D_0} is due to the fuselage in the form of skin friction, wind-shield, base drag and up-sweep; 33% is attributable to the wing (skin friction and interferences with fuselage and nacelles), whereas the remaining is divided between nacelles (12%), tail-planes (9%), cooling (5%) and excrescences (5%). Figure 1.14

TABLE 1.4: ATR-72 main characteristics and conditions

W_{TO} (kg)	23000
Engine	PW127F
SHP (hp)	2750
SFC (lb/hph)	0.45
η_p	0.85
Geometry	
Fuselage length (m)	27.17
Fuselage diameter (m)	2.7
S (m^2)	61.00
b (m)	27.05
AR	12.0
root airfoil	NACA 23018
tip airfoil	NACA 23013
$S_H(m^2)$	12.00
$b_H(m)$	8.10
AR_H	4.4
$\frac{S_H}{S}$	0.19
V_H	1.13
$S_V + S_f(m^2)$	16.00
b_V(m)	4.34
AR_V	1.57
$\frac{S_V}{S}$	0.20
V_V	0.10
Conditions	
M	0.43
Re	11.5e6
Oswald's factor e	0.85

shows the estimated drag polar according to the Eq. 1.1. The ATR-72 cruise condition are in the C_L range between 0.35 - 0.5 and climb condition in the range between 0.8 - 1.0. As it is shown in Fig. 1.14 in cruise condition the drag coefficient C_D is about 20% higher than zero lift drag coefficient C_{D_0}, whereas in climb condition the drag coefficient is almost twice the C_{D_0}. The level flight performance (such as the maximum speed or fuel consumption) are mainly dependent from the zero lift drag coefficient and they could be

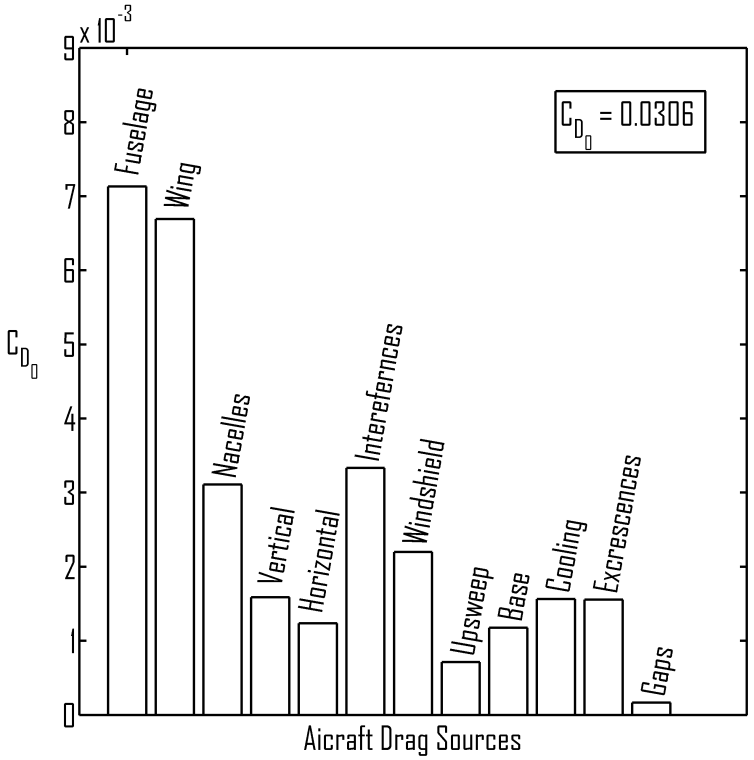

FIGURE 1.12: ATR-72 drag breakdown main sources

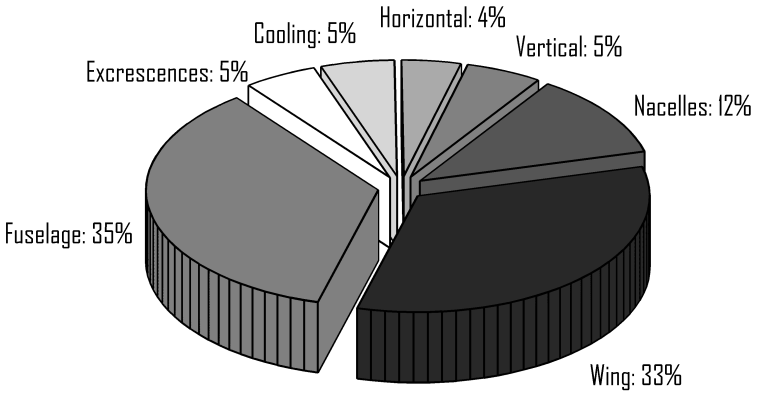

FIGURE 1.13: ATR-72 drag contribution

improved with a more accurate aerodynamic design focused on the aircraft components optimization during these flight conditions. On the other hand climb and ceiling performance are primarily influenced by the drag due to lift and they could be directly improved acting on this drag contribution. In Sec.1.3.2 an ATR-72 performance estimation has been carried out while Sec.1.3.3 shows the influence on the performance of drag reduction.

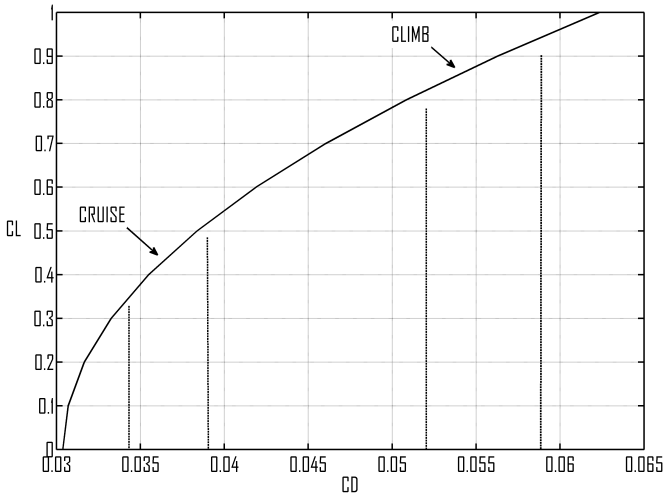

FIGURE 1.14: ATR-72 drag polar

1.3.2 Performance evaluation

A performance analysis of the ATR-72 has been carried out to evaluate possible improvements due to drag reduction. The performance analysis is based on the evaluation of required and available power. The ATR-72 is equipped with 2 Pratt&Whitney Canada PW127F engines and Hamilton Standard six blade 568F propellers with maximum horse power $P_0 = 2750hp$ and a propeller efficiency of $\eta = 0.85$ (see Tab. 1.4). Typical turboprop engine horse power ratio (for a cruise rating) used for performance evaluation is shown in Fig. 1.15. The estimated performance are summarized in Tab. 1.5 [10]. Typical 200 nm mission has been assumed as reference, ground performance have been estimated in standard condition at sea level and fuel consumption has been evaluated also considering weight variation during the mission.

[10]Performance have been evaluated according Ref. [11]. All the used data are summarized in Tab. 1.4 and Fig. 1.12. Engine rating during Climb is 10% higher than cruise shown in Fig. 1.15

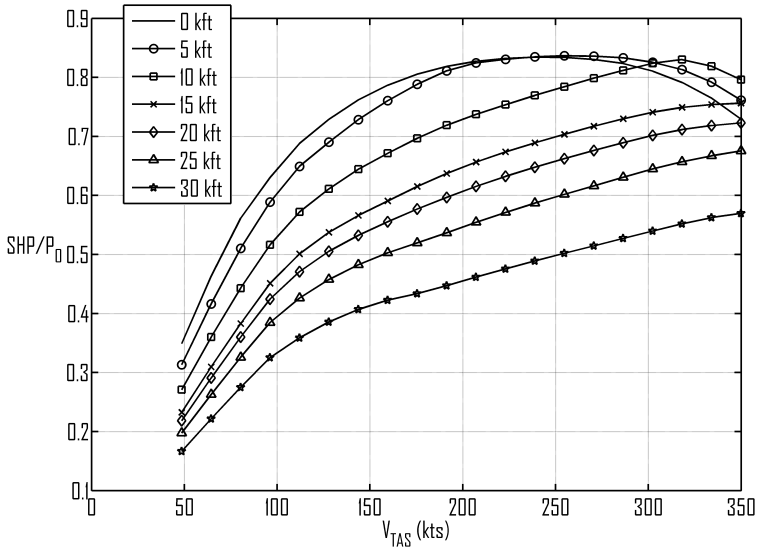

FIGURE 1.15: Turboprop power ratio

TABLE 1.5: ATR-72 Estimated performance

Performance	
FAR S_{TO} (ft)	4065
FAR S_{LAN} (ft)	3176
R/C s.l. AEO (ft/min)	1437
R/C 10 kft AEO (ft/min)	1063
R/C s.l. OEI (ft/min)	345
R/C 10 kft OEI (ft/min)	209
Net Ceiling AEO (ft)	23561
Net Ceiling OEI (ft)	10968
Maximum V_{TAS} at 20kft (kts)	262
Fuel consumption for a 200 nm mission (kg)	594

1.3.3 Performance improvements due to drag reduction

Assuming as reference values for the zero lift drag coefficient shown in Fig. 1.12 $C_{D_0} = 0.0306$ and Oswald factor $e = 0.85$, the influence of these two parameters improvement on the performance has been investigated.

1.3.3.1 Zero lift drag coefficient reduction

Aircraft performance have been evaluated according to Ref. [11] varying the zero lift drag coefficient of ± 15 drag counts. Figure 1.16 and Fig. 1.17 show variation of maximum true airspeed and fuel consumption respect to the reference conditions shown in 1.3.2. A C_{D_0} reduction of 10 drag counts leads to a maximum speed improvement of about 4 knots at typical cruise flight

altitude (15 to 20 kft). It is possible to say that for each knot of maximum true airspeed improvement it is necessary a drag reduction of about 2.5 drag counts. Figure 1.17 shows that a drag reduction of about 15 knots leads to a fuel consumption reduction of about 3% on the typical mission of 200 nm shown in the same figure legend. Climb performance are slightly modified in the range of C_{D_0} variation with values around 1%.

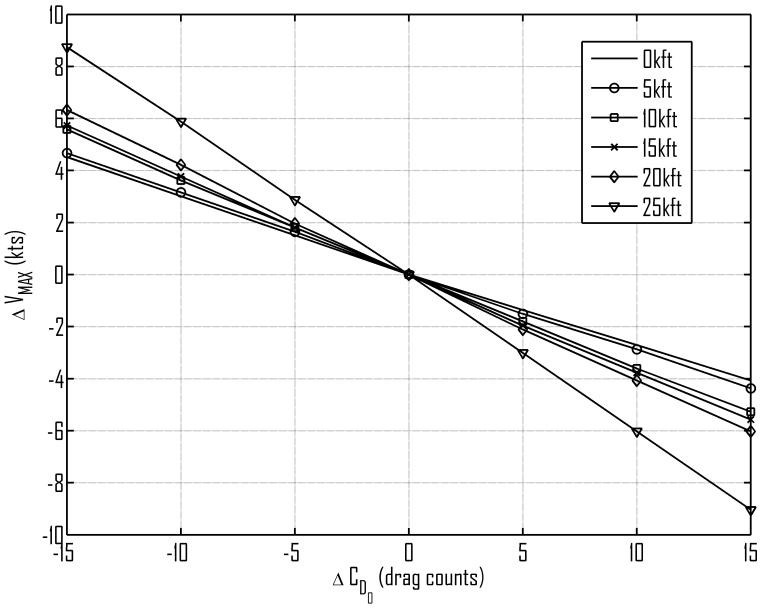

FIGURE 1.16: Maximum true airspeed variation due to zero lift drag coefficient

1.3.3.2 Oswald factor improvement

Equation 1.1 shows the typical parabolic drag polar approximation where the Oswald's factor (e) appears. This term could be especially improved with an accurate wing design, carefully controlling the wing span loading. A typical approach to improve it is to provide wing of particular wingtip devices, the winglet, aiming the reduction of induced drag, which is responsible for 30% of the total drag of a transport aircraft during its standard mission. The author have gained experience in winglet design and further analyses are under development as shown in Ref. [12–16]. Section 3.6 is dedicated entirely to the winglet design of turboprop aircraft. Ignoring how *Oswald factor* can be improved, the influence of this parameter has been analysed varying e of $\pm$ 20% respect to the reference value of 0.85 and $C_{D_0} = 0.0306$.

Figure 1.18 shows the maximum true airspeed variation due to Oswald factor percentage change. As it can be seen the effects are not linear (of course the induced drag contribution depends from C_L^2 and the improvements in the V_{MAX} are smaller than the reductions at equal range of Oswald factor

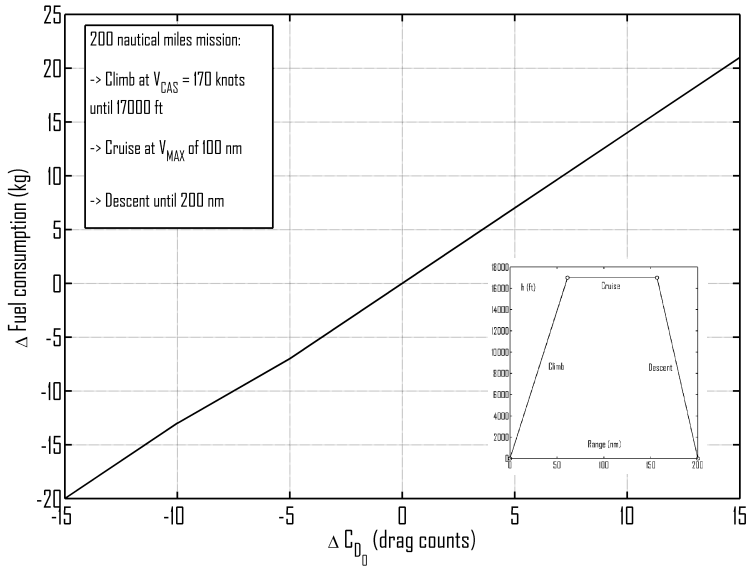

FIGURE 1.17: Fuel consumption variation due to zero lift drag coefficient

variation. It has to be noted that a gain in e can be associated in practice to an increase in the zero lift drag coefficient, as it happens with winglets installation, and it is not taken into account in these calculations. Results show that an Oswald factor improvement of about 10% could increase maximum speed of about 2-4 knots. This is even more evident on high wing loading aircraft where cruise lift coefficient is about 0.5. Improvements on the Oswald factor leads to also a fuel consumption reduction as shown in Fig. 1.19. Fuel consumption decreases during the whole flight conditions, especially during climb. As it can be seen a 10% of e improvement yields a fuel consumption reduction on a typical 200 nm mission of about 20 kg (3% of the total mission consumption). As it has been shown in Fig. 1.14, the major improvements due to Oswald factor could be achieved in climb condition. Figure 1.20 and 1.21 show rate of climb and ceiling altitude variation due to e respectively. Dashed lines represent OEI conditions while solid line the AEO conditions. Again variations are not linear and decreases are greater than increases. It is evident that higher variations are in one engine inoperative conditions, in particular in Fig. 1.20 the R/C_{OEI} can be improved of about 30% with an Oswald factor increment of 10%. Ceiling altitude performance is also very important because it can or cannot preclude some airlines routes. A net ceiling improvement of about 10% means an altitude limit increasing of more than 1000 ft.

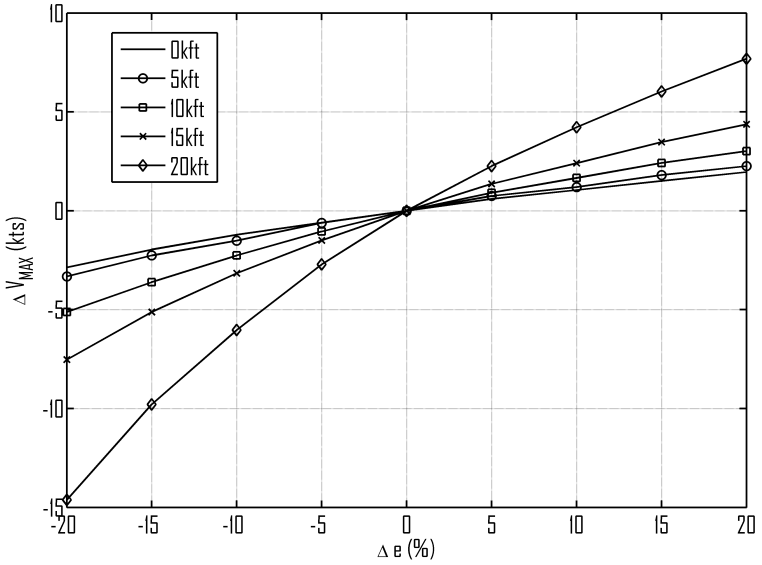

FIGURE 1.18: Maximum true airspeed variation due to Oswald factor e

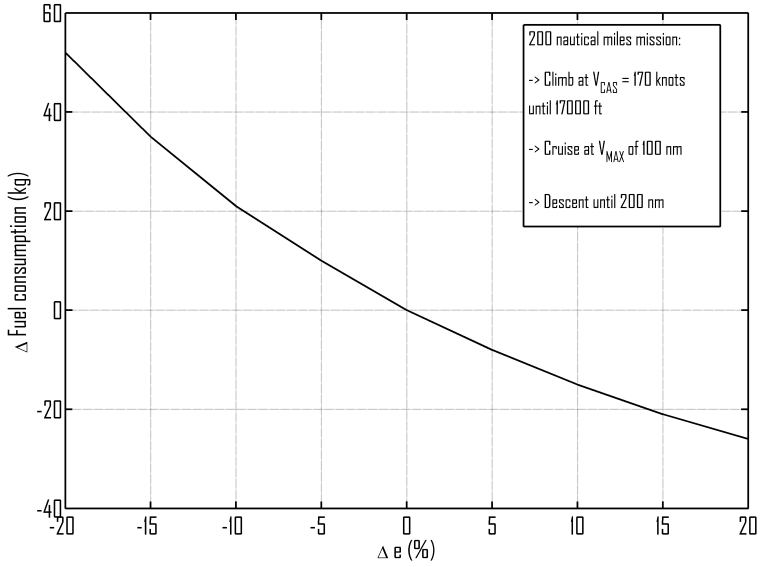

FIGURE 1.19: Fuel consumption variation due to Oswald factor e

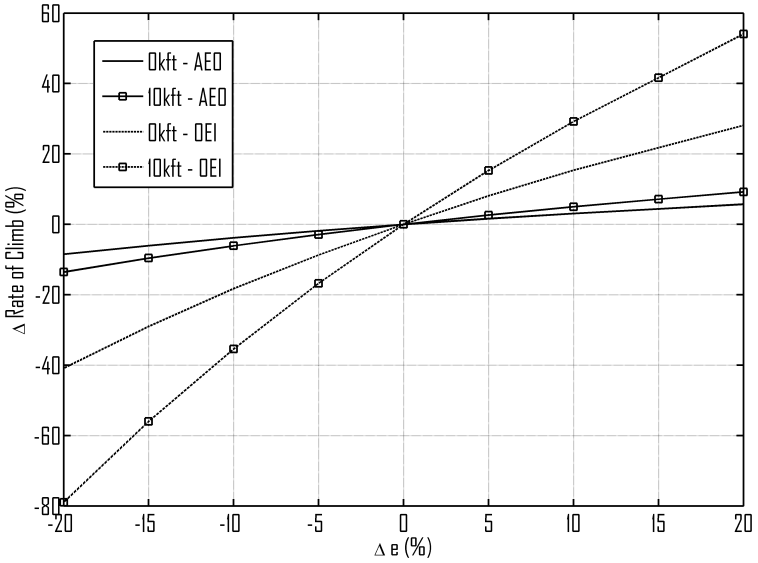

FIGURE 1.20: Maximum rate of climb variation due to Oswald factor e

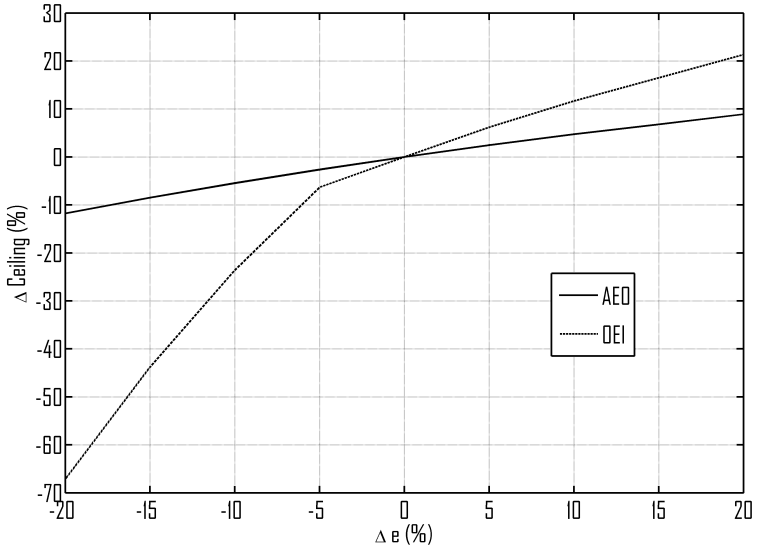

FIGURE 1.21: Ceiling altitude variation due to Oswald factor e

1.4 Goals and Structure of this research work

The market challenges discussed above constitute the motivations at the basis of this research work. Indeed, the main goal of this work consists of the development of methodologies and instruments able to sustain the aerodynamic design of new turboprop and commuter aircraft. Such design methods and tools should facilitate and improve the aerodynamic of turboprop and commuter aircraft design with the aim to improve performance during the entire flight envelope.

The description of the work has been structured as follows:

Chapter 2 In this chapter the development of an airfoil optimization tool, named AOT, is introduced. This tool is fully embedded into MATLab environment and can easily managed via graphical interface (GUI) or via input text file (see Appendix A for any clarification). The AOT allows the constrained multi-objectives optimization of any airfoil geometry through three different aerodynamic solvers: Xfoil, MSES and Fluent. Different geometry parameterization techniques are described and implemented, highlighting the pros and cons of each ones and three optimization algorithm can be used in the process. This tool has been extensively tested and used also for industrial applications and main results have been published into this research work.

Chapter 3 This chapter is fully dedicated to some particular aircraft components design and optimization: fuselage nose, wing-fuselage junction, undercarriage vane and wing-tip devices. An accurate design of these components can lead to non negligible improvements in aircraft performance and it could establish new aerodynamic guidelines in the design of modern aircraft models. Also in this case a tool has been developed into MATLab environment which allows to import, optimize and export CAD useful file of a particular aircraft component. NURBS geometry technique has been implemented and used into the optimization loop, while an available three dimensional panel code aerodynamic solver has been used for the aerodynamic analysis to evaluate the objective function. Particular attention has been aimed to the effect of the optimization on the aircraft performance, highlighting improvements for level flight, climb and ground performance.

Chapter 4 A new semi-empirical methodology to design and analyze the vertical tail for stability and control has been carried out and it is described into Chapter 4. The method, named VeDSC, is build up through more than 300 CFD Navier-Stokes aerdynamic analysis.

Typical semi-empirical methodologies to design the vertical tailplane, as USAF DATCOM and ESDU, have been compared in parametric studies. The two methods lead to close results for certain aircraft configurations, but are quite different for other configurations, e.g. those providing the horizontal stabilizer mounted in fuselage, giving differences up to 20-40%.

To perform with a higher level of accuracy and reliability the estimation of vertical tail contribution several CFD analyses were planned on a modular

configuration with different size and position of aircraft components. About 300 CFD analyses were executed to better understand the aerodynamic interference among aircraft components for configurations derived from a regional turboprop. Comparison between new methodology and semi-empirical methods shows that both DATCOM and ESDU methodologies tend to overestimate (respect to VeDSC) the interference effects, especially those due to low-wing position and horizontal tailplane position. The new methodology has been also used in the preliminary design of the new commuter aircraft Tecnam P2012.

Chapter 5 Finally in this chapter the main achievements of this research work are summarized and some conclusions are drawn.

Chapter 2

Airfoil Design and Optimization

2.1 Introduction

Airfoil shape optimization is today a common practice used in several design engineering field. As outlined by Song and Keane [17] the airfoil aerodynamic design can be divided into two main approaches: Inverse Design (ID) and Direct Numerical Optimization (DNO). The first method relates to search an airfoil shape to satisfy a fluid-dynamic characteristic (such as the pressure or the skin friction distribution). On the other hand, DNO methods couple a geometry definition and aerodynamic analysis code in an iterative process to produce optimum design subject to various constraints. However both the approaches share the need to modify an airfoil geometry to achieve a goal. Depending on whether the goal is a small local airfoil modification or a completely new design, different methods of shape parameterization must be employed. In this research work the DNO approach will be carried out and three different parameterization techniques will be addressed.

The geometry definition must be subsequently coupled with an optimization technique, which must properly take into account for the airfoil parametrization. Optimization algorithm has to be considered as a driver of the optimization process under such constraints and conditions. In the literature, a lot of optimization methods [18–21] have been proposed and developed, often starting from theoretical concepts and logics very far each others. In general it is very difficult to state which method is the best because each one has several advantages and, at same time, disadvantages; just referring to a particular application, or problem, it is possible to operate this choice.

Finally a crucial role is played by the aerodynamic solver employed to evaluate the objective function. Again it is not possible to a priori establish if a solver is better than another, but it is necessary to well define which is the objective to be reached, and, on the basis of this consideration, which is the better aerodynamic solver able to predict the objective function.

In this work an *Airfoil Optimization Tool* (AOT) has been developed in MATLab environment. Appendix A shows some details of this tool. AOT is a multi objective, constrained airfoil optimization tool. It can be used via graphical user interface or via batch mode. It embeds three different geometry parameterization methods (Bezier, Legendre and PARSEC), three different optimization techniques (Gradient based, Genetic Algorithm and NashGA Algorithm) and three different aerodynamic solvers (Xfoil, MSES ans Fluent). The user have to choose the parameterization technique, then he/she can choose geometrical and aerodynamic constraints, optimization technique, conditions of analysis and kind of aerodynamic solver for each condition. Finally the user builds up the objective function in terms of airfoil aerodynamic coefficients. AOT structure is illustrated in the Fig. 2.1.

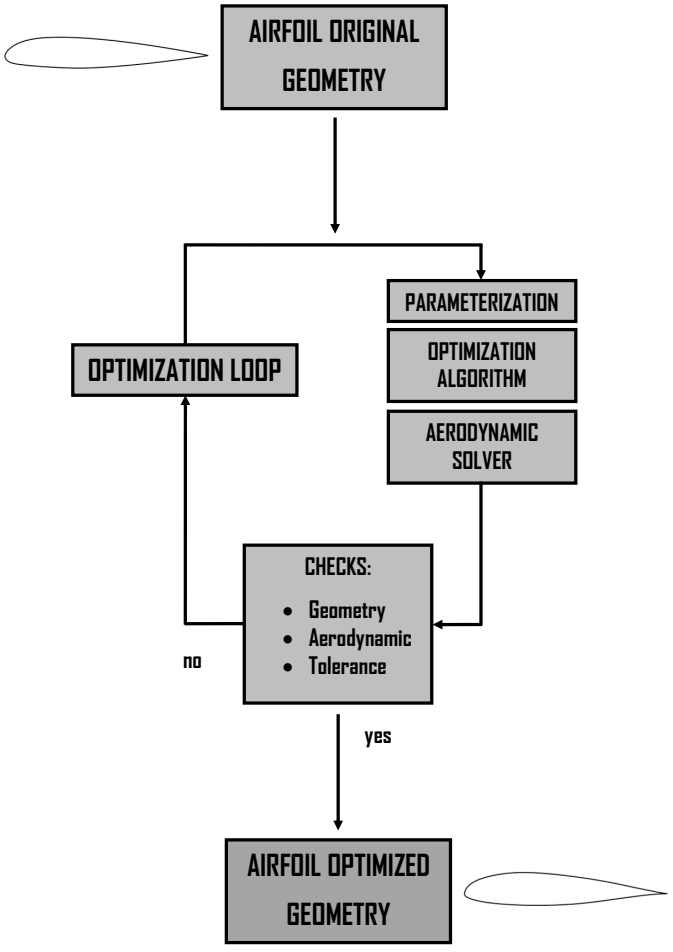

FIGURE 2.1: Direct Numerical Optimization scheme

2.2 Geometry Parameterization

A right question could be why is airfoil parameterization useful or necessary? The answer should be primarily because variables must be reduced. As a matter of fact an airfoil is given by its coordinates, typically a set of 150-200 points; evidently, it is not possible to use directly the airfoil's coordinates as design variables due to their high numbers and to difficulty to control airfoil shape. So in order to reduce variables' number able to completely describe airfoil's shape without loss, the above mentioned parameterization techniques have been introduced.

In the literature several airfoil parameterization methods can be found, one more suitable than other depending on whether the goal is a small local airfoil modification or a completely new design. A survey on parameterization method can be seen in Samareh [22]. Local airfoil shape modifications are usually obtained by smooth perturbations of the original airfoil coordinates through analytical function, such as Legendre, Chebischev or Bernstein polynomials [23–25]. This methods have the advantages to have smooth local modifications but they have not direct geometry relationship and sometimes lead to undulating curves [25]. The design of a new concept airfoil needs a parameterization method able to accommodate a wider range of new shapes. B-splines and Bezier curves have been widely used to fit airfoil shapes via interpolation methods [26, 27]. These methods are very useful to reconstruct and optimize an airfoil (using several artifices on geometry curvatures) but they lead to some problems due to the difficulties to control the relative control points position (see also [27]). Analytical functions have also been derived to represent families of airfoils, for example, in the work reported by Hicks and Henne [28]. Although this method results very powerful to represent several families of airfoil, it cannot be useful in a radical new concept design. More physically intuitive method is to use typical airfoil parameters to define the airfoil shape such as leading edge radius, airfoil thickness or trailing edge angle. A methodology of this type is presented by Sobieczky in [29, 30]. This method uses 11 parameters to represent an airfoil. These parameters are directly linked to the airfoil geometry (thickness, curvature, maximum thickness abscissa, etc.) and they indicate to a designer the real concept of which will be the airfoil shape. The main problems of this parameterization technique is the difficulty to build up a datum airfoil and the capability to radically modify the input airfoil. However it is not possible to establish a priori if a technique is better than another and this strongly depend on which are the goals.

In this work three different parameterization approaches have been considered:

- Bezier Curves
- Legendre Polynomials
- PARSEC Method

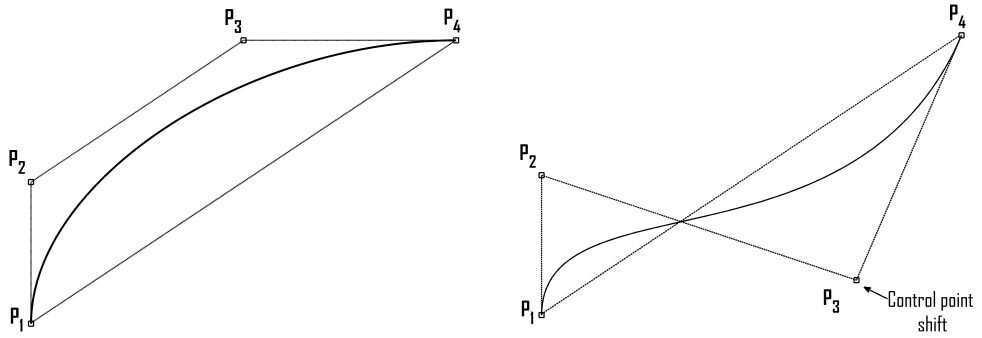

(a) Standard Curve (b) Modified Curve

FIGURE 2.2: Single 3^{rd} order Bezier curve

2.2.1 Bezier Curves

Bezier Curves airfoil parameterization is based on the Bernstein expression of 3^{rd} order Bezier curve, shown in Eq. 2.1.

$$P(t) = P_1(1-t)^3 + 3P_2t(1-t)^2 + 3P_3t^2(1-t) + P_4t^3, \quad t \in [0,1] \qquad (2.1)$$

The points P_1, P_2, P_3 and P_4 are the control points of the Bezier curve and the convex polygon defined by them is known as Bezier polygon as shown in Fig. 2.2. In order to build a Bezier curve, its four coefficients P_1, P_2, P_3 and P_4 are necessary. These four coefficients represent the coordinates of the control points of the polygonal domain that contains the curve. Main Bezier curves properties are following summarized:

- External control points (such as P_1 and P_4 in Fig. 2.2) coincide with coordinate begin and end curve
- Segment $P_1 - P_2$ and $P_3 - P_4$ are equivalent to the tangents at the beginning and at the end of the curve
- The curve is inside the convex domain generated by the control points

A single control points movement affects all the curve. In order to achieve local modifications and better reconstruct a datum airfoil, four 3^{rd} order Bezier curves have been used to build up a single geometry as suggested in Ref. [27]. In this way the airfoil geometry is divided in four sectors and an independent Bezier curve is used for each sector. Figure 2.3 shows the four 3^{rd} order Bezier curves used in the optimization tool. Limits points of the four curves have been fixed in leading edge, trailing edge and upper and lower coordinate as shown in Fig. 2.3. With reference at Fig. 2.3, the control points from 1 to 4 cover the first sector, the control points from 4 to 7 the second sector, the control points from 7 to 10 the third one, the control points from 10 to 13 the fourth one. The control points 4, 7 and 10 are intersections between different Bezier

curves and they should be managed in a special way as shown in Ref. [27]. The

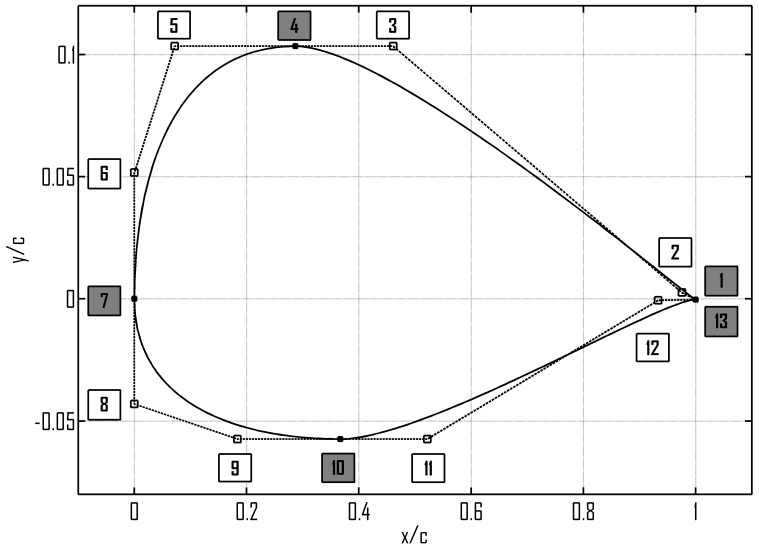

FIGURE 2.3: Bezier airfoil geometry reconstruction

airfoil is therefore completely defined by a set of 13 control points instead of n-points of the original one. The variation of such control points can be easily managed and controlled so that, at every iteration of the optimization process, a new geometry can be obtained just varying the position of one control point. This reconstruction has been applied at every iteration where a shift in x or y coordinate has been imposed to the original control points in order to obtain a new set of 13 control points that uniquely define a new airfoil geometry to test. As highlighted by Grasso in Ref. [27] the 3^{rd} order Bezier curves offer a very general approach to obtain smooth airfoil geometries, especially for typical aeronautical airfoil used for commuter aircraft. Figure 2.4 shows three airfoils geometry reconstruction through Bezier technique the NACA 23015, NACA 0012 and Selig S809 respectively. Typical commuter aircraft airfoils such as NACA 4 and 5 digits are well approximated via Bezier piecewise approach, while the approximation quality becomes lower for particular airfoil such as the S809 shown in Fig. 2.4. In this case approximation difficulties are related to several inflection points and very low leading edge radius. To avoid these problems other approaches can be taken into account. The connection points between two consecutive Bezier curves has been treated as suggested in [27]. However for standard NACA airfoil Bezier parameterization is reliable and very useful to explore a wide space of analysis.

2.2.2 Legendre Polynomials

Another type of reconstruction used in the optimization process deals with Legendre polynomials as suggested by Hicks and Vanderplaats in Ref. [23].

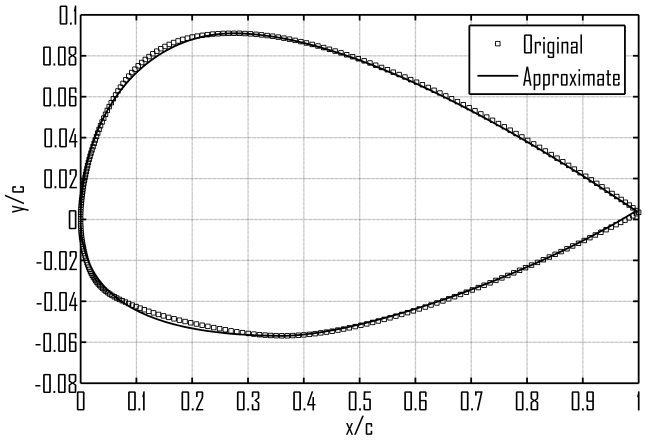

(a) NACA 23015 airfoil

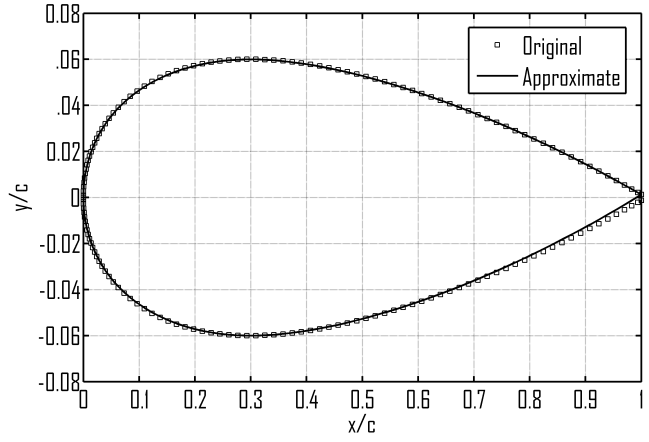

(b) NACA 0012 airfoil

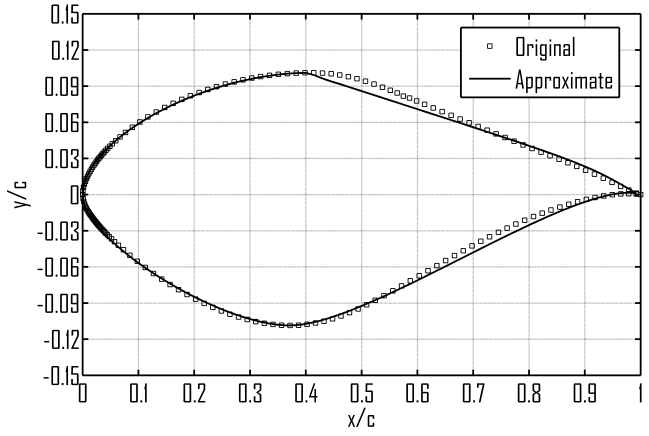

(c) Selig S809 airfoil

FIGURE 2.4: Bezier airfoil approximation, piecewise technique

A Legendre polynomial is a function that satisfies the Legendre's differential equations whose expression is shown in Eq. 2.2:

$$\frac{\mathrm{d}}{\mathrm{d}x}\left[(1-x^2)\frac{\mathrm{d}}{\mathrm{d}x}P(x)\right]+n(n+1)P(x) \tag{2.2}$$

The ordinary differential equation is quite frequent in mathematics and physics since it allows to solve Laplace's equation in spherical coordinates and several partial derivative differential equation. Legendre's differential equation can be solved through standard methods applying power series so that converging solutions are obtained if $|x|<1$. Converging solutions are obtained also if $x=\pm 1$ and n is a natural integer (i.e. $n=0,1,2,...$). In such cases the solutions according to n form a polynomial succession called Legendre's polynomials succession. The generic Legendre's polynomial $P_n(x)$ of n degree can be expressed through the following Eq. 2.3:

$$P_n(x)=(2^n n!)^{-1}\frac{\mathrm{d}^n}{\mathrm{d}x^n}[(x^2-1)^n] \tag{2.3}$$

Several artifices have been adopted in order to use Legendre's polynomials for the optimization process according to Ref. [23]. Airfoil thickness distributions are given by summing a perturbation on the original geometry as shown in Eq. 2.4:

$$y(x)_{new}=y(x)_{old}+\Delta y(x)_{(up/low)} \tag{2.4}$$

where $y(x)_{old}$ represents the original airfoil y coordinate and Δy the perturbation term for the upper and lower surfaces ordinates. This term is evaluated according to Eq. 2.5:

$$\begin{aligned}\Delta y(x)_{up}=(1-x)^3\big[&\sqrt{a_1 x}+a_2\,(P_2+1)+a_3\,(P_3-1)\\&+a_4\,(P_4+1)+a_5\,(P_5-1)+a_6\,(P_6+1)\big]\end{aligned} \tag{2.5}$$

$$\begin{aligned}\Delta y(x)_{low}=(1-x)^3\big[&\sqrt{b_1 x}+b_2\,(P_2+1)+b_3\,(P_3-1)\\&+b_4\,(P_4+1)+b_5\,(P_5-1)+b_6\,(P_6+1)\big]\end{aligned} \tag{2.6}$$

where and P_2 , ..., P_6, are Legendre polynomials given by Eq. 2.7 and shown in Fig. 2.5. The coefficients a_1,..., a_6 and b_1,...,b_6 are the design variables perturbed by the optimization program to achieve optimum design. The square root term in Eq. 2.5 and 2.6 allows a blunt leading edge and assures matching of upper-surface and lower-surface derivatives of all orders at the leading edge. The term $(1-x)^3$ allows to optimize the airfoil in a chosen chord range. This

term could be removed by specifying that the whole airfoil has to be optimized.

$$\begin{aligned} P_2 &= 2x - 1 \\ P_3 &= 6x^2 - 6x + 1 \\ P_4 &= 20x^3 - 30x^2 + 12x - 1 \\ P_5 &= 70x^4 - 140x^3 + 90x^2 - 20x + 1 \\ P_6 &= 252x^5 - 630x^4 + 560x^3 - 210x^2 + 30x - 1 \end{aligned} \tag{2.7}$$

As a matter of fact if Bezier curves allow to entirely modify the airfoil through

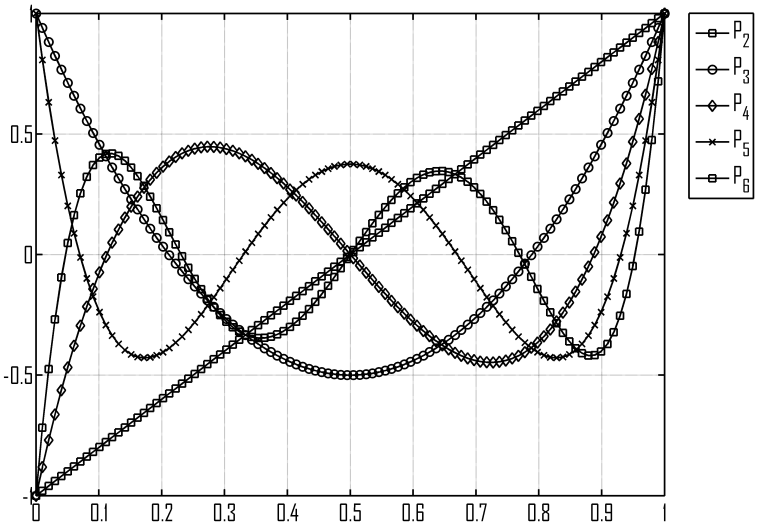

FIGURE 2.5: Legendre polynomials

its reconstruction, Legendre's polynomials also allow to restrict the modification to particular chord length. Once chosen that length, the modification involves just the y coordinates whereas the x coordinates remain unaltered. Legendre's polynomials parameterization approach is very useful when local airfoil modifications and optimization have to be performed starting from an original geometry not reconstructed (such as it happens with Bezier (Sec. 2.2.1) or PARSEC (Sec. 2.2.3) techniques). Figure 2.6 shows three example of Legendre parameterization technique applied to airfoil optimization. Figure 2.6(a) shows a Legendre polynomials approach on a NACA 23015 airfoil. Abscissa variation range is $\pm 1\%$ of the chord and 30% length. Figures 2.6(b) and 2.6(c) show different range space and chord length modifications on S809 and S1223 airfoil respectively. Legendre's polynomials parameterization could be very useful to optimize these airfoil geometry, characterized to very high airfoil camber, very small airfoil leading edge radius and low trailing edge angle. As highlighted in Ref. [23] airfoils developed during the optimization process using Legendre polynomials approximation may exhibit minor imperfections (e.g. reflexed curvature). In this work no attempt was made to eliminate such

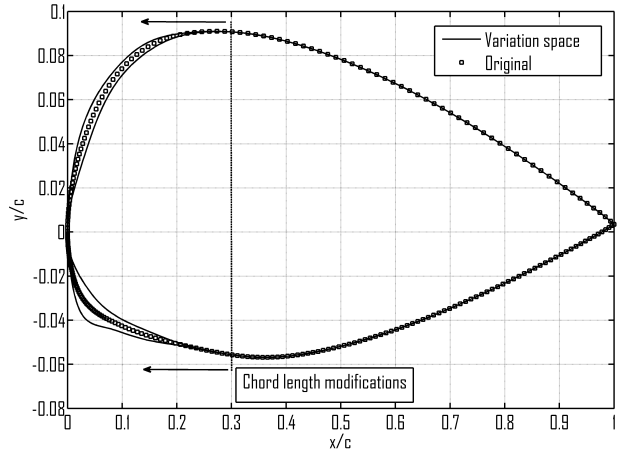

(a) NACA 23015 airfoil, range variation ±1% of c

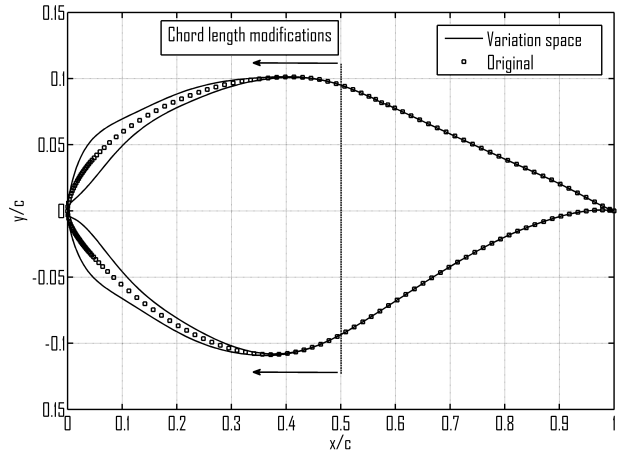

(b) S809 airfoil, range variation ±2% of c

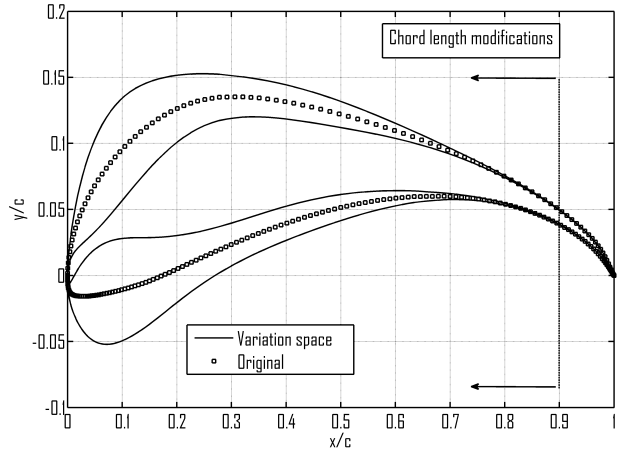

(c) S1223 airfoil, range variation ±5% of c

FIGURE 2.6: Legendre's airfoil modification, small perturbation technique

minor flaws since the primary purpose of this effort was to demonstrate a technique rather than to finalize the design of specific airfoils. Irregularities and imperfections could be easily eliminated by additional constraints on the airfoil geometry or by modifying expression for the thickness distribution of Eq. 2.5 and 2.6.

2.2.3 PARSEC Method

The PARSEC airfoil shape parameterization as proposed by Sobieczky [29, 30] uses eleven parameters to represent an airfoil. In Figure 2.7 it is shown the PARSEC variables definition, summarized in Tab. 2.1. Parsec analytical

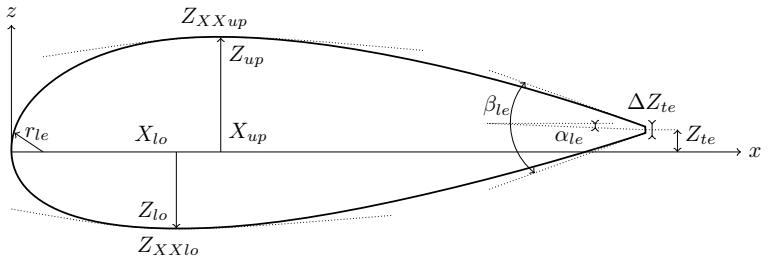

FIGURE 2.7: PARSEC variable definition

TABLE 2.1: PARSEC parameters definition

PARSEC Parameter	Geometry Parameter	Definition
p_1	r_{le}	leading edge radius
p_2	X_{up}	upper crest position in horizontal coordinates
p_3	Z_{up}	upper crest position in vertical coordinates
p_4	$Z_{XX_{up}}$	upper crest curvature
p_5	X_{lo}	lower crest position in horizontal coordinates
p_6	Z_{lo}	lower crest position in vertical coordinates
p_7	$Z_{XX_{lo}}$	lower crest curvature
p_8	Z_{te}	trailing edge offset in vertical sense
p_9	ΔZ_{te}	trailing edge thickness
p_{10}	α_{te}	trailing edge direction
p_{11}	β_{te}	trailing edge wedge angle

formulation is shown in Eq. 2.8

$$y_{up} = \sum_{i=1}^{n=6} a_{up}^{i} \cdot x^{i-\frac{1}{2}},\ y_{lo} = \sum_{i=1}^{n=6} a_{lo}^{i} \cdot x^{i-\frac{1}{2}}, \tag{2.8}$$

where y_{up}, y_{lo} are, respectively, the ordinate of the upper and lower surface, x is the horizontal, or chordwise, coordinate normalised in $[0, 1]$. The coefficients a_{up}, a_{lo} are to be computed by using the 11 given parameters as follows Eq. 2.9

$$C_{up} \times a_{up} = b_{up},\ C_{lo} \times a_{lo} = b_{lo} \tag{2.9}$$

where both coefficient matrices (C_{up}, C_{lo}) and right hand sides (b_{up}, b_{lo}) are defined as shown in Eq. 2.11

$$C_{up} = \begin{bmatrix} 1 & 1 & 1 & 1 & 1 & 1 \\ p_2^{\frac{1}{2}} & p_2^{\frac{3}{2}} & p_2^{\frac{5}{2}} & p_2^{\frac{7}{2}} & p_2^{\frac{9}{2}} & p_2^{\frac{11}{2}} \\ \frac{1}{2} & \frac{3}{2} & \frac{5}{2} & \frac{7}{2} & \frac{9}{2} & \frac{11}{2} \\ \frac{1}{2}p_2^{-\frac{1}{2}} & \frac{3}{2}p_2^{\frac{1}{2}} & \frac{5}{2}p_2^{\frac{3}{2}} & \frac{7}{2}p_2^{\frac{5}{2}} & \frac{9}{2}p_2^{\frac{7}{2}} & \frac{11}{2}p_2^{\frac{9}{2}} \\ -\frac{1}{4}p_2^{-\frac{3}{2}} & \frac{3}{4}p_2^{-\frac{1}{2}} & \frac{15}{4}p_2^{\frac{1}{2}} & \frac{35}{4}p_2^{\frac{3}{2}} & \frac{63}{4}p_2^{\frac{5}{2}} & \frac{99}{4}p_2^{\frac{7}{2}} \\ 1 & 0 & 0 & 0 & 0 & 0 \end{bmatrix} \tag{2.10}$$

$$b_{up} = \begin{bmatrix} p_8 + p_9/2 \\ p_3 \\ \tan(p_{10} - p_{11}/2) \\ 0 \\ p_4 \\ \sqrt{2p_1} \end{bmatrix},\ b_{lo} = \begin{bmatrix} p_8 - p_9/2 \\ p_6 \\ \tan(p_{10} + p_{11}/2) \\ 0 \\ p_4 \\ \sqrt{2p_1} \end{bmatrix}, \tag{2.11}$$

where coefficient matrix C_{up} (C_{lo}) depends only on p_2 (p_5) (simply using lo and 5 as subscript in Eq. 2.11) , while the righ hand sides b_{up}, b_{lo} differ for the use of p_3 instead of p_6 and parameters addiction/subtraction.

A generic airfoil can be completely defined by using the 11 PARSEC parameters. Figure 2.8 shows three examples of PARSEC airfoil approximation. As it can be seen this parameterization does not fit very well the original coordinate. However it gives the possibility to the designer to define an airfoil through its fundamental parameters which could be easily related to airfoil performance. On the basis of this consideration, in this work the PARSEC parameterization technique has been coupled with an innovative optimization algorithm developed by Mallozzi et alii in Ref. [31, 32] at the University of Naples.

2.3 Optimization Algorithms

Numerical optimization process aims to solve a nonlinear, constrained problem to find the set of design variables, X_i, i = 1,...,N, contained in vector X that

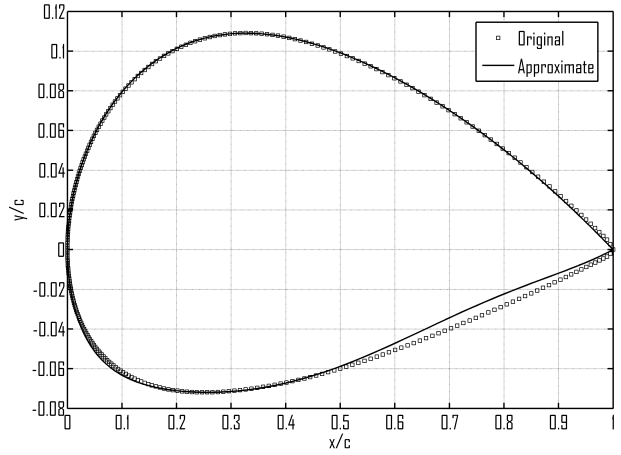

(a) NACA 2418 airfoil

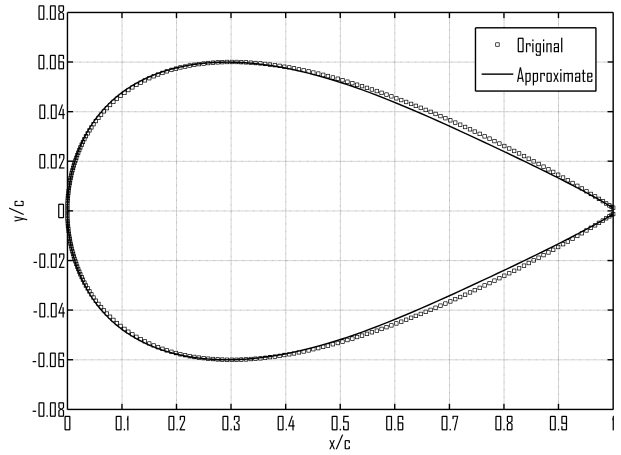

(b) NACA 0012 airfoil

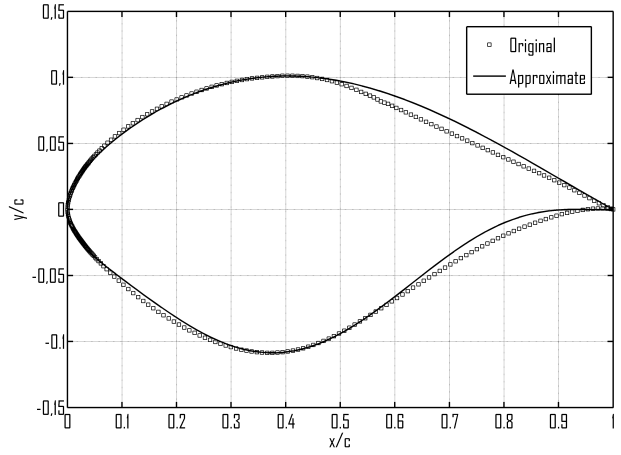

(c) S809 airfoil

FIGURE 2.8: Legendre's airfoil modification, small perturbation technique

will satisfy:

$$minimize \quad F(X) \tag{2.12}$$

subject to:

$$g_j(X) \leq 0 \qquad j = 1, M \tag{2.13}$$

$$g_k(X) \leq 0 \qquad k = 1, L \tag{2.14}$$

$$X_i^L \leq X_i \leq X_i^U \qquad i = 1, N \tag{2.15}$$

Equation 2.12 defines the objective function which depends on the values of the design variables, X. Equations 2.13 and 2.14 represent inequality and equality constraints respectively, and Eq. 2.15 defines the region of search for the minimum. The bounds defined by Eq. 2.15 are referred to as side constraints. In this research work MATLab standard optimization algorithm have been used (GB and GA) while a new optimization algorithm approach, named NashGA, carried out at University of Naples in [31, 32], has been used in particular applications. This algorithm has been also used in aircraft structural application by the author in Ref. [33].

2.3.1 Gradients Based

MATLab GB approach has been used. The function is the *fmincon.m* which attempts to find a constrained minimum of a scalar function of several variables starting at an initial estimate. This is generally referred to as constrained non-linear optimization or non-linear programming. Any details can be found in MATLab user guide[1].

2.3.2 Genetic Algorithm

Also MATLab GA solver algorithm has been used. The function is the *ga.m* which, in the more general condition, finds a constrained minimum of function using genetic algorithm. Any details can be found in MATLab user guide[2].

2.3.3 NashGA Algorithm

The NashGA algorithm has been developed at the University of Naples and well described into Ref. [31, 32]. It consists of a genetic algorithms optimization method to find a Nash equilibrium. The algorithm is organized in several steps following summarized and shown in Fig. 2.9.

1. Creating two different random populations, one for each player only at the first generation. Player 1's optimization task is performed by population 1 and vice versa.

[1]Details on *fmincon.m* can be found in the user guide http://www.mathworks.it/it/help/optim/ug/fmincon.html.

[2]Details on *ga.m* can be found in the user guide http://www.mathworks.it/it/help/gads/ga.html.

2. The classification is made on the basis of the evaluation of a fitness function, typical of GAs, that takes into account the results of matches between each individual of population 1 with all individuals of population 2, scoring 1 or -1, respectively, for a win or loss, and 0 for a draw.

$$\begin{cases} \text{if } f_1(u_i^k, v^{k-1}) > f_1(u^{k-1}, v_i^k), \text{fitness}_1 = 1 \\ \text{if } f_1(u_i^k, v^{k-1}) < f_1(u^{k-1}, v_i^k), \text{fitness}_1 = -1 \\ \text{if } f_1(u_i^k, v^{k-1}) = f_1(u^{k-1}, v_i^k), \text{fitness}_1 = 0 \end{cases} .$$

   Similarly, for player 2:

$$\begin{cases} \text{if } f_2(u_i^k, v^{k-1}) < f_2(u^{k-1}, v_i^k), \text{fitness}_2 = 1 \\ \text{if } f_2(u_i^k, v^{k-1}) > f_2(u^{k-1}, v_i^k), \text{fitness}_2 = -1 \\ \text{if } f_2(u_i^k, v^{k-1}) = f_2(u^{k-1}, v_i^k), \text{fitness}_2 = 0 \end{cases} .$$

   In this way a simple sorting criterion can be established. For equal fitness values individuals are sorted by objective function f_1 for population 1 (player 1) and by objective function f_2 for player 2.

3. A mating pool for parent chromosome is generated and common GA techniques as crossover and mutation are performed on each player population. A second sorting procedure is needed after this evolution process.

4. At the end of *k-th* generation optimization procedure player 1 communicates his own best value u^k to player 2 who will use it at generation $k+1$ to generate its entire chromosome with a unique value for its first part, i.e. the one depending on player 1, while on the second part comes from common GAs crossover and mutation procedure. Conversely, player 2 communicates its own best value v^k to player 1 who will use it at generation $k+1$, generating a population with a unique value for the second part of chromosome, i.e. the one depending on player 2.

5. A Nash equilibrium is found when a terminal period limit is reached, after repeating the steps 2-4.

The main idea is to couple the PARSEC parametrization method with NashGA equilibrium solution. This approach gives the chance to avoid a more arbitrary and less physically based airfoil geometry partition among the different objective functions (as shown in Ref. [26, 34]), using instead a more engineering reliable variables assignment based on well known airfoil shape parameter.

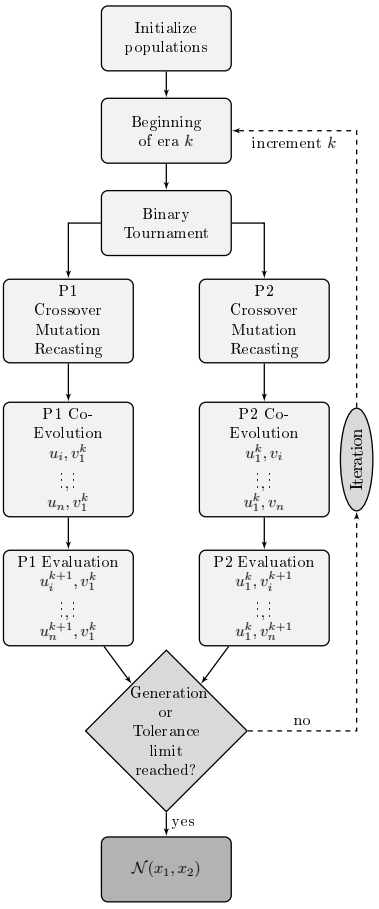

FIGURE 2.9: Nash genetic algorithm structure

2.4 Constraints Selection

The AOT allows to execute a multi-objective constrained optimization. According to the chosen parameterization technique, the optimization tool allows to select upper and lower boundaries of control points in term of percentage shift of the chord length along x and y coordinates. Then geometrical (Sec. 2.4.1) and aerodynamic constrains (Sec. 2.4.2) could be selected by the user in order to perform the desired constrained optimization.

2.4.1 Geometrical constraints

Geometrical constraints are required in airfoil design in order to obtain a more realistic and feasible geometry. Table 2.2 summarizes the AOT geometrical constraints. User can choose which constraints enable or disable through a check box. As it is summarized in Tab. 2.2, the AOT allows to set limitations both on the maximum and minimum thickness. This possibility is very useful in the aircraft design practice. As matter of fact wing design must satisfy several

requirements in terms of systems specifications and structural dimensions. Wing fuel tanks, command lines, wires and cables could require particular geometrical dimensions which must be taken into account during the design. Weight limitations and structural strength could be also considered in this phase. Another important feature is the possibility to set limits on the airfoil trailing edge gap. This fact allows from one hand to avoid upper and lower surface inversion during the optimization process and from the other hand to set a specific value according to the technological process. Finally the airfoil leading edge can be constrained. Once again this feature can be very useful looking forward in a wing design where could be necessary to install on the leading edge particular device (such as anti or de-icing device).

TABLE 2.2: AOT geometrical constraints

Geometrical Constraints	
Maximum thickness	Δy_{max}
Minimum thickness	Δy_{min}
Minimum trailing edge gap	$\Delta y_{t.e.}$
Minimum leading edge radius	$l.e._{radius}$

2.4.2 Aerodynamic constraints

Airfoil aerodynamic constraints are very useful for the designer to establish values of crucial aerodynamic coefficients especially in particular operative conditions. For example in aircraft design by knowing aircraft flight envelope, the designer could require a particular value of the cruise lift coefficient together with a minimization of drag coefficient in the same condition. Another non negligible item in the aircraft design is the value of wing pitching moment coefficient (clearly dependent from wing airfoil pitching moment coefficient). This value directly affects the aircraft tail loads and so the dimension of the tail. This is due to the fact that tail plane (usually the horizontal tail) has to balance a negative value of the wing pitching moment coefficient. If this value increases tail balancing load must increase and so also the horizontal tail geometry must be greater with a consequent weight growth. Table 2.3 shows the AOT aerodynamic constraints that can be used during the optimization process.

TABLE 2.3: AOT aerodynamic constraints

Aerodynamic Constraints	
Minimum pitching moment coefficient	$C_{m_{min}}$
Maximum pitching moment coefficient	$C_{m_{max}}$
Minimum lift coefficient	$C_{l_{min}}$
Maximum lift coefficient	$C_{l_{max}}$

2.5 Objective function

The core of an optimization process is the objective function, often called fitness function. This function can be related to a single objective or multi-objectives. In general a multi-objectives approach gives a more realistic representation of a design problem that involves several design conditions and so several objectives. Moreover this conditions are usually in contrast each other and this fact implies searching a solution as a compromise between design conditions.

In this research work an a priori scalarization approach has been used to perform a multi-objective optimization, without a priori knowledge of objective space. This procedure allows to create a single objective function from a weighted of the (k) multiple objectives a priori defined as shown in Eq. 2.16:

$$\text{Objective function} \quad = \sum_{i=1}^{k} w_i f_i \tag{2.16}$$

where w_i is a weight associated to the i condition and f_i represents the objective function of the i condition. This function is built up by the user by combining the scalar values summarized in Tab. 2.4 through proper weights. Example of most generic single condition objective function is shown in Eq. 2.17

$$\begin{aligned} f_i = &- k_{l_i} s_{f_{l_i}} \mathbf{C_{l_i}} + k_{d_i} s_{f_{d_i}} \mathbf{C_{d_i}} - k_{m_i} s_{f_{m_i}} \mathbf{C_{m_i}} \\ &- k_{E_i} s_{f_{E_i}} \mathbf{E_i} - k_{E_{c_i}} s_{f_{E_{c_i}}} \mathbf{E}_{\text{climb}_\mathbf{i}} \\ &+ k_{l,\text{target}} s_{f_{l,\text{target}}} \mathbf{C}_{\mathbf{l},\text{target}} + k_{E,\text{target}} s_{f_{E,\text{target}}} \mathbf{E}_{\text{target}} \end{aligned} \tag{2.17}$$

where:

- k_{l_i}, k_{d_i}, k_{m_i}, k_{E_i}, $k_{E_{c_i}}$, $k_{l,\text{target}}$ and $k_{E,\text{target}}$: weights for lift coefficient, drag coefficient, moment coefficient, efficiency, climb efficiency, target lift coefficient and target efficiency relative to the i condition, chosen by the user;

- $s_{f_{l_i}}$, $s_{f_{d_i}}$, $s_{f_{m_i}}$, $s_{f_{E_i}}$, $s_{f_{E_{c_i}}}$, $s_{f_{l,\text{target}}}$ and $s_{f_{E,\text{target}}}$: scale factors for lift coefficient, drag coefficient, moment coefficient, efficiency, climb efficiency, target lift coefficient and target efficiency relative to the i condition, to normalize values at the same magnitude, modifiable by the user;

- C_{l_i}, C_{d_i}, C_{m_i}, E_i, E_{climb_i}, $C_{l,\text{target}}$ and E_{target}: scalar values obtained through aerodynamic analysis, shown in Tab. 2.4;

All the scalar values of Tab. 2.4 represent a results of an aerodynamic analysis, directly obtained from an aerodynamic analysis or simply derived(such as for E_i, E_{climb_i}, $C_{l,\text{target}}$ and E_{target}). The estimation of these parameters requires an aerodynamic solver able to well predict the objective, as described, as described in Sec. 2.6.

TABLE 2.4: Objective function scalar values

Scalar value	
Lift coefficient	C_l
Drag coefficient	C_d
Moment coefficient	C_m
Aerodynamic Efficiency	E
Aerodynamic Efficiency during climb	E_{climb}
Target lift coefficient	$C_{l,\text{target}}$
Target aerodynamic efficiency	E_{target}

2.6 Solvers

If the objective function represents the core of an optimization process, it needs an accurate method to evaluate its own scalar parameters. In most general case airfoil performance vary from high speed, low angle of incidence, to very low speed, high angle of incidence. In aircraft design, three main operative conditions are defined which identify three different operative functioning of an airfoil: *i)* cruise, *ii)* climb and *iii)* stall flight conditions. Of course this is a simplification of a more complicated aircraft flight envelope, but the airfoil design process is focused on them. It is well known that airfoil performance estimation is a difficult tasks, especially in high lift, stall and post stall conditions. Others effects concerns to Mach and Reynolds numbers, which also complicate the airfoil performance estimation. To better predict these performance on the more wide possible range of analysis, in this work three aerodynamic solvers have been integrated into the optimization loop: Xfoil [35, 36], MSES [37] and Fluent, each one with some pros and cons features.

XFOIL[3] is an interactive program for the design and analysis of subsonic isolated airfoils written by Prof. Mark Drela. It is very useful, fast and and reliable in low and medium airfoil angle of incidence as shown by Drela [35].

MSES[4] code is a multi-element airfoil analysis and design system based on the Euler equations, written again by Prof. Mark Drela. It is very useful in the analysis and design of high lift devices thanks to its fastness and accuracy.

Ansys Fluent is a Navier-Stokes equations solver. It is very reliable both for low and high angles of attack. It needs of a suitable airfoil computational domain to correctly solve the equations and compared to Xfoil and MSES solvers it needs to more computational time to gives a solution. In Fig. 2.10 the comparison between solvers is shown applied to NACA 23015 airfoil. Experimental data are from Abbott [38]. As it can be seen from Fig. 2.10

[3]Details about Xfoil can be found on the MIT web site at http://web.mit.edu/drela/Public/web/xfoil/.

[4]Details about MSES can be found on the MIT web site at http://web.mit.edu/drela/Public/web/mses/.

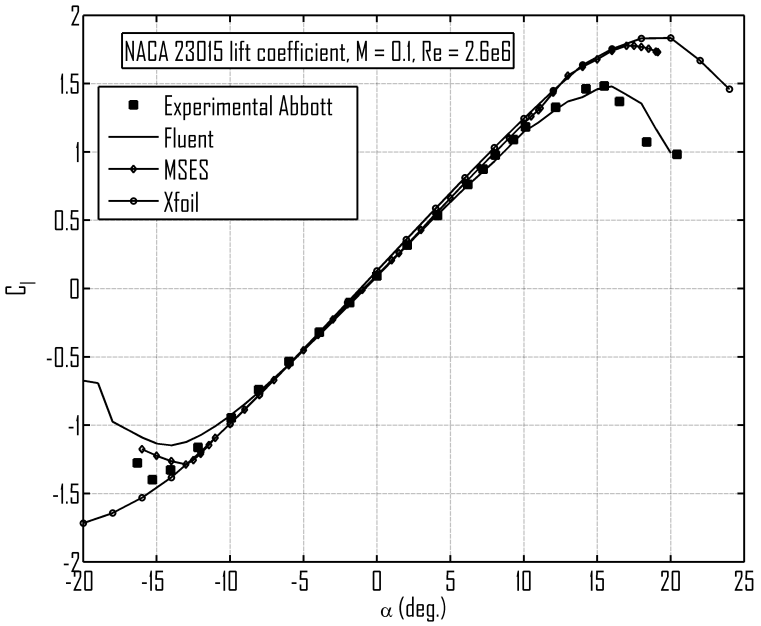

FIGURE 2.10: NACA 23015 lift coefficient, solvers comparison, $M = 0.1$, $Re = 2.6\,10^6$

the three solvers well predict the linear range of the airfoil lift coefficient (i.e. $-10deg. \leq \alpha \leq +10deg.$). Fluent solver well estimates direct stall lift coefficient, while it is not too accurate in reverse stall lift coefficient.

It has to be noted that all the aerodynamic solvers have been completely embedded into the optimization loop, and all the reading and writing operations are not visible to the user. In particular the Fluent solver needs a computational domain creation, the mesh. Once chosen the airfoil to optimize, parameterization technique and termo-fluidynamics conditions, an automated fully structured mesh is created into MATLab environment. To better predict viscous effects, automated boundary layer refinement is carried out, in order to guarantee and y^+ value of magnitude order about 1. For each generated mesh 30 layers are placed into the entire boundary layer thickness. An example of automated generated mesh is shown in 2.11.

2.7 Applications

AOT has been widely tested and applied on several geometries reaching a good confidence on which parameterization - optimization algorithm and aerodynamic solver combination is more suitable than others. In this section only a few examples of AOT applications are shown. It has to be highlighted that several optimized airfoils obtained by using this tool has been also applied in the design of wing and fan blade with very good results.

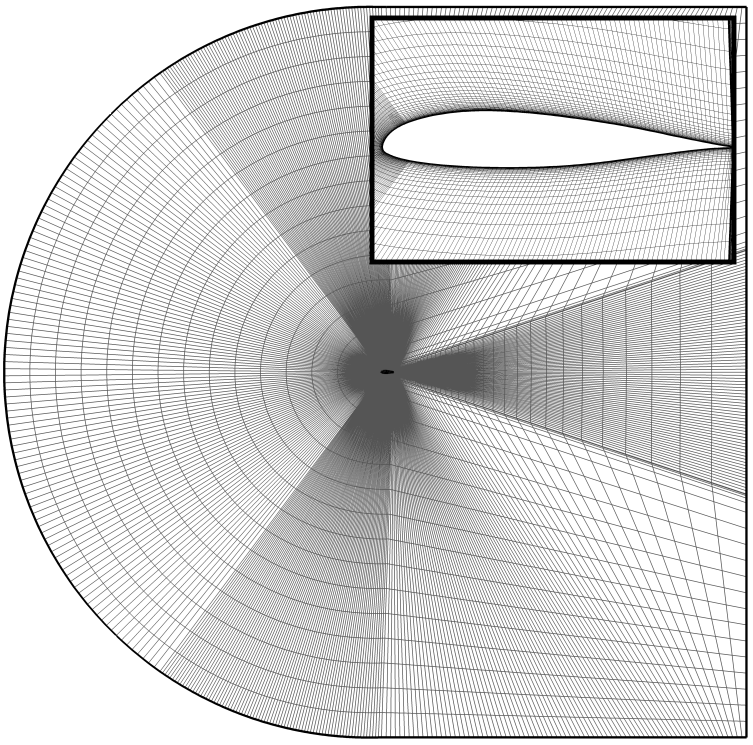

FIGURE 2.11: Automated structured airfoil mesh used in the optimization loop

2.7.1 Single case optimization

In this section results of the single case aerodynamic optimization of a NACA five digits airfoil shown previously in Fig. 2.4(a) are presented and discussed. Several conditions have been analyzed under fixed constraints in order to show the optimization tool capabilities. Paramaterization technique used in these applications has been Bezier curves whereas GB and GA optimization algorithm also have been compared. Aerodynamic reference conditions used in this section are summarized in Tab. 2.5. Geometrical constraint has been applied on the minimum airfoil thickness equal to 14.5 % of the chord. Xfoil and Fluent have been used as aerodynamic solvers.

TABLE 2.5: Reference aerodynamic conditions

Condition		M	Re
Cruise	$\alpha = 2.0$ deg. or $C_l = 0.5$	0.43	$11.5 \cdot 10^6$
Climb	$\alpha = 5.0$ deg. or $C_l = 1.0$	0.30	$7.0 \cdot 10^6$
Stall	α_{stall}	0.15	$4.5 \cdot 10^6$

1. **Low drag in cruise**

The optimization has been performed using aerodynamic condition for cruise indicated in Tab. 2.5. Constraints have been given on the minimum airfoil thickness (14.5% of c) while the objective function has been set equal to the drag coefficient. Several upper and lower bounds have been selected using both GB and GA optimization algorithm and relative results are then reported and discussed. Moreover, Xfoil is selected as the solver (see also Tab. 2.6).

TABLE 2.6: AOT settings, low drag in cruise airfoil optimization

Starting Airfoil	NACA 23015
Algorithm	GA and GB
Objective function	C_d
Condition	Cruise
Geom constraints	$\Delta y_{min} = 0.145$
Aero constraints	fixed transition at x/c = 0.05
Solver	Xfoil
Parameterization	Bezier
Results	
C_d Initial	0.00761
GA	
C_d Optimal	0.00702
Elapsed time (min)	$5'01''$
Objective eval. calls	601
GB	
C_d Optimal	0.00710
Elapsed time (min)	$4'40''$
Objective eval. calls	565

Results are summarized in Fig. 2.12 and Tab. 2.6. Boundaries of Bezier parameters vary between 0 and 0.08. Both the optimization algorithm converge to similar results, with a comparable number of iterations (565 for GB and 601 for GA). Improvements in drag coefficient has been about 5-6 drag counts, for fixed transition. It has to be noted that lift and pitching moment coefficient are respectively lowered from 0.384 to 0.351 and from -0.0061 to -0.0099 for the best obtained results.

2. **High efficiency in climb**

In flight mechanics efficiency in climb is the term $C_l^{3/2}/C_d$ and it has been set as single objective function. Geometric constraint has been imposed on the minimum percentage thickness (14.5%) whereas aerodynamic constraints have been given on minimum pitching moment coefficient ($C_{m_{min}} = -0.012$) and transition abscissa ($x/c = 0.05$). Bezier curves

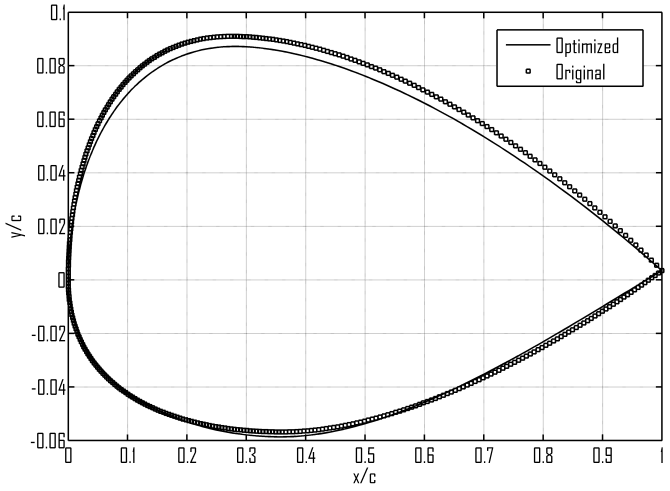

(a) Airfoils comparison, GA, Upper and Lower boundaries = 0.08

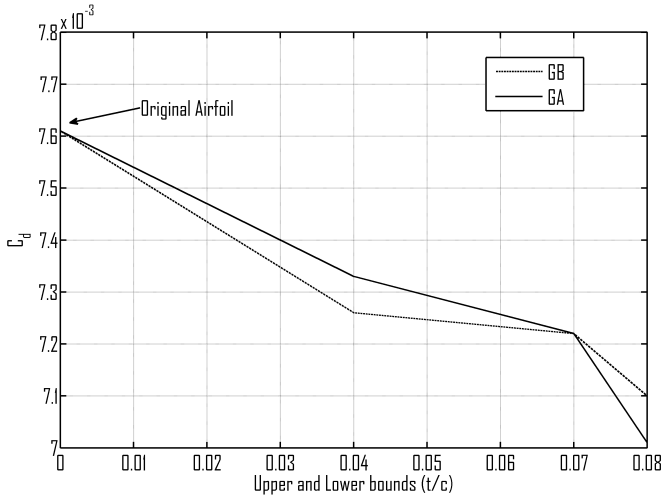

(b) Objective function vs boundaries, GB and GA optimization algorithm

FIGURE 2.12: AOT single optimization of C_d, results, fixed transition

are adopted as parameterization method and both GB and GA algorithm have been used and compared. All the AOT settings are summarized in Tab. 2.7. The best geometry has been found for an absolute percentage variations of lower/upper bounds equal to 0.08 using the gradient descent algorithm. The optimized geometry is characterized by an increase of the climb efficiency from about 72 to 135 mostly due to an increase of lift coefficient from 0.762 to 1.153. It is interesting to notice that Fig. 2.13 shows how the two algorithms effectively work. GB algorithm tends to gradually evolve in the way of minimizing the objective function so that,

TABLE 2.7: AOT settings, high efficiency in climb airfoil optimization

Starting Airfoil	NACA 23015
Algorithm	GA and GB
Objective function	$\frac{C_l^{3/2}}{C_d}$
Condition	Climb
Geom constraints	$\Delta y_{min} = 0.145$
Aero constraints	fixed transition at x/c = 0.05
	$C_{m_{min}} = -0.012$
Solver	Xfoil
Parameterization	Bezier
Results	
$\frac{C_l^{3/2}}{C_d}$ Initial	72
GA	
$\frac{C_l^{3/2}}{C_d}$ Optimal	115
Elapsed time (min)	$6'30''$
Objective eval. calls	779
GB	
$\frac{C_l^{3/2}}{C_d}$ Optimal	135
Elapsed time (min)	$9'45''$
Objective eval. calls	1171

increasing variations of the boundaries, climb efficiency linearly increases toward the optimum value. GA randomly varies control points, therefore an increment of the boundaries does not necessarily lead to an increment in the climb efficiency so that its variation is not linear. The number of iterations of this application has been equal to 1171 for GB and 779 for GA at 0.08 x/c boundary variation.

3. **Maximum lift coefficient in stall**

   Stall is the most critic condition since flow separation occurs and it is necessary to adopt an aerodynamic solver that is capable to well predict when this situation happens and how it affects the performance of the airfoil. Therefore Fluent has been necessarily selected as the aerodynamic solver thus increasing computational time either for each airfoil analysed and for the whole process of optimization. Constrains are here fixed only on minimum percentage thickness(14.5%) with the purpose to maximize the lift coefficient. Moreover, it has been previously observed that best results in cruise and climb conditions occur when the absolute variations of lower/upper boundaries is set equal to 0.08 and

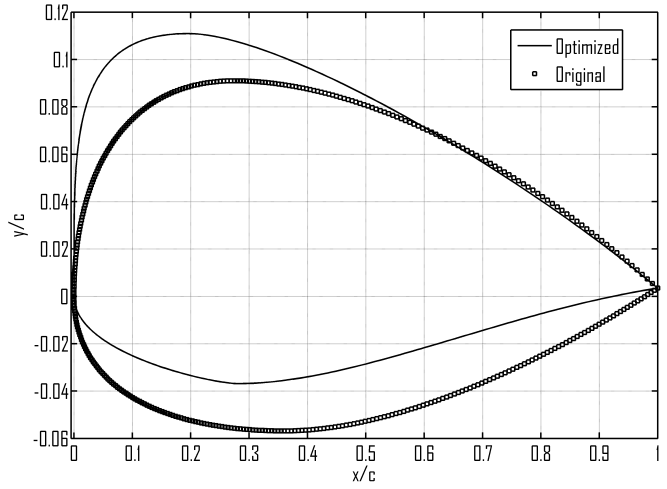

(a) Airfoils comparison, GB, Upper and Lower boundaries = 0.08

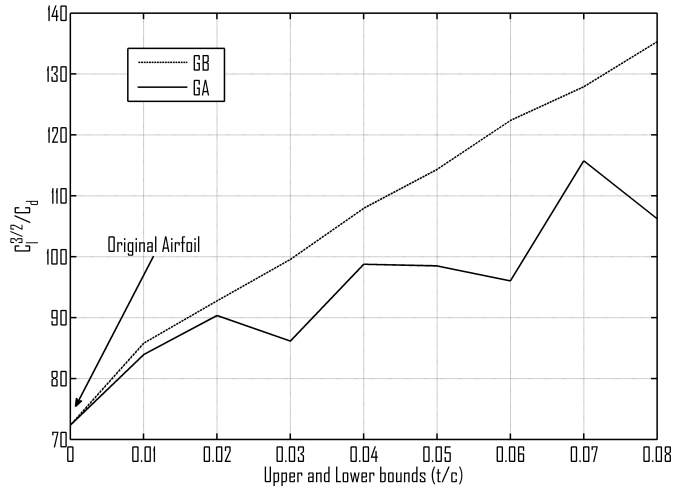

(b) Objective function vs boundaries, GB and GA optimization algorithm

FIGURE 2.13: AOT single optimization of $\frac{C_l^{3/2}}{C_d}$, results, fixed transition

using gradient algorithm of optimization. Therefore, since computational time is very high, the optimization in stall condition has been performed just with the mentioned settings and adopting, as already discussed, Bezier curves for the reconstruction of the airfoils as summarized in Tab. 2.8. The stall-optimized airfoil shows an average increase in lift coefficient equal to 0.186 so that a lower incidence is demanded in order to obtain the same lift coefficient. In particular the stall lift coefficient is improved of about 12% going from 1.5 to about 1.7. This

TABLE 2.8: AOT settings, maximum lift coefficient in stall airfoil optimization.

Starting Airfoil	NACA 23015
Algorithm	GB
Objective function	$C_{l_{max}}$
Condition	Stall
Geom constraints	$\Delta y_{min} = 0.145$
Aero constraints	fully turbulent
Solver	Fluent
Parameterization	Bezier
Results	
$C_{l_{max}}$ Initial	1.49
$C_{l_{max}}$ Optimal	1.69
Elapsed time (hours)	$15^h10'$
Objective eval. calls	152

gain is mainly due to an high cambered airfoil, with an higher pitching moment coefficient (from -0.01 to -0.06 of the optimized ones). It has to be noted that the request to use a N-S solver increases the elapsed optimization time at about 15 hours on a 8 CPU 2.67 Ghz desktop PC.

The airfoils presented in the Sec. 2.7.1 are the results of single case optimization so that they have been obtained just to meet specific demands such as minimization of cruise drag coefficient, maximization of climb efficiency and maximization of maximum lift coefficient. The Sec. 2.7.2 and Sec. 2.7.3 show results of multi cases optimization performed on the NACA 23015 airfoil.

2.7.2 Turboprop aircraft airfoil in cruise and climb

The present optimization has the purpose to optimize the airfoil performance in cruise and in climb conditions. This means that a minimization of cruise drag coefficient and a maximization of climb efficiency are demanded at the same time. Cruise and climb conditions are those indicated in Tab. 2.5 and they have been used in the optimization tool. The objective function considered for this case is a proper weighted combination of cruise drag coefficient and climb efficiency as shown in Eq. 2.18. Formerly, the problem is solved as a single objective problem for a bi-objective problem and the value of k_{C_d} and k_{E_c} are both equal to 1. s_{f_d} and $s_{f_{E_c}}$ represent scale factors to give the same magnitude at the single objectives.

$$f_{obj} = +k_{C_d} s_{f_d} \mathbf{C_d} - k_{E_c} s_{f_{E_c}} \mathbf{E}_{\text{climb}} \tag{2.18}$$

The aerodynamic solver for both conditions is Xfoil and airfoil parameterization is Bezier curve. AOT settings for this multi-cases optimization is summarized

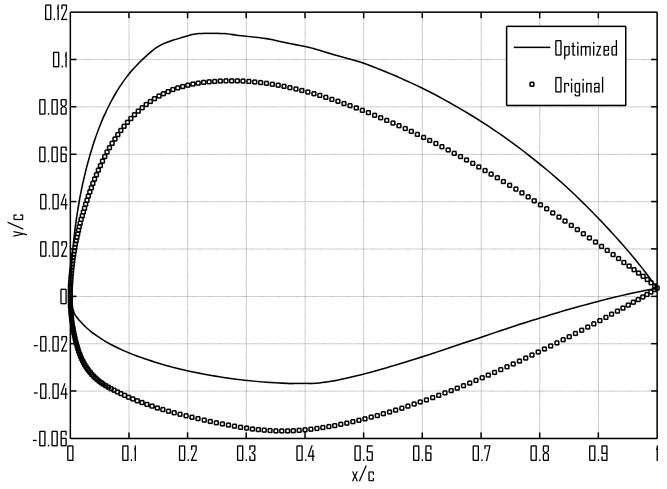

(a) Airfoils comparison, Upper and Lower boundaries = 0.08

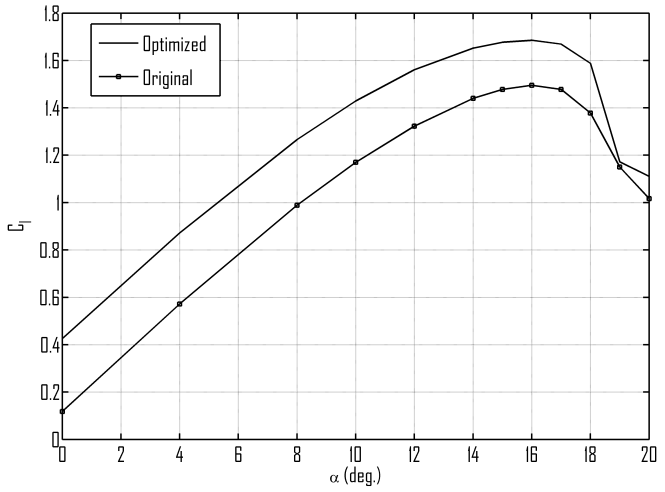

(b) Lift coefficient, Fluent solver

FIGURE 2.14: AOT single optimization of $C_{l_{max}}$, results, fully turbulent flow.

in Tab. 2.9. AOT results are shown in Fig. 2.15 and summarized in Tab. 2.10. Cruise-Climb optimized solution is the dashed red curve and it is compared to only Cruise solution (obtained by posing $k_{E_c} = 0$) and only Climb solution (obtained vice-versa by posing $k_{C_d} = 0$). It is possible to see that all the three optimized solutions given an improvement of the original airfoil performance. Single condition optimizations (only Cruise and only Climb) give a major improvement for the reference condition. As it can be seen in Fig. 2.15 the multi-optimization condition provides a result which is good compromise

between the two single condition and it allows a better airfoil performance for both optimized flight condition as summarized in Tab. 2.9. It has to be considered that the enforcement of geometrical and aerodynamic constraints do not upset the original airfoil geometry and this capability can be very useful for the designer in the preliminary design phase as discussed in Sec. 2.4.

TABLE 2.9: AOT settings, Cruise $C_{d_{min}}$ and Climb maximum efficiency optimization.

Starting Airfoil	NACA 23015
Algorithm	GB
Parameterization	Bezier
Objective 1	
Objective function	$C_{d_{min}}$
Condition	Cruise
Geom constraints	$\Delta y_{min} = 0.145$
Aero constraints	fixed transition at x/c = 0.05
Solver	Xfoil
Objective 2	
Objective function	$\frac{C_l^{3/2}}{C_d}$
Condition	Climb
Geom constraints	$\Delta y_{min} = 0.145$
Aero constraints	fixed transition at x/c = 0.05
	$C_{m_{min}} = -0.012$
Solver	Xfoil
Elapsed time (min)	$22'20''$
Objective eval. calls	1337*

* The effective Xfoil calls are twice

TABLE 2.10: AOT results, Cruise $C_{d_{min}}$ and Climb maximum efficiency optimization.

	$C_d(C_l = 0.5)$	$\frac{C_l^{3/2}}{C_d}(C_l = 1.0)$
Cruise condition		
Original	0.007527	111.12
Optimized Cruise	0.007327	116.53
Optimized Climb	0.007533	116.88
Optimized Cruise-Climb	0.007298	116.57

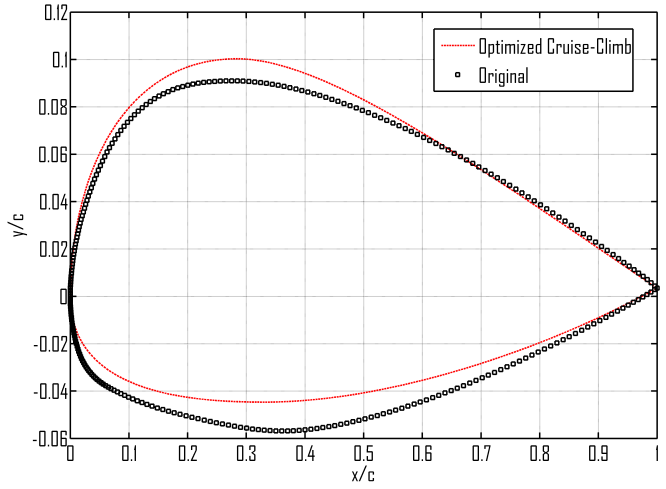

(a) Airfoils comparison

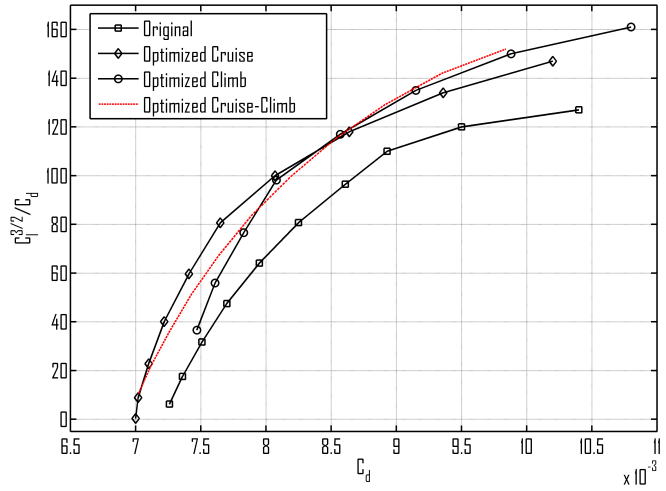

(b) Climb efficiency vs Drag coefficient, Xfoil solver

FIGURE 2.15: AOT multi-optimization of Cruise $C_{d_{min}}$ and Climb maximum efficiency, results, fixed transition, $M = 0.43$, $Re = 19.5\ 10^6$

2.7.3 Turboprop aircraft airfoil in cruise, climb and stall

The present optimization has the purpose to optimize and to improve the behaviour of the airfoil in cruise, climb and stall condition. The goal is to give a suitable airfoil for a new regional turboprop aircraft which aims to improve the performance in the whole aircraft flight envelope. This means that a minimization of cruise drag coefficient, a maximization of efficiency in climb and a maximization of maximum lift coefficient in stall are demanded

at the same time. These three flight conditions are those reported in Tab. 2.5. Cruise and Climb condition are evaluated through Xfoil aerodynamic solver while maximum lift coefficient has been evaluated with Fluent solver. The objective function considered for the case is a proper weighted combination of the three flight conditions as the following Eq. 2.19 reports:

$$f_{obj} = +k_{C_d} s_{f_d} \mathbf{C_d} - k_{E_c} s_{f_{E_c}} \mathbf{E}_{\text{climb}} - k_{C_{l_{max}}} s_{f_{C_{l_{max}}}} \mathbf{C_{l_{max}}} \tag{2.19}$$

The terms s_{f_d}, $s_{f_{E_c}}$ and $s_{f_{C_{l_{max}}}}$ represent scale factors to give the same magnitude at the single objectives. Gradient descent algorithm has been used as optimization algorithm with a Bezier reconstruction and a maximum upper/lower variation of the control points fixed to 0.08 of the chord percentage.

TABLE 2.11: AOT settings, Cruise $C_{d_{min}}$ and Stall $C_{l_{max}}$ optimization.

Starting Airfoil	NACA 23015
Algorithm	GB
Parameterization	Bezier
Objective 1	
Objective function	$C_{d_{min}}$
Condition	Cruise
Geom constraints	$\Delta y_{min} = 0.15$
Aero constraints	free transition
	$C_{m_{min}} = -0.035$
Solver	Xfoil
Objective 2	
Objective function	$\frac{C_l^{3/2}}{C_d}(C_l = 1.0)$
Condition	Climb
Geom constraints	$\Delta y_{min} = 0.15$
Aero constraints	fixed transition at
	x/c = 0.05
Solver	Xfoil
Objective 3	
Objective function	$C_{l_{max}}$
Condition	Stall
Geom constraints	$\Delta y_{min} = 0.15$
Aero constraints	fully turbulent
Solver	Fluent
Elapsed time (h)	$24^h 5'$
Objective eval. calls	241*

* The effective calls are: two Xfoil and one Fluent

A geometrical limitation on minimum percentage thickness has been set to 15% while minimum moment coefficient has been limited to -0.035 in

cruise condition (computed by Xfoil). These constraints are related to design requirements to have a wing with a root thickness of 15% and a pitching moment coefficient not too high to reduce tail plane balancing loads. All settings are summarized in Tab. 2.11. The multi-optimization process applied on NACA 23015 airfoil has given the results shown in Figures 2.16 and 2.18. The optimized airfoil results as a compromise between low drag, high climb efficiency and better maximum lift coefficient airfoil, as requested by AOT settings shown in Tab. 2.11. As a matter of fact optimized airfoil geometry shown in Fig. 2.16 exhibits typical characteristics of laminar airfoil for the ventral zone to reduce drag coefficient, high leading edge radius and higher trailing edge curvature for maximum lift coefficient and higher climb efficiency. Aerodynamic results are summarized in Fig. 2.18 divided for the three flight conditions which correspond to the single objective functions. Figure 2.18(a) show that in cruise condition ($0.35 < C_l < 0.55$), drag coefficient is reduced of about ten drag counts. As a matter of fact the best improvement of drag coefficient is obtained around $C_l = 0.5$ which is the AOT setting imposed for the objective 1. Climb efficiency is also improved, as it is shown in Fig. 2.18(b). In the typical climb lift coefficient range ($0.8 < C_l < 1.2$) the airfoil performance gains is about 10-20% at the same drag coefficient. Lift coefficient curve computed in stall condition through Fluent solver is shown in Fig. 2.18(c). Stall lift coefficient is improved of about 8%. This gain is also related to an increment in pitching moment coefficient which goes from -0.012 to -0.035. It has to be noted that the overall elapsed time of the optimization process is about one day. Only about five minutes is the time for the Xfoil solver calls compared to 24 hours for fluent analysis.

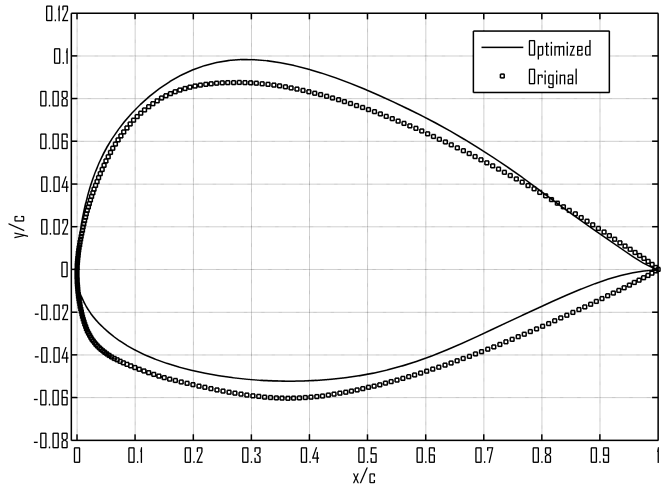

FIGURE 2.16: AOT multi-optimization in Cruise, Climb and Stall Conditions, airfoils comparison.

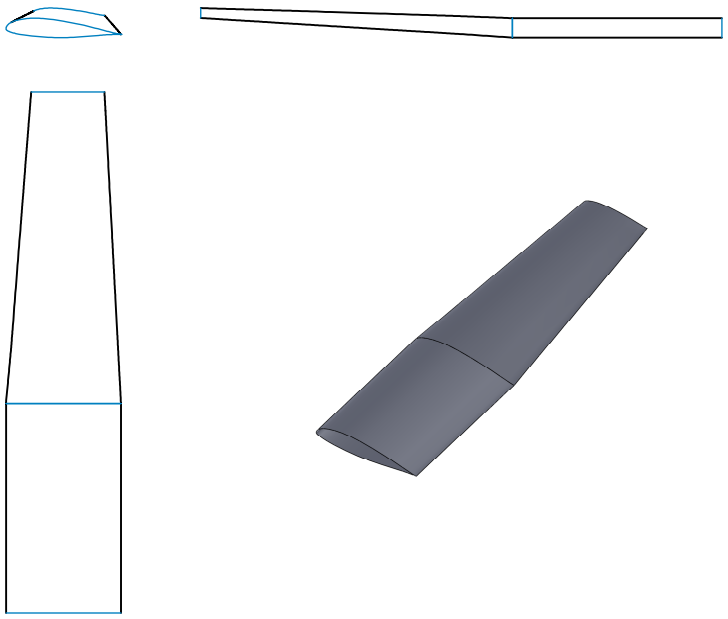

FIGURE 2.17: Example of turboprop wing designed with otpimized airfoil in cruise, climb and stall condition. Root airfoil $t/c = 0.15$, tip airfoil $t/c = 0.13$. This wing could improve drag in cruise condition, efficiency in climb and maximum stall lift coefficient.

TABLE 2.12: AOT results, Cruise $C_{d_{min}}$ Climb maximum efficiency, Stall lift coefficient.

	$C_d(C_l = 0.5)$ Cruise cond.	$\frac{C_l^{3/2}}{C_d}(C_l = 1.0)$ Climb cond.	$C_{l_{MAX}}$ Stall cond.
Original	0.00582	97.2	1.49
Optimized	0.00483	101.0	1.61

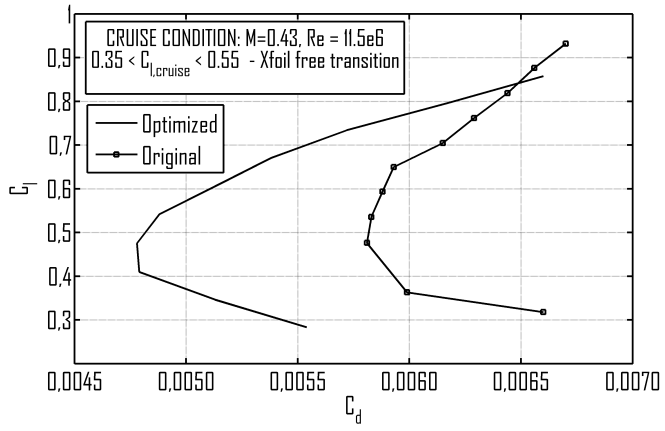

(a) Lift vs Drag coefficient, Cruise

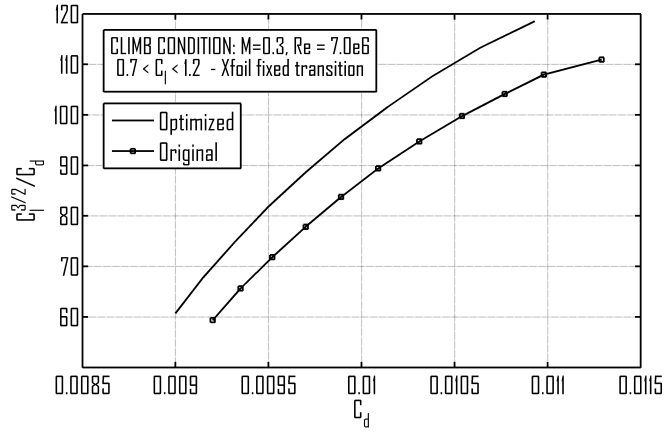

(b) Climb efficiency vs Drag coefficient, Climb

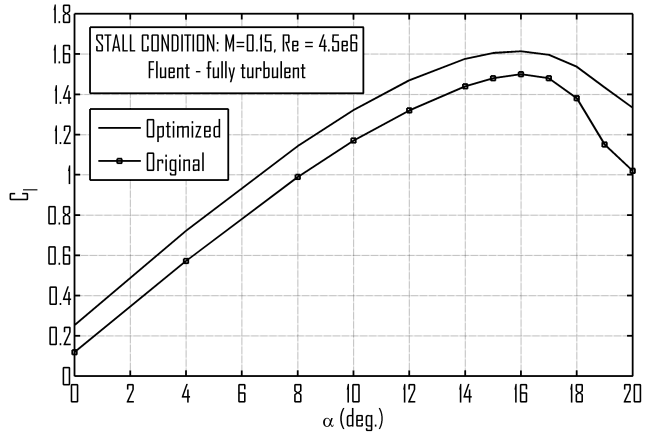

(c) Lift coefficient vs α, Stall

FIGURE 2.18: AOT multi-optimization in Cruise, Climb and Stall Conditions, results

2.7.4 High efficiency airfoil applied to fan design

AOT tool has been used also to design a suitable airfoil for a fan blade. In particular this airfoil has been carried out to be applied on the fan blade of the wind-tunnel facility of the University of Naples. For the purpose of the optimization, an high efficiency airfoil optimization has been performed starting from a NACA sixth series laminar airfoil. Constraints have been imposed on the minimum thickness (equal to 14.5%) and on the flow transition at 5% of c, where leading edge protections are stitched. A multi-objective optimization has been performed choosing as objective 1 the maximum airfoil efficiency at low angle of attack and as objective 2 the maximum efficiency at medium-high angle of attack. Xfoil has been used as aerodynamic solver for both objectives and Bezier parameterization has been used. The AOT settings are summarized in Tab. 2.13. The optimized fan airfoil is shown in

Table 2.13: AOT settings, Wind-Tunell Fan high efficiency airfoil optimization.

Starting Airfoil	NACA 64_3615
Algorithm	GB
Parameterization	Bezier
Objective 1	
Objective function	E
Condition	$\alpha = 2$ deg.
Geom constraints	$\Delta y_{min} = 0.145$
Aero constraints	fixed transition at x/c = 0.05
Solver	Xfoil
Objective 2	
Objective function	E
Condition	$\alpha = 7$ deg.
Geom constraints	$\Delta y_{min} = 0.145$
Aero constraints	fixed transition at x/c = 0.05
Solver	Xfoil
Elapsed time (min)	$8'10''$
Objective eval. calls	351*

* The effective Xfoil calls are twice

Fig. 2.19(a) and main aerodynamic results are shown in Fig. 2.19(b). As it can be seen airfoil efficiency has been improved in the whole range, in particular at $\alpha = 7deg.$ which corresponds to the objective 2 setting of the AOT. The wind-tunnel fan blade of the University of Naples has been following designed on the basis of the optimized airfoil. Figure 2.20(a) and Fig. 2.20(b) show the designed and the wind-tunnel installed fan respectively. The new fan designed

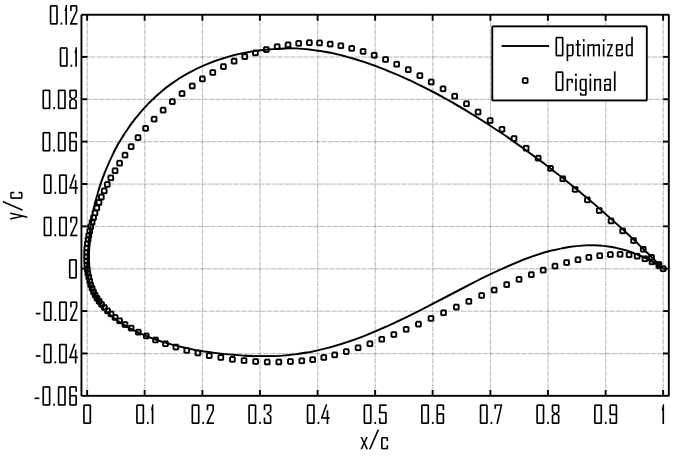

(a) AOT high efficiency airfoil optimization, geometries

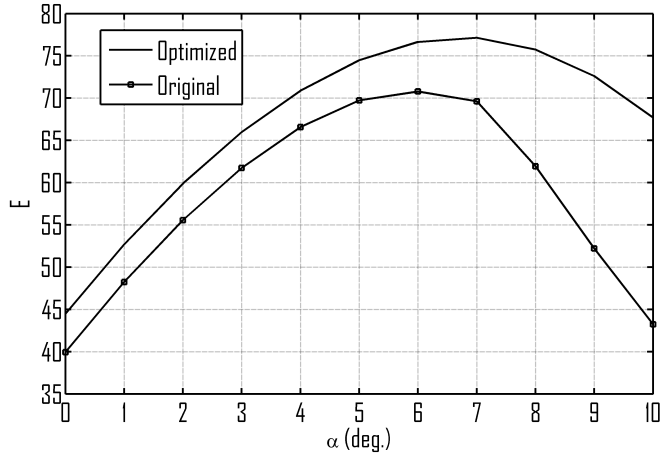

(b) Aerodynamic efficiency

FIGURE 2.19: AOT high efficiency airfoil, aerodynamic results, fixed transition

by the ADAG[5] allowed an higher test-section speed than the older fan (from 40 to 50 m/s at the same rotation speed).

[5]Aircraft Design and AeroFlightDynamics Group. University of Naples Federico II

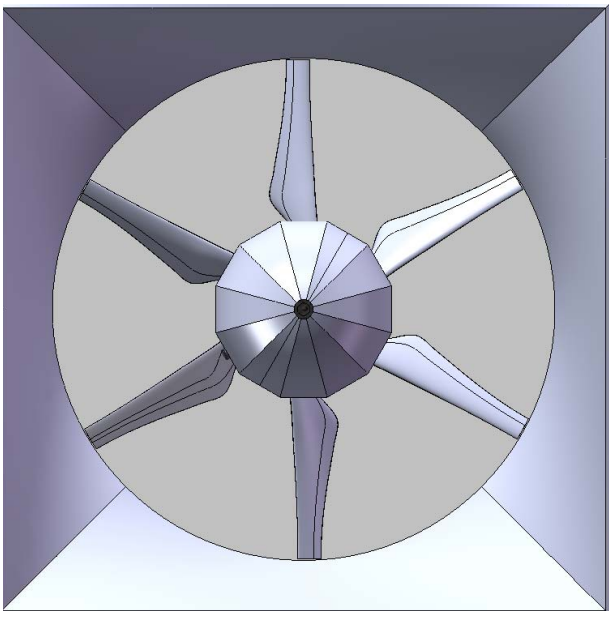

(a) FAN design at ADAG, CAD Drawings rear view

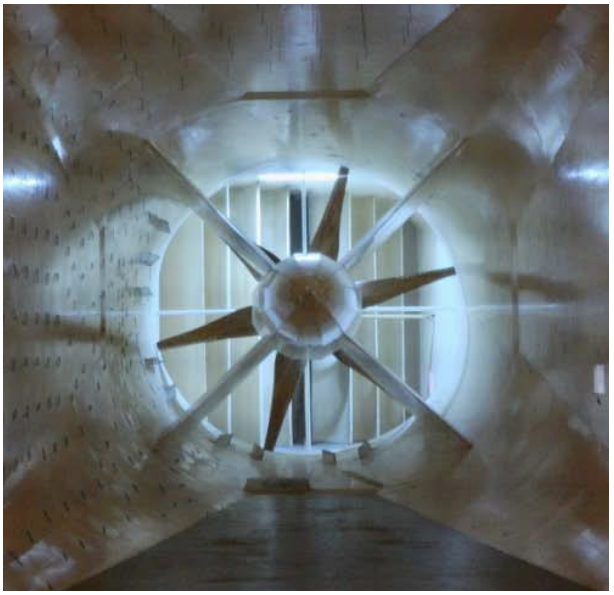

(b) FAN design at ADAG, Wind-tunell installation front view

FIGURE 2.20: Fan of wind-tunell at DII.

2.7.5 High efficiency airfoil applied to wind turbine

In this example an innovative optimization process for airfoil geometry is introduced. AOT has been set coupling of PARSEC parametrization (described in Sec. 2.2.3) for geometries and GA and NashGA algorithms optimization method (described in Sec. 2.3.3). The main valuable contribution is to join the PARSEC parameterization method with Nash solution. From an engineering point of view PARSEC has the intrinsic capability of relating airfoil definition design variables to aerodynamic coefficients behavior, since it would be intuitive linking leading edge radius or maximum thickness abscissa with drag coefficient, or camber and trailing edge angle with stall lift coefficient or pitch moment coefficient. On the other hand, the optimization under Nash solutions would be more attractive to use when a well posed distinction between players variables exists. Here the PARSEC design variables are intended to play the role of game players' variables.

The idea is to assign variables to players under a more physics-related correspondence (as it can be seen in Fig. 2.21):

- the lift coefficient C_l is mainly dependent on upper crest curvature ($Z_{XX_{up}}$ or shortened as p_4), the lower crest curvature ($Z_{XX_{lo}}$ or p_7), the trailing edge offset in vertical sense (Z_{te} or p_8) and the trailing edge direction (α_{te} or p_{10});
- the drag coefficient C_d is mainly dependent on leading edge radius (r_{le} or p_1), the trailing edge thickness (ΔZ_{te} or p_9) and trailing edge wedge angle (β_{te} or p_{11});
- both C_l and C_d are influenced by the upper crest position in horizontal and vertical coordinates (X_{up} or p_2, Z_{up} or p_3) and lower crest position in horizontal and vertical coordinates (X_{lo} or p_5, Z_{lo} or p_6).

(a) Variable assignment for C_l (b) Variable assignment for C_d

FIGURE 2.21: AOT Variable assignment scheme.

The *white* portion of Fig. 2.21(a) and 2.21(b) contains, respectively, the C_l and C_d related variables, that appears, of course, in the *black* portion of the other objective function. The *gray* area is used as a shared portion between players (i.e. objective functions for C_l and C_d), and in the following a sensitivity analysis on *gray* variables distribution between players is conducted to evaluate Nash equilibrium with different strategy parameters set: the total number of combination is $C_{n=4,k=2} = \sum_{i \in n_0} \frac{n!}{i!(n-i)!} = 16$, where n is the

number of *gray* variables, k the number of players among which the variables should be divided, and $n_0 = [0, ..., n]$.

AOT boundaries have been selected assuming that 2 of the eleven PARSEC variable, namely Z_{TE} and ΔZ_{TE} are set equal to 0, while the remaining with a 10 percent range of variation with respect to the starting ones. Flow condition have been imposed to a Reynolds number equal a to $\mathrm{Re}_\infty = 2.0^6$, a Mach number equal to $\mathrm{M}_\infty = 0.1$ and an angle of attack equal to $\alpha = 5.3\,\mathrm{deg}$ with fixed transition location imposed at 5% in chord on upper and lower side, starting from a NREL S809 airfoil (see Fig. 2.8(c)) using as aerodynamic solver Xfoil. Objective function has been set to maximum aerodynamic

TABLE 2.14: AOT settings, Maximum Airfoil efficiency optimization.

Starting Airfoil	NREL S809
Algorithm	GA and NashGA
Optimization 1	
Objective function	E
Condition	$\alpha = 5.3deg.$
Geom constraints	-
Aero constraints	fixed transition at x/c = 0.05
Solver	Xfoil
Parameterization	PARSEC
Optimization 2	
Objective function	E
Condition	$\alpha = 5.3deg.$
Geom constraints	$\Delta y_{min} = 0.20$
Aero constraints	fixed transition at x/c = 0.05
Solver	Xfoil
Parameterization	PARSEC
GA - Pareto, Optimization 1	
Objective eval. calls	4880 *
NashGA, Optimization 1	
Objective eval. calls	2400 +
* Population size is 100 and Generation limit is 50	
+ This is the number for only one nash point	

efficiency. Both unconstrained and constrained thickness optimization have been performed and main results are summarized in Fig. 2.23. All the AOT settings are summarized in Tab. 2.14.

In Fig. 2.22 are shown the airfoil shapes. Solid line represents the original S809 airfoil geometry while dashed line indicates the solution for a Nash equilibrium in which player 1 holds all the *gray* variables, for which the lift coefficient, C_l, requirement is pursued by the majority of the chromosome, so

that the final shape exhibits higher thickness, longer suction portion and bigger trailing edge curvature. In dotted line is indicated the solution for a Nash equilibrium in which player 2 holds all the *gray* variables, for which the drag coefficient, C_d, requirement is pursued by the majority of the chromosome, so that the final shape exhibits lower thickness and a sharper nose portion.

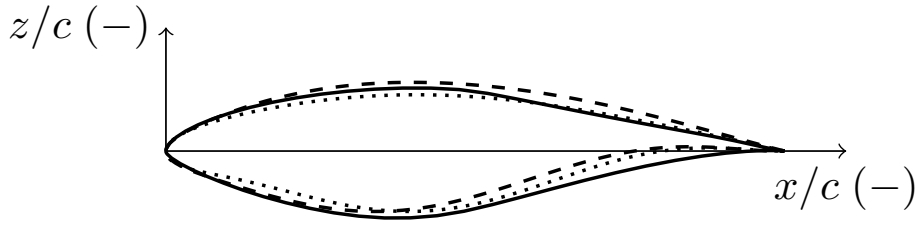

FIGURE 2.22: Original and Optimized NashGa Airfoils. Example of solutions.

In Fig. 2.23 optimization results are shown compared to the original S809 airfoil (shown as + marker) and both pareto frontier and NashGA 16 points are shown. In particular the Fig. 2.23 caption divides results as following:

- the filled square and circle indicates the assignment of all the *gray* variables, respectively, to player 1 and 2;
- the not filled squares and circles indicate, respectively an assignment of 3 *gray* variables to player 1 and 1 to player 2, and 1 *gray* variable to player 1 and 3 to player 2;
- the triangles indicate the assignment of 2 *gray* variables to both players.

The results show an efficiency improvement of more than 15% for both constrained and unconstrained optimization. Moreover it has been shown that some Nash equilibrium points lie on the Pareto front, but with respect to the Pareto front solution they have been obtained in very less time. In particular a single nash point, which means an optimized airfoil, is obtained in about 45 minutes while the entire pareto frontier needs of about 3 hours.

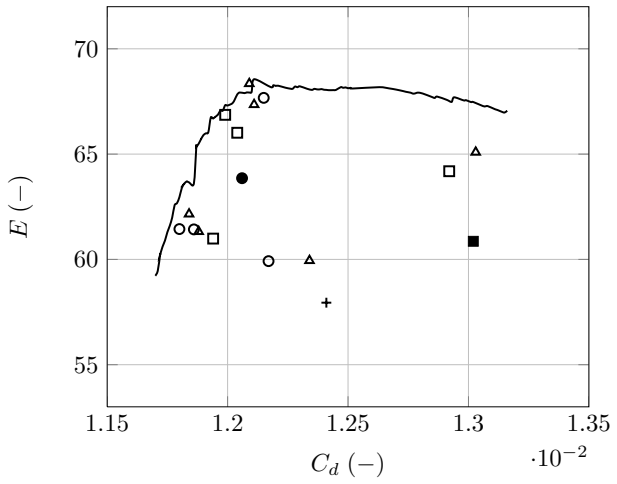

(a) Variable assignment for C_l

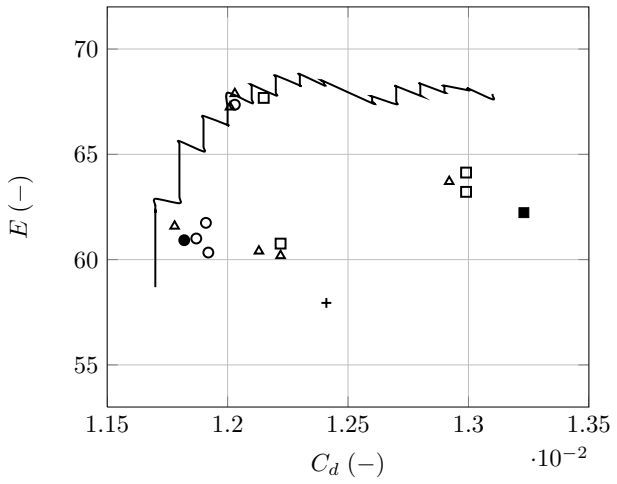

(b) Variable assignment for C_d

FIGURE 2.23: Aerodynamic efficiency vs. drag coefficient for both not constrained and constrained case
■ $4P_1\&0P_2$, □ $3P_1\&1P_2$, △ $2P_1\&2P_2$, ◯ $1P_1\&3P_2$, • $0P_1\&4P_2$, + S809, — Pareto

Chapter 3

Aircraft Components Design and Optimization

3.1 Introduction

The aerodynamic design of an airplane has been constantly improved since its introduction in the 1920's. The design of a new flight vehicle was soon accompanied by theoretical research and wind tunnel testing. These new design techniques required not only sophisticated design tools, but also high capabilities to realize the designed geometries and to sustain the costs. Past research activities on aircraft design aimed to drag reduction and usually they were focused on wing and lifting surface design, and especially on airfoil design, as it has been widely discussed in Chapter 2. However, especially at high speed conditions (low lift coefficient and then low induced drag), an accurate fuselage design is very important to reduce the total drag of an aircraft. As it has been shown in Chapter 1 in Fig. 1.12 and Fig. 1.13, for a typical large turboprop aircraft about 35% of C_{D_0} is due to the fuselage and a drag reduction could give an improvement of the aircraft performance especially in cruise condition. A 10% fuselage drag coefficient reduction means a 3.5% drag reduction of the total drag coefficient in these conditions, which can give a non negligible level flight performance improvement (as shown in Fig. 1.16 and Fig. 1.17). On the basis of these calculations aimed to reduce aerodynamic drag, improve flight performance and endurance, the junction between wing and body (and generally the fuselage design of an aircraft) are of great interest. With the junction term is identified the connection of bodies with different aircraft components, in this special case the wing and the free-form shaped body of the aircraft. In particular, this junction induces interactions between the components, especially the combined boundary layers cause a flow phenomena very difficult to describe and simulate as well explained in Simpson [39], Hoerner [40] and Schlichting [41].

As suggested by Siegel [42], in order to achieve improvements, there are several ways to manipulate the flow around the junction:

- Optimize the relative wing-body position.
- Adapt the junction shape with fillets and fairings.
- Manipulate the flow with active installations.

Extensive experimental research was done in the past at NACA, such as the broad investigations by Jacobs and Ward [43] on the relative wing-body position and fillet-specific investigation by Muttray [44]. The drag characteristics of wing-body junctions were summarized by Hoerner [40] and Schlichting and Truckenbrodt [41]. Subsequently improvements of measurement systems and numerical simulations made it possible to focus on the flow phenomena itself. Remarkable investigations were made by Fleming et al. [45], extensive measurements can be obtained from Oelcmen [46] and a detailed summary is given by Simpson [39]. More in detail the influence on lift and drag of the wing-body relative position was extensively investigated by Jacobs [43]. The main results of this work were *i)* drag coefficient gradient C_{D_α} increases greatly for high-wing configuration, especially as the wing bottom surface is tangent to the fuselage surface; *ii)* short lengthwise position of the wing to the fuselage nose has a small positive effect in reducing parasite drag. However it was also shown in Ref. [43] that, in order to achieve a fitting curvature of the intersection lines, fairings, fillets and fuselage design at these positions provide the chance to reduce drag to acceptable magnitudes similar to middle or far outer wing mount position. Especially sharp angles between body and wing cause early separation, thereby wider join angles reduce drag. An interesting approach for these wider join angles in combination with cambered high-mounted sailplane wings was done by Boermans et alii in Ref. [47].

Perhaps the most useful approach to reduce fuselage drag is the adoption of fillets and fairings between wing and body, and an accurate fuselage design, so called stream-line fitted body-shaping as described in Ref. [47]. White did extensive research [48] on a 1929 low-wing motorplane wing-body junction and measured a greatly reduced separation and drag reduction. Also leading edge and trailing edge fillets were investigated in Ref. [48–50] showing that an accurate design of these parts can reduce drag.

In this research work particular attention has been posed to the wing-body junction, wing-body fairing, undercarriage vane and on the fuselage nose. As a matter of fact, in these zone several geometry discontinuities or abrupt change in curvatures can occurr especially for typical turboprop aircraft as shown in Ref. [14, 51]. To better highlight the most critical areas in terms of aerodynamic behavior, a typical 70 passengers turboprop aircraft is taken as reference starting point, the ATR-72 shown in Fig. 1.9. An aerodynamic analysis of the reference geometry is performed through a panel code available at DII (Department of Industrial Engineering) and deeply tested and used in Ref. [14, 15, 51]. In particular the wing-body geometry has been analyzed because the objective is to investigate the fuselage aerodynamics.

Once identified the critical components, an automatic procedure implemented in MATLab allows to import and modify these geometries using interpolating curves and surfaces. The entire optimization scheme procedure is shown in Fig. 2.1. Starting from the reference wing-body geometry, the

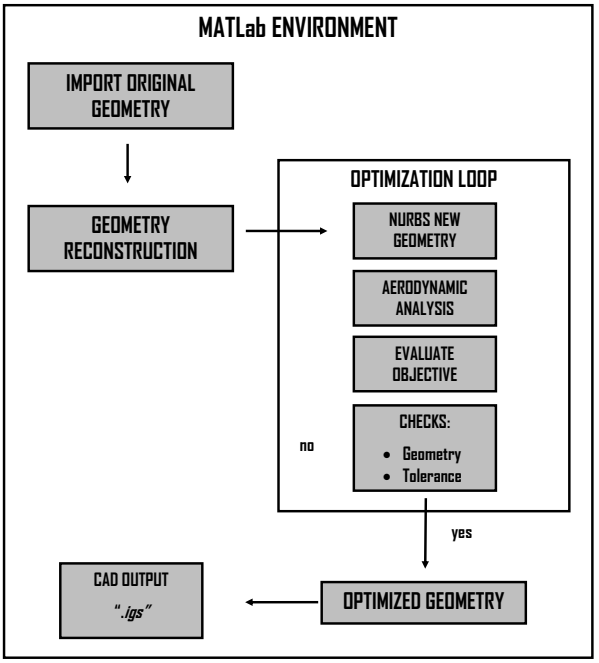

FIGURE 3.1: Optimization strategy scheme. MATLab Environment

aerodynamic behavior of some components is investigated to know if and how they can be optimized in terms of drag reduction (Sec. 3.4). Once defined the components to optimize, the original shape is reconstructed via NURBS approximation (see Sec. 3.2). Then a number of control points (usually a pair), which can vary within a predetermined space (constrained optimization), are selected. The new surface geometry is then built according to the control points position and then analyzed with the panel code solver until the convergence criterion is satisfied. A MATLab gradient based algorithm has been used as optimization algorithm, as shown in Sec. 2.3.1. The objective function has been always set to aircraft drag coefficient, in particular it has been adopted the Young [52] formulation (see Sec. 3.3), which is based on integral quantities of the boundary layer, evaluated at the body's trailing edge or separation zone. At the end of the process an iges file (.igs), suitable for CAD processing, is automatically generated. All the phases are automatically managed in MATLab environment.

In this chapter another major focus is the wing tip design, mainly aimed to the performance improvements (in particular rate of climb with One Engine Inoperative and OEI ceiling). Winglet installation on transport aircraft is becoming a main aerodynamic topic design to improve performances and save

fuel. The author have gained experience in winglet design and further analysis are under development (see Ref. [12–16, 53]). A MATLab code, written at DII, allows to define winglet geometry by setting a reference wing geometry and several winglet design parameters (such as *cant* angle, toe angle, winglet height, etc.). Then an automated procedure performs aerodynamic calculations with the aforementioned panel code. Several analyses have been carried out in order to improve the wing induced drag factor e_w, and the results on the optimized winglet are here presented, focusing the attention on performance improvements.

3.2 NURBS parameterization

In the present paragraph a general overview on NURBS is presented, since this approach has been used in the optimization process shown in Fig. 2.1. Non-uniform Rational B-Splines (NURBS) provide a convenient and efficient manner to generate curved lines and surfaces which can be smooth at any viewing distance. Since these surfaces are generated parametrically, only a small amount of data need to be provided for describing complex surfaces. The non-uniform rational B-spline (NURBS), are extensively used in CAD application and several books and articles have been written about this argument in computer aided science (see Ref. [54–59]). According to one of the NURBS fathers', Piegl [55], NURBS curves are vector-valued piecewise rational polynomial functions. NURBS are used within this work to calculate an approximation of given surface grid points that represent the original shape. This is a powerful technique to change the grid points position and therefore the shape of the objects by adjusting the control points as outlined by Becker and Schafer [60]. In contrast to the amount of grid points, the amount of control points is rather small.

In general every curve or surface can be defined by a set of parametric functions. For instance, (x, y, z) coordinates of the points of the curve can be given by Eq. 3.1:

$$x = X(t), y = Y(t), z = Z(t) \tag{3.1}$$

where t is the parameter and X, Y, Z are polynomial functions in t. If X, Y, and Z are 1^{st} degree polynomials, a line segment will be defined. In that case, only two unknowns, that are two points or a point and a slope, will be sufficient to define this curve. If X, Y, and Z are 2^{nd} degree polynomials, a parabola segment will be defined and 3 unknowns will be necessary to describe it, that are 3 points or 2 points and a tangent. For higher degree polynomials, describing the curve involves more unknowns. This number of unknowns define the order of the curve, and it is always given by the degree of the curve plus 1. Most of the time, cubic polynomials are used to represent curves. Indeed more unknowns are needed for higher degree polynomials, which makes modeling difficult to handle. On the other hand, lower degree polynomials describe too

restrictive curves, being either lines or parabolas, which are always planar curves. Various approach have been imagined by mathematicians, for instance Beizer curves, Hermite curves, Catmull-Rom splines and B-splines. In this chapter B-splines are used and described next.

3.2.1 B-Splines

Foley et alii in Ref. [59] say that "*the term spline goes back to the long flexible strips of metal used by drafts persons to lay out the surfaces of airplanes, cars and ships. Ducks, weights attached to the splines, were used to pull the spline in various directions*". This fact was the inspiration of a mathematical model that was built and allows to define a curve blending control points by polynomials, introducing the concept of natural spline. The main issue with natural splines is that modifying a control point would affect the whole curve, as each polynomial coefficient depend on every control point. B-Splines, consisting in several natural spline segments, each of them is defined by a reduced set of control points. Thus, polynomial coefficients will only depend on the control points of the curve segment considered. This is called local control, because modifying a control point will only affect a few curve segments.

$$x = \frac{X(t)}{W(t)}, y = \frac{Y(t)}{W(t)}, z = \frac{Z(t)}{W(t)} \tag{3.2}$$

B-Splines blend a set of $p+1$ control points:$\{P_0, P_1, \ldots, P_p\}$ and consist in curve $p-(n-1)$ segments: $\{Q_n, Q_{n+1}, \ldots, Q_p\}$. Let's define a common parameter t rather than considering a parameter t in the interval $[0, 1[$ for each segment, thus, for each curve segment Q_i, t will belong to the interval $[t_i, t_{i+1}[$, with $n \leq i \leq p$. Moreover, each segment Q_i will only be affected by n control points: P_{i-n}, P_i. For each $i \geq n$ there is a knot between Q_i, Q_{i+1} and for the value t_i of the parameter t. There is a total of $p-n-2$ knots for the B-Spline. Here comes the concept of uniformity: if the knots are uniformly distributed on the interval $[0, 1[$ (i.e. $\forall i \in [n, p[, t_{i+1} - t_i = t_{i+2} - t_{i+1}$) the B-Spline is defined *uniform*, otherwise *non-uniform*. It is worth mentioning the fact that those definitions imply that the knots are increasing (i.e. $\forall i \in [n, p], t_i \leq t_{i+1}$). Now, assuming that the coordinates (x, y, z) of a point of the curve are given by ratios of polynomials as in the following Eq. 3.2, the B-Spline will be said rational, otherwise it will be said non-rational. To sum up what we have just seen, we can distinguish 4 different types of B-Splines:

- Uniform Non-rational
- Non-uniform Non-rational
- Uniform Rational
- Non-Uniform Rational

The last case is the most common and used for modeling and relatives curves are better known as **NURBS** that stands for *Non-Uniform Rational B-Splines*.

3.2.2 NURBS Curves and Surfaces

In a work named "NURBS: a Survey" [61], Professor Les Piegl simply introduces NURBS and highlights their properties. He also gives an historical perceptive about NURBS, underlining the main ingredients which are the rational polynomials and B-splines, saying that Versprille extended B-splines to rational B-splines and his work in 1975 was the first written account of NURBS [56]. Piegl [61] said that "*the mathematical definitions of NURBS curves and surfaces are relatively simple*". NURBS curve is a vector-valued piecewise rational polynomial function of the form of Eq. 3.3:

$$C(u) = \frac{\sum_{i=0}^{n} w_i P_i N_{i,p}(u)}{\sum_{i=0}^{n} w_i N_{i,p}(u)} \tag{3.3}$$

where the w_i are the so-called weights, the P_i are the control points (just as in the case of non-rational curves), and $N_{i,p}(u)$ are the normalized B-spline basis functions of degree p, defined recursively as following Eq. 3.4:

$$\begin{aligned} N_{i,0} &= \begin{cases} 1 \text{ if } u_i \leq u \leq u_{i+1} \\ 0 \quad \text{otherwise} \end{cases} \\ N_{i,p} &= \frac{u - u_i}{u_{i+p} - u_i} N_{i,p-1}(u) + \frac{u_{i+p+1} - u}{u_{i+p+1-u_{i+1}}} N_{i+1,p-1}(u) \end{aligned} \tag{3.4}$$

where u_i are the so-called knots forming a knot vector of Eq. 3.5:

$$U = \{u_0, u_1, \ldots, u_m\} \tag{3.5}$$

An example of a NURBS curve with 5 control points can be seen in Fig. 3.2

A NURBS surface is the rational generalization of the tensor product non-rational B-spline surface and it is defined as follows:

$$S(u,v) = \frac{\sum_{i=0}^{n} \sum_{j=0}^{m} w_{i,j} P_{i,j} N_{i,p}(u) N_{j,q}(v)}{\sum_{i=0}^{n} \sum_{j=0}^{m} w_{i,j} N_{i,p}(u) N_{j,q}(v)} \tag{3.6}$$

where $w_{i,j}$ are the weights, $P_{i,j}$, form a control net, and $N_{i,p}(u)$ and $N_{i,q}(v)$ are the normalized B-splines of degree p and q in the u and v directions, respectively, defined over the knot vectors of Eq. 3.7:

$$U = \{0, 0, \ldots, 0, u_{p+1}, \ldots, u_{r-p-1}, 1, 1, \ldots, 1\} \tag{3.7}$$

$$V = \{0, 0, \ldots, 0, u_{q+1}, \ldots, u_{s-q-1}, 1, 1, \ldots, 1\} \tag{3.8}$$

where the end knots are repeated with multiplicities $p+1$ and $q+1$, respectively, and $r = n + p + 1$ and $s = m + q + 1$. Although the surface of Eq. 3.6 was

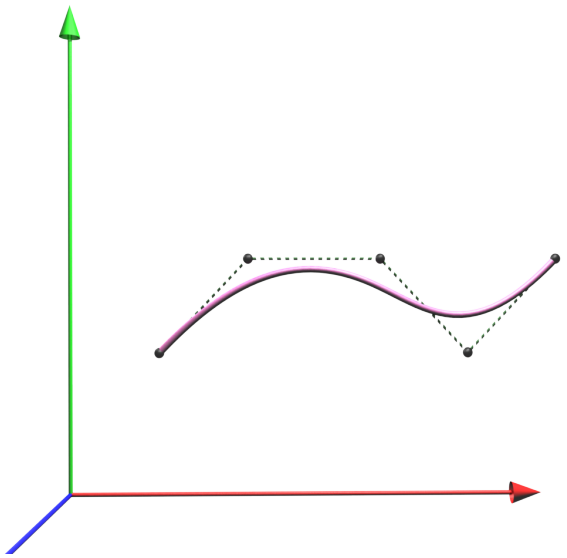

FIGURE 3.2: NURBS curve, an example.

obtained by generalizing the tensor-product surface form, a NURBS surface is, in general, not a tensor-product surface. A NURBS patch surface example can bee seen in Fig. 3.3.

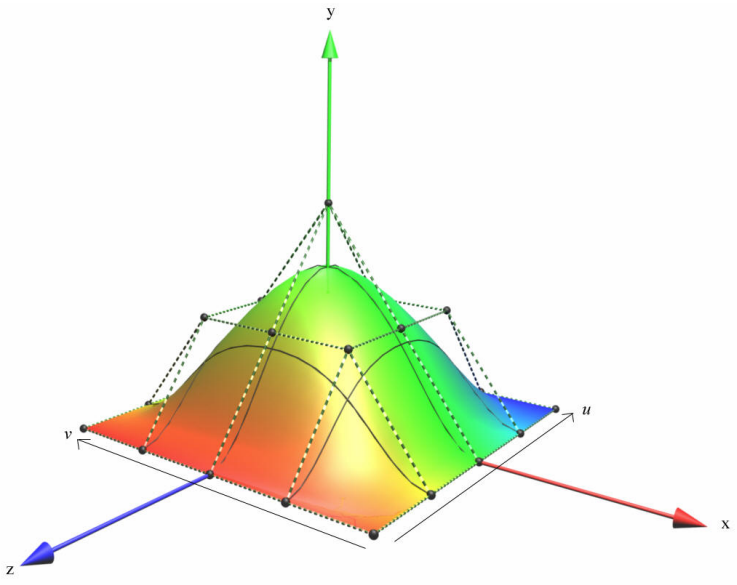

FIGURE 3.3: NURBS surface, an example.

According to what summarized by Piegl [61], to better highlight the NURBS properties, the curve form of Eq. 3.3 can be rewritten into the

following equivalent form:

$$C(u) = \sum_{i=0}^{n} P_i R_{i,p}(u) \tag{3.9}$$

$$R_{i,p}(u) = \frac{w_i N_{i,p}(u)}{\sum_{i=0}^{n} w_j N_{j,p}(u)} \tag{3.10}$$

where $R_{i,p}(u)$ are rational basis functions. Their analytic properties determine the geometric behavior of curves. The most significant properties are:

- Generalization: If all the weights are set to 1, then

$$R_{i,p}(u) = \begin{cases} B_{i,p}(u) \text{ if } U = \{0, 0, \ldots, 0, 1, 1, \ldots, 1\} \\ N_{i,p}(u) \quad \text{otherwise} \end{cases} \tag{3.11}$$

  where the $0's$ and $1's$ in U are repeated with multiplicity $p + 1$, and $B_{i,p}(u)$ denote the Bernstein polynomials of degree p.

- Locality: $R_{i,p}(u) = 0$ if $u \notin [u_i, ui + p + 1)$
- Partition of unity: $\sum_i R_{i,p}(u) = 1$
- Differentiability: In the interior of a knot span, the rational basis functions are infinitely continuously differentiable if the denominator is bounded away from zero. At a knot they are $p - k$ times continuously differentiable where k is the multiplicity of the knot.
- $R_{i,p}(u; w_i = 0) = 0$
- $R_{i,p}(u; w_i \to \infty) = 1$
- $R_{i,p}(u; w_j \to \infty) = 0 \quad j \neq i$

As a consequence, the NURBS curve will exhibit the following geometric characteristics:

- Bezier and nonrational B-spline curves are special cases.
- Local approximation: If a control point is moved or a weight is changed, it will affect the curve only in $p + 1$ knot spans.
- Strong convex hull property: if $u \notin [u_i, u_{i+1})$, then $C(u)$ lies within the convex hull of $P_{i-p}, \ldots, P_i$.
- Invariance under affine and perspective transformations.
- The same differentiability property as with the basis functions.
- If a particular weight is set zero, then the corresponding control point has no effect at all on the curve.

- if $w_j \to \infty$, then $C(u) = \begin{cases} P_i(u) \text{ if } u \in (u_i, u_{i+p+1}) \\ C(u) \quad \text{otherwise} \end{cases}$

NURBS surfaces can be analyzed similarly using the bivariate rational basis functions:

$$R_{i,p;j,q}(u,v) = \frac{w_{i,j} N_{i,p}(u) N_{j,q}(v)}{\sum_{r=0}^{n} \sum_{s=0}^{m} w_{r,s} N_{r,p}(u) N_{s,q}(v)}. \tag{3.12}$$

3.2.3 NURBS in MATLab environment

NURBS curves and surfaces have been implemented into MATLab environment using several examples on the file exchange of the Matworks MATLab central [1]. To better understand NURBS capability into MATLab environment, in this section a brief description of the main NURBS function implemented is proposed.

A simple NURBS curve can be easily created into MATLab by choosing the number of control points, the order of the curve and the desired number of points which will represent the curve itself. Of course also the inverse problem can be accomplished: given a curve through a set of coordinates (x, y) then the NURBS curve can be extracted. In Fig. 3.4(a) an example of NURBS curve realized in MATLab is shown. This is a 3$^{\text{rd}}$ order, 6 control points mono spaced curve. The generated NURBS entity of Fig. 3.4(a) can be modified just moving a control point or more control points. It is possible to translate, rotate or combine this entity to modify the geometry in the space. In Fig. 3.4(b) and Fig. 3.4(c) two examples of control points modification on NURBS of Fig. 3.4(a) are shown. Figure 3.4(b) shows the modification effect of the 3$^{\text{rd}}$ control points along z axis, whereas Fig. 3.4(c) shows the creation of two new NURBS curves obtained modifying the y and z directions of the control points of the NURBS curve of Fig. 3.4(a). Subsequently these curves can be easily used to obtain a NURBS surface, using a lofting approach as it is shown in Fig. 3.4(d).

Another typical approach used in this research work is the NURBS of Coons. In this case the surface is obtained inside of the four boundary NURBS curves and a surface patch can be generated. Figure 3.5(a) shows four different NURBS curves closed to form a polygon. As it can be seen in Fig. 3.5(b) NURBS coons can be obtained among the boundary curves. This is very useful in design and optimization, because it gives the possibility to choose which are the boundary curves and which are the curves to optimize through control points variations. Figure 3.6 shows a simple example of wing and fuselage reconstruction through NURBS curves and surfaces. In particular Fig. 3.6(a) shows a wing reconstruction with three simple airfoils (root, kink and tip airfoil) and Fig. 3.6(b) a simple fuselage obtained through eleven sections

[1] Matworks MATLab central page. File exchange.
http://www.mathworks.it/matlabcentral/.

NURBS curves. It is useful to notice that all the NURBS curves used in the Fig. 3.6 have several control points that can be easily managed to modify the generated surface. In Sec. 3.5 the applications of this technique are shown.

3.3 Objective Function

The objective of this chapter is to improve the aerodynamics of turboprop aircrafts via drag coefficient reduction to improve the performance. For this reason the drag coefficient has been assumed as objective function; it has been computed with the Young [52] formula, which is based on integral quantities of the boundary layer, evaluated at the body's trailing edge or separation zone as shown in Eq. 3.13.

$$C_D(s) = \frac{2\pi}{S_{\text{ref}}}\big[r_T(s)\theta(s)\big]U_{e,T}(s)^{\frac{H_T(s)+5}{2}} \tag{3.13}$$

where C_D is the drag coefficient, S_{ref} is a reference area (usually the maximum frontal area, in this case the wing planform area), r_T is the radius, θ is the boundary layer momentum thickness, $U_{e,T}$ is the inviscid external velocity and H_T is the boundary layer shape factor. The subscript T indicates that all quantities are to be evaluated at the body tail (x/L=1.0), or at the separation point. This is considered an approximate method to perform viscous calculations for general fuselages (non axial-symmetric bodies). As reported in Ref. [62, 63], comparisons with experiments have shown reasonably good agreement with experimental drag coefficients not only in case of axial-symmetric bodies, but also for some fuselages tested at Delft University in Ref [64]. Moreover the analysis performed in this work aims to provide an improvement of a reference geometry, thus it is out of the scope to get the true drag coefficient of a given geometry. The viscous calculations along some streamlines of the body has been performed. In particular six streamlines (3 in the upper and 3 in the lower zone) have been taken as reference for the calculation of the drag coefficient. The radius is considered as the mean value of the fuselage height, at each x-station, for both upper and lower streamlines. A drag coefficient can be obtained for both streamlines (Eq. 3.13) leading to six values. The fuselage drag coefficient will be taken as the average of average upper and average lower values. It is clear that this represents an approximate method because the boundary layer on the fuselage is three-dimensional, and axial-symmetric viscous calculations are not an accurate representation of a non-axial-symmetric flow condition on a non-axial-symmetric body. It is evident that the results are more and more inaccurate as the fuselage shape is far from an axial-symmetric body. A steepest gradient method GB algorithm is used to minimize the objective function.

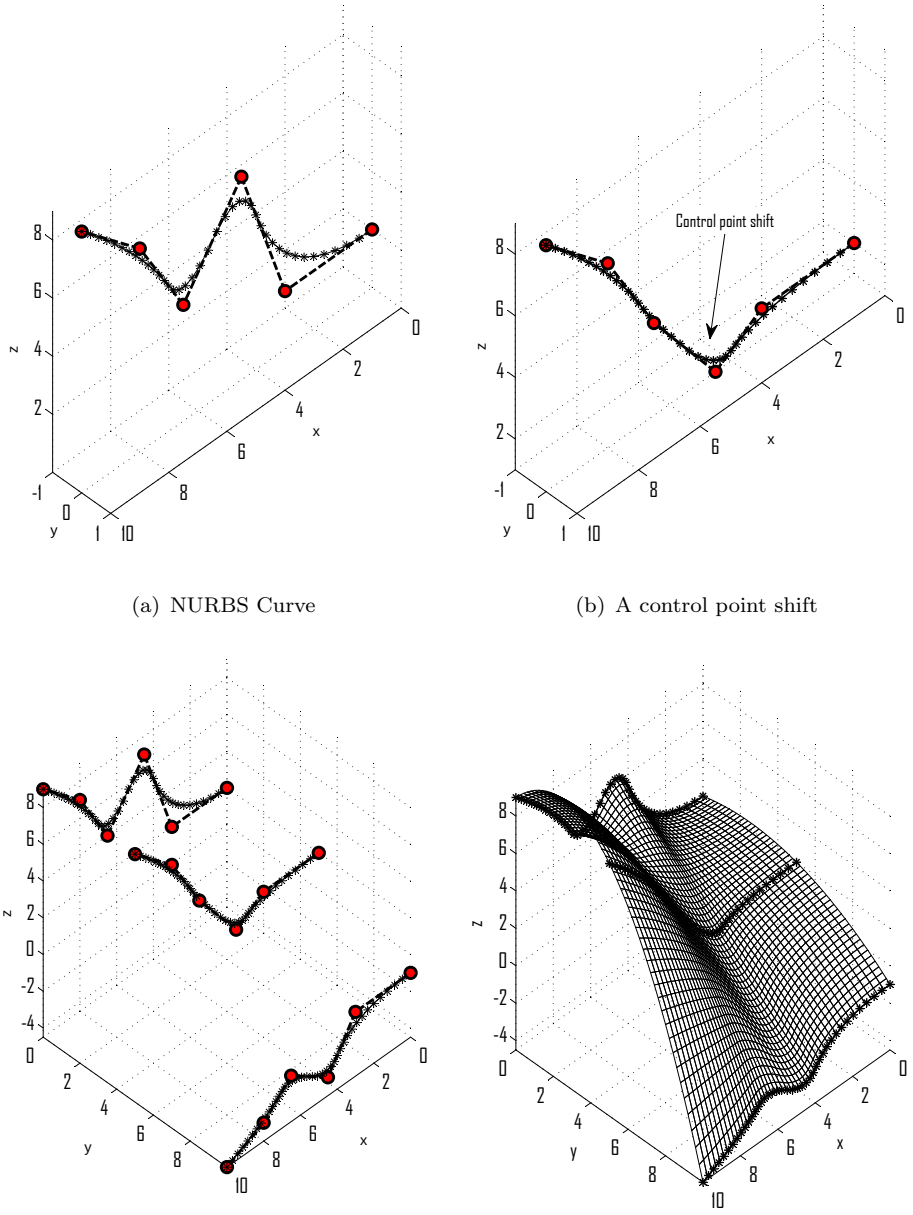

(a) NURBS Curve

(b) A control point shift

(c) Traslation and modifications along y and z

(d) NURBS lofting Surface

FIGURE 3.4: NURBS Curves and Surface example and modifications.

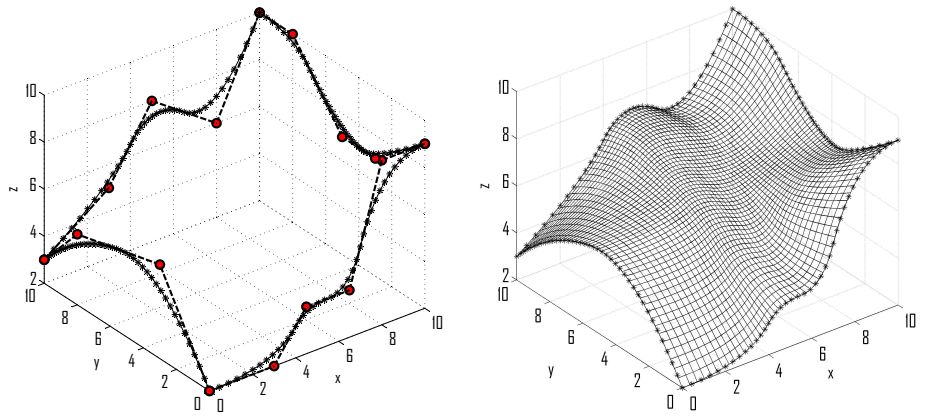

(a) NURBS Curve. Polygon for Coons surface (b) NURBS Coons surface

FIGURE 3.5: NURBS example of Coons surface creation

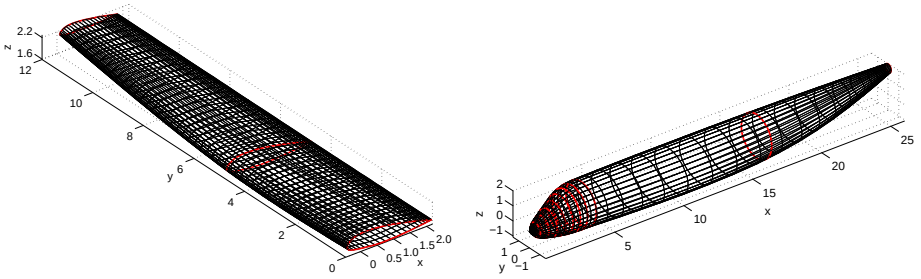

(a) NURBS wing reconstruction (b) NURBS fuselage reconstruction

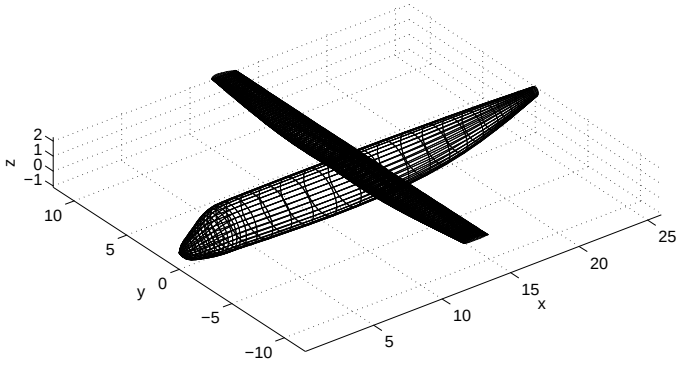

(c) NURBS wing-fuselage reconstruction

FIGURE 3.6: NURBS example wing-fuselage reconstruction

3.4 Turboprop Aerodynamic Analysis

A typical turboprop aircraft is considered as reference starting point, assuming characteristics shown in Tab. 1.4 and Fig. 3.7 for the ATR-72 aircraft. The reference aircraft performance have been widely discussed in Sec. 1.3.2 and they are used in following analysis as reference performance to compare with the optimized ones.

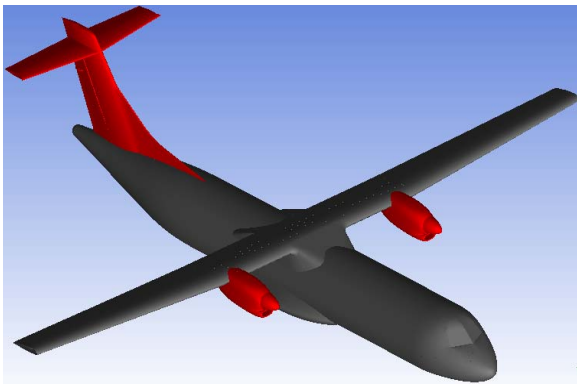

(a) ATR-72 complete model.

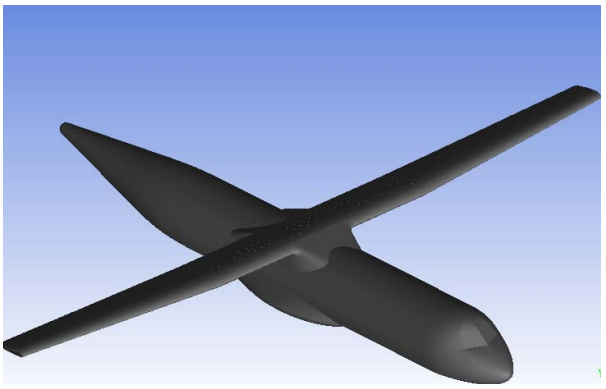

(b) ATR-72 wing body model.

FIGURE 3.7: ATR-72 model for the aerodynamic analysis.

A preliminary aerodynamic analysis is necessary to define zones on the aircraft where the flow behavior negatively affects total drag coefficient because of quasi-stagnations and separations. The aerodynamic analysis has been performed through a fast and reliable panel code solver available at DII deeply tested and used in Ref. [14, 15, 51]. This software allows the calculation of the nonlinear aerodynamic characteristics of arbitrary configurations in subsonic flow. Potential flow is analyzed with a subsonic panel method; the program is a surface singularity distribution based on Green's identity. Nonlinear effects of wake shape are treated in an iterative wake relaxation procedure; the effects of viscosity are treated in an iterative loop coupling potential flow

and integral boundary layer calculations. The compressibility correction is based on Prandtl-Glauert rule.

In order to reduce computational time the analysis has been carried out on the wing body configuration of the aircraft shown in Fig. 3.7(b). The geometry has been properly meshed and covered with about 12000 body panels subdivided into 5 components such as Fuselage nose, Fuselage tail, Karman, Fairing and Wing (shown in Fig. 3.8) with 3200 wake panels. The aerodynamic analysis has been performed at two reference flight condition, which are typical cruise and climb condition as shown in Tab. 3.1.

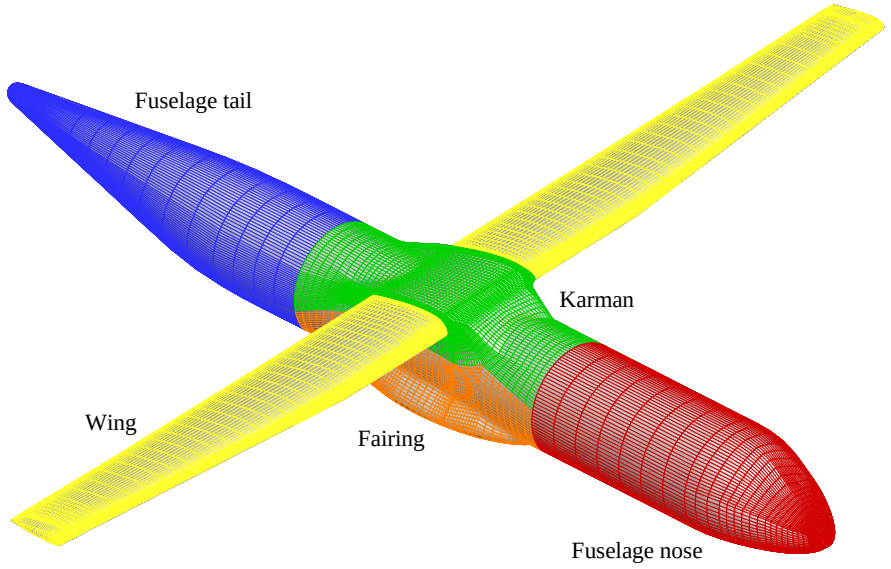

FIGURE 3.8: ATR-72 wing body mesh components.

TABLE 3.1: Reference aerodynamic conditions

Condition		M	Re
Cruise	$\alpha = 2.0$ deg. or $C_l = 0.5$	0.43	$11.5 \cdot 10^6$
Climb	$\alpha = 5.0$ deg. or $C_l = 1.0$	0.30	$7.0 \cdot 10^6$

The main aerodynamic results in terms of pressure coefficient and skin friction coefficient are here discussed, emphasizing more critical issues. The pressure distribution over the aircraft fuselage shows that a locally convex curvature causes the pressure to decrease and a locally concave curvature will lead to an increase in pressure especially along the upper ($\Theta = 0$ deg) and lower ($\Theta = 180$ deg) streamlines as shown in Fig. 3.9. A large suction peak over the crest of the Karman component ($C_p = -1.4$) occurs (see Fig. 3.9 and Fig. 3.10). Moreover a locally strong increase in the pressure is found where the local radius of concave curvature is very small, such as on the nose,

on the front/rear Karman zone and on the Fairing component (Fig. 3.9 and Fig. 3.10). As outlined by Schlichting [41] and Obert [65] these rapid flow variation should be controlled in the design phase. Geometry discontinuity (as those between Karman-fuselage and Fairing-fuselage) should be avoided or reduced. A more regular pressure distribution will result in lower drag than one with large variation [65].

This behavior not too suitable in terms of pressure distribution is also reflected in the skin friction coefficient distribution, as shown in Fig. 3.11 and Fig. 3.12. The viscous analysis highlights a critical turbulence separation in the rear zone of the Karman component as shown in Fig. 3.11. This behavior is clearly due to the entire boundary layer development, from the nose until the separation zone along the upper fuselage zone (see $\Theta = 0$ deg. in Fig. 3.11). The middle and lower streamlines ($\Theta = 90$ deg and $\Theta = 180$ deg in Fig. 3.11) show a normal development until a separation on the rear fuselage cone, mainly due to the upsweep angle. As it can be seen in Fig. 3.9 to Fig. 3.12, the flow on the cockpit after the stagnation point, suddenly accelerates (fuselage transition point has been fixed at $x = 0.5$ m from the aircraft nose). The flat windshield with protruding frame causes several vortices formation and a smoother transition between the cockpit and the windshield should be suitable, as also highlighted by Roskam [9], Obert [65] and de Mattos et alii [66].

Results reported in the present section are taken as the reference conditions for the following geometry optimization and they will be compared once terminated the optimization process.

Following Tab. 3.2 shows the aerodynamic results at reference cruise flow condition, divided for each components shown in Fig. 3.8. It is evident that almost the same drag coefficient contribution are given by wing and fuselage (0.00952 and 0.00883 for wing and fuselage respectively). Those of the fuselage will be used as reference value in the optimization process.

Table 3.2: Wing-Body reference analysis, Cruise Condition.

Reference aerodynamic analysis		
Components	C_D	C_L
Fuselage tail	0.00331	0.00732
Fuselage nose	0.00122	0.00955
Karman	0.00226	0.04174
Fairing	0.00204	-0.01023
Wing	0.00952	0.40240
TOTAL	0.01835	0.45078

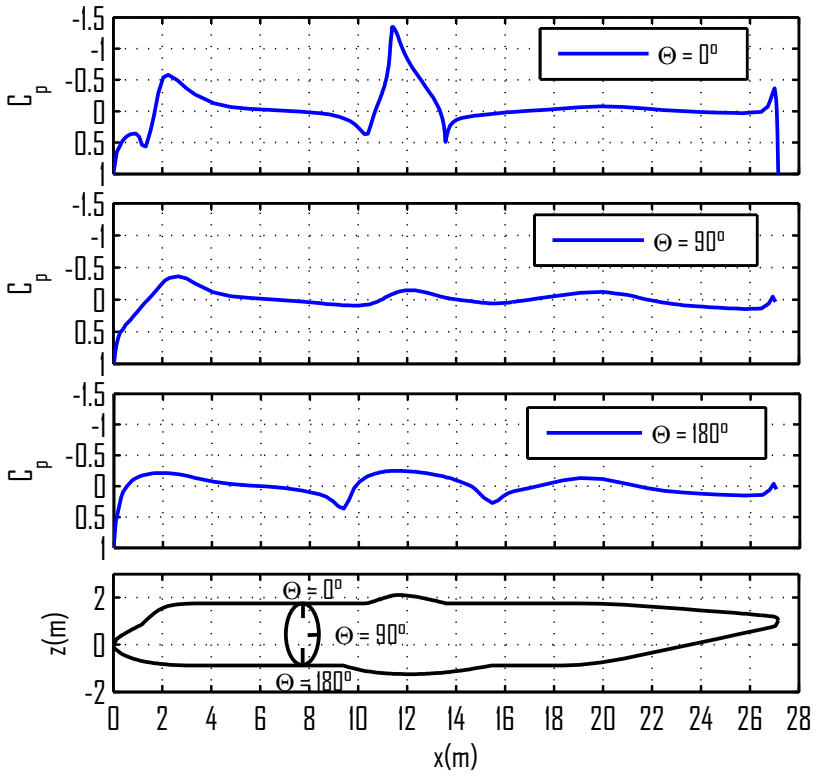

FIGURE 3.9: C_p distribution along upper, middle and lower streamlines, Cruise condition.

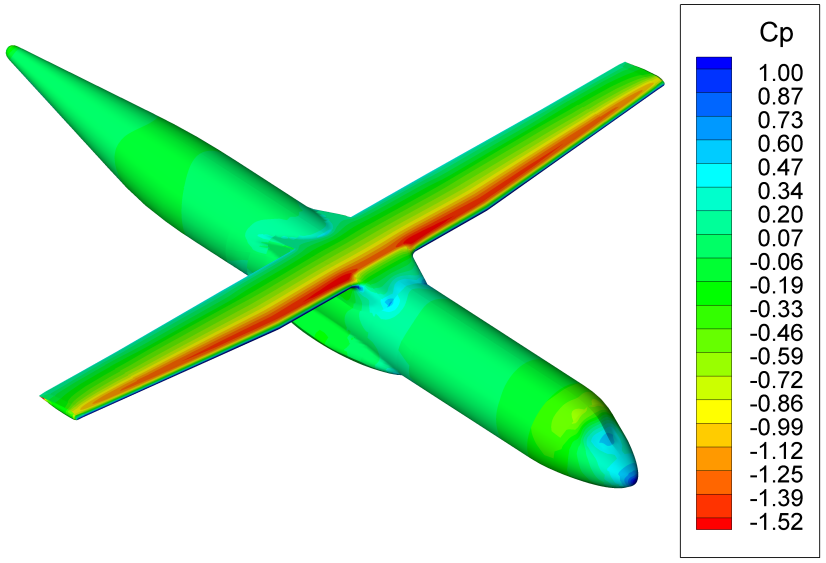

FIGURE 3.10: C_p contour, Cruise condition.

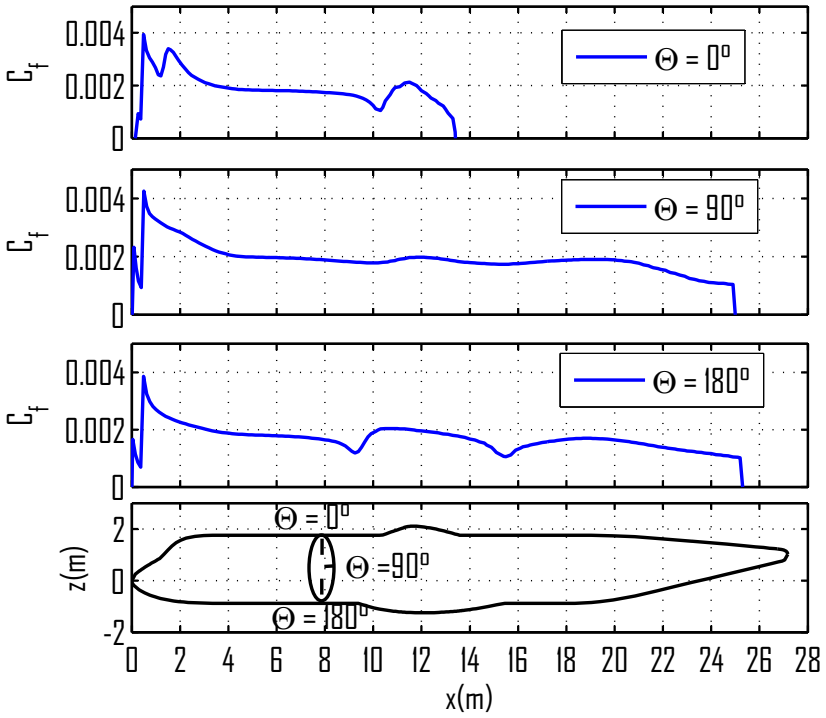

FIGURE 3.11: C_f distribution along upper, middle and lower streamlines, Cruise condition.

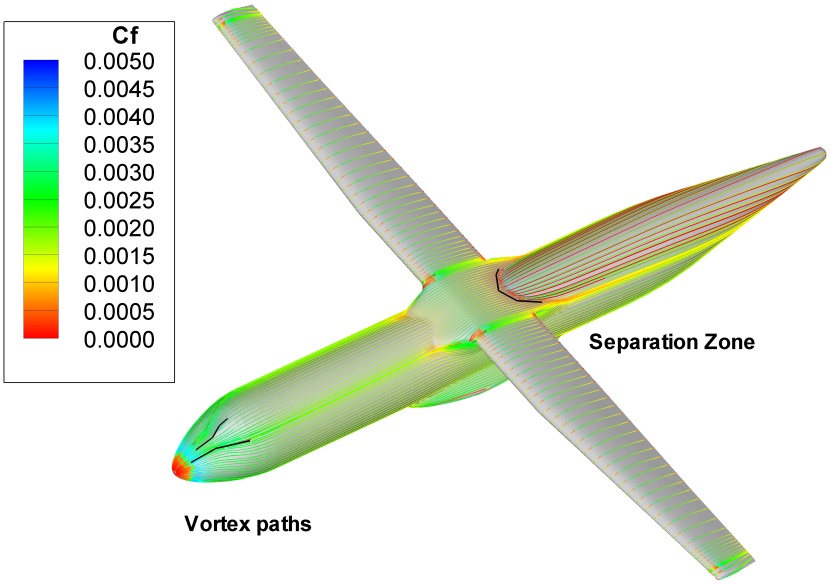

FIGURE 3.12: C_f contour, Cruise condition.

3.5 Applications

The optimization process has been introduced in Sec. 3.1 and shown in Fig. 2.1. As it has been discussed previously, the shape optimization is performed using a special set of curves and surfaces, the NURBS. These are modeled with a number of control points, which are given proper weights and moved in space during the optimization loops.

The strategy of optimization consists in defining a component of the aircraft to be optimized (for example the Karman component illustrated in Fig. 3.8 in green). By an appropriate input file the user can define what portion should be optimized by defining the boundary curves shown as red lines in Fig. 3.13. Along these boundary curves the tangential direction is preserved thanks to several control points C, as represented in Fig. 3.13. The NURBS control points A and B allow the geometry variation in height and in span-wise respectively. The user has also to set the variation range of the A and B control points of Fig. 3.13.

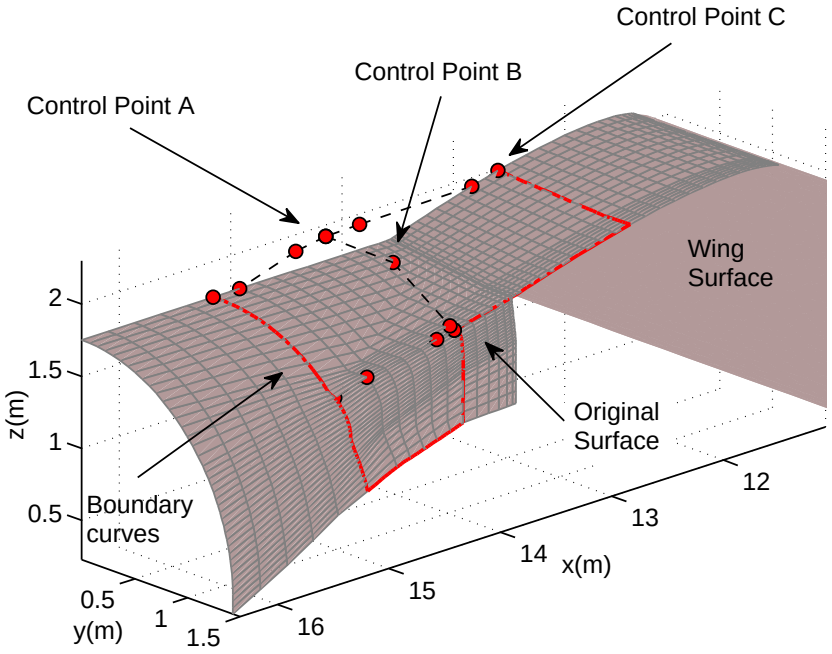

FIGURE 3.13: Example of NURBS control points and boundary curves, Karman component application, rear view

According to the control points position and boundary curves, the NURBS curves are built [54, 61]. Subsequently the NURBS modified surface can be carried out through these curves, as represented in Fig. 3.14. The new surfaces are put on the reference wing-body geometry; finally the new configuration is analyzed through the panel code solver. This process is iterated until the optimized geometry is found. The drag coefficient has been assumed as the

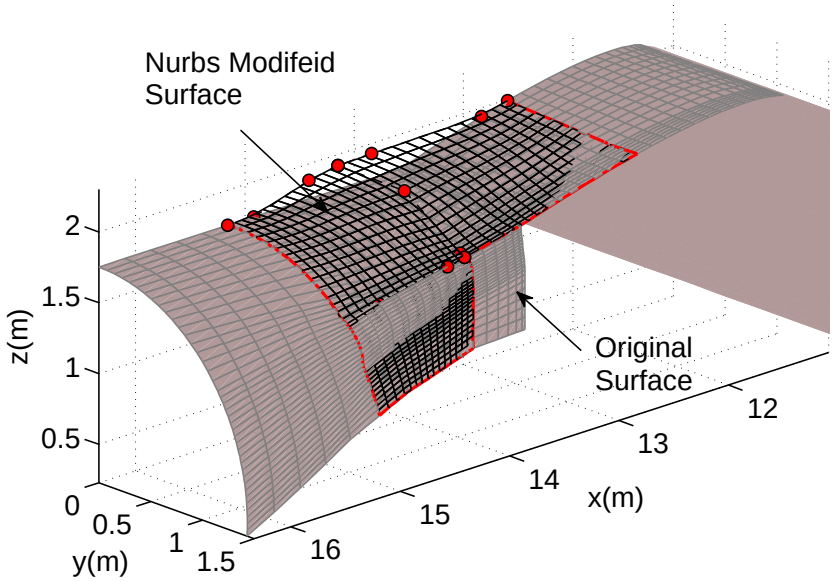

FIGURE 3.14: Example of NURBS surface, Karman component application, rear view.

objective function; it has been computed with the Young formula (see Eq. 3.13), which is based on integral quantities of the boundary layer, evaluated at the body's trailing edge or separation zone. A steepest gradient method is used to minimize the objective function.

In the following sections three applications of the above mentioned procedure have been performed to improve the aerodynamic behavior of the reference aircraft analyzed in Sec. 3.4:

- Aircraft Fuselage nose.
- Aircraft Wing-Fuselage junction (named Karman component).
- Aircraft Undercarriage vane (named Fairing component).

Drag coefficient reduction and its effect on the aircraft performance are put in evidence.

3.5.1 Aircraft Fuselage nose

The aircraft nose is a part of the Fuselage nose component shown in Fig. 3.8. Only a subdomain of this component will be involved in the optimization process (shown in red in Fig. 3.15(a). However the whole optimization is performed on the wing-body geometry. The aircraft nose geometry modification has been performed in the optimization loop through NURBS technique. All modifications starts from a standard reference geometry (which is, at the beginning, the original nose geometry shown in Fig. 3.15(a)); in particular the

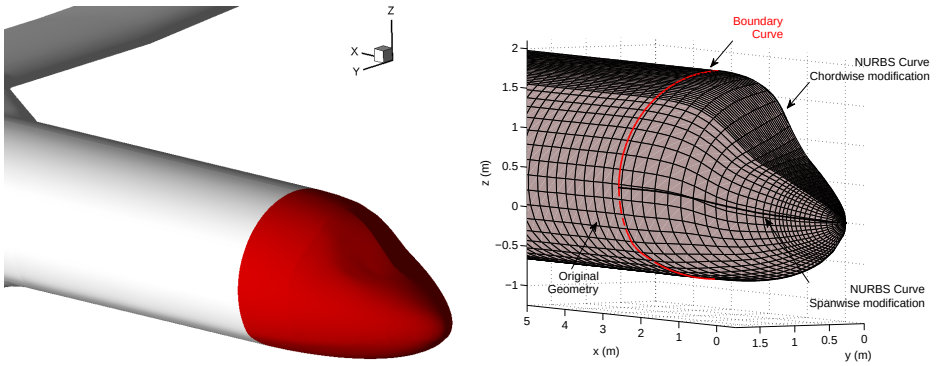

(a) Aircraft nose component. (b) Aircraft nose NURBS reconstruction.

FIGURE 3.15: Aircraft nose geometry involved in the optimization loop.

first constant fuselage cross-section has been assumed as a boundary NURBS curve (red curve in Fig. 3.15(b)), whereas the solid black curves are NURBS curves, which can vary in height, width and length. These two NURBS curves can be moved into a predetermined space set by the user, given the possibility to modify the original shape in all direction. In particular, starting from the original geometry of the nose, a range of variations of $-1.5\text{m} \leq x \leq +0.5\text{m}$, $-0.2\text{m} \leq y \leq +0.5\text{m}$ and $-0.5\text{m} \leq z \leq +0.5\text{m}$ have been imposed along x, y and z axis respectively. An example of NURBS curves variation in height and length is shown in Fig. 3.16. Moreover a geometrical constraints has been

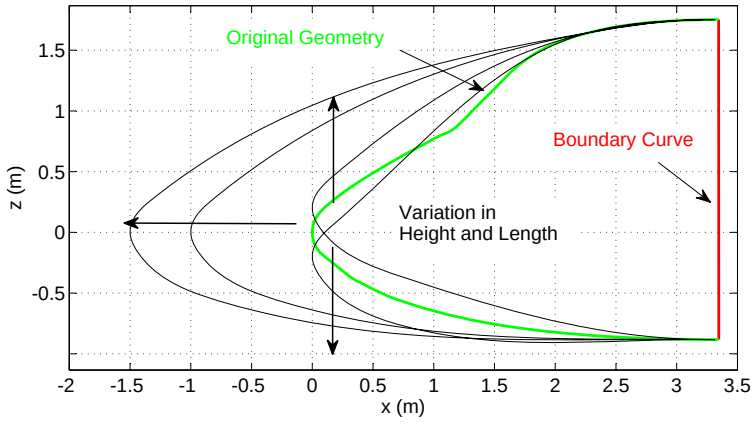

FIGURE 3.16: Aircraft nose NURBS variation in height and length.

also imposed on the pilot head angle of visibility, which have to satisfy what required by the regulation (angle not below $15deg$ as prescribed in CS 25.775 that establishes this minimum inclination of the cockpit windscreen respect to the longitudinal axis of the airplane in order to avoid reflection and aberration Ref. [67]). Transition has been always fixed at 0.5 m from the aircraft more forward x coordinate. The optimization of the aircraft nose has been performed

in cruise condition shown in Tab. 3.1 and all the settings are summarized in Tab. 3.3.

TABLE 3.3: Fuselage Nose Optimization, Cruise condition

Fuselage Nose Optimization	
Algorithm	GB
Objective function	$C_{D_{\text{fus}}}$
Condition	Cruise
Boundary	$-1.5m \leq x \leq +0.5m$
	$-0.2m \leq y \leq +0.5m$
	$-0.5m \leq z \leq +0.5m$
Geom constraints	Windscreen angle $\leq$ 15 deg [67]
Aero constraints	fixed transition at
	$x/l_f = 0.05$
Solver	Panel method
Parameterization	NURBS
Results	
C_D Initial	0.01835
$C_{D_{\text{fus}}}$ Initial	0.00882
C_D Optimal	0.01802
$C_{D_{\text{fus}}}$ Optimal	0.00849
Elapsed time (h)	$12h05'$
Objective eval. calls	214

Results of the optimization have given a drag coefficient reduction of the wing-body reference aircraft configuration of about 3.3 drag counts in cruise condition. This reduction is all due to the nose components as shown in Tab. 3.3 (which is the only one involved in the optimization process). The best geometry is translated forward of about 0.5 m and downward of about 0.5 m respect to the reference one, whereas in width is almost equal to the reference one (this is also related to the respect of the boundary conditions). Sections comparison of the original and optimized nose geometry are shown in Fig. 3.17, whereas a sketch of the drag coefficient in the optimization process is shown in Fig. 3.18. The optimized nose geometry allows to reduce forward compression on the upper zone as highlighted in Fig. 3.19(a) with a slightly higher suction on the lower zone as shown in Fig. 3.19(a). Effects of nose geometry optimization can be better understood considering the behavior of the pressure coefficient along the streamlines of the fuselage as reported in the following Fig. 3.20. In this figure it is possible to see that the modified geometry allows to eliminate the first peak of compression (due to windscreen on the original geometry) leading to a more gradual successive expansion on the upper part of the nose ($\Theta = 0$ deg of Fig. 3.20). Upper peak of expansion has been reduced from a value of pressure coefficient equal to -0.6 to a value less than -0.5. Figure 3.20 shows that the lower peak of expansion is increased

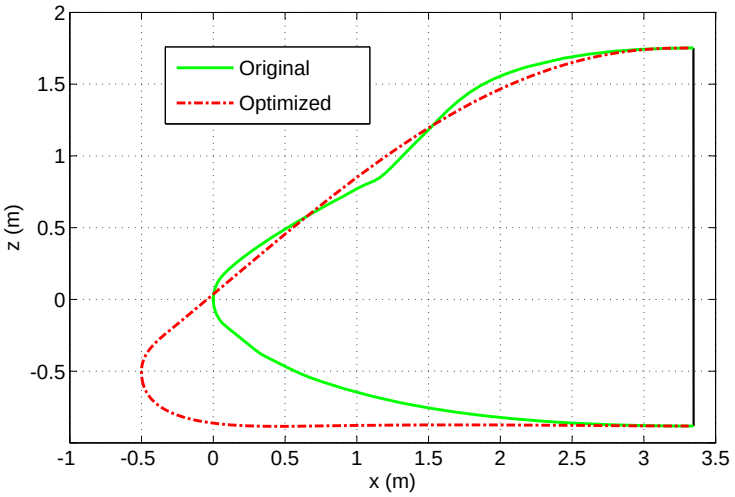

FIGURE 3.17: Aircraft nose sections comparison.

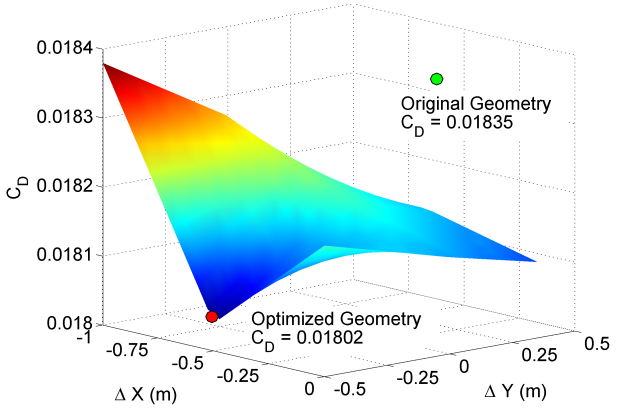

FIGURE 3.18: Aircraft nose drag coefficient during optimization process.

and anticipated, leading to a more gradual compression in the following lower part. It is evident that the optimized geometry could also lead to further improvement in laminar flow condition. Moreover, the new configuration accomplishes the regulations in term of pilot angle of visibility [67]. Since the optimized geometry of the nose is stretched the fuselage instability is 5% higher of the reference one. Finally an interesting consideration directly derive from the observation of the real nose geometry between the two main large turbo-propeller competitors, ATR-72 and Dash Q-400: looking to the Fig. 3.21 it is clearly visible as the Dash Q-400 nose geometry is quite similar to the optimized geometry, with a smother surface than the ATR-72.

The performance improvement due to nose optimization are summarized in Sec. 3.5.4. The main effect is to improve the maximum cruise true airspeed of about 2 knots.

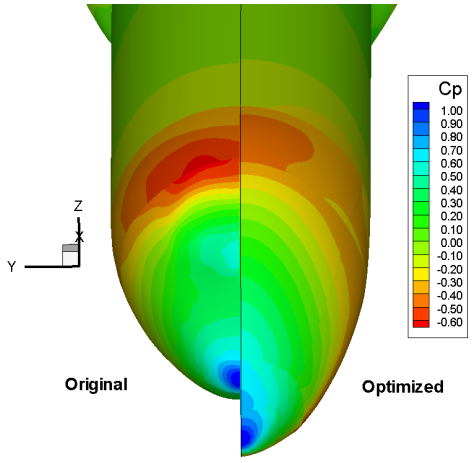

(a) Aircraft nose comparison, front view.

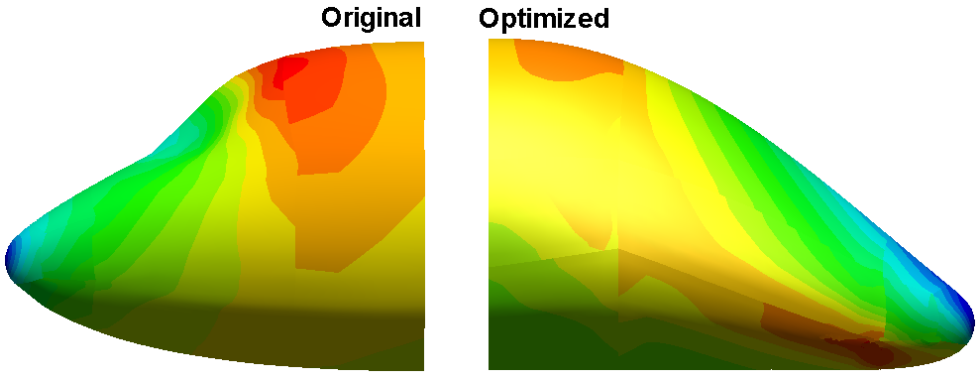

(b) Aircraft nose comparison, side view.

FIGURE 3.19: Aircraft nose pressure coefficient comparison, Original and Optimized geometry.

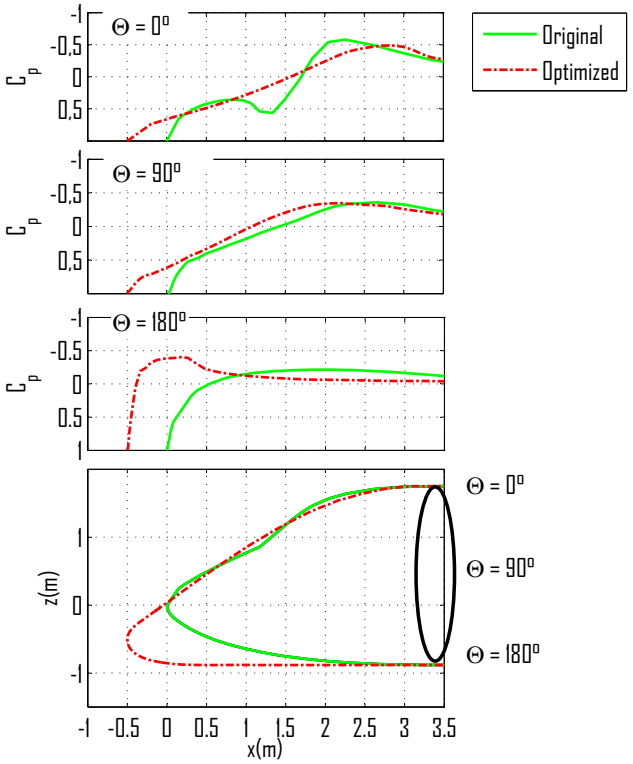

FIGURE 3.20: C_p distribution along upper, middle and lower streamlines, Cruise condition. Comparison of Original and Optimized nose geometry.

(a) ATR-72 Particular of nose geometry. (b) Dash Q-400 Particular of nose geometry.

FIGURE 3.21: ATR-72 and Bombardier Dash Q-400 Nose geometry.

3.5.2 Wing-Fuselage junction

The optimization process applied to the wing-fuselage junction, named Karman (green one in Fig. 3.8), aims to avoid the separation zone shown in Fig. 3.11 and Fig. 3.12 through better airflow behavior on the entire component and reduce fuselage drag coefficient. It has been imposed as geometrical constraint that the minimum upper height should be equal to the maximum height coordinate of the reference geometry, and the tangential direction with the fuselage must be ensured everywhere. To better define the karman component geometry, in the optimization loop two separated zone has been identified: karman forward zone and kaman rear zone (see Fig. 3.22). It has been necessary to define

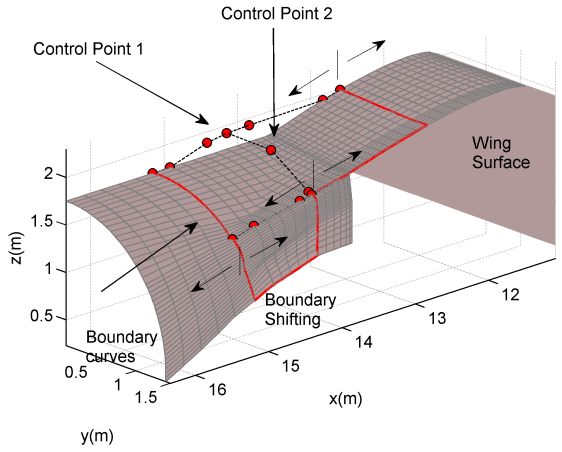

(a) NURBS and control points for Karman rear part.

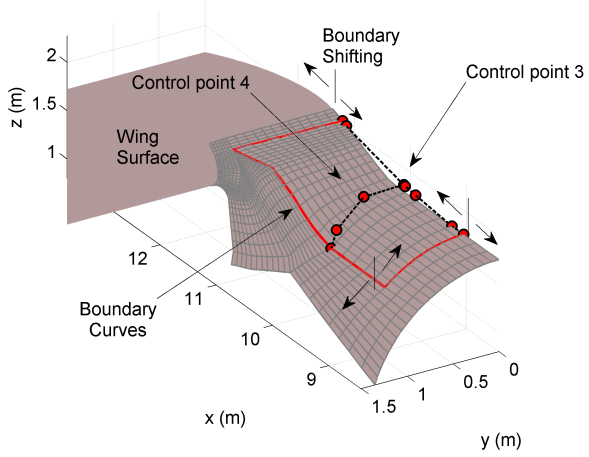

(b) NURBS and control points for Karman forward part.

FIGURE 3.22: NURBS and control points for Karman optimization.

both forward and rearward parts through NURBS technique and a set of 4 control points have been used in the optimization loop as shown in Fig. 3.22.

These control points can vary during the optimization, whereas the others are derived from these ones. In particular control points 1 and 3 allow the height modification of the associated NURBS curves, whereas control points 2 and 4 allow span-wise modifications. It has to be noted that the optimized geometry is constrained to stay all upper the original geometry. The boundary curves are those shown as example in red in Fig. 3.22 and they have been set to vary along the entire Karman component during the optimization process. The tangential control points have to be defined in order to maintain the tangential direction respect to the original geometry. These control points are automatically computed on the basis of the control points 1 to 4 and of the boundary curves. It is worth to notice that the new curves are perfectly tangent to the original surface and that the new surface is quite smooth. The main settings for this application are summarized in Tab. 3.4.

TABLE 3.4: Wing-fuselage junction Optimization, Cruise condition.

Fuselage junction Optimization	
Algorithm	GB
Objective function	$C_{D_{\text{fus}}}$
Condition	Cruise
Range of variation	
Control point 1	$0 \leq \Delta z \leq +0.3m$
Control point 2	$-0.3m \leq \Delta y \leq +0.3m$
Control point 3	$0m \leq \Delta z \leq +0.3m$
Control point 4	$-0.3m \leq \Delta y \leq +0.3m$
Geom constraints	Upper of the original geometry
Aero constraints	fixed transition at $x/l_f = 0.05$
Solver	Panel method
Parameterization	NURBS
Results	
C_D Initial	0.01835
$C_{D_{\text{fus}}}$ Initial	0.00882
C_D Optimal	0.01768
$C_{D_{\text{fus}}}$ Optimal	0.00815
Elapsed time (h)	$19h55'$
Objective eval. calls	299

The optimization process applied to the karman component has given a fuselage drag coefficient reduction of about 7 drag counts in cruise condition. Time elapsed during the process has been of about 20 hours due to about 300 objective function evaluation calls. Comparisons between optimized and original geometry are represented in Fig. 3.23 and Fig. 3.24. The abrupt geometrical discontinuities are avoided both on the front and the rear zone, thanks to a smoother and slightly longer component. The optimized geometry

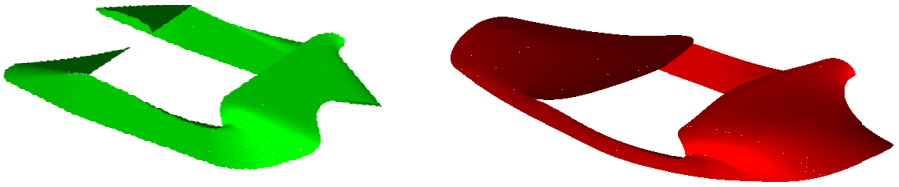

FIGURE 3.23: Karman geometry comparison,
Original (green), Optimized (red).

is higher than the original one both in the front and rear zone as shown in the sections of Fig. 3.24. It has to be noted that the optimized geometry creates a better geometrical ramp for the airflow and also the recovery of the flow behind wing trailing edge is better than the original one. The aerodynamic optimization has also highlighted a better behavior in terms of pressure and friction distributions. The pressure gradients are reduced along the entire component and the separation in the rear part of the Karman (shown in Fig. 3.11 and Fig. 3.12) is avoided as it can be seen in Fig. 3.25. The optimization effects of the karman geometry can be better understood considering the behavior of the pressure and friction coefficients along the symmetric middle streamline of the fuselage as shown in Fig. 3.26. The optimized geometry allows to realize a gradual recovery of pressure in the front zone of the Karman so that the pressure coefficient reaches a value approximately equal to 0.2, whereas the original geometry leads to a value equal to 0.4. Also the expansion in correspondence of top of the wing is more gradual and the pressure coefficient reaches a value equal to $C_p = -1.1$ instead of $C_p = -1.4$. In the rear karman zone, as evidenced in the Fig. 3.26, the flow re-compression is approximately equal to $C_p = 0.2$, whereas, in the original geometry, it is equal to $C_p = 0.5$. This leads to a better recovery of pressure in the rear upper zone so that flow does not separate anymore and pressure drag is reduced as shown in Fig. 3.26. In particular, it can be noticed that the peak of pressure, that appeared in Fig. 3.25 and Fig. 3.26 where the Karman joins the fuselage (that is at $x = 13.50$ m station), has been eliminated leading to a gradual variation of pressure along the spanwise direction avoiding separation. Finally, it is possible to say that the optimization of Karman leads to a better behavior of pressure along the fuselage causing a reduction of pressure drag and avoiding separation phenomena.

As it has been said before, total drag coefficient is reduced of about 7 counts, giving a maximum true airspeed improvement of 3.5 knots . The drag coefficient reduction grows with the aircraft angle of attack because of the separation zone reduction on the optimized geometry. The performance improvement due to the karman optimization are summarized in Sec. 3.5.4. ATR-72 and Dash Q-400 top view during flight are shown in Fig. 3.27. Both the aircrafts show a large wing-fuselage junction that could be improved according to the guidelines proposed in this optimization.

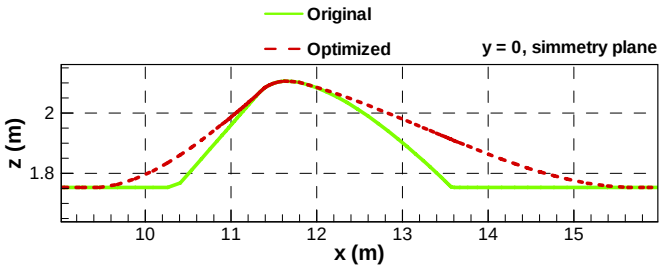

(a) Karman simmetry plane comparison, $y = 0$.

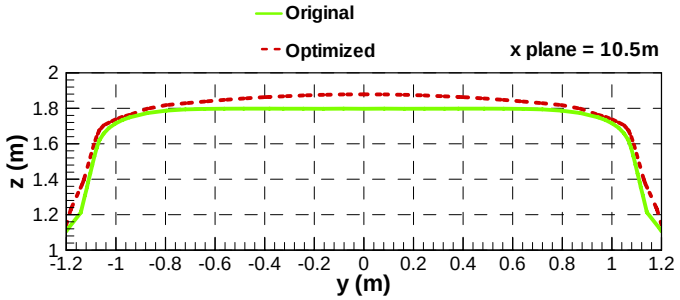

(b) Karman x planes comparison, $x = 10.5$ m.

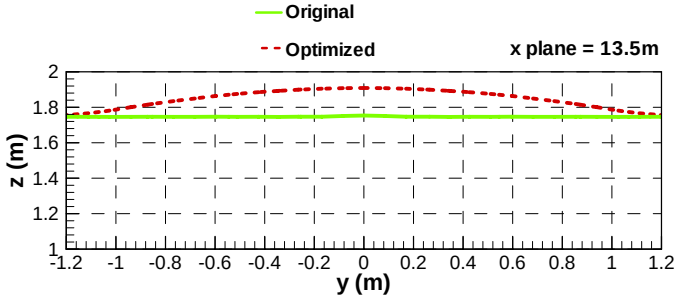

(c) Karman x planes comparison, $x = 13.5$ m.

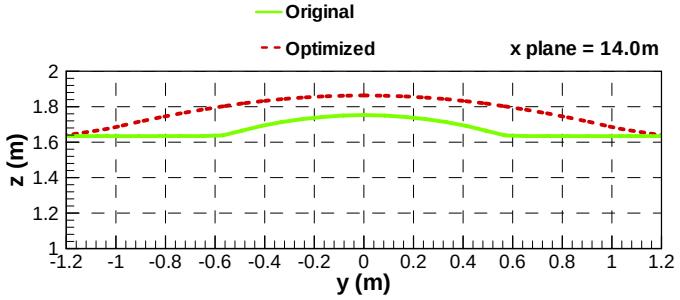

(d) Karman x planes comparison,$x = 14.0$ m.

FIGURE 3.24: Karman main sections geometry comparison, Original (green), Optimized (red).

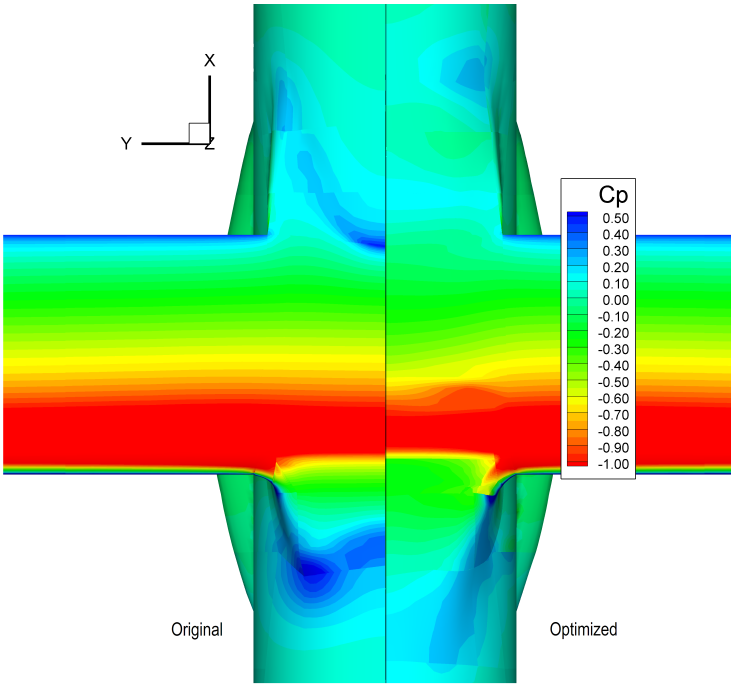

(a) C_p contour, Original and Optimized geometry, Cruise condition, top view.

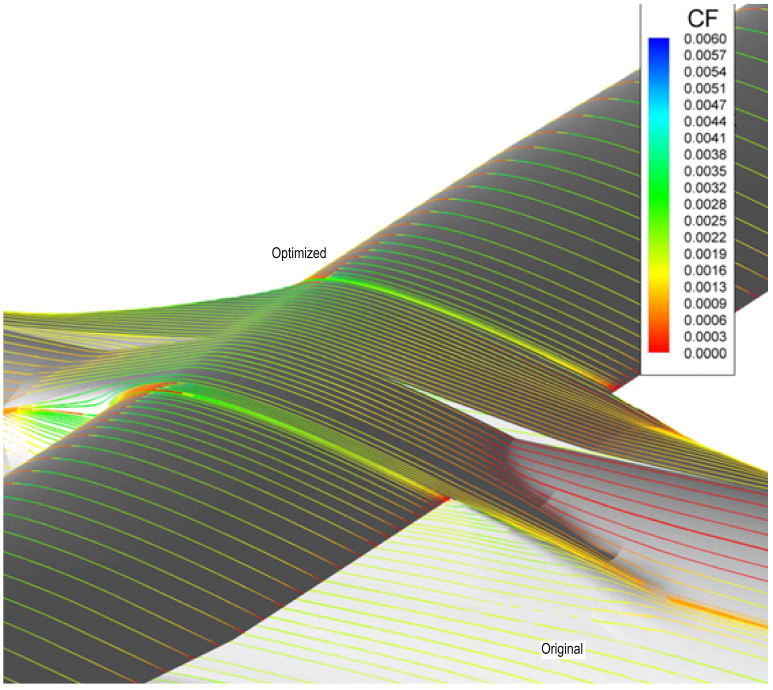

(b) C_f along on-body streamlines, Original and Optimized geometry, Cruise condition, rear view.

FIGURE 3.25: Pressure and friction coefficient on the Original and Optimized Karman geometry.

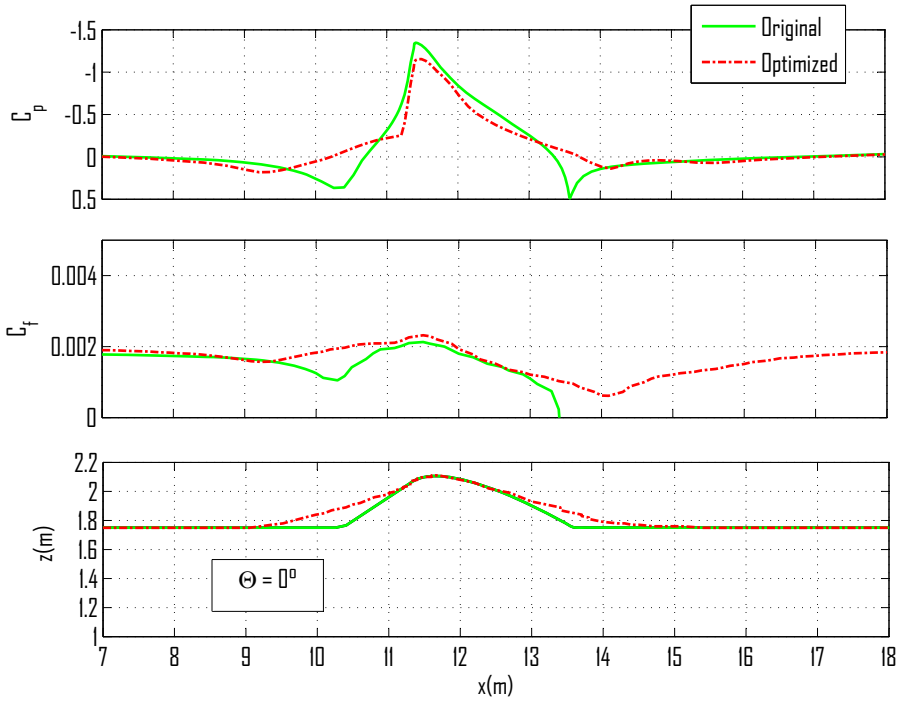

FIGURE 3.26: C_p and C_f distribution along upper streamline, Cruise condition. Comparison of Original and Optimized karman geometry.

(a) ATR-72, top view. (b) Bombardier Dash Q-400, top view.

FIGURE 3.27: ATR-72 and Bombardier Dash Q-400.

3.5.3 Undercarriage vane

The undercarriage vane is of course very dependent on the aircraft configuration, in particular on the landing gear position. In general the large turbo-propeller aircrafts traditionally have the undercarriage in the fuselage and they need of a geometry that contains it because it is not possible to have the entire undercarriage geometry into the fuselage due to ground performance stability. The reference undercarriage vane is a fairing geometry and it has a good aerodynamic shape with a slender geometry on the sides but it offers an obstacle to the flow in the forward zone similar to the karman geometry as shown in the pressure coefficient distribution in Fig. 3.9. For this reason this application aims to reduce the compression in this zone, to obtain a better pressure recovery and to reduce total drag. Several control points are considered both for modification and for maintaining the tangential direction respect to the original surfaces. Figure 3.28 shows the NURBS approach applied to the fairing component. Control point 1 allows variations in height along the z coordinate while control point 2 allows variations in width along the y coordinate. Varying the positions of the parametric points it is possible to build different geometries by tracing the relative interpolating surfaces, as shown in Fig. 3.28. Geometrical constraints have been imposed to the

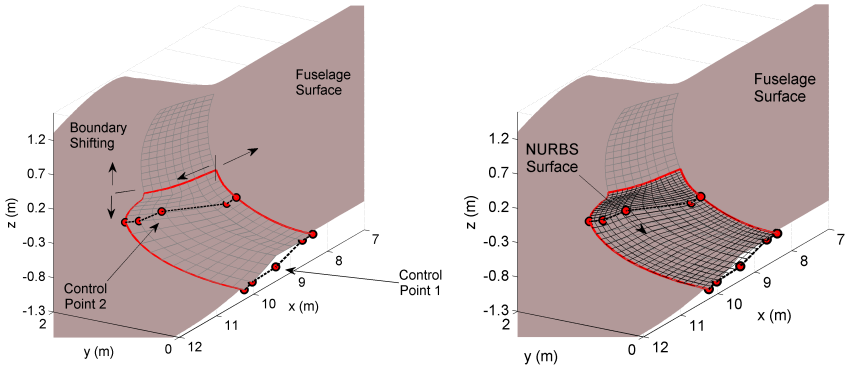

(a) NURBS and control points for Fairing component.

(b) NURBS surface for Fairing component.

FIGURE 3.28: NURBS for Fairing component optimization.

optimization process in terms smallest allowable surface (the original one) and compliance with tangential directions. The main settings used during the optimization process are summarized in Tab. 3.5. After about 100 iterations the value of fuselage drag coefficient has been reduced of about 1.5 drag counts. The optimized geometry is longer than the original of about 40 cm. Results show that the optimized geometry allows to sensibly reduce compression in the anterior part of the fairing giving a positive influence on total drag. Pressure coefficient peak has been reduced from 0.4 to about 0.25 for the symmetric middle streamline coincident with the axis of symmetry of the aircraft as

TABLE 3.5: Fairing Optimization, Cruise condition

Fairing Optimization	
Algorithm	GB
Objective function	$C_{D_{\text{fus}}}$
Condition	Cruise
Range of variation	
Control point 1	$0 \leq \Delta z \leq +0.3m$
Control point 2	$0 \leq \Delta y \leq +0.3m$
Geom constraints	Lower of the original geometry
Aero constraints	fixed transition at $x/l_f = 0.05$
Solver	Panel method
Parameterization	NURBS
Results	
C_D Initial	0.01835
$C_{D_{\text{fus}}}$ Initial	0.00882
C_D Optimal	0.01820
$C_{D_{\text{fus}}}$ Optimal	0.00867
Elapsed time (h)	$6h46'$
Objective eval. calls	101

shown Fig. 3.29(a) and also the compression on the fairing leading edge has been reduced from about 0.5 to 0.3 as shown in Fig. 3.29(a). In the following Sec. 3.5.4 the performance improvement due to the optimization components is shown.

3.5.4 Performance improvement due to Optimization

Sections 3.5.1, 3.5.2 and 3.5.3 have shown how the drag coefficient of a turboprop fuselage can be reduced, giving also some guidelines to future design. In particular has been highlighted that:

- Rapid flow variation should be controlled, by controlling geometry change of curvature and radii of curvature.
- Geometry discontinuity should be avoided or reduced.
- Any flow separation must be avoided.
- Where it is possible, longer slender geometries have to be applied. Of course a compromise have to be reached.

However the proposed applications have shown the capability of the optimization procedure to give interesting results not only in terms of drag reductions but also in terms of flow behavior interpretations. Of course the

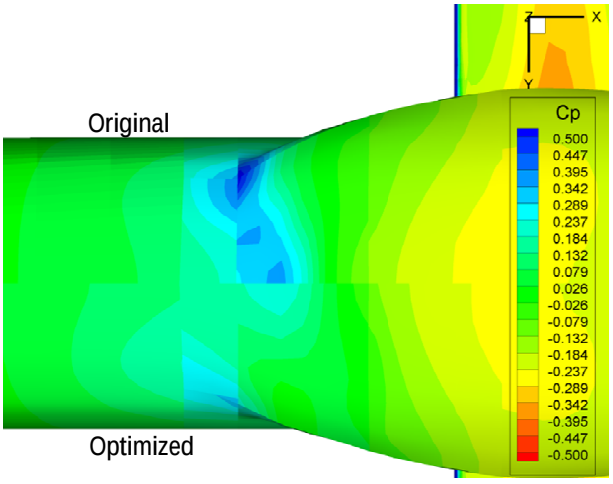

(a) C_p contour, Original and Optimized geometry, Cruise condition, bottom view.

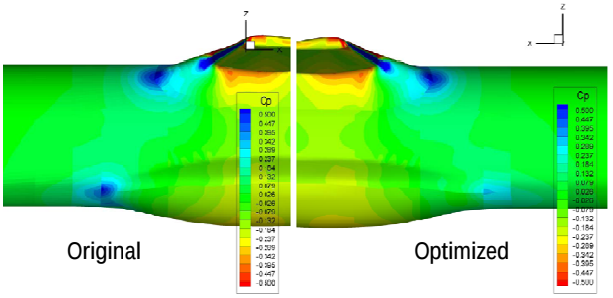

(b) C_p contour, Original and Optimized geometry, Cruise condition, side view.

FIGURE 3.29: Original and Optimized Fairing geometry and pressure coefficient.

drag reduction objective is the crucial aspect of the aircraft design with all the implications in terms of aircraft performance and economic success. In Tab. 3.6 the results of the above mentioned optimizations are summarized for both cruise and climb reference condition of Tab. 3.1. The three proposed applications give a drag coefficient reduction of about 12 to 14 drag counts in cruise and climb conditions respectively. It means a percentage reduction respect to reference $C_{D_0} = 0.0306$ of between 4 to 5%. As it has been discussed in Sec. 1.3 the level flight performance (such as the maximum speed or fuel consumption) are mainly dependent from the zero lift drag coefficient and they could be improved with the suggestions derived from the optimization applications (it is interesting to see the effect on the performance of zero lift drag coefficient reduction shown in Fig. 1.16 and Fig. 1.17).

In this section performance of the aircraft with optimized components are compared to the reference performance computed in Sec. 1.3.2 and shown

TABLE 3.6: Optimized results, drag coefficient reduction for Nose, Karman and Fairing components

Optimized results, drag coefficient reduction		
Components	$\Delta\ C_{D_{CRUISE}}$ (counts)	$\Delta\ C_{D_{CLIMB}}$ (counts)
Nose	3.3	3.5
Karman	6.7	8.2
Fairing	1.5	2.2
Total	11.5	13.9
% of reduction respect to reference	-3.8 %	-4.5%

Reference C_{D_0} value of 0.0306 (306 counts) computed in Sec. 1.3.

in Tab. 1.5. All of the optimized aircraft performance has been computed assuming the drag coefficient reduction obtained during cruise. This is a conservative way respect to use the climb results. As it has been said before drag coefficient reduction gives a maximum true airspeed of about 2% respect to the reference aircraft equal to 5 kts. This value is not negligible for the airlines and for aircraft industries. On a typical 200 nm mission the optimized aircraft allows a fuel consumption reduction of about 2.6%, which means a "free flight" every 40 flights! Of course also ground and climb performance are improved due to drag reduction, whereas the effects on take-off and landing distances (which are mainly influenced by high lift aerodynamic) are negligible. It has to be noted a 5.7% of rate of climb improvement in OEI condition and negligible values in terms of ceiling performance (around 1%).

TABLE 3.7: Original and Optimized Aircraft performance comparison.

Aircraft configuration	Original	Optimized	
C_{D_0}	0.03060	0.02945*	
e	0.85	0.85	
Performance			% of improvement
FAR S_{TO} (ft)	4065	4058	−0.2%
FAR S_{LAN} (ft)	3176	3166	−0.3%
R/C s.l. AEO (ft/min)	1437	1453	+1.1%
R/C 10 kft AEO (ft/min)	1063	1081	+1.6%
R/C s.l. OEI (ft/min)	345	355	+2.9%
R/C 10 kft OEI (ft/min)	209	221	+5.7%
Net Ceiling AEO (ft)	23561	23773	+0.9%
Net Ceiling OEI (ft)	10968	11178	+1.9%
Maximum V_{TAS} at 20kft (kts)	262	267	+1.9%
Fuel consumption for a 200 nm mission (kg)	594	579	−2.6%

* Cruise condition optimization result

3.6 Winglet Design

Historically the first recognized concept of a wing-tip device dates back to 1897 and it is due to the English engineer Frederick W. Lanchester, who used and patented wing end-plates as a method for controlling wingtip vortices [68]. After several years, in 1930, the American engineer Vincent Burnelli received an US patent for his *End Plating Wing Tips* [69]. Also at NACA the effect of the end plate at wing tip were investigated [70], with particular attention to the wing lift coefficient distribution. One of the greatest contributions on both theoretical and experimental investigations of the wingtip physical phenomena was due to Sighard Hoerner [71]. He investigated the aerodynamic characteristics of wing tips, and he did experimental investigations concerning the mechanism of the tip vortices and the lift/drag ratio of a wing fitted with several differently shaped tip caps. Hoerner's concept was further developed at NASA's Langley Research Center. During the seventies Whitcomb *et alii* [72–74] designed winglet for modern transport aircraft. In these works the effects of the winglet on the aerodynamic forces and moments was highlighted, especially the reduction of the drag coefficient at lifting conditions. Fletchner and Whitcomb indicated [73, 74] that the basic effect of the winglet is a vertical diffusion of the tip vortex flow just downstream of the tip, which leads to drag reduction. The main result obtained by Whithcomb *et alii* was a 20% reduction of induced drag and a 9% increase in wing lift over drag ratio, both obtained by mounting upper and lower winglet on a jet transport wing characterized by a lift coefficient equal to 0.44 and flying at a Mach number equal to 0.78. These results clearly showed the effectiveness of winglet. Just a year later Whitcomb published his findings, Learjet's chief test pilot, Peter T. Reynolds, flew a Learjet fitted with the "Longhorn" wing, which was a 20-series Learjet wing from which the tip tanks were removed and six-foot wing extensions and winglet were added. On a 1200 nm mission, the Learjet 29 burned 16.5% less fuel than a Learjet 25D, according to Reynolds' report. Much of the improvement was due to lower wing loading and higher aspect ratio. The improvement attributable to winglet was close to 7% at long-range cruise. Gulfstream Aerospace also explored winglet in the late 1970s incorporating winglet in the Gulfstream III, IV and V, thus improving their performance (especially the range). Following the remarkable successes, the study and implementation of end-tip devices had a wide distribution on several aircraft categories. Particular attention was paid to the choice of materials. Even before NASA did flight testing on winglet, Burt Rutan incorporated them in his innovative Rutan VariEze homebuilt aircraft design, which made its first flight with winglet on May 21, 1975. The VariEze pioneered glass-reinforced plastic composite construction in homebuilt aircraft as well as simplified fabrication of the winglet.

Nowadays all transport aircrafts include wing tip devices, prevalently made of composite materials. These tip appendages (blended winglet, tip fences,

raked wingtip and sharklet winglet) must achieve the goal of reducing induced drag. However, the requirements to be met by wingtip devices throughout the various flight conditions are different. As outlined in [75], it must be a compromise of these various conflicting requirements, resulting in less than optimal effectiveness in each flight condition (e.g. little or great additional surface for, respectively, low cruise parasite drag and high climb/descent performance).

The author has gained experience in winglet design analysis and tests of several aircraft categories. In 2008 winglet were designed, tested in wind-tunnel facility [53, 76], realized and tested in flight [12, 13] for the twin-engine four seater Tecnam P2006T aircraft. In this experience, calculations performed in the design and optimization of the winglet shown an increment of induced drag factor due to the winglet of about 0.09. In addition, wind-tunnel tests measured increment of the induced drag factor of 0.08 was noticed [76]. Finally flight tests gave an increment of the Oswald factor of about 0.09 [13] with a huge increment of climb performance and without any penalty of the cruise performance. Several others winglet designs have been performed in 2011-2012 [14–16] and others experimental analysis are still in progress, as inflatable wing-tip devices shown in Ref. [16].

Applications of winglet in turboprop and commuter aircraft is today a crucial item to reduce drag and improve performance. In Fig. 3.30 a typical mission profile for a turboprop aircraft is shown. As it can be seen, climb and descent phases cover the same horizontal distance of the cruise phase. In particular during these phases the aircraft attitude is higher than in cruise condition. Moreover turboprop aircrafts fly in a lift coefficient range of medium magnitude. For all these reasons winglet installation could improve not only the climb and descent performance but also the cruise performance.

3.6.1 Aerodynamics of the winglet

Before detailing the steps of winglet design, a short descriptions of basic aerodynamic principles related to winglet seems to be necessary for completeness sake. A wing moving in an air flow produces a lift force due to the pressure difference between upper and lower wet surfaces. More in detail, the shape of wing section is such that a low pressure airflow arises on wing upper surface, whereas a high pressure airflow characterizes the lower surface; as a consequence, because of wing finiteness, an inward spanwise flow is generated on the upper surface and an outward spanwise flow on the lower surface, as depicted in Fig. 3.31. At the wing tip, the merging of these two flows having different directions generates a vorticity that is shed from a finite wing and it is the origin of induced drag (Fig. 3.31). It has been known for over a century that an end-plate at the tip of a finite wing can reduce the spanwise flow and thereby reduce the induced drag. A winglet, rather than a simple tip end-plate, carries an aerodynamic load that produces a flow field that interacts with the main wing flow, thus reducing the amount of span-wise flow [77]. As a matter of

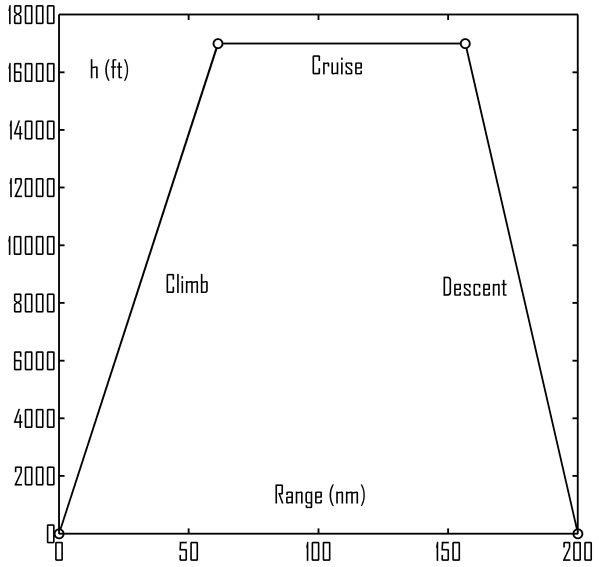

FIGURE 3.30: Typical turboprop mission profile.

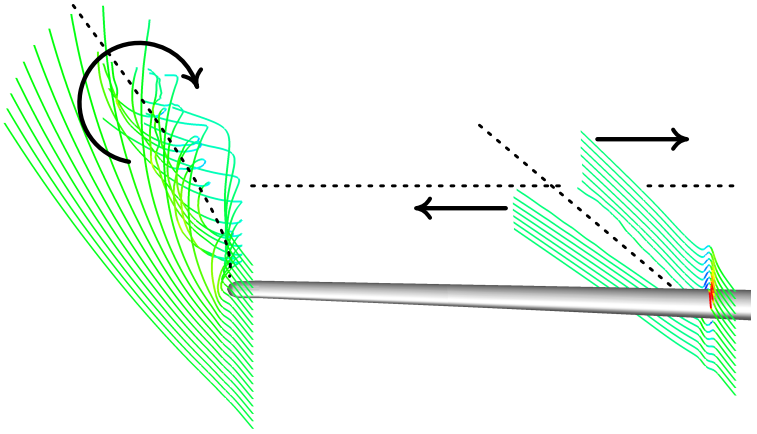

FIGURE 3.31: Vorticity due to finite wing

fact, the winglet diffuses or spreads out the influence of the tip vortex (see Fig. 3.31) such that the downwash and, thereby, the induced drag are reduced. From another point of view, the effect of the winglet is to produce a vertical diffusion of the vorticity at the tip region. This diffusion process is also realized as an expansion of the wake in the far field due to induced velocities from the non-planar components of the winglet. The out of plane bound vortex on an upward winglet induces horizontal velocities on the free wake that causes a spanwise spreading of the wake field. When referenced to the actual span, the resulting efficiency can be greater than that of an elliptical loading, emulating the effect of a span increase [78].

A number of design variables must be considered in the course of designing a winglet, resulting in a very difficult design problem. These parameters are primarily the toe-in (or out) angle, winglet height, cant angle, leading edge sweep angle, the chord and aspect ratio of the winglet, as is shown in Fig. 3.32. The design of a winglet is further complicated by the operational profile of an aircraft, which combines a low-speed, high-lift coefficient climb phase with a high-speed, low-lift coefficient cruise phase [79]. For these reasons, the design of winglet usually involves the compromise of maximizing the low speed improvement without sacrificing high speed performance.

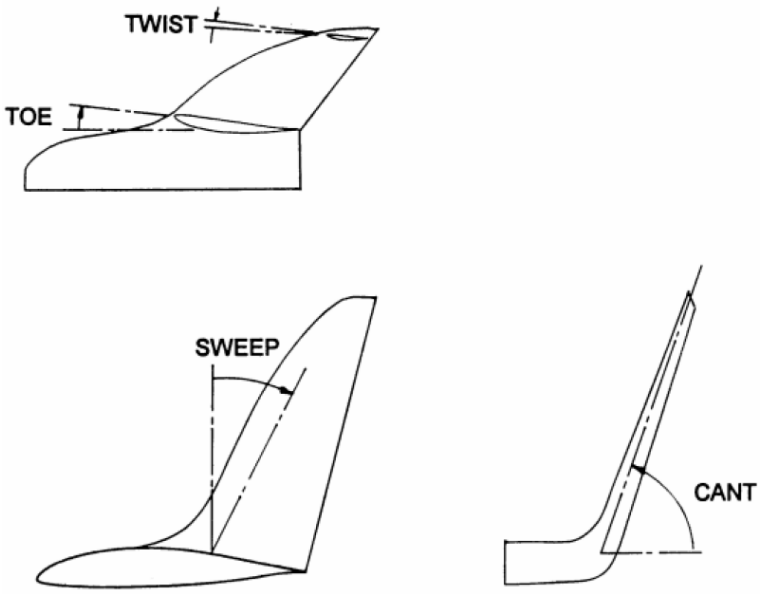

FIGURE 3.32: Winglet's main design parameters

3.6.2 Turboprop winglet design

The present section deals with winglet design for a typical large turboprop aircraft and with the effect of the winglet introduction on the aircraft performance. In general a winglet design follows these main steps:

1. Consider a reference wing on which winglet will be designed.

2. Perform an aerodynamic analysis of the reference wing, which will represent the comparison term. It will be necessary to extract all the main parameters and coefficient (i.e. wing induced drag factor, wing span load, lift coefficient, etc.).

3. Define all the winglet parameters (winglet airfoils, main dimensions, etc.), fixing constraints and boundary.

4. Perform design and optimization by varying the winglet definition parameters.

5. Compare wing and wing with winglet aerodynamic results. The final chosen will be a compromise among several considerations.

1. The reference wing geometry is shown in Fig. 3.33 and the main data are summarized in Tab. 3.8 which represents the ATR-72 wing geometry.

TABLE 3.8: Reference wing geometry.

Main geometrical wing characteristics	
c_{root} (m)	2.56
c_{tip} (m)	1.11*
b (m)	13.5
S (m^2)	61.0
root airfoil	NACA 23018
tip airfoil	NACA 23013

* Chord of the tip aileron.

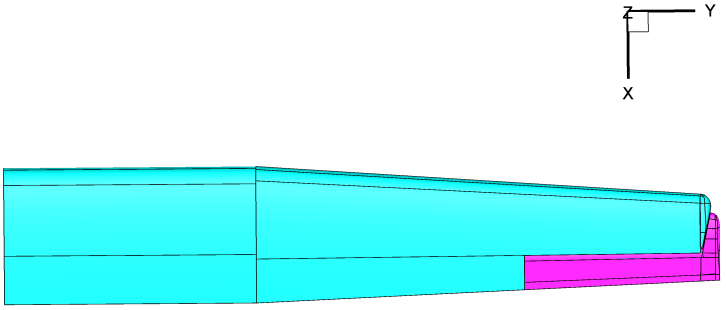

FIGURE 3.33: Reference wing geometry.

2. The wing analysis has been performed with a code based on three-dimensional panel method (the same code shown in previous optimization), thus the reference wing geometry has been properly meshed with about 3000 wing panels and 500 wake panels as shown in Fig. 3.34(a). All the aerodynamic analyses have been performed in two different conditions, which represent typical cruise and climb condition and they are summarized in Tab. 3.1. Figure 3.34(b) shows the pressure coefficient contour on the reference wing in climb condition, whereas in Fig. 3.35 it is shown the variation of the square value of the lift coefficient versus the induced drag coefficient. This curve is useful to estimate the wing induced drag factor e_w. As a matter of fact, the aim of a winglet is to reduce the induced drag and give an increment of Oswald's factor, with a consequent performance improvement. In order to

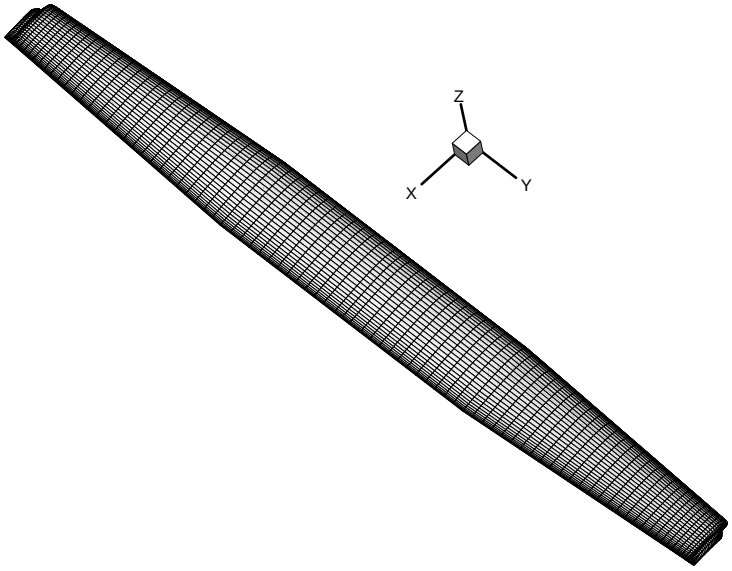

(a) Reference wing mesh.

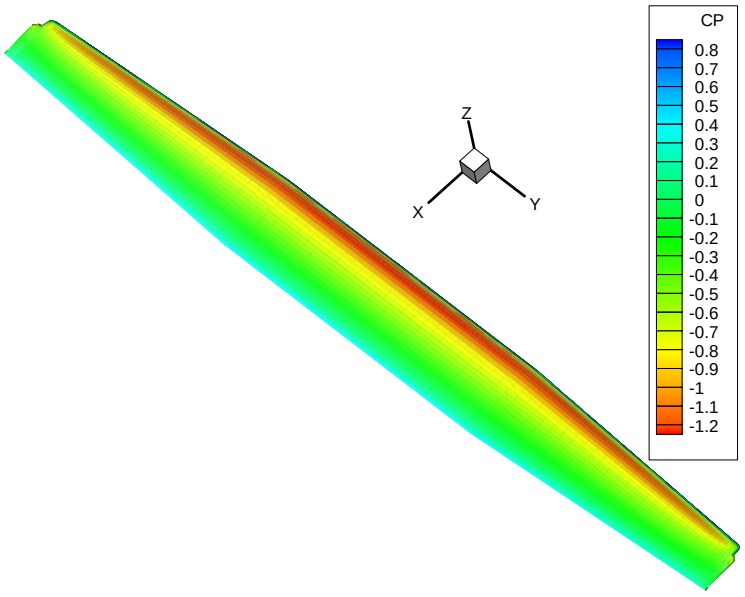

(b) C_p contour.

FIGURE 3.34: Reference wing mesh and pressure coefficient, Cruise condition

appreciate the increment in Oswald's factor given by the introduction of a winglet, the wing induced drag factor coefficient must be first estimated for the reference wing, which will be the reference value respect that evaluate. Assuming a parabolic drag polar formulation as shown in Eq. 3.14,

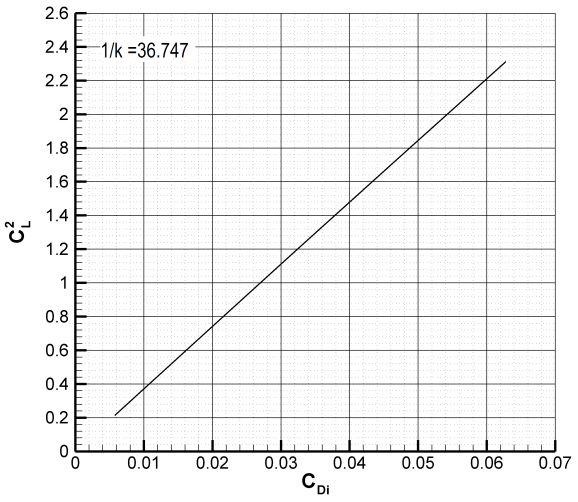

FIGURE 3.35: Reference wing, square lift coefficient versus induced drag, Climb condition

$$C_D = C_{D_0} + kC_L^2 \tag{3.14}$$

the second term of the right member of the equation is the induced drag coefficient, $C_{D_i} = kC_L^2$. If this value is known from the numerical analysis, it is possible to calculate the value of k, which contains the wing induced drag factor as shown in Eq. 3.15.

$$e_w = \frac{1}{\pi\, AR\, k} \tag{3.15}$$

The value of constant k, can be found by evaluating the slope of the curve of Fig. 3.35. The value of wing induced drag factor of the reference wing is equal to 0.975 for climb and 0.976 for cruise condition. These values will be assumed as reference values. Fig. 3.36(a) and Fig. 3.36(b) show the lift coefficient and wing span loading distributions at several angles of attack in climb condition respectively. The analysis is performed on the isolated wing without taking into account the fuselage effect. The lift coefficient peak in the area of the aileron horn is produced by the local twist angle of the horn sections (as matter of fact those sections have a twist angle of 4-10 degrees) and this leads to an increasing in local lift coefficient distribution.

3. Once terminated the reference wing analysis, the geometry of the winglet has been defined. A MATLab internal developed code, written at DII, allows to define winglet geometry by starting form a reference wing geometry and several winglet design parameters (such as cant angle, toe angle, winglet height, winglet airfoil, etc.) shown in Fig. 3.37. Then an automated procedure performs aerodynamic calculation with the aforementioned panel code .

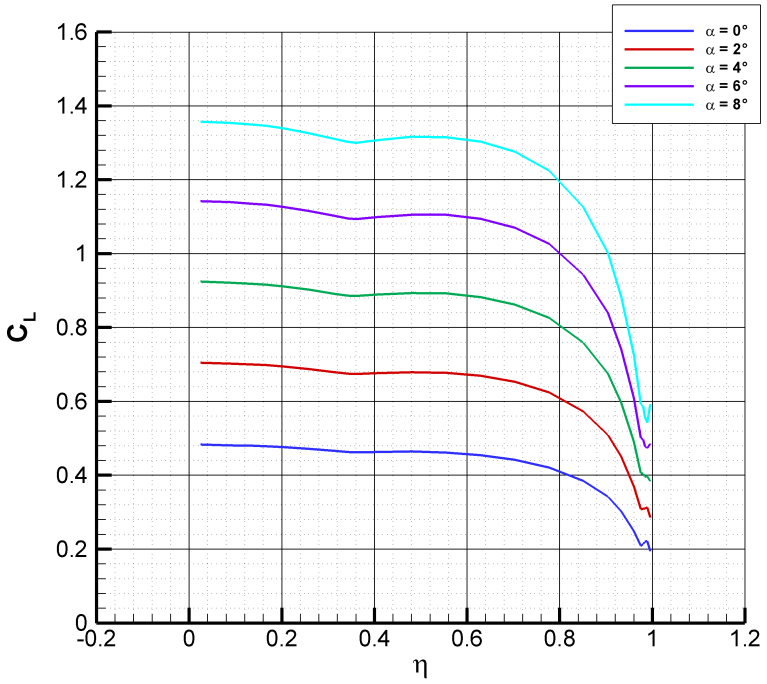

(a) Lift coefficient distribution.

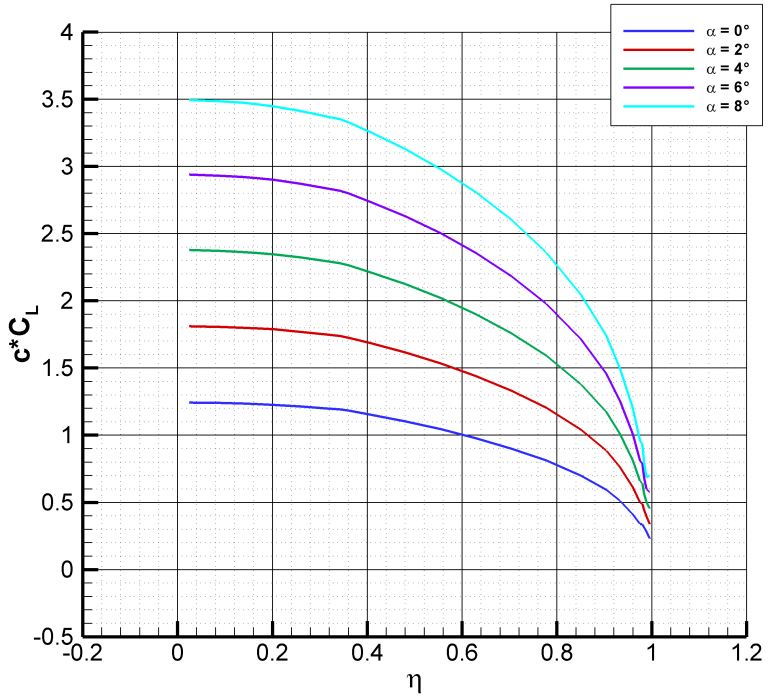

(b) Wing span loading distribution.

FIGURE 3.36: Reference wing lift and wing span loading distribution, Climb condition

Several analyses has been carried out in order to improve the wing induced drag factor, and the results on the optimized winglet are here presented, focusing the attention on the performance. The winglet design parameters

Winglet parameters	
Δ_W	Sweep angle
$cant_W$	Cant angle
h_W	Height
$r_{le\,1}, r_{le\,2}, r_{le\,3}$	Leading edge radii
$r_{te\,1}$	Trailing edge radius
r_W	Radius of winglet-wing tip junction
$\lambda_W = \frac{c_{root}}{c_{tip}}$	Winglet taper ratio
b_{extra}	Total wing span
toe_W	Toe angle
ε_W	Twist angle ($toe_{W\,TIP} - toe_{W\,ROOT}$)
$x_{le\,r}$	back shift of the winglet L.E. to the wing tip L.E.

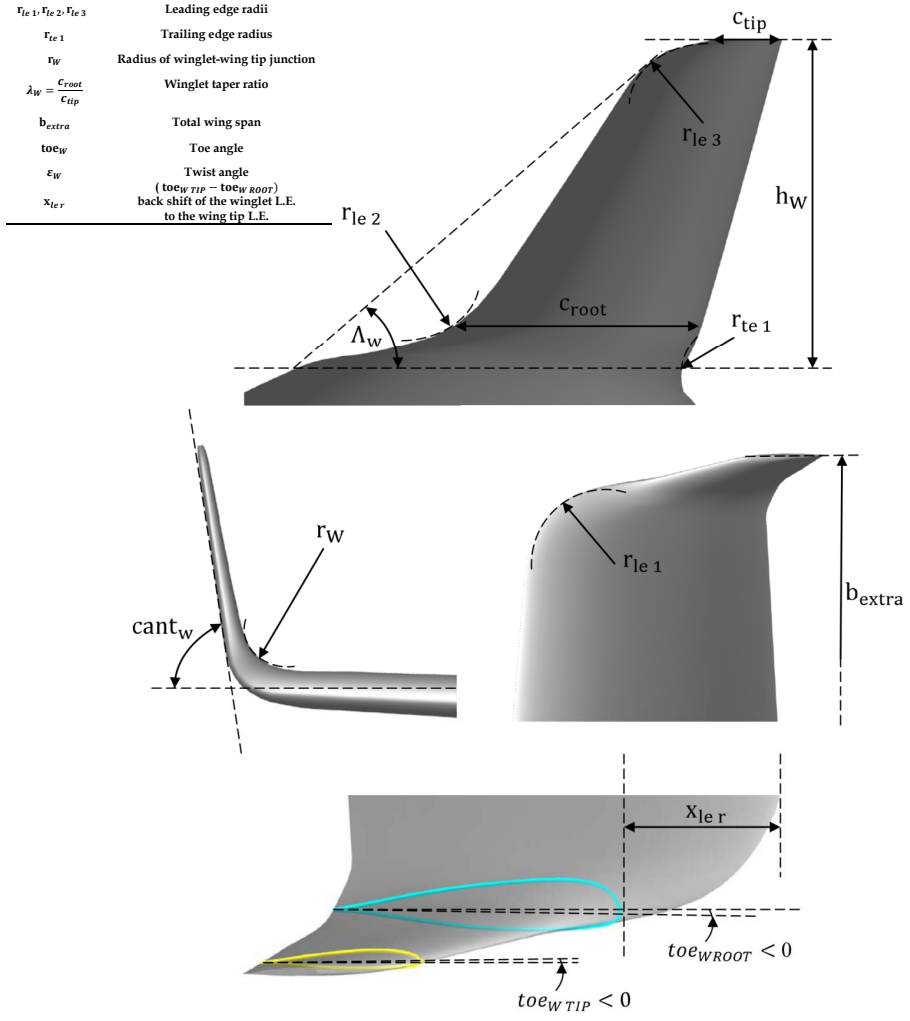

FIGURE 3.37: Winglet design parameters.

useful in the code are indicated in Fig. 3.37. Many of these parameters are dictated by experience and they are fixed at the first step of winglet design. In particular here the winglet shape design has been carried out through the evaluation of the wing-induced drag factor e_w for several configurations defined by combination of the following parameters (see Fig. 3.37):

- *toe* (deg), toe angle

- h_w (m), winglet height;
- Δ_w (deg), winglet sweep angle;
- cant_w (deg), winglet cant angle.

These can be considered the main winglet design parameters because their definitions involve aerodynamic and structural items of the wing and performance are mainly dependent to these parameters. In general structural reasons impose a maximum winglet height equal to nearly 10% of wing span. The range of variation for Δ_w is connected to the wing sweep angle in order to preserve a sort of continuity in geometrical shape. However previous works [53, 76] have highlighted that sweep back angle is preferable in the design. A range for cant angle cant_w is assumed considering that original wing span does not need an excessive increase. Finally, according to previous works [13, 53, 76], a winglet developed airfoil (PSU) has been chosen[2]. The starting winglet reference parameters are summarized in Tab. 3.9, whereas the range of variation of main design parameters are shown in Tab. 3.10.

TABLE 3.9: Winglet reference parameters.

Winglet reference parameters.	
Δ_w (deg.)	55
cant_w (deg.)	80
h_w (m)	1.30
$r_{le,1}$ $r_{le,2}$ $r_{le,3}$(m)	0.6, 0.8, 0.5
$r_{te,1}$ (m)	0.4
r_W (m)	0.45
λ_W	0.3
b_{extra} (m)	13.825
toe (deg.)	-8
ϵ_W (deg.)	3

TABLE 3.10: Winglet parameters variation range.

Winglet parameters variation range.	
Δ_w (deg.)	$50 \leq \Delta_w \leq 60$
cant_w (deg.)	$75 \leq \text{cant}_w \leq 85$
h_w (m)	$75 \leq h_w \leq 85$
toe (deg.)	$-12 \leq toe \leq -4$

4. In order to supply the best winglet geometry many aerodynamic aspects need to be controlled. First of all, the introduction of a winglet

[2]PSU airfoil is a winglet developed airfoil of the Pennsylvania State University. This airfoil is thin and highly cambered allowing good performance at higher angles and higher lower critical Mach number thus avoiding compressibility problems.

introduces a different lift and wing load distribution at wing tip respect to the wing without winglet. This is due obviously to the lifting surface of the winglet. This means that the wing tip will show a peak in the local lift coefficient distribution as is shown in Fig. 3.38(a). This peak in lift coefficient must be kept under control through toe angle variation. It has to be noted that an high lift coefficient on the winglet component can cause the stall of the winglet itself and the subsequently bad functioning. Therefore the first parametric analysis performed on the winglet configuration deals with the determination of a good value for the toe angle. Figure 3.38(a) and Fig. 3.38(b) show the lift coefficient distribution and the wing induced drag factor due to *toe* angle variation respectively. While the increment in toe angle leads to a good reduction of the peak in lift coefficient distribution over the wing span wise, by the other side an excessive increment (in negative sign) of this angle leads to a sensitive reduction of the wing induced drag factor, it might even be reached a value of this factor lower than that of the original wing. From this analysis it can be concluded that a good choice for the toe angle should be of -6 degrees. This choice guarantees a good compromise between the need to reduce the peaks in the lift coefficient and the need to have a good increment for the wing induced drag factor respect to the wing.

Once the toe angle has been chosen, a second parametric analysis on the others winglet geometrical design parameters has been performed. As previously stated, the parameters which may vary are: the winglet height, the winglet sweep angle and the winglet cant angle. From Fig. 3.39 to Fig. 3.43 the results of parametric analyses are shown.The figures 3.39, 3.40, 3.41 and 3.42 show the contour of the variation of wing induced drag factor, wing Aspect Ratio, effective Aspect Ratio (ARe_w) and the ratio between the wet area and wing reference area, respect to the winglet height and cant angle at 50 degrees of winglet sweep angle respectively. Figure 3.43 shows the winglet sweep angle effect on the wing induced drag factor. The winglet sweep angle Δ_w can be considered the less effective parameter, as shown in Fig. 3.43. Indeed for a given winglets' height, the sweep angle effect on the wing-induced drag factor is lower than 1% except for $h = 1.35$ m. As it could be expected, the main effect on the wing-induced drag factor is due to the winglets height (see Fig. 3.39). It can be noticed that each winglets configuration gives an improvement of the wing-induced drag factor, which is maximum at the greater winglet height of 1.4 m. Another effect to highlight is the cant angle effect. The angle of cant has not a high effect on the wing induced drag factor (as shown in Fig. 3.39) but it increase the wing geometrical aspect ratio as shown in Fig. 3.40 and Fig. 3.41. As a matter of fact a lower cant angle means an higher wing aspect ratio, which can give other problems in terms of weight and structures. For this reasons is interesting to see which is the effect of these parameters on the wing bending moment. In the literature is shown that the major effects are due to the winglet height and winglet cant angle [80, 81]. As a matter of fact a typical winglet cant angle is not lower 70 degrees which corresponds

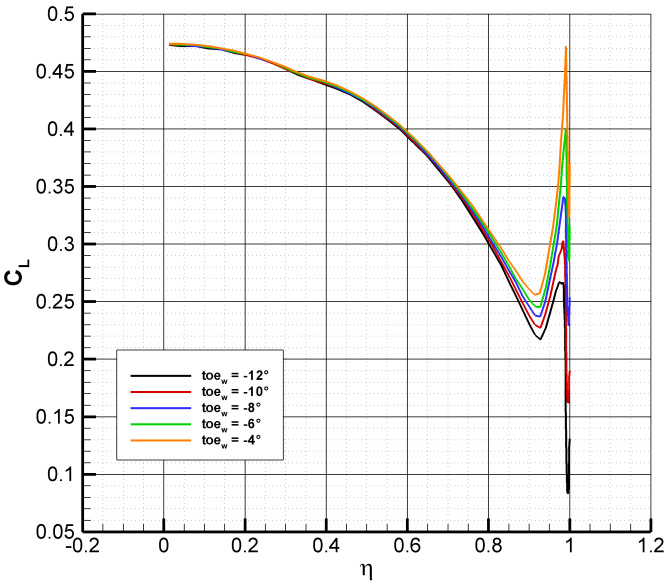

(a) Lift coefficient distribution, toe variation, $\alpha = 0$ deg.

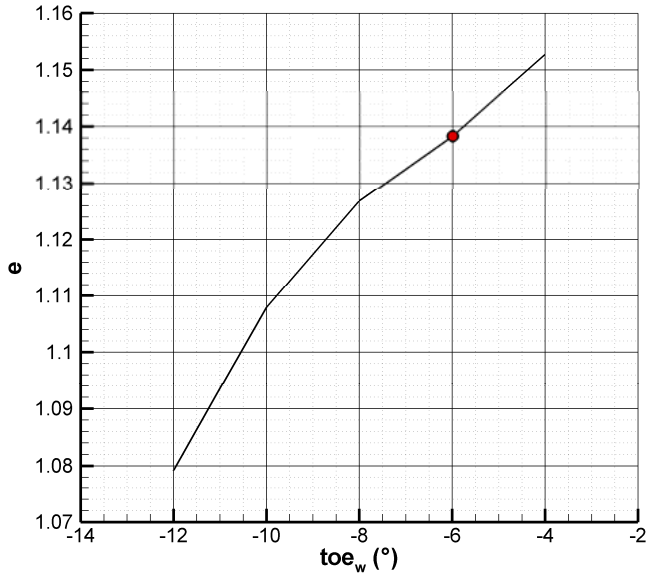

(b) Wing induced drag factor versus toe angle variation

FIGURE 3.38: Wing lift coefficient distribution and Oswald factor variation due to toe angle.

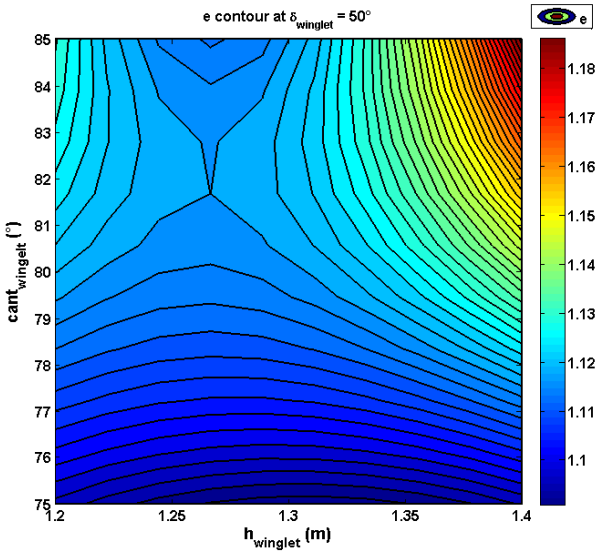

FIGURE 3.39: Effect of cant and winglet height on e_w.

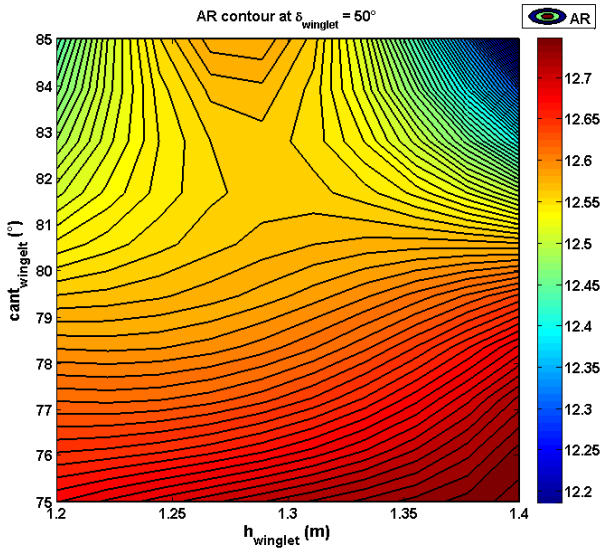

FIGURE 3.40: Effect of cant and winglet height on AR.

a bending moment increment of about 3-5% [80, 81]. Also winglet height has typical values around $0.1b/2$ which gives a bending moment increment of about 3-4% [80, 81]. Sweep angle has a negligible effect on the wing bending moment. From this large amount of data it can be picked up the case which seems to be the best winglet configuration. To perform the best choice, several aspects must be taken into account, first of all which is the targets of the design. If the target is to achieve a winglet arrangement that reduce at least a wing redesign, so the geometrical parameters of the new wing equipped with

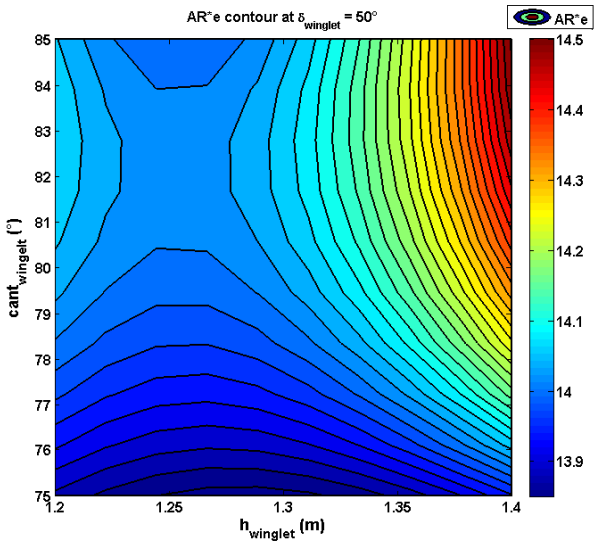

FIGURE 3.41: Effect of cant and winglet height on ARe_w.

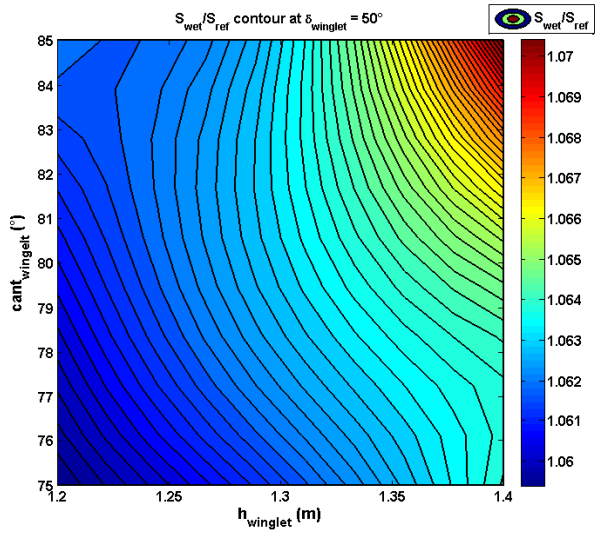

FIGURE 3.42: Effect of cant and winglet height on S_{wet}/S_{ref}.

winglet, should be not so different from the reference wing, in terms of span, and wing aspect ratio.In fact, the choice of the winglet configuration has to be performed not only by looking at the increment in the wing induced drag factor, but it should be also performed by taking into account the increment in the wing span, the increment in the wing aspect ratio, the increment in the wet area and the increment in bending moment. All these variables should be as close as possible to the reference wing geometry corresponding values. If the target is a new wing-winglet design, the choice has to be dictated by a

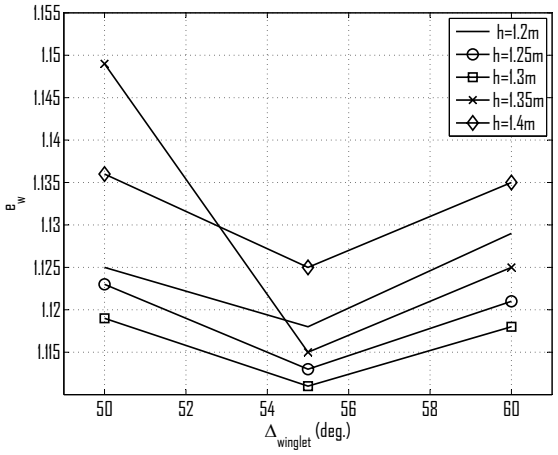

FIGURE 3.43: Effect of winglet sweep on e_w.

compromise among improvement in wing induced drag factor and geometrical and structural constraints. Of course a new design gives a wide range of possibilities. Thus at the end of this parametric analysis it can be concluded that the best choice of winglet geometrical parameters should be those with the following parameters:

- $toe = -6$ deg.
- $h_w = 1.35$ m
- $cant_w = 85$ deg.
- $\Delta_w = 50$ deg.

TABLE 3.11: Results for the optimal winglet.

	reference Wing	Wing with optimal winglet	% of variation
b (m)	27.050	27.650	+2.21
S (m^2)	61.0	61.375	+0.61
S_{wet} (m^2)	63.1	65.422	+3.68
AR	12.0	12.46	+3.84
e_w	0.975	1.141	+17.0
ARe_w	11.56	14.22	+23.05
Bending			+3.5

This choice gives a wing induced drag factor $e_w = 1.141$ about 17% higher than that for the reference wing and leads to the results summarized in Tab. 3.11. It has to be noted that adding the winglets gives an increment of the zero lift drag coefficient of about 5 drag counts estimated in the calculations, due to the increment of the wet area. The optimized winglet shape could be defined

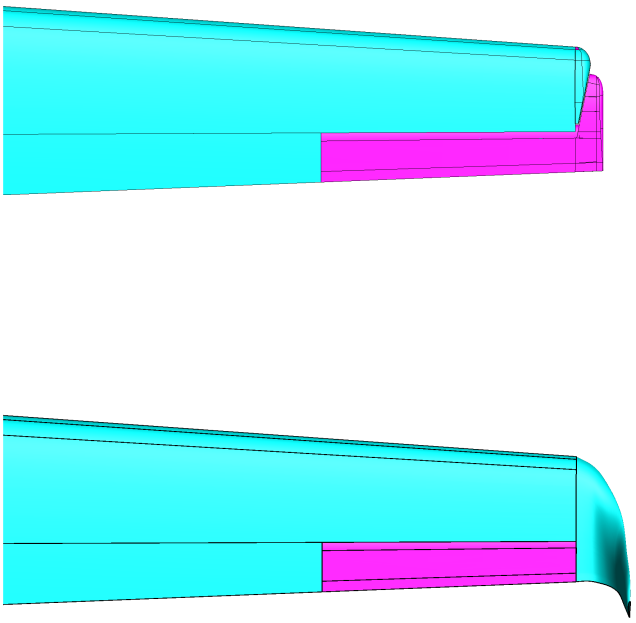

FIGURE 3.44: Wing and Winglet geometry comparison.

as a semi-blended winglet. Its geometry and pressure coefficient distribution are shown in Fig. 3.44 and Fig. 3.45 while lift coefficient and wing span load are shown in Fig. 3.46(b) and Fig. 3.46(a). Pressure coefficient results regular on the entire winglet surface, and lift coefficient distribution shows a regular behavior also on the winglet zone.

3.6.3 Performance improvements due to Winglet

The aircraft drag polar has been computed assuming the reference values obtained for the optimal winglet geometry of $C_{D_0} = 0.0311$ and $e = 0.9711$. In Fig. 3.47, the difference between aircraft total drag coefficient without winglet (reference wing) and the total drag coefficient with the winglet vs lift coefficient is depicted; it is interesting to notice that the winglets give a reduction of the total aircraft drag coefficient in a wide range of aircraft lift coefficient, starting from a $C_L = 0.32$. The major improvements due to winglet are in climb condition where the drag coefficient can be reduced until 30-50 drag counts. This result is mainly impacting on the climb performance of the aircraft which is improved especially in OEI condition, as it can be seen in Tab. 3.12. As outlined in Ref. [13] the winglet give a increment of about 30 to 50% for climb performance in OEI condition. Maximum true airspeed in cruise condition is also improved of about 4 knots at typical mission weight.

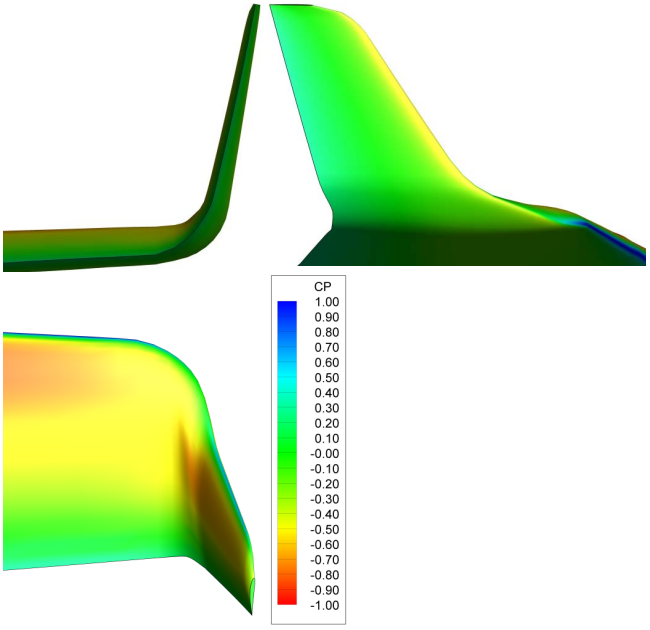

FIGURE 3.45: Winglet pressure coefficient distribution.

FAR ceiling with winglet is enhanced of about 2000 ft and a fuel reduction of about 18 kg during a typical 200 nautical miles mission has been obtained.

TABLE 3.12: Original and Winglet Aircraft performance comparison.

Aircraft configuration	Original	Winglet	
C_{D_0}	0.03060	0.0311	
e	0.85	0.971	
Performance			% of variation
FAR S_{TO} (ft)	4065	4039	−0.7%
FAR S_{LAN} (ft)	3176	3150	−0.1%
R/C s.l. AEO (ft/min)	1437	1508	+4.9%
R/C 10 kft AEO (ft/min)	1063	1149	+8.1%
R/C s.l. OEI (ft/min)	345	434	+25.8%
R/C 10 kft OEI (ft/min)	209	312	+49.2%
Net Ceiling AEO (ft)	23561	25489	+8.2%
Net Ceiling OEI (ft)	10968	13177	+20.1%
Maximum V_{TAS} at 20kft (kts)	262	267	+1.9%
Fuel consumption			
for a 200 nm mission (kg)	594	576	−3.1%
Wing root bending moment			+3.5%

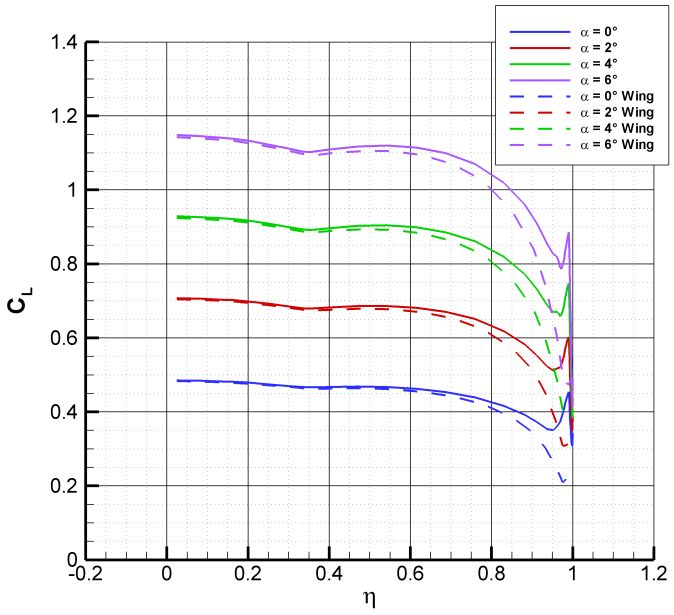

(a) Lift coefficient distribution.

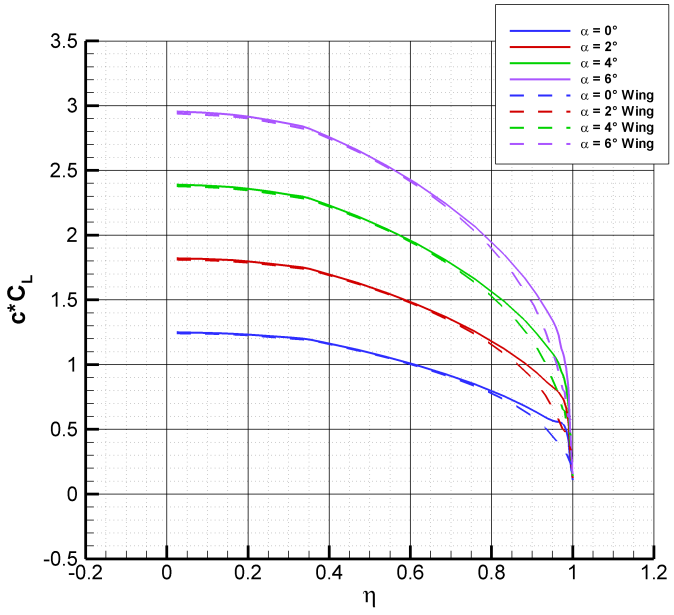

(b) Wing span loading distribution.

FIGURE 3.46: Comparison of lift coefficient and wing span loading distribution for reference wing and optimal winglet, Climb condition.

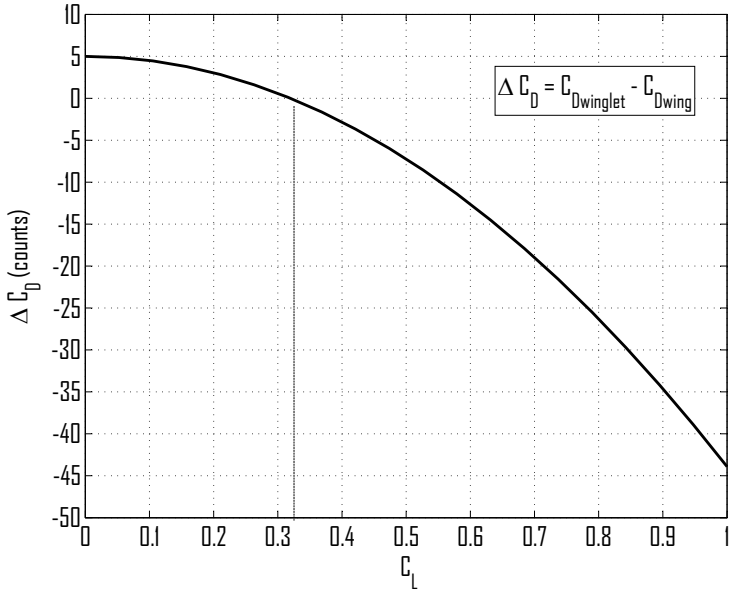

FIGURE 3.47: Aircraft drag coefficient variation due to winglet.

Chapter 4

Vertical Tail Design

4.1 Introduction

This chapter presents a new method to design a vertical tail for commuter and turboprop aircraft. The new method, named VeDSC (Vertical tail Design Stability and Control) gives the possibility to estimate the vertical tail derivatives also with the rudder control surface. It has been obtained with more than 300 CFD Navier-Stokes analysis and all the analyzed configurations are summarized in Appendix B.

A deep investigation on the aerodynamics of the vertical tail, in particular on the sideforce coefficient that affects the directional stability and control of the airplane has been performed. A reliable tailplane design needs an accurate determination of the stability and control derivatives. Extreme flight conditions often set severe design requirements for tail surfaces, like minimum control speed with One Engine Inoperative (OEI) or maximum cross-wind aircraft capability: stability and control must be ensured even in very large angles of sideslip, up to 25 deg. [67]. These requirements are stated by the Federal Aviation Authorities (FAA) and by the European Aviation Safety Agency (EASA). This is a crucial topic for all twin-engine commuter aircraft because all the ground performance are strictly related to the minimum control speed (V_{MC}) which mainly depends from the engine failure speed (V_{EF}), clearly related to vertical tail design. As a matter of fact both part 23 and part 25 of the aircraft regulations relates the certification speeds (especially for ground performance) to the V_{MC}; much lower will be the last, much better will be the performance. Moreover a performance improvement also means the commercial success of an aircraft, given the capability to be more competitive in several scenarios respect to competitors.

Vertical plane design criteria also depend on the type of airplane (and so the flow regime), engine numbers and position, wing-fuselage and horizontal tail position [82]. These factors affect the estimation of stability derivatives (the variation of aerodynamic coefficients with the independent variable, the angle of

sideslip). This process is somewhat complicated since it involves asymmetrical flow behind the wing-fuselage combination and lateral cross-control.

From the '30s to the '50s, in the USA, the National Advisory Committee for Aeronautics (NACA) provided a huge amount of results on the directional stability on isolated vertical tailplanes, partial and complete aircraft configurations obtained through many hours of wind-tunnel tests. These results were summed up in a new design procedure completely reported and described in the United States Air Force Data Compendium (USAF DATCOM) by Finck [83]. The investigations were focused on the attempt to separate the effects of fuselage, wing and horizontal tail from the isolated vertical tail. Lots of geometries were tested, from the early years to the '50s, i.e. rectangular, elliptical and swept wings, symmetrical and unsymmetrical airfoils, slender bodies with rounded or sharp edges, tails of different aspect ratio and size [43, 84–87]. Performed tests dealt with geometries quite different from the actual transport airplanes, being more similar to World War II fighter aircraft. In fact most of the work of the NACA was pushed by war and if the aim of the early tests was to gain a certain knowledge on the physics of the problem of directional stability and control [86] and on the mutual interference among aircraft components [43], later tests aimed to improve stability and maneuverability of high speed combat aircrafts [87].

A first effect studied (1939) by Bamber and House [84] was the aerodynamic interference of the wing-fuselage relative position on the aircraft sideslip derivatives. The general trend revealed an increase in sideforce coefficient due to sideslip C_{Y_β} and yawing moment derivative C_{N_β} when moving the wing from high to low position in fuselage, mainly due to the sidewash induced on the vertical tail by the wing-body combination. Interestingly, the effect of the angle of attack on C_{N_β} is very small.

Queijo and Wolhart [87] evaluated the effect of the fuselage on the vertical tailplane by defining an effective aspect ratio A_{v_e}. The vertical tail effectiveness increased as vertical tail became small compared to the fuselage. No wing and no horizontal tailplane were mounted.

The effect of size and position of horizontal tail was studied by Brewer and Lichtenstein [85]. The final fin (as they called vertical tail) effective aspect ratio was found to be a function of both fuselage and horizontal tail position and size, being maximum when the horizontal plane is located on the fuselage or on the tip of the vertical tail. Apart from the NACA, in the United Kingdom, the Engineering Science Data Unit (ESDU) proposed an alternative method to compute the vertical tailplane contribution to directional stability in presence of body, wing and horizontal tailplane, described by Gilbey et al. [88]. This method contemplates conventional geometries, a circular fuselage and a value for the sidewash held constant respect to wing aspect ratio. It is a synthesis of experimental analyses done from NACA, British Aerospace, SAAB and others, from the '40s to the '70s, linked together with potential flow theory where the data were highly scattered. The theory at the base is found

in the work of Weber and Hawk [89], who suppose that a fin-body-tailplane combination at incidence (or sideslip) develops a complex vortex system that induces a constant velocity along the fin span.

Until the '70s only wind-tunnel tests could provide useful informations about directional stability, especially for the high subsonic and supersonic flow regimes, because of vorticity and shock waves, then computer programs appeared on the scene. Examples of panel codes used for evaluation of airplane directional stability and control can be found in Lamb et al. [90] and in Park et al. [91]. Other and more recent (last 15 years) CFD methods make use of finite differences [92], Finite Element Method (FEM) [93] and finite volume methods and any further step in stability and control analysis techniques saw a return to the study of the low subsonic flow field [91, 93]. The complexity and costs of wind-tunnel tests and the increasing viscosity effects at high angles of incidence led to more and more complex CFD tools, as panel methods that account for viscosity and Navier-Stokes solvers [94–96]. These last approach have been used in advanced design phase, just to analyze a single data configuration.

Nowadays the preliminary evaluation of lateral-directional stability derivatives for subsonic airplanes is mainly based on a couple of reports [85, 87] that were dealing with swept wings and stabilizers and mainly sharp elliptical bodies. Important charts were derived from these reports, though they can be applied (and are still applied today) to conventional airplanes. Moreover, all the analyses done in the past dealt with specific aircrafts and no one, except for the semi-empirical methods cited above, approached the aircraft stability and control problem from a methodological point of view. Discrepancies between semi-empirical methods, considering also the obsolete and particular (like military airplanes) geometries on which they are based (completely different respect to a regional turboprop configuration), pushed the author to attempt a different approach through the CFD. In ref. [15] the author has experimented the use of panel code in tail plane design to better predict the mutual effect among the aircraft components. Panel code method gives fast and reliable enough results, but it does not well predict the effect of the wing-body wake on the tail planes. For this reason the author have investigated the vertical tail aerodynamic via CFD analysis as shown in Ref. [97, 98] to better predict the mutual effects and interferences among components.

The aims of this chapter is to build a new methodology through CFD calculations. Before to describe the results and the methodologies in Sec. 4.1.1 semi-empirical methodologies of USAF DATCOM and ESDU are compared applied on a typical turboprop aircraft. Parametric analysis has been performed to put in evidence the discrepancies between the two methodologies. Then in Sec. 4.2.1 three CFD test cases are solved via CFD analysis to show the CFD capability especially in the lateral directional stability estimation.These test cases are based on NACA reports which are to the base of USAF DATCOM method [43, 84, 87].

In Sec. 4.2 the new CFD approach is proposed. Starting from the analysis of the vertical tail without rudder, the effects on this components from the others aircraft components are estimated. Subsequently the effects on the vertical tail with rudder are proposed (Sec 4.3.3).

4.1.1 Semi-Empirical Methods

USAF DATCOM [83] and ESDU [88] proposed different approaches to account for the influence of wing, body and horizontal tail on the sideforce generated by the vertical tail. Both methods are valid for low speed (subsonic) in cruise configuration (low angle of attack, low angle of sideslip) and do not account for flaps or engine effects. The basic equation is the definition of the lift curve slope for tapered wings proposed by Diederich [99] (shown in Eq. 4.1) and then each method computes its corrective factors in different ways.

$$C_{L_\alpha} = \frac{2\pi\, A}{2 + \left[\frac{B^2 A^2}{\kappa^2}\left(1 + \frac{\tan^2 \Lambda_{c/2}}{B^2}\right) + 4\right]^{\frac{1}{2}}} \tag{4.1}$$

where

A is the wing (or tail) aspect ratio, b^2/S

B is the compressibility parameter, $\sqrt{(1-M^2)}$

κ is the ratio of *section* lift-curve slope to theoretical thin-section value, $c_{l_\alpha}/(2\pi/B)$, and for thin airfoil ($c_{l_\alpha} \approx 2\pi$) it is equal to B

$\Lambda_{c/2}$ is the sweep angle at half chord.

In the USAF DATCOM [83] the sideforce derivative due to sideslip $C_{Y_{\beta,V}}$ is influenced by three interference effects on fin lift curve slope: body-fin (due to body induced cross-flow at fin root and fuselage end-plate effect on fin), horizontal surface interference, wing-body wake and sidewash effect (the latter two lumped into a single effectiveness parameter). The first two define an effective aspect ratio (see Eq. 4.3) that has to be included in the Diederich formula (Eq. 4.1) to calculate the $C_{L_{\alpha,V}}$ and then the $C_{Y_{\beta,V}}$ according to Eq. 4.2.

$$C_{Y_{\beta,V}} = -k_V C_{L_{\alpha,V}} \left(1 + \frac{d\sigma}{d\beta}\right) \eta_V \frac{S_V}{S} \tag{4.2}$$

$$A_{v_{\text{eff}}} = \frac{A_{v(f)}}{A_V} A_V \left[1 + K_{vh}\left(\frac{A_{v(hf)}}{A_{v(f)}} - 1\right)\right] \tag{4.3}$$

where

$C_{L_{\alpha,V}}$ is the lift curve slope corrected by $A_{v_{\text{eff}}}$ defined in Eq. 4.3

$(1 + d\sigma/d\beta)\,\eta_V$ is the *sidewash* effect

S_V/S is the ratio of the vertical tail area to the wing area.

A_V is the vertical tail geometric aspect ratio, b_V^2/S_V

$A_{v(f)}/A_V$ is the ratio of the vertical tail aspect ratio in the presence of the fuselage to that of an isolated vertical tail, defined in Ref. [83]

$A_{v(hf)}/A_{v(f)}$ is the ratio of the vertical tail aspect ratio in the presence of the horizontal tail and the fuselage to that of the fuselage alone, defined in Ref. [83]

K_{vh} is a factor which accounts for the relative size of the horizontal and the vertical tail, defined in Ref. [83].

The method proposed by Gilbey et al. [88] published by ESDU is simpler: there's no effective aspect ratio to calculate and the formulation used is a simple product of three coefficients to take into account body, wing and horizontal tail effects on vertical tail. The lift curve slope of the isolated vertical tailplane (see Eq. 4.1) is corrected by multiplying three empirical factors, J_B, J_T, J_W, respectively body-fin, tailplane and wing correction factor, and scaled by the surface ratio S_F/S. Factors J_T and J_W are located on different curves, depending on the horizontal tail position (fuselage or fin)

$$Y_{v_F} = -J_B J_T J_W \, C_{L_{\alpha,F}} \, \frac{S_F}{S} \tag{4.4}$$

where $C_{L_{\alpha,F}}$ is the $C_{L_{\alpha,V}}$ defined in Eq. 4.1 when the fin aspect ratio

$$A_F = 2\,\frac{b_F^2}{S_F} \tag{4.5}$$

is substituted to A_V, so that this procedure is initially quite different from the DATCOM method.

It is interesting to compare the results of the USAF DATCOM [83] and ESDU [88] methods applied to a certain configuration. This has been accomplished with a user-defined MATLab script to evaluate the influence of each parameter. Only the sideforce due to sideslip derivative of the vertical tail is here computed, since the other coefficients have the following expressions of Eq. 4.6, and Eq. 4.7, where l_V and z_V are the distance between vertical tail aerodynamic center and aircraft center of gravity along x and z axis respectively.

$$C_{N_\beta,V} = -C_{Y_{\beta,V}} \frac{[l_V \cos(\alpha) + z_V \sin(alpha)]}{b} \tag{4.6}$$

$$C_{L_\beta,V} = C_{Y_{\beta,V}} \frac{[z_V \cos(\alpha) - l_V \sin(alpha)]}{b} \tag{4.7}$$

The above mentioned methods are here applied to the ATR-42 regional turboprop (Fig. 4.1). A side-by-side result cannot be made since the two methods define different approaches. Here it is remarked that even a common starting point is difficult to achieve, since USAF DATCOM defines the vertical tailplane aspect ratio as $A_V = b_V^2/S_V$ while ESDU defines it as $A_F = 2b_F^2/S_F$ where V stands for "vertical tail" and F stands for "fin" (with the same meaning), so even for the same planform aspect ratios and lift curve slopes are differently defined. The geometric aspect ratios and the lift curve slopes of the isolated vertical tailplane are reported in Tab. 4.1, while results are reported in Tab. 4.2, showing that, for this particular configuration, the two methods estimate approximately the same values for the three derivatives. Starting

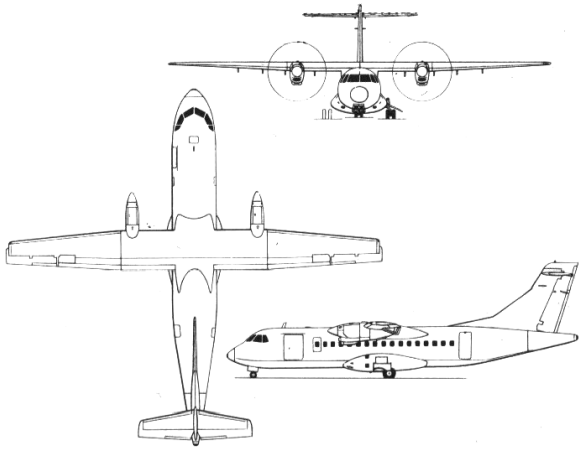

FIGURE 4.1: ATR-42 three-view.

TABLE 4.1: ATR-42 geometric parameters.

	DATCOM	ESDU
Aspect ratio	1.6	3.2
Lift curve slope $(rad^{-1})^*$	2.243	3.619

* Computed with Diederich formula [99]

from the geometrical data of the ATR-42 aircraft, parametric analyses have been carried out. For each analysis only one parameter can change (e.g. the aspect ratio of the vertical tail or the position of the horizontal tailplane or something else), while the others are kept constant, and the calculations show how stability derivatives vary with that parameter. Below each plot it is shown the percentage difference between the results given by the two methods, a deviation from the USAF DATCOM result. Normalization of the coefficients is realized with the ATR-42 wing planform area. All units are per rad.

Figure 4.2 shows the results variation with the vertical tail aspect ratio. It is apparent the linearity of the methods involved. Differences in absolute value are small, while they increase in percentage for low aspect ratio tails.

TABLE 4.2: Results comparison for the ATR-42, DATCOM and ESDU method

Derivative	Symbol	DATCOM	ESDU	Δ %
Sideforce	$C_{Y_{\beta,V}}$	-0.669	-0.642	4.0
Yawing moment	$C_{N_{\beta,V}}$	0.375	0.355	5.4
Rolling moment	$C_{L_{\beta,V}}$	-0.090	-0.086	3.6

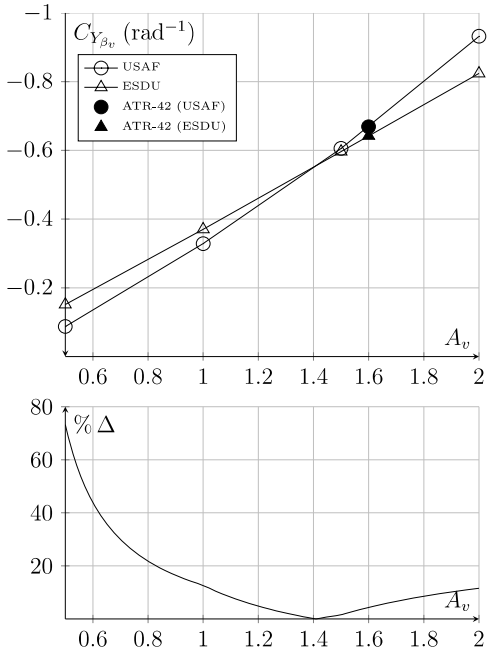

FIGURE 4.2: Sideforce due to sideslip coefficient as a function of vertical tail aspect ratio.

Figure 4.3 shows the effect of wing position. Low wing has the maximum effect and this effect is bigger with the ESDU method. The maximum difference is around 20%. In Fig. 4.4 the wing aspect ratio is changed. It is apparent that the ESDU method considers a constant sidewash, however differences between methods are small, with a maximum of 4% for the aspect ratio range considered. The effect of changing the horizontal tail position is displayed in Fig. 4.5. End-plate effect is apparent at extreme positions. Bodymounted tailplanes should be out of chart range, since zero abscissa indicates tailplanes mounted at the fin root. They are mounted on fuselage centerline instead and are plotted on the y-axis only for comparison. The trend with tailplanes'

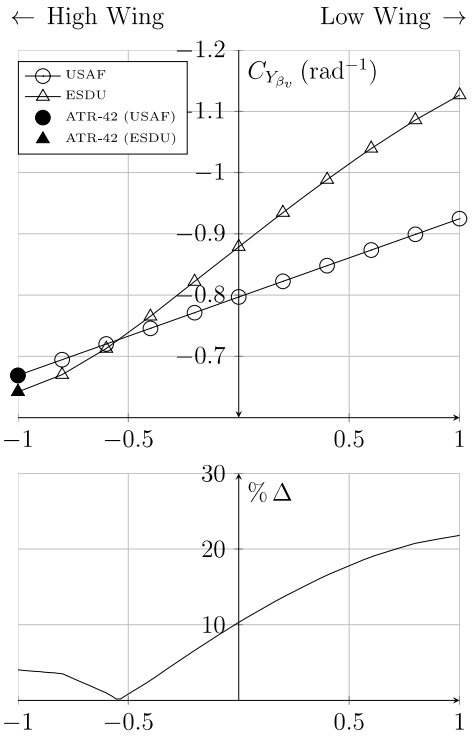

FIGURE 4.3: Sideforce due to sideslip coefficient as a function of wing position.

surface ratio is similar and reported in Fig. 4.6. Here the horizontal plane has a constant aspect ratio of 4.5, planform area and span increase at the same time. The body effect is well represented in Fig. 4.7. It is expected an increase of sideforce derivative with the fuselage depth (thickness). Both methods provide it, but USAF DATCOM contemplates a particular effect at low ratios. Fig. 4.7 is obtained varying $b_V/2r$, that is the ratio of the vertical tail span on the fuselage thickness about the location of vertical tail's aerodynamic center. It is possible to see a higher difference at small values of $b_V/2r$ where the two methods have a different approach to represent this effect (see Ref. [83, 88]). Differencies between two methodologies are around the 60% in the extreme zone of $b_V/2r = 2$ with an average distance around 20%.

These parametric analysis has highlighted that the more used semiempirical approach for the preliminary design of the vertical tail leads to different results and is not possible to establish a priori which is the closer to the real values to estimate. For this reason a new method for turboprop and commuter aircraft vertical tail design is proposed using CFD Navier-Stokes aerodynamic analysis.

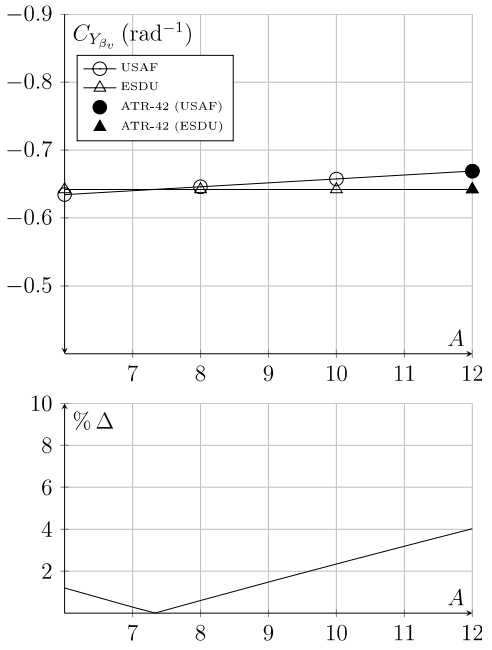

FIGURE 4.4: Sideforce due to sideslip coefficient as a function of wing aspect ratio.

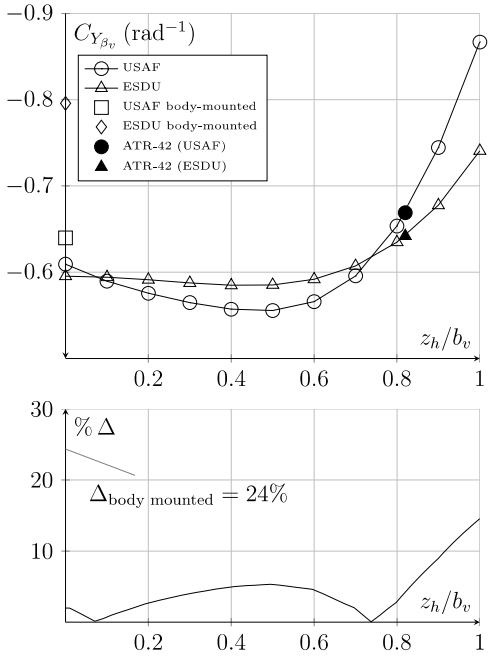

FIGURE 4.5: Sideforce due to sideslip coefficient as a function of horizontal tailplane position.

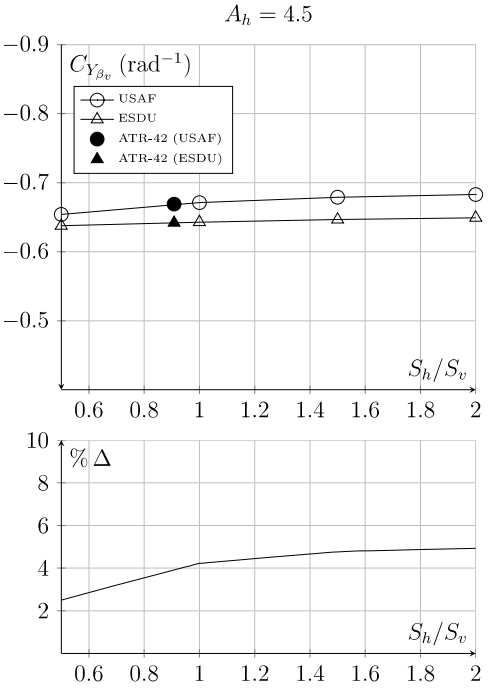

FIGURE 4.6: Sideforce due to sideslip coefficient as a function of tailplanes' relative size.

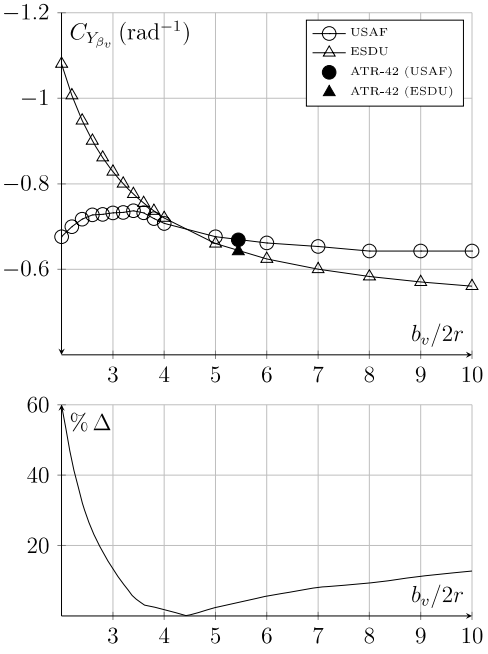

FIGURE 4.7: Sideforce due to sideslip coefficient as a function of fuselage depth.

4.2 CFD Approach

The new approach adopted at DII consists in the use of the commercial CFD software Star-CCM+ to better investigate the whole effects on the vertical tail plane on a typical large propeller aircraft. This software allows to work in an integrated environment, where it is possible to import (or generate, if the model is very simple) the CAD geometry, automatically generate a mesh, easily setup the physics, run the analysis and visualize the results as plots and scenes. One of its interesting features is the polyhedral cells mesh type: every cell is a polyhedral with an average of 14 faces.This permits a smaller number of cells in a numerical domain, thus saving memory used per CPU. Star-CCM+ was often used on the University's grid computing infrastructure SCoPE [100] to simulate lots of configurations in a short amount of time. A number of 128 licenses (one per CPU) were available for this investigation. Convergence of the simulations is judged by looking at the residual plot. Once the residuals drop to a very low value (usually around 10^{-7}), the aerodynamic coefficients are evaluated. The turbulent model chosen is Spalart-Allmaras since it is fast (it solves a single transport equation that determines the turbulent viscosity) and reliable for external aerodynamics, even at high angles of attack and high lift configurations for certain geometries [101, 102], provided that the mesh is fine enough. With this model, it must be verified if the value of the dimensionless wall distance y^+ is of order of magnitude as unity. The numerical domain is a parallelepiped and the model is located on the longitudinal plane of symmetry, at one third of the block length from the inlet face. The dimension of the block is reported in tables in the appropriate sections.

4.2.1 Test Cases

In order to check the compliance of the CFD results with available test data, three test cases have been performed. These are a longitudinal test case and two directional test cases (see also Ref. [98]). It has to be noted that these test cases are performed on the geometries whose DATCOM and ESDU methods are based.

1. In the work of Eastmen and Kenneth [43] 209 wing-fuselage combinations were tested in the NACA variable-density wind tunnel, to provide information about the effects of aerodynamic interference between wings and fuselage at a large value of the Reynolds number (3100000) in symmetric flow at several angles of attack. The wing section was a NACA 0012 airfoil. Three of these combinations (mid-, high- and low-wing) plus a wing-alone configuration were chosen for the test case. Briefly, for each combination, a round fuselage with a rectangular wing has been analyzed at various angles of incidence, in symmetric flow condition. No discussion is made on the results since the primary interest of this section is the check of the previously stated compliance. Here, only the mid-wing combination is shown, see Fig. 4.8. Mesh data are available in Tab. 4.3 and shown in Fig. 4.9. CFD analyses show good

agreement with the result of Ref. [43], except at high flow separation. Results in terms of the aerodynamic lift, effective profile drag and moment coefficients CL , CDe and CM are shown in Fig. 4.10.

TABLE 4.3: Mesh and physics data for NACA Report 540.

Model analysis	Wing-body semi-model
Mesh type	Polyhedral cells
Base size	50.0 m
Farfield dimensions	$30b \times 20b \times 10b$ (b = wing span)
Number of prism layers	20
Prism layer stretching	1.3
Number of cells	2000000 (wing-body combination)
Min. cell size	0.02% base size
Target cell size	0.20% base size
Prism layer size	0.03% base size
Angle of attack	From -4 deg. to 16 deg.
Reynolds number	3100000 (based on wing chord)
Mach number	0
Flow regime	Fully turbulent (Spalart-Allmaras model)

2. In the report of Bamber and House [84] a NACA 23012 rectangular wing with rounded tips was tested with a round fuselage (Fig. 4.11) at several angles of sideslip, in a high-, mid- and low-wing combination. Moreover each combination was tested with and without fin. The fin was made to the NACA 0009 section with an area of 45 in^2 (0.029 m^2). No dihedral angle and no flap device are considered in this test case. The Reynolds number is 609000 based on wing chord. Results are evaluated in terms of the rolling moment,

TABLE 4.4: Mesh and physics data for NACA TN-730.

Model analysis	Wing-body-fin
Mesh type	Polyhedral cells
Base size	1.0 m
Farfield dimensions	$30b \times 20b \times 10b$ (b = wing span)
Number of prism layers	20
Prism layer stretching	1.2
Number of cells	5000000 (wing-body-fin combination)
Angle of attack	0 deg.
Angle of sideslip	From 0 deg. to 5deg
Reynolds number	609000 (based on wing chord)
Mach number	0
Flow regime	Fully turbulent (Spalart-Allmaras model)

yawing moment and sideforce due to sideslip coefficients C_{L_β} , C_{N_β} and C_{Y_β}.

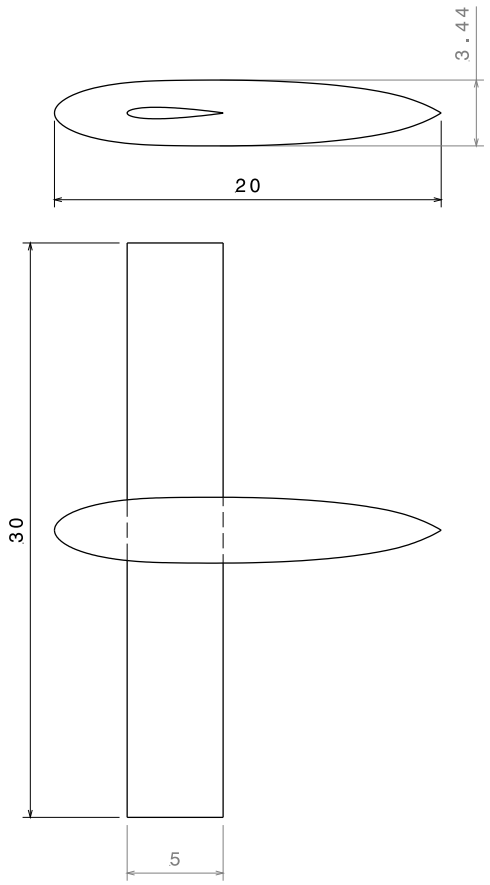

FIGURE 4.8: CAD drafting of the model of NACA Report 540.

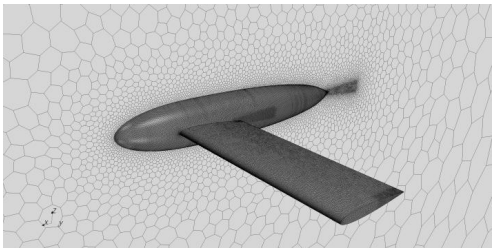

FIGURE 4.9: Mesh of NACA 540 test case.

All derivatives are per degree and evaluated assuming linearity with β between 0 deg. and 5 deg. Mesh data are reported in Tab. 4.4 and Tab. 4.5 and shown in Fig. 4.12. Results are shown for the wing-body-fin combination in Fig. 4.13, where directional stability, measured by C_{N_β} , is maximum for the low-wing combination. The rolling moment derivative C_{L_β} changes sign because of the cross-flow over the wing-fuselage system, resulting in an antisymmetric distribution of the normal velocities along the span that is equivalent to an

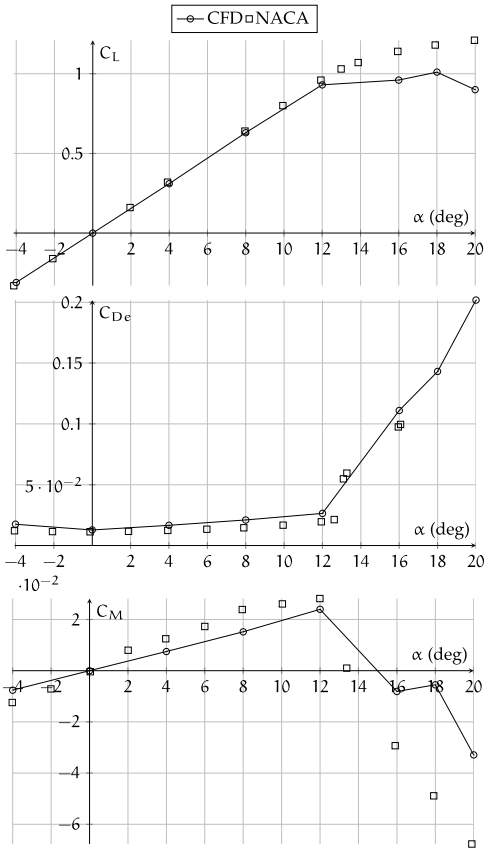

FIGURE 4.10: Results of the mid-wing combination of NACA Report 540.

antisymmetric angle of attack distribution [41]. Results are in good agreement especially for the sideforce coefficient which is the object of the investigation.

TABLE 4.5: Mesh size (in % base size) for NACA TN-730.

	Min.	Target	Prism layer
Wing	0.08	1.0	0.11
Fuselage	0.1	10.0	0.2
Vertical	0.05	0.5	0.1

3. The aim of the work of Queijo and Wolhart [87] was to investigate the effects of vertical tail size and span and of fuselage shape and length on the static lateral stability characteristics of a model with 45 deg. swept back (quarter chord line) wing and vertical tail, NACA 65A008 airfoil. For the purpose of the test case, only the combination with the round fuselage is considered, see Fig. 4.14 . The mesh data are reported in Tab. 4.6 and Tab. 4.7 and shown in Fig. 4.15. Results are shown in Fig. 4.16 in terms of force

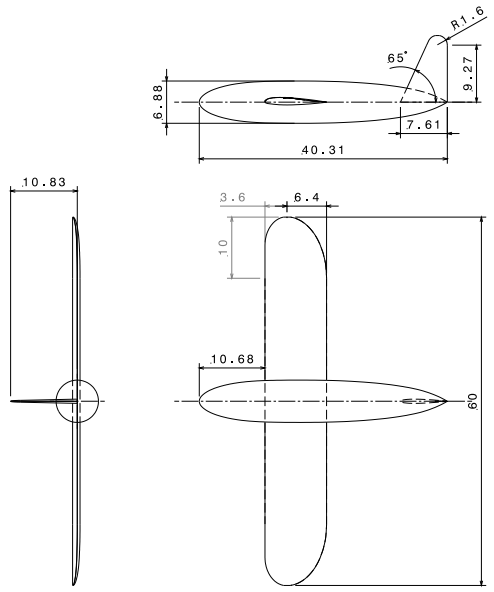

FIGURE 4.11: CAD drafting of the model of NACA TN-730.

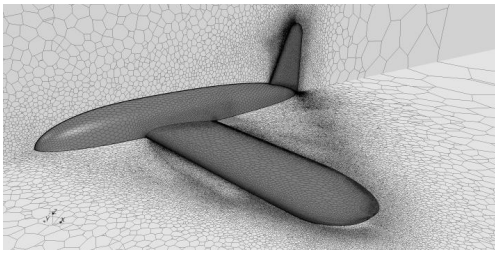

FIGURE 4.12: Mesh of NACA TN-730 test case.

and moment coefficients for the wing-body-fin combination. Reference [87] directly presents the lateral-directional derivatives at several angles of attack, while CFD provides the force and moment coefficients, not their derivatives. Numerical results have been obtained at several angles of sideslip and they are symmetric, though their variation is non-linear with the sideslip angle. This non-linearity is due to (*i*) the amplification of the vertical tail contribution due to the fuselage and wing, (*ii*) the reduction of the fuselage instability and (*iii*) a smaller effect due to the swept wing. However results are in good agreement also in this particular aircraft configuration.

Finally it is possible to conclude that the CFD calculations show a good agreement with experimental data, encouraging the use of this tool to investigate the interference effects, which mainly determine the vertical tailplane directional stability and control contribution. Other wind-tunnel tests will be performed at University of Naples facility on typical commuter and turboprop aircraft.

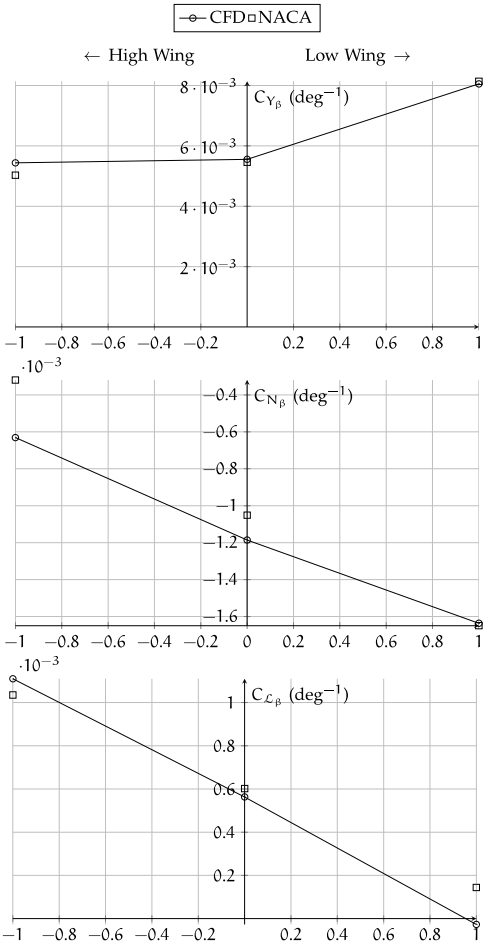

FIGURE 4.13: Results of the body-wing-fin combination of NACA TN-730.

TABLE 4.6: Mesh and physics data for NACA Report 1049.

Model analysis	Wing-body-fin
Mesh type	Polyhedral cells
Base size	10.0 m
Farfield dimensions	$30b \times 20b \times 10b$ (b = wing span)
Number of prism layers	20
Prism layer stretching	1.3
Number of cells	4000000 (wing-body-fin combination)
Angle of attack	0 deg.
Angle of sideslip	From -10 deg. to 10deg
Reynolds number	710000 (based on wing chord)
Mach number	0
Flow regime	Fully turbulent (Spalart-Allmaras model)

TABLE 4.7: Mesh size (in % base size) for NACA Report 1049.

	Min.	Target	Prism layer
Wing	0.05	1.0	0.11
Fuselage	0.01	0.1	0.11
Vertical	0.005	0.1	0.11

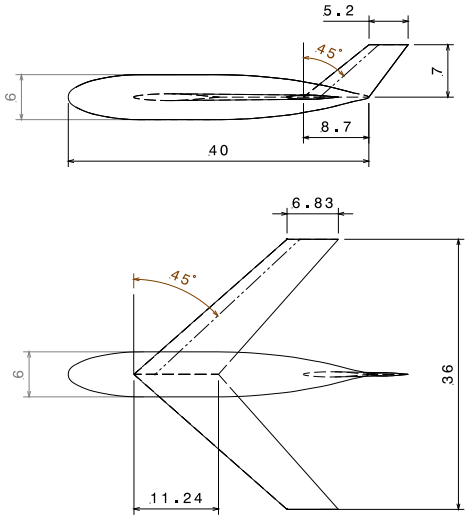

FIGURE 4.14: CAD drafting of the model of NACA Report 1049.

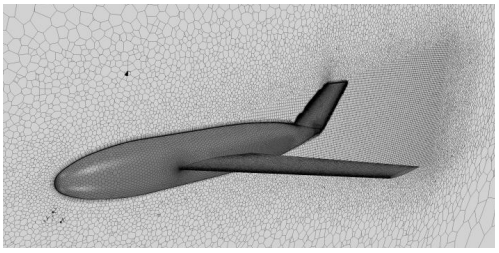

FIGURE 4.15: Mesh of NACA 1049 test case.

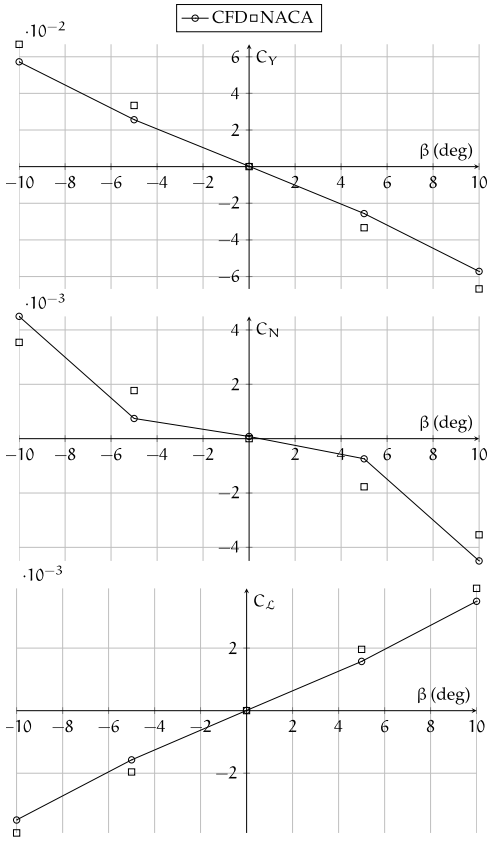

FIGURE 4.16: Results of the fuselage-wing-vertical combination of NACA Report 1049.

4.3 Parametric Analysis on typical turboprop geometries

Since the test cases complied with the experimental data, it seemed reasonable to proceed with further CFD investigations on a general turboprop geometry, shown in Fig. 4.17. The objective is to provide data on the mutual aerodynamic interference among the airplane components on the sideforce generated by the vertical tail to build up a new methodology to design the vertical tail and rudder control surface. The aircraft model, named CFD model, has the typical characteristics (e.g. fuselage slenderness and wing aspect ratio) of the regional turboprop airplanes, as the ATR-72 and a possible generic new configuration of a 90 seats regional turboprop (with 5 abreast) called NGTP-5 (shown in Ref. [14]). These parameters are shown in Tab. 4.8 to 4.10. The wing model airfoil is the NACA 23015, while both tailplanes (vertical and horizontal) use the NACA 0012 airfoil. The flow conditions (Reynolds number) were chosen in such a way to get results also useful for comparison with future experimental data to be obtained through wind-tunnel tests of a modular model to be tested in the low-speed wind tunnel of the Department of Industrial Engineering of the University.of Naples "Federico II". As a matter of fact, to confirm the results of CFD analyses, the author highlights the necessity to perform also wind-tunnel tests in the near future to have a correct estimation of the mentioned interference effects and to have a complete validation of all trends estimated through the extensive numerical analyses presented in this paper.

Table 4.8: Fuselage parameters. CFD Models and reference turboprop.

	l_f/d_f	l_f/l_n	l_f/l_c	$x_{w_{LE}}/l_f$
ATR-72	10.3	1.3	3.2	0.41
NGTP-5	9	1.3	3.3	0.47
CFD model	9	1.3	3.3	0.45

Table 4.9: Vertical tailplane parameters. CFD Models and reference turboprop.

	A_V	λ_V	$\Lambda_{V_{LE}}$ (deg.)	$\Lambda_{V_{TE}}$ (deg.)	S_V/S	$x_{V_{LE}}/l_f$	V_V
ATR-72	1.56	0.61	32	17	0.20	0.83	0.098
NGTP-5	1.43	0.63	29	15	0.24	0.85	0.110
CFD model	Var.	Var.	30	15	Var.	Var.	Var.

The dimensions of the model and the configurations involved are reported in Fig. 4.17 and Fig. 4.18. The CAD model with mid-wing and body-mounted horizontal tailplane is shown in Fig. 4.19. From now to on, the expression CFD model indicates the CAD / CFD geometry of the future model to be

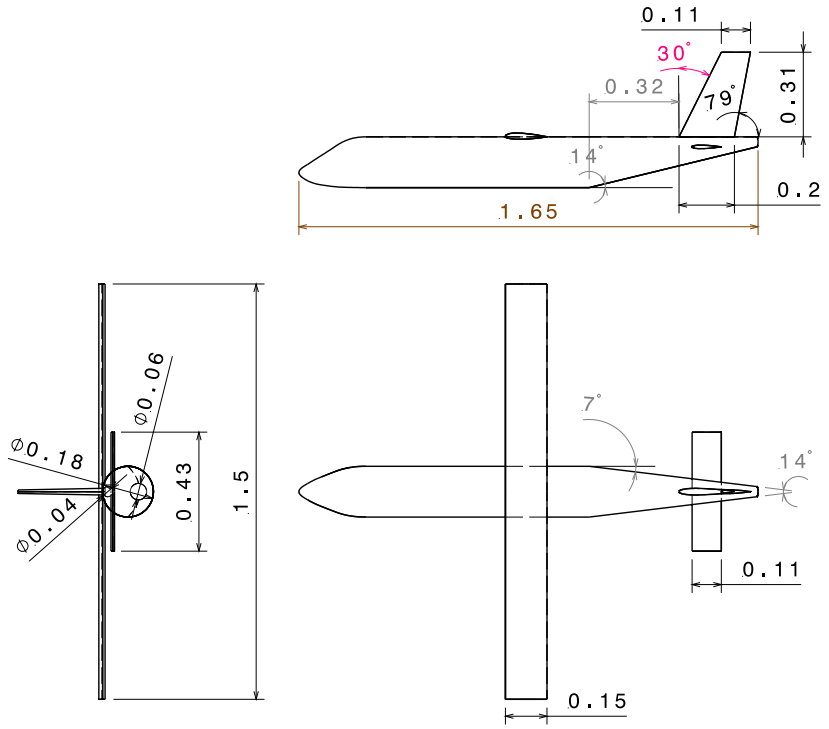

FIGURE 4.17: CAD drafting of the CFD model.

TABLE 4.10: Horizontal tailplane parameters. CFD Models and reference turboprop.

	A_H	λ_H	$\Lambda_{H_{LE}}$	$\Lambda_{H_{TE}}$	S_H/S	$x_{H_{LE}}/l_f$	V_H
ATR-72	4.1	n.a.	n.a.	n.a.	0.19	n.a.	0.19
NGTP-5	4.1	n.a.	n.a.	n.a.	0.25	n.a.	0.19
CFD model	4.1	0	0 deg.	0 deg.	Variable	Variable	Variable

realized. Additional geometries will be presented in the appropriate sections. As it can be seen many configurations have been analyzed in terms of vertical tail, wing, horizontal tail dimensions and positions, while fuselage dimensions and shape has been kept constant.

4.3.1 Preliminary CFD analyses

Some CFD simulations about base size, number of CPUs and Reynolds number are necessary to set the correct mesh and flow parameters. The base size is the reference length of the model to which all cells parameters are related. Changing the base size affects the mesh and hence the solution, as shown in Fig. 4.20. It is apparent that, for no sideslip or incidence angle, a base size of 1.65 m, equal to the fuselage length of the CFD model, is an optimum value

and then 10 millions of polyhedral cells are sufficient to obtain a converged solution. The configuration chosen is the complete airplane with high wing and body-mounted tailplane, since this is the most complicated in terms of computational grid (due to the intersections among components), see Fig. 4.21. The computational time is a non-linear decreasing function with CPUs number, on a linear plot. On a logarithmic plot it is a linear function instead. Fig. 4.22 represents the time necessary to obtain a converged solution vs. CPUs number, in a logarithmic scale. These data were obtained running a body-vertical configuration on SCoPE [100]. For a complete airplane, it is convenient to operate between 32 and 64 CPUs, to optimize time and computing power. In fact, Ref. [103] recommends to employ a CPU every 250 000 cells. Given the base size, Fig. 4.23 shows a little sensitivity of the vertical tail sideforce coefficient about Reynolds number, thus, to account for later wind-tunnel test, the Reynolds number chosen (based on wing chord) has the same order of magnitude of that of the faculty's wind tunnel, $Re = 1000000$. The turbulence model chosen is Spalart-Allmaras. The check of the results was done, once residuals were oscillating around 10^{-7}, by looking at the wall y^+ distribution of magnitude around one.

4.3.2 CFD model analyses and discussion

CFD analyses. Results and discussion Due to the high number of mesh cells, most of the analyses were solved on the SCoPE grid infrastructure (see Section 3). The polyhedral mesh and the Spalart-Allmaras turbulence models were chosen to solve the asymmetrical flow field. All of the runs were solved in incompressible flow, $Re = 1000000$, at $\alpha = 0$ deg. and $\beta = 0$ and 5 deg. The mesh parameters, common to all analyses, are reported in Tab. 4.11 and Tab. 4.12. The numerical domain is again a parallelepiped and the model is located on the longitudinal plane of symmetry, at one third of the block length from the inlet face as shown in Fig 4.24.

Table 4.11: Mesh and physics data for the CFD model.

Mesh type	Polyhedral cells
Base size	1.65 m
Farfield dimensions	$30b \times 20b \times 20b$ (b = wing span)
Number of prism layers	20
Prism layer stretching	1.1
Number of cells	10000000 (complete high-wing airplane)
Angle of attack	0 deg.
Angle of sideslip	From 0 deg. to 5 deg.
Reynolds number	1000000 (based on wing chord)
Mach number	0
Flow regime	Fully turbulent (Spalart-Allmaras model)

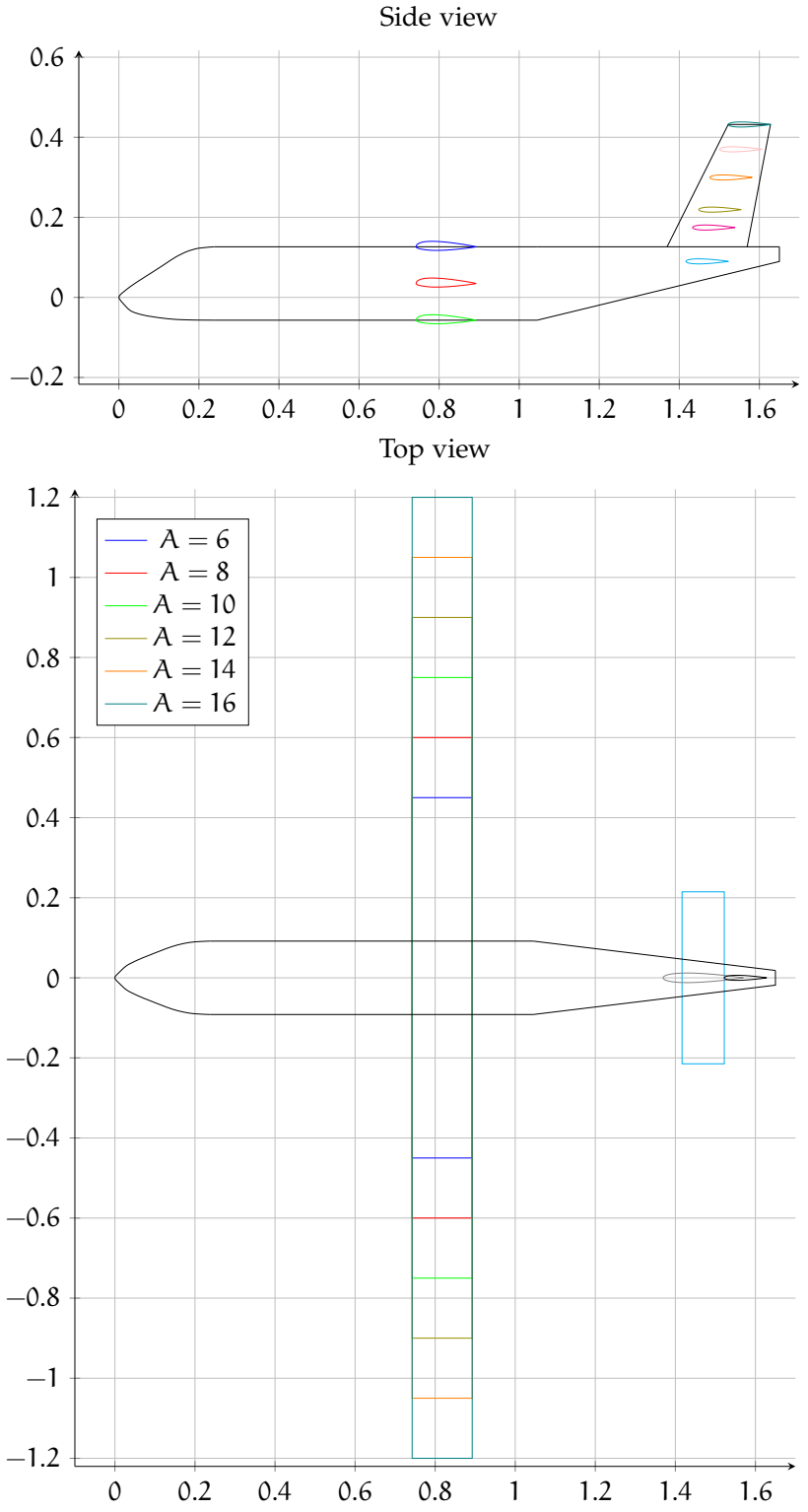

FIGURE 4.18: The configurations of the CFD model. For the sake of clarity, here it is only shown the vertical tailplane with $A_V = 2$. Units are in m.

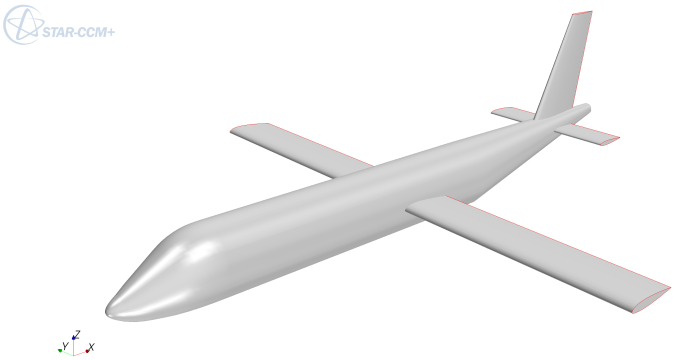

FIGURE 4.19: The CAD model imported in Star-CCM+.

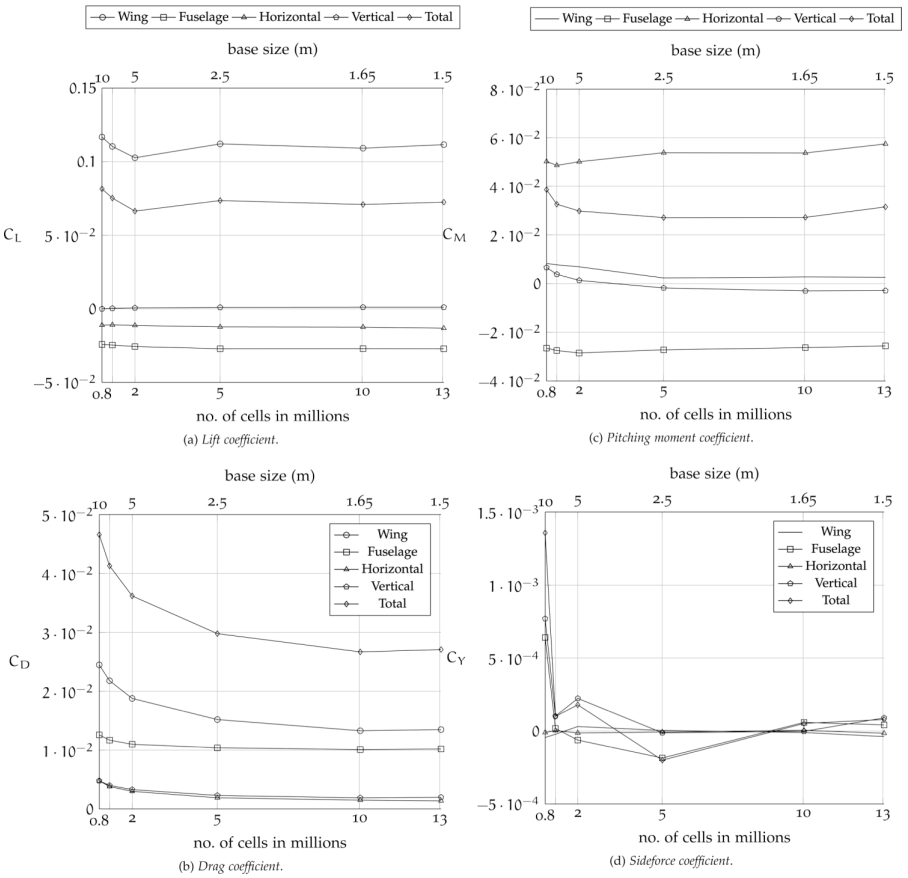

(a) *Lift coefficient.* (c) *Pitching moment coefficient.*

(b) *Drag coefficient.* (d) *Sideforce coefficient.*

FIGURE 4.20: Aerodynamic coefficients as a function of base size and number of cells for the configuration of Fig. 4.21. The contribution of each component is shown as well as their sum. $\alpha = 0$ deg., $\beta = 0$ deg., $Re = 1e6$.

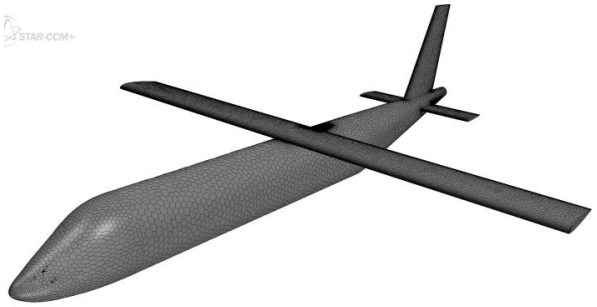

FIGURE 4.21: Mesh on the model used for the base size trend study.

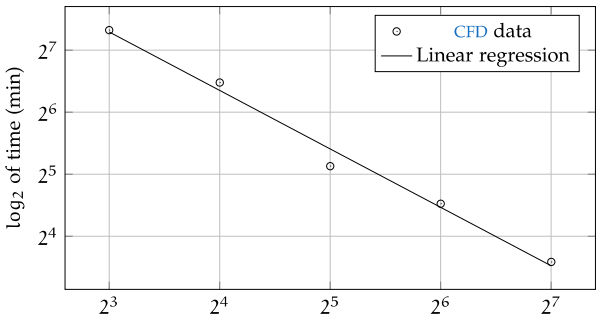

FIGURE 4.22: CPUs scalability for a body-vertical configuration with 1800000 polyhedral cells.

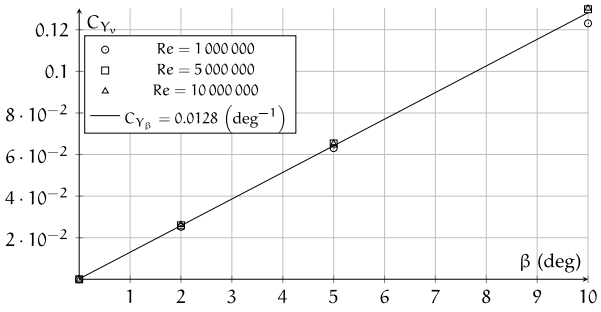

FIGURE 4.23: Influence of the Reynolds number on the complete aircraft model (same configuration of Fig. 4.21), with 10000000 polyhedral cells.

TABLE 4.12: Mesh size (in % base size) for the CFD model.

	Min.	Target	Prism layer
Wing	0.04	0.5	0.02
Fuselage	0.1	1.0	0.02
Horizontal	0.04	0.5	0.02
Vertical	0.05	0.5	0.01

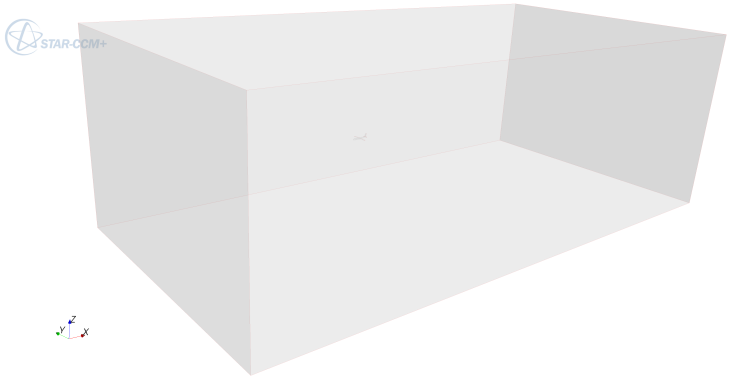

FIGURE 4.24: Block shape that defines the fluid domain around the model. Dimensions $60 \times 30 \times 20\ m^3$.

In order to achieve the objective of this chapter, the CFD analyses were so organized:

1. the lift curve slope of the isolated vertical tailplane has been evaluated and compared to that provided by theory (Sec. 4.3.2.1);

2. to estimate the effect of the body on the vertical tail, the body-vertical tail configuration has been analyzed and each result of the vertical tail's sideforce coefficient was scaled by the homologous result of the isolated vertical tail, so as to evaluate the interference effect on the C_{Y_V} (Sec. 4.3.2.2);

3. similarly it has been done for the wing, by adding it to the previous body-vertical combination and measuring the effects in terms of C_{Y_V} ratios. This has been done for wings of various aspect ratio and position in fuselage (Sec. 4.3.2.3);

4. finally, the effect of the horizontal tailplane position and size was measured as done with the previous effects (Sec. 4.3.2.4).

5. In Sec. 4.3.3 the effects of the presence of a rudder control surface are shown, highlighting the increment of vertical tail sideforce also with zero sideslip angle, due to interference among rudder and aircraft components.

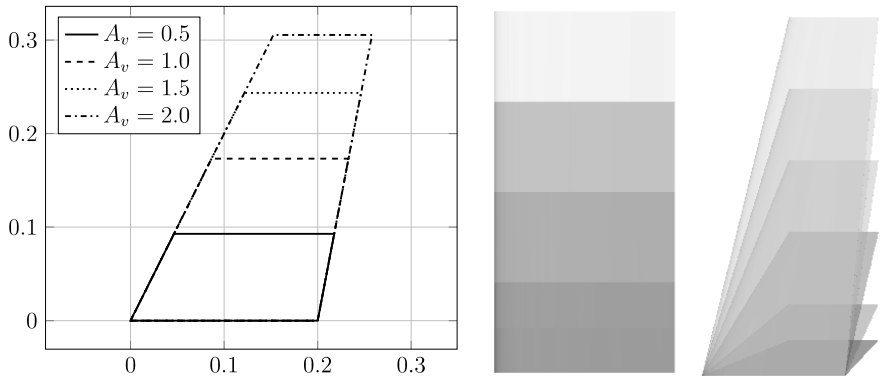

(a) The modular vertical tail of the CFD model. (b) Additional vertical tailplanes involved in the CFD investigation.

FIGURE 4.25: Isolated vertical tail geometries analyzed.

Results are published as ratios of C_{Y_V}, that is, given a configuration, all the effects of adding a component are scaled by the results of the configuration without that component, for example the body effect is evaluated by dividing the C_{Y_V} of the body-vertical configuration by the C_{Y_V} of the isolated vertical tailplane. In this way the effect (increase or decrease of the coefficients) of the aerodynamic interference is highlighted. In fact, as stated above, the objective of the new procedure is to define corrective coefficients for the $C_{L_{\alpha_V}}$ of the vertical tailplane. Derivatives are calculated as an approximation of the incremental ratio as shown in Eq. 4.8.

$$C_{Y_V} \approx \frac{C_{Y_V} - 0}{5^\circ - 0^\circ} = \frac{C_{Y_V}}{5}\,\mathrm{deg}^{-1} \tag{4.8}$$

It has to be noted that, unless otherwise stated, the derivatives are dimensionless with wing surface.

4.3.2.1 Isolated Vertical tail

The vertical tail alone has to be analyzed for three reasons: CFD results must verify linearity, they should be compared with theory (usually used in preliminary design calculations) and provide the vertical tailplane lift curve slope $C_{L_{\alpha_V}}$ to be considered to estimate the interference effects due to fuselage, wing and horizontal tailplane. For the isolated tailplane, it has been considered a constant-sweep geometry (see Fig. 4.25(a)) and also two constant tapered geometries with two different taper ratios (see Fig. 4.47(b)) both with different aspect ratio values (in the range between 0.25 and 4). The CFD analyses performed with the above mentioned shapes allow the estimation of variation of lift curve slope versus aspect ratio. As it can be observed in Fig. 4.26(a), the results predicted by CFD calculations are in good agreement

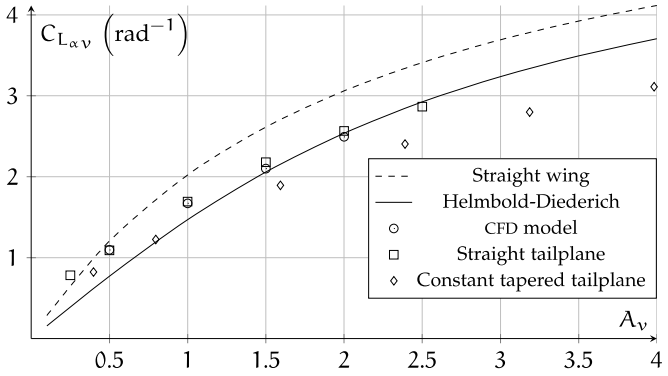

(a) Lift gradient vs. aspect ratio for the isolated vertical tailplanes.

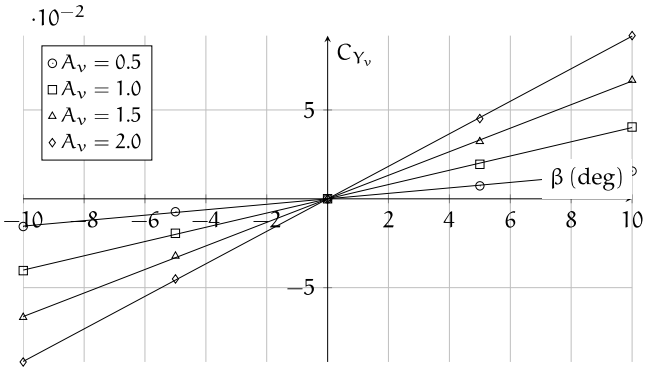

(b) Linearity of sideforce coefficient C_{Y_V} vs. the angle of sideslip β. CFD data of isolated vertical tailplanes (CFD model), Re = 1000000. Black lines are linear regression curves of CFD data.

FIGURE 4.26: Lift gradient vs. aspect ratio for the isolated vertical tailplanes and sideforce coefficient.

with semi-empirical formulation proposed by Diederich [99] and often used for the estimation of isolated vertical tail (or in general low aspect ratio wings) lift curve slope. Calculations performed on the tailplane shape with taper ratio equal to 1 and zero sweep angle show only a slightly higher trend respect to the swept case and this is in contrast with theory that provides a much higher lift gradient. The constant taper vertical tailplane geometry (Fig. 4.47(b) right) does not agree with the semiempirical curve (obtained at a fixed sweep angle) simply because it has variable sweep with aspect ratio and hence it should not be compared with a single (fixed sweep) semi-empirical curve. The linearity of vertical tailplane lift curve versus angle of sideslip (up to 10 deg. sideslip angle) for the constant-sweep model of Fig. 4.25(a) is shown in Fig. 4.26(b). These last results are used in the following section as comparison term.

4.3.2.2 Fuselage Effect

The first interference effect studied was that of fuselage. This effect is measured by the ratio between the sideforce coefficients of the body-vertical configurations and those of the same isolated vertical tails previously analyzed in Sec. 4.3.2.1, see Fig. 4.27. According to Perkins and Hage [104], NACA

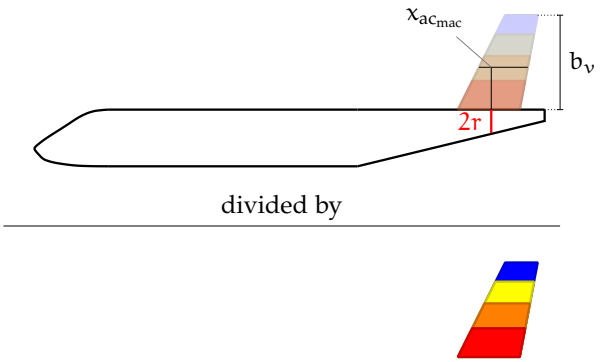

FIGURE 4.27: Configuration involved in the analysis of the effect of the fuselage: the C_{Y_V} of the body-vertical combination is divided by the C_{Y_V} of the isolated vertical tail, four vertical tailplanes (A_V = 0.5, 1.0, 1.5, 2.0) with one fuselage. $\alpha = 0$ deg., $\beta = 5$ deg., $Re = 1000000$.

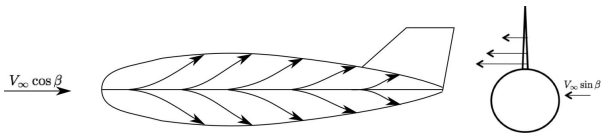

FIGURE 4.28: Streamlines approaching the vertical tailplane. Because of the fuselage's shape, the local velocity increases near the tail root, thus increasing the angle of sideslip.

experiments [87], and theory [89] the fuselage acts as a cylinder at the vertical tail root, accelerating the flow and increasing the sideforce on the vertical tail root region close to fuselage junction, see Fig. 4.28. The results, in terms of the C_{Y_V} ratios (for different vertical tailplane geometries described in Sec. 4.3.2.1) plotted versus the parameter $b_V/2r$, are shown in Fig. 4.29(a). Here b_V is considered as the geometric tailplane span of the isolated vertical tail, while the parameter 2r is the average fuselage diameter considered in a cross-section located at the aerodynamic center of the vertical tailplane (see Fig. 4.29(b)). The obtained CFD results show a low scatter among the interference effects estimated for different tailplanes with different aspect ratios, sweep angles and taper ratios. This occurred also at low $b_V/2r$ ratios (i.e. little tailplanes on a big fuselage). The obtained numerical CFD curve presents a lower scatter of that one proposed by Queijo and Wolhart [87], where there's a remarkable effect of different aspect ratio tailplanes on the above mentioned trend.

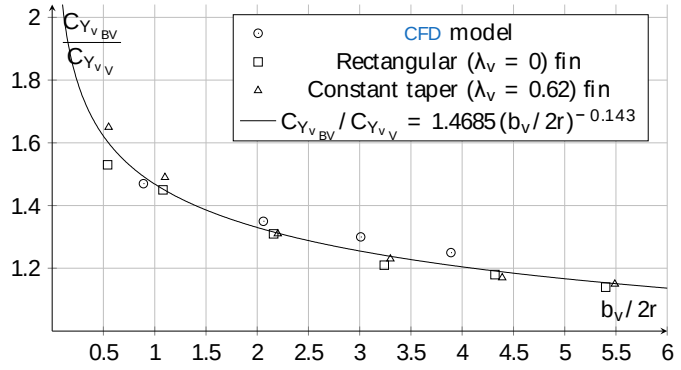

(a) Body (fuselage) effect. See Fig. 4.29(b) for definitions of b_V and $2r$.

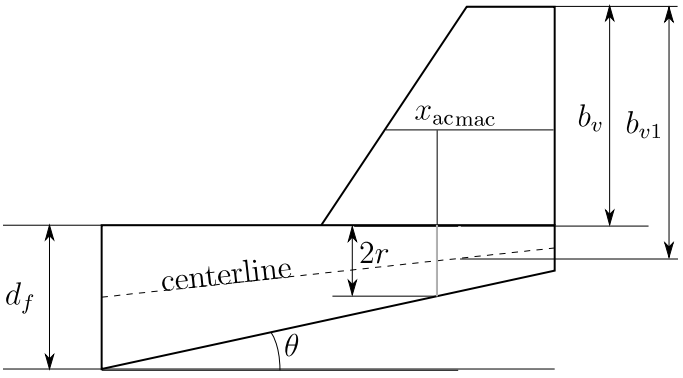

(b) Some definitions: $2r$ is the fuselage depth (thickness) in the region of vertical panels, b_V is the vertical tail span, b_{v_1} is the vertical tail span extended on the fuselage centerline.

FIGURE 4.29: Lift gradient vs. aspect ratio for the isolated vertical tailplanes and sideforce coefficient.

4.3.2.3 Wing Effect

The objective of these analyses is the evaluation of the effect of wing position and wing aspect ratio on the vertical tailplane sideforce. In order to achieve this goal, several rectangular wings, of different aspect ratio, were simulated at high, mid and low positions in fuselage. The effect has been measured by the ratio between the vertical tail contribution to sideforce coefficient C_{Y_V} for wing-fuselage-vertical configuration compared with the same coefficient obtained for the fuselage-vertical combination previously analyzed in Sec. 4.3.2.2. In this way the interference effect of wing on vertical tail aerodynamics can be extracted. All the geometries that have been considered are depicted in Fig. 4.30, while results are shown, in terms of the above mentioned C_{Y_V} ratio, in Fig. 4.31. The analyses have been performed with two different values for the vertical tail aspect ratio, $A_V = 1$ and $A_V = 2$. The results in Fig. 32 show

that the scatter between these values is not remarkable, thus it can be argued that the effect of the wing on the C_{Y_V} is almost independent from the vertical tailplane shape.

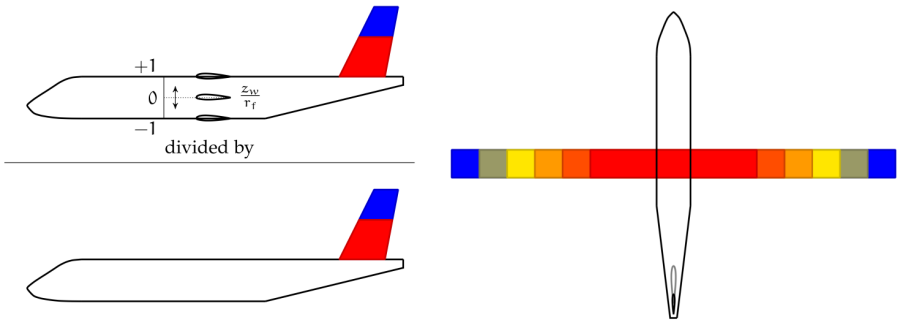

FIGURE 4.30: Configurations involved in the analysis of the effect of the wing. The C_{Y_V} of the wing-body-vertical combination is divided by the C_{Y_V} of the body-vertical combination. Three wing positions are tested and for each position the aspect ratio A is varied from 6 to 16, with a step of 2. Two vertical tailplanes with $A_V = 1$ and $A_V = 2$ are considered. $\alpha = 0$ deg., $\beta = 5$ deg., $Re = 1000000$.

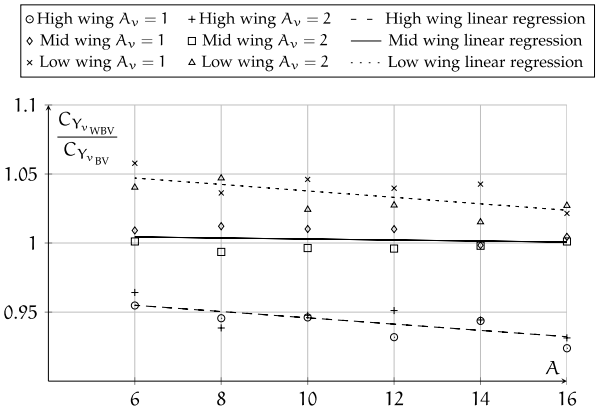

FIGURE 4.31: Effect of the wing at various aspect ratios and positions, with two vertical tailplanes, for the configurations depicted in Fig. 4.30

For high-wing position, it can be observed that the vertical tailplane sideforce coefficient C_{Y_V} decreases with respect to the same coefficient without wing (body-vertical configuration) of about 5% (being about 0.95 times that value). The effect of wing aspect ratio on that reduction seems to be low, slightly increasing this reduction from 0.95 to 0.93 when considering an increase in wing aspect ratio from 8 to 16. In the average range of wing aspect ratio A for transport aircraft (8 to 12) the effect seems to be close to 0.95 (0.94 for A = 12). Mid wing has not remarkable effects, being the ratio (measuring the effect) close to 1. The wing in mid position is neutral in terms of wing

effect on aircraft directional stability, as reported by Perkins and Hage [104]. For low-wing arrangement the C_{Y_V} ratio (the wing influence) is higher than 1 (showing a sort of symmetrical value respect to the high-wing position case). The increase of vertical tail effectiveness due to the wing is about 5% (1.05) for wing A = 8 and only up to 2.5% (1.025) for wing A = 16. Thus, as for the high-wing case, also for this configuration the wing aspect ratio has a small effect, in the wing A range considered. The average increment in vertical tail effectiveness is about 3-4% with wing A between 8 and 12. While the aspect ratio effect is quite small in the range (8 to 12) considered for both high-wing and low-wing configurations, it has a completely different trend on the two wing-body arrangements. In fact, it can be observed that while the high-wing reduction effect on vertical tail effectiveness increases with A, the low-wing amplification on vertical tail effectiveness decreases with A. Thus the higher the wing aspect ratio, the lower the vertical tail effectiveness in sideslip. This is the opposite of that predicted by USAF DATCOM [83], while ESDU [88] ignores the effects of the aspect ratio. A resume of the wing effects explained above is reported in Fig. 4.32.

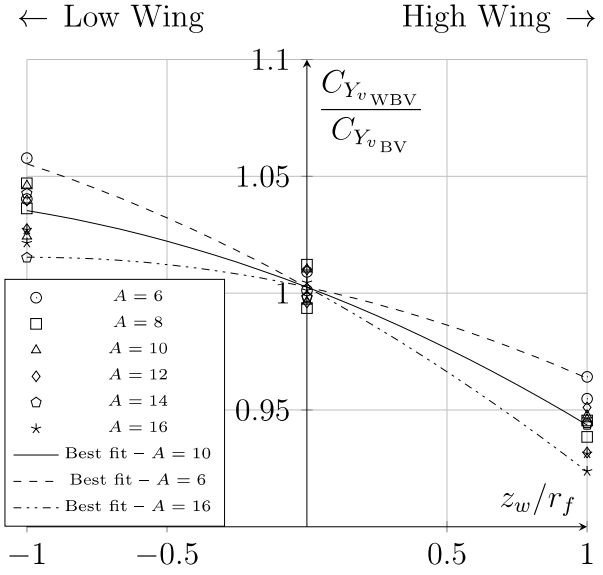

FIGURE 4.32: Resume of wing effect. For low aspect ratios add 2%, while for high aspect ratios subtract 2%, both on high- and low-wing positions. For mid-wing position all values should be considered as unity, since the scatter is less than 1%. $\alpha = 0$ deg., $\beta = 5$ deg., $Re = 1000000$.

Concerning the general effect of wing position independently from wing aspect ratio A, the physical aspects related to this influence on vertical tailplane sideforce contribution are mainly correlated to the sidewash (local increase of angle of sideslip for the vertical tail) induced by the arrangement on the vertical tail. The high-wing position mainly provides the flow on the fuselage to be concentrated on the lower side in the tail area (convey of fuselage streamlines

on lower side behind the wing), while the opposite happens for low-wing position (the body streamlines are conveyed toward the fuselage upper side). The mid-wing position has not remarkable effect on the influence of flow streamlines on the fuselage behind the wing and thus it should not be expected any sensible difference with the case without the wing (fuselage-vertical tail). Concerning the influence of wing aspect ratio, it is due to the combination of several effects, in particular the effect on the fuselage streamlines and also the possible influence of sideslip induced angle on the vertical tail due to the two wing-tip vortices spreading downstream the wing. The increase in wing aspect ratio obviously increases the distance of vortices from the vertical tail and consequently reduces the induced angles cited above. Fig. 4.33 qualitatively illustrates it.

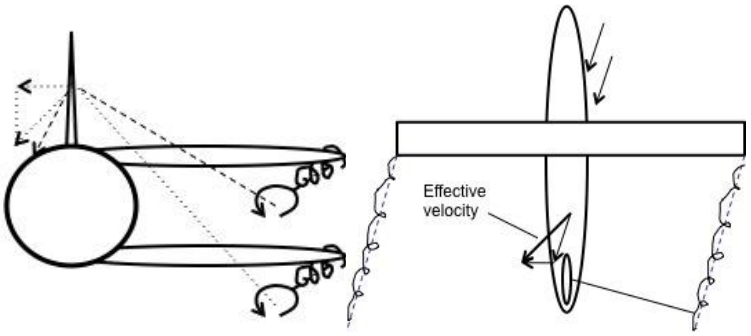

FIGURE 4.33: Qualitatively representation of the windward wing-tip vortices. The low wing induces a bigger lateral velocity than the high wing. A higher aspect ratio moves away the tip vortices, reducing their effect.

4.3.2.4 Horizontal tailplane effect

The horizontal tailplane influences the vertical tailplane with its position and size. The former is a major effect, while the latter has a minor influence, especially for tailplanes of comparable size. A straight horizontal tailplane, of constant size and aspect ratio, is mounted in five positions on the vertical tail and one on the fuselage as shown in Fig. 4.34(a). For each position the same horizontal tailplane, initially centered in chord, is moved forward and rearward by 25% of the local vertical tailplane chord, see Fig. 4.34(b).

Results are shown in Fig. 4.35, in terms of C_{Y_V} ratios between the wing-body-fin-horizontal configuration (i.e. the complete airplane) and the wing-body-fin configuration (tail off). The trend is much similar to that proposed by Brewer and Lichtenstein [85], where the effect on vertical tail effectiveness is almost the same for horizontal tailplane positioned on the fuselage and on the vertical tail tip, leading in both cases to an increase of about 15% of vertical tail sideforce. It is apparent that the end-plate effect

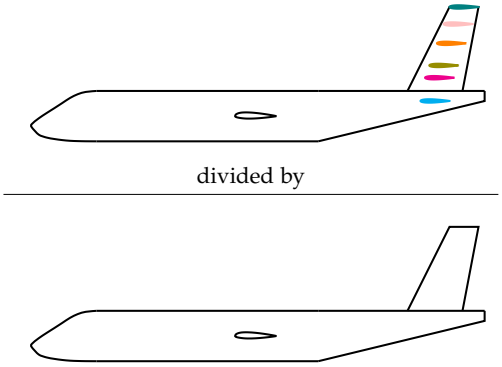

(a) Tailplanes' configuration in height.

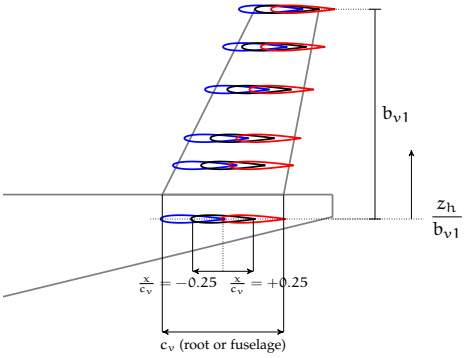

(b) Tailplanes' configuration in tail chord.

FIGURE 4.34: Horizontal tailplanes' configuration. The C_{Y_V} of the complete airplane (wing-body-vertical-horizontal) is divided by the C_{Y_V} of the wing-body-vertical combination. Only mid wing with A = 10 and the vertical tailplane with $A_V = 1$, 1.5 and 2 are considered. Mid points of tailplanes' chords are coincident. $\alpha = 0$ deg., $\beta = 5$ deg., $Re = 1000000$.

of the horizontal tailplane is maximum at extreme positions and decreases moving the horizontal tailplane forward in chord.

TABLE 4.13: Effects of the tip-mounted horizontal tail on different vertical tail aspect ratios.

A_V	$C_{Y_{V,(HV)}}$	$C_{Y_{V,(V)}}$	ratio
1.0	0.0253	0.0194	1.30
1.5	0.0394	0.0322	1.22
2.0	0.0521	0.0451	1.15

There is also another effect due to the vertical tail aspect ratio. For T-tail configurations, the lower the aspect ratio, the bigger the sideforce coefficient, as shown in Tab. 4.13. This is due to the screen that the horizontal tail makes

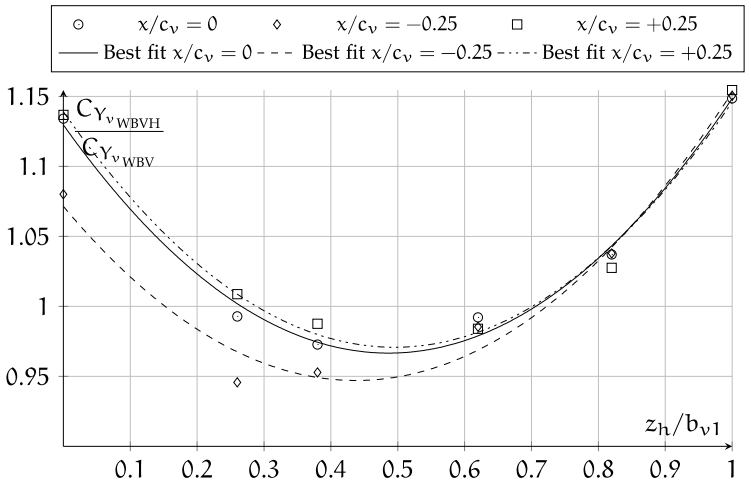

FIGURE 4.35: Horizontal tailplane position effect. $A_V = 2.0$. The A_V effect of Tab. 4.13 will be consider into in the method. The length b_{v_1} is the vertical tail span extended to the horizontal tailplane position in fuselage, see Fig. 4.29(b). This span stretch is mandatory if a unique chart with all possible tailplane's positions is desired. $\alpha = 0$ deg., $\beta = 5$ deg., $Re = 1000000$.

on the tip vortex of the vertical tail, acting like a big winglet on the vertical tail. It has to be noted that this effect is not present until the horizontal tail is mounted at $z_H/b_{v_1} = 0.85$. This effect will be properly take into account in the method explained in Sec. 4.4.

The effect of tailplanes' relative size is shown in Fig. 4.36, where the ratio C_{Y_V} between the complete airplane with the horizontal tail varying in size and the same configuration with a ratio S_H/S_V close to unity (the original horizontal tailplane) is represented as shown in Fig. 4.37. Two extreme positions were analyzed, the body-mounted and tip-mounted tailplanes. A bigger horizontal stabilizer increases the end-plate effect on the vertical tail, as expected. Typical ratio between large turboprop tailplanes is around 1 (1.1-1.3), whereas for commuter aircraft can be also around 2 and this factor gives only a small variation of the sideforce coefficient as shown in Fig. 4.36 of about 1-3%.

4.3.3 Rudder Effect

The objective of the analyses is to evaluate the vertical tail lateral force coefficient $C_{Y_{V_{\delta_r}}}$, which is the main contribution to the aircraft lateral force and directional control, generated by a rudder deflection.

This lateral force coefficient is affected by the aerodynamic interference (respect to the isolated vertical plane) due to the aircraft fuselage, wing and horizontal tail. Corrective factors can be defined to evaluate this aerodynamic

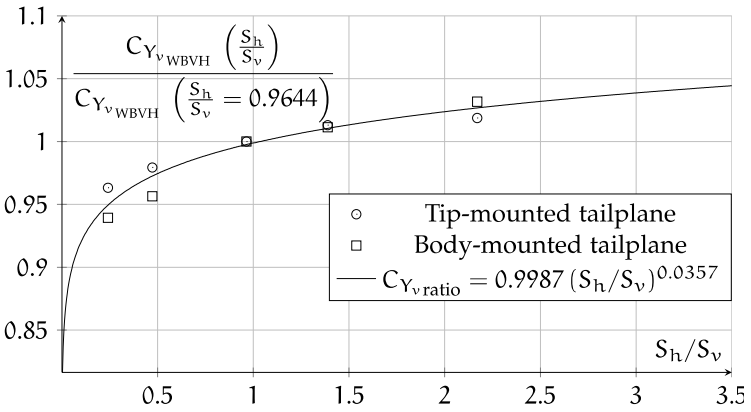

FIGURE 4.36: Effect of the relative size of tailplanes. It is negligible at a first approximation, since most airplanes have Sh /Sv ratios close to unity. $\alpha = 0$ deg., $\beta = 5$ deg., $Re = 1000000$.

interference by evaluating the ratio between several aircraft configuration as illustrated in the previous sections. In this case the configurations used in the CFD analyses to evaluate the interference effects are: body-vertical (BV), wing-body-vertical (WBV), and wing-body-vertical-horizontal combination ($WBVH$) as shown in Fig. 4.38 In all these configurations a rudder geometry has been used on the vertical tail: the vertical tailplane is characterized by a swept planform (as shown in Fig. 4.25(a)) with a plain flap as rudder, as shown in Fig. 4.39.In particular the vertical tail airfoil is a NACA 0012 with the trailing edge rotated at 65% of the chord as shown in Fig. 4.39. More than 50 configuration have been analyzed to establish the rudder effect and the results are summarized in Appendix B.

4.3.3.1 Isolated vertical tail with rudder Effect

The isolated vertical tail with rudder has been analyzed to predict the sideforce coefficient. Tailplanes with $A_V = 1.0$, $A_V = 1.5$ and $A_V = 2.0$ have been analyzed. Several δ_r have been used (from 0 to 25 deg.), but to estimate the effect among aircraft components only the $\delta_r = 10$ deg. has been used. Figure 4.40 and Fig. 4.41 show the linearity at several angles of sideslip and rudder deflection of the lateral force coefficient C_{Y_V} for the isolated vertical tailplane of aspect ratio 2. These results will be used as comparison terms in the following sections.

4.3.3.2 Body Effect on vertical tail with rudder

This section provides a description about the aerodynamic interference effects between fuselage and the vertical tailplane, see the upper part of Fig. 4.25(a). The effect of a body at the root of the vertical tailplane is to increase the crossflow due to a rudder deflection even at zero sideslip angle. In fact, the

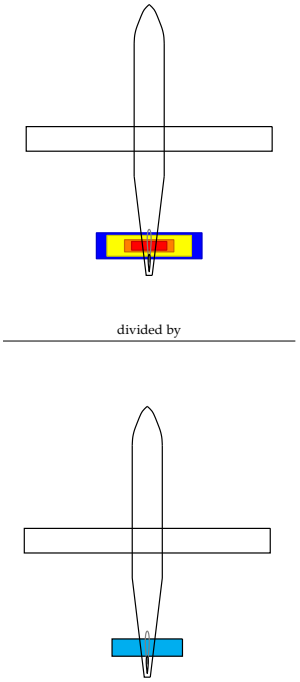

FIGURE 4.37: Configurations involved in the analysis of the relative size of the tailplanes. The reference model has $S_H/S_V = 0.9644$. For the sake of clarity, only the body-mounted tailplanes are shown.

deflection of the rudder creates a local sideslip angle due to the pressure change on the surfaces of the vertical tailplane and in general due to circulation induced by the vertical tail lift. This leads to an asymmetric streamlines path only near the tail as shown in Fig 4.42. Thus, the local cross-component of the velocity on the rear part of the fuselage is accelerated like the flow past of a cylinder, increasing the vertical tail angle of attack close to its root and consequently the lift force generated. Table 4.14 shows this increment for three body-vertical (BV) combinations obtained through tailplanes of different aspect ratio, as shown in Fig. 4.25(a) top. Queijo and Wolhart [87] showed that this effect is stronger for tailplanes which span is small compared to the fuselage diameter (also shown in Fig. 4.29(a)). Also, the independent variable is the ratio between the vertical tail span b_v and the fuselage diameter r at the vertical tail aerodynamic center, since the effect depends on the relative dimensions of the two components. The fuselage interference factor (BV/V) has a range from 1.15 to 1.10 for an increasing tail span from twice to four times the fuselage diameter r.

Figure 4.43 shows that linearity is conserved at angles of sideslip up to 10 deg. for vertical tailplanes of low aspect ratio (given a certain sweep angle). The interference factors calculated at no sideslip and shown in Tab. 4.14 do not vary with sideslip in the linear range of the curves of Fig. 4.43.

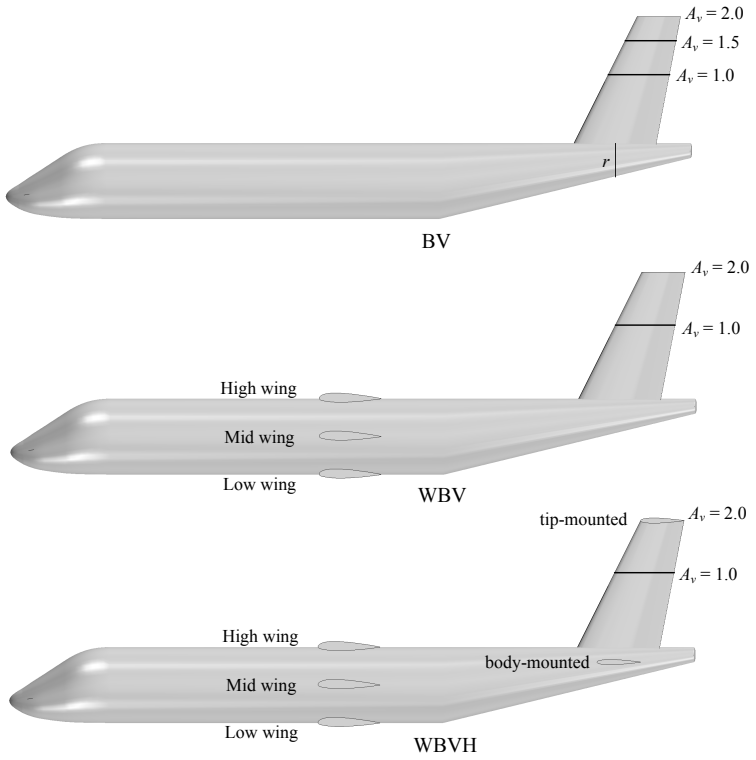

FIGURE 4.38: Configurations involved in the rudder effect.

TABLE 4.14: Fuselage interference factors.

A_V	$b_v/2r$	$C_{Y_V}(V)$	$C_{Y_V}(BV)$	BV/V
1.0	2.06	0.0303	0.0348	1.15
1.5	3.01	0.0505	0.0563	1.12
2.0	3.89	0.0682	0.0751	1.10

4.3.3.3 Wing Effect on vertical tail with rudder

Three wing positions (high, mid and low in fuselage) and two vertical tails aspect ratios (Av = 1 and Av = 2) represent 6 different wing-body-vertical (WBV) configurations, as shown in Fig. 4.25(a) center. Figure 4.44 shows that the wing position slightly affects the vertical tail sideforce. As already outlined in Sec. 4.3.2.3, considering sideslip conditions without rudder deflection, the high wing leads to a vertical tail effectiveness reduction of about 4%, the low wing leads to an increase of about 5%, and the mid wing position does not affects the vertical tail aerodynamics. Results at no sideslip with a rudder deflection $\delta_r = 10$ deg. are shown in Tab. 4.15, where the last two columns refer respectively to force coefficients ratio between wing-body-vertical combination and body-vertical combination WBV/BV, and wing-body-vertical combination to isolated vertical tailplane WBV/V, to highlight the total effect. In these

FIGURE 4.39: The vertical tailplane and the NACA 0012 airfoil with the trailing edge rotated to simulate a rudder deflection.

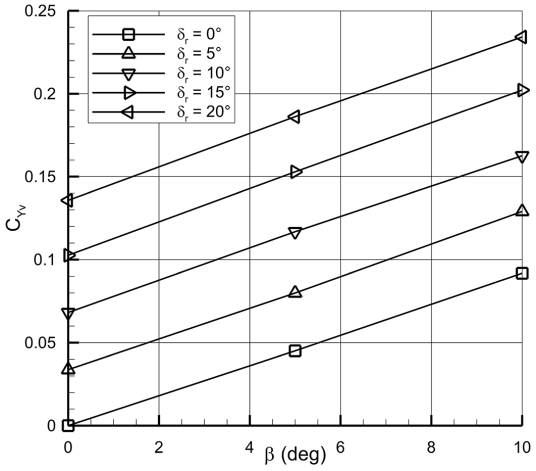

FIGURE 4.40: Linearity of the lateral force coefficient at several angles of sideslip and rudder deflection for the isolated vertical tailplane with $A_V = 2$.

conditions, the average force increase obtained adding the wing to the body-vertical combination is around 1% and hence negligible. The above mentioned sidewash effect is absent in case of rudder deflection with no sideslip, since the wing is located far upstream from the local sideslip flow induced by the rudder deflection.

4.3.3.4 Horizontal tailplane Effect on vertical tail with rudder

A straight horizontal tailplane, is initially mounted on the fuselage and then on the tip of the vertical tailplane, for a total of 12 different aircraft configurations, see Fig. 4.25(a) bottom. The horizontal tailplane, as well known, acts as an end-plate if mounted on the tip of the vertical tailplane, delaying the tip vortex

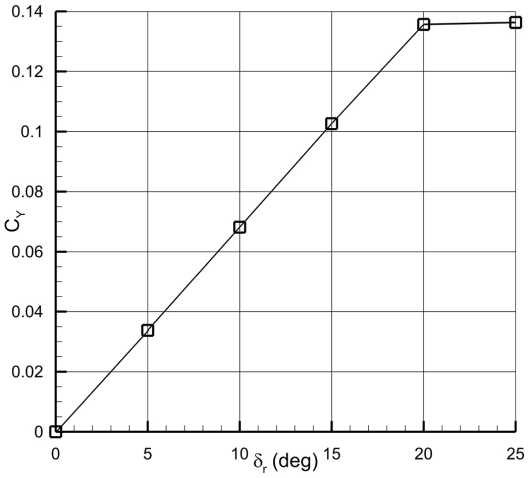

FIGURE 4.41: The lateral force coefficient vs. rudder deflection at zero sideslip angle for the isolated vertical tailplane with Av = 2.

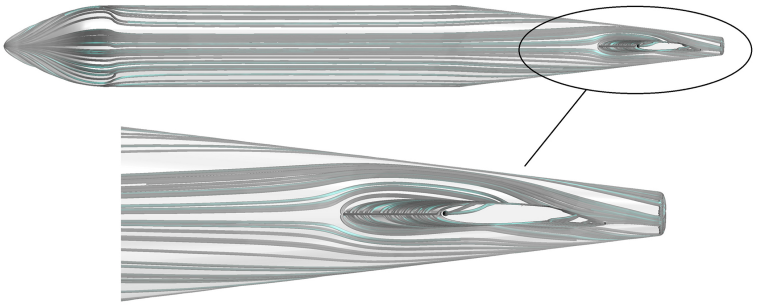

FIGURE 4.42: Streamlines showing the asymmetric flow path in the rear part of the fuselage. Body-vertical combination with $A_V = 1$, $\delta_r = 10$ deg.

and hence increasing the lateral force coefficient. Tab. 4.16 shows results for the complete airplane (wing-body-vertical-horizontal combination, WBVH). The horizontal tailplane in T-tail configurations is able to increase the vertical tail with rudder aerodynamic effectiveness of about +20% for $A_V = 1$ and about +13% for $A_v = 2$, with respect to the wing-body-vertical (WBV) configuration. Conversely, results for the body-mounted horizontal tailplane does not depend on vertical tail aspect ratio, as shown in Tab. 4.17, because the vertical tail root vortex is controlled in the same manner independently of the A_V. The average increase of the sideforce coefficient in this case is +8% with respect to the wing-body-vertical (WBV) configuration.

As expected, the aerodynamic interference is stronger for configurations involving the horizontal tail located on the top of the vertical tail, especially for short tailplanes, because of the end-plate effect on the vertical tail tip vortex. In case of body-mounted horizontal tailplane the interference effect is mainly due to the increase of the fuselage effect. Obviously, the horizontal

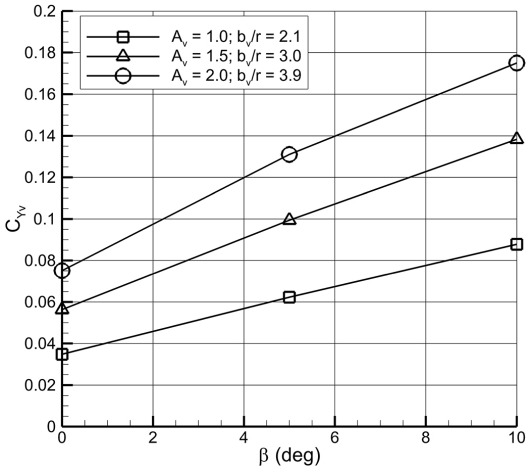

FIGURE 4.43: Values of the vertical tail lateral force coefficient at several angles of sideslip and $\delta_r = 10$ deg. for the body-vertical combinations with three different aspect ratios.

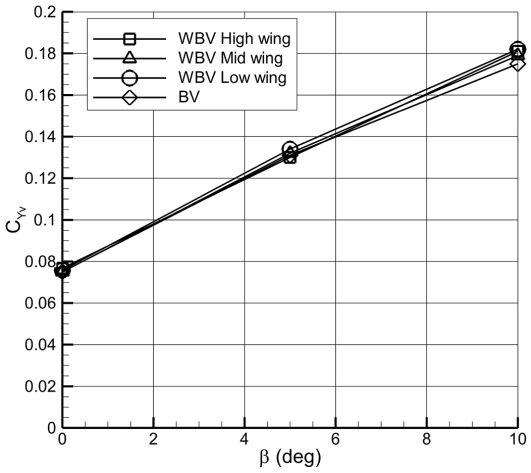

FIGURE 4.44: Comparison of the three wing-body-vertical combinations and the body vertical combination at several angles of sideslip and $\delta_r = 10$ deg., $A_V = 2$.

tailplane mounted on the fuselage does not affect the vertical tail tip vortex, hence the interference factor does not depend on the vertical tailplane aspect ratio. Figure 4.45 clearly shows the different streamlines path for the two tailplanes configurations.

4.3.3.5 Final remarks on rudder Effect

Results of the previous Sec. 4.3.3 highlight that, at no sideslip, there is an increase in the sideforce provided by the rudder deflection due to the

TABLE 4.15: Wing interference factors.

Configuration	A_V	$C_{Y_V}(WBV)$	WBV/BV	WBV/V
WBV mid	1.0	0.0350	1.00	1.16
WBV high	1.0	0.0350	1.01	1.16
WBV low	1.0	0.0352	1.01	1.16
WBV mid	2.0	0.0750	1.00	1.10
WBV high	2.0	0.0768	1.02	1.13
WBV low	2.0	0.0758	1.01	1.11

TABLE 4.16: Tip-mounted horizontal tail interference factors.

Configuration	A_V	$C_{Y_V}(WBVH)$	$WBVH/WBV$	$WBVH/V$
WBVH mid	1.0	0.0416	1.19	1.38
WBVH high	1.0	0.0419	1.20	1.38
WBVH low	1.0	0.0425	1.21	1.40
WBVH mid	2.0	0.0852	1.14	1.25
WBVH high	2.0	0.0865	1.13	1.27
WBVH low	2.0	0.0846	1.12	1.24

TABLE 4.17: Body-mounted horizontal tail interference factors.

Configuration	A_V	$C_{Y_V}(WBVH)$	$WBVH/WBV$	$WBVH/V$
WBVH mid	1.0	0.0379	1.09	1.25
WBVH high	1.0	0.0379	1.08	1.25
WBVH low	1.0	0.0375	1.07	1.24
WBVH mid	2.0	0.0807	1.08	1.18
WBVH high	2.0	0.0807	1.06	1.18
WBVH low	2.0	0.0805	1.06	1.18

aerodynamic interference among the aircraft components. This interference is conserved at angles of sideslip.

Figure 4.46 shows the vertical tailplane lateral force coefficient for the previously described configurations at several angles of sideslip and rudder deflection, for the vertical tailplane with $A_V = 2$. Values at $\beta = 0$ deg are the same of those reported in Tab. 4.14 to Tab. 4.17 for $A_V = 2$. The solid lines, starting from the origin of the axes, represent the configurations with the mid wing, body-mounted horizontal tail, $A_V = 2$ in sideslip, with no rudder deflection ($\delta_r = 0$ deg.). Adding the aircraft components as fuselage, wing, and horizontal tailplane to the vertical tailplane increases the curve slope. This is modeled in USAF DATCOM [83] as an increase in the vertical tailplane (effective) aspect ratio. The dashed lines represent the same configurations at three angles of sideslip with a rudder deflection of $\delta_r = 10$ deg. It can be observed that adding aircraft components both (solid and dashed curves)

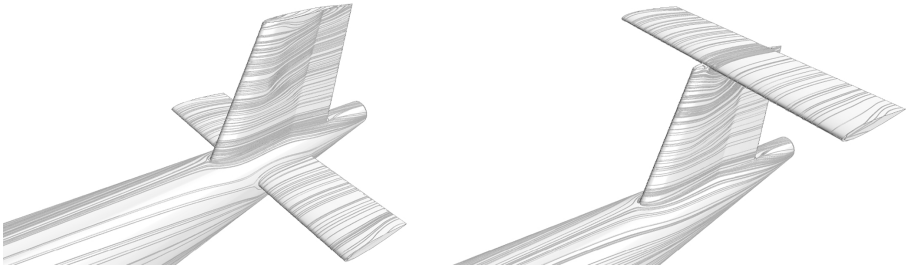

FIGURE 4.45: Streamlines around tailplanes for body-mounted and tip-mounted horizontal stabilizer configurations. $A_V = 1$, $\delta_r = 10$ deg.

change the slope and translate, except for the wing, which contribution is negligible. Linearity is conserved up to 5-8 deg of sideslip. In the linear range, the dashed lines are parallel to the equivalent configuration solid lines, hence the slope is conserved and the directional stability derivative $dC_{Y_V}/d\beta$ is unaffected. Thus, the deflection of the rudder simply translates the solid lines, as Obert [65], Schlichting and Truckenbrodt [41] predicted, giving an increase of the force coefficients even at no sideslip but preserving the curve slope, which is predicted by the directional stability term.

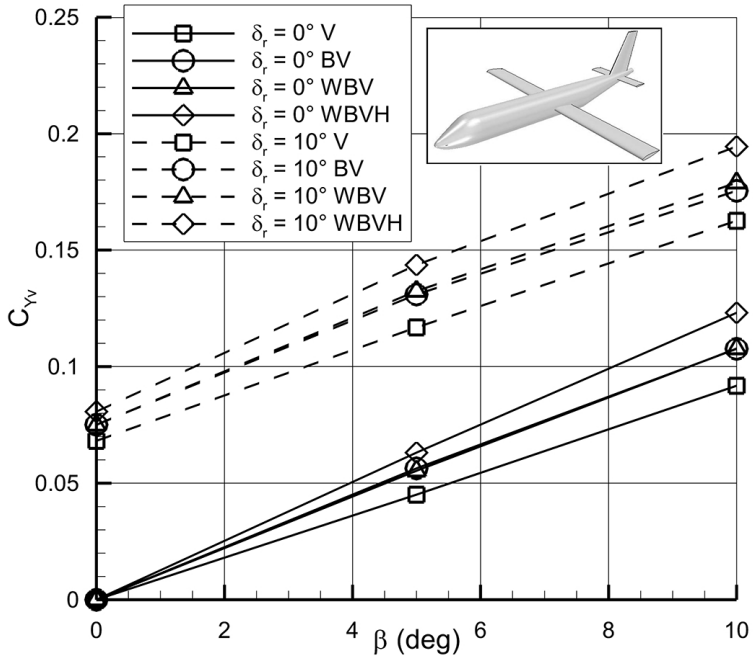

FIGURE 4.46: Comparison among 3 angles of sideslip and 2 angles of rudder deflection for the mid wing, body-mounted configuration with $A_V = 2$, $\delta_r = 10$ deg.

4.4 New Vertical Tail Design Method

In this section a new approach to the evaluation of the vertical tailplane and rudder sideforce is proposed. The method is named **VeDSC** method as Vertical tail Design Stability and Control and it is based on the investigations described in Sec. 4.3 and hence it is suitable for regional turboprop and commuter airplanes in subsonic flow regime and cruise conditions.

The vertical tailplane sideforce is calculated as

$$C_{Y_V} = C_{Y_{\beta_V}}\,\beta + C_{Y_{\delta_r}}\,\delta_r \tag{4.9}$$

where

$C_{Y_{\beta_V}}$ is the sideforce derivative of the vertical tailplane in the complete aircraft computed according Eq. 4.10.

$C_{Y_{\delta_r}}$ is sideforce derivative of the rudder control surface in the complete aircraft computed according Eq. 4.11.

$$C_{Y_{\beta_V}} = K_{\mathrm{F}}\,K_{\mathrm{W}}\,K_{\mathrm{H}}\,C_{L_\alpha V}\,\frac{S_V}{S} \tag{4.10}$$

where

$C_{L_\alpha V}$ is the lift curve slope of the isolated vertical tailplane (Sec. 4.4.1)

$K_{\mathbf{F}}$ is the factor for the fuselage effect (Sec. 4.4.2)

$K_{\mathbf{W}}$ is the factor for the wing effect (Sec. 4.4.3)

$K_{\mathbf{H}}$ is the factor for the horizontal tailplane effect (Sec. 4.4.4)

and

$$C_{Y_{\delta_r}} = K_{\delta_r}\,C_{L_\alpha V}\,\tau_{\delta_r}\,\frac{S_V}{S} \tag{4.11}$$

where

$C_{L_\alpha V}$ is the lift curve slope of the isolated vertical tailplane (Sec. 4.4.1)

K_{δ_r} is the factor to account for fuselage and horizontal tail effect (Sec. 4.4.5)

τ_{δ_r} is the rudder effectiveness according to Roskam [9]

$\frac{S_V}{S}$ is the vertical tail surface on wing surface ratio.

The meanings of these corrective factors is the following: K_{F} is the effect on C_{Y_V} of adding the fuselage to the isolated vertical tail, K_{W} is the effect of adding the wing to the body-vertical combination, and K_{H} is the effect of adding the horizontal tailplane to the wing-body-vertical combination[1] and K_{δ_r} is the effect to deflect a rudder in the complete aircraft configuration.

[1] It has been verified that there's no difference in K_{H} when not considering the wing, that is the K_{H} calculated on the wing-body-vertical-horizontal combination is the same of that calculated on the body-vertical-horizontal combination.

4.4.1 Isolated vertical tailplane lift curve slope

The vertical stabilizer alone is a wing, whose lift gradient can be expressed by the Helmbold-Diederich formula [99], here rewritten

$$C_{L_\alpha V} = \frac{2\pi\, A_V}{2 + \left[\frac{B^2 A_V^2}{\kappa^2}\left(1 + \frac{\tan^2 \Lambda_{v_{c/2}}}{B^2}\right) + 4\right]^{\frac{1}{2}}}$$

where

A_V is the aspect ratio, b_V^2/S_V

B is a compressibility parameter, $\sqrt{(1-M^2)}$

κ is the ratio of *section* lift-curve slope to theoretical thin-section value $c_{l_\alpha}/(2\pi/B)$, and for thin airfoil ($c_{l_\alpha} \approx 2\pi$) it is equal to B

$\Lambda_{v_{c/2}}$ is the sweep angle at half chord (Figure 4.47(a)).

The product $C_{L_\alpha V}\, S_V/S$ is the C_{Y_V} of the isolated vertical tail.

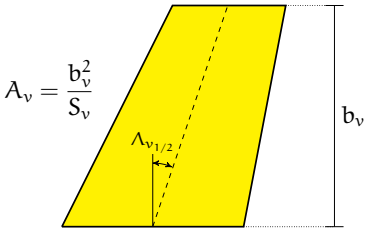

(a) The modular vertical tail of the CFD model.

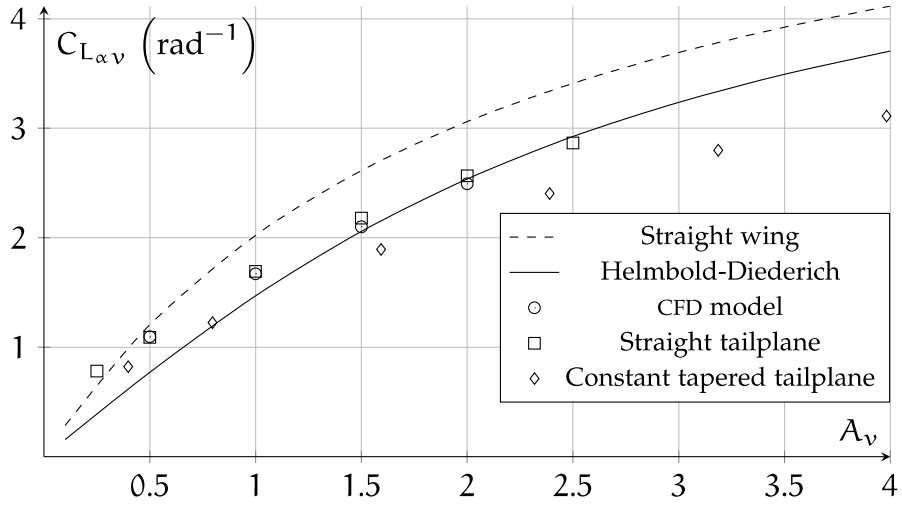

(b) Example of Lift slope fow low aspect ratio wing. Several approaches and vertical tailplanes.

FIGURE 4.47: Definition of the isolated vertical tail.

4.4.2 Fuselage correction factor

The factor K_{F} is function of the ratio between the vertical tailplane span b_V and the fuselage thickness $2r$. These parameters are defined in Figure 4.48. The curve has equation

$$K_{\mathrm{F}} = 1.4685 \left(\frac{b_V}{2r}\right)^{-0.143} \tag{4.12}$$

and it is plotted in Figure 4.49. In the event of vertical tailplane submerged in fuselage, tail span b_V is the longest vertical distance on wetted surface from tail root to tail tip.

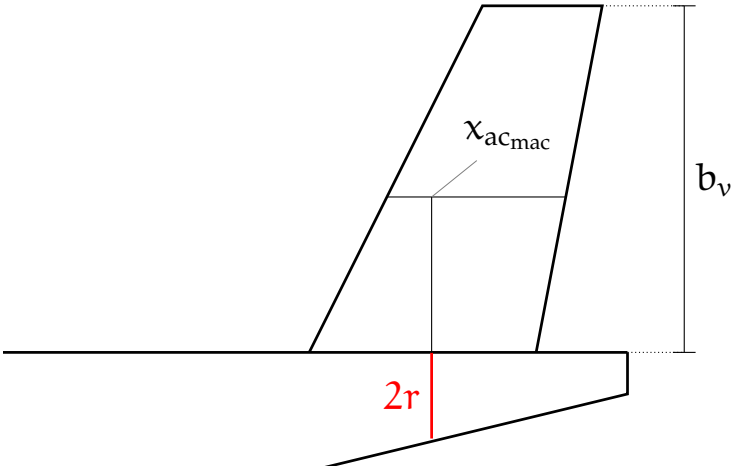

FIGURE 4.48: Definitions of b_V and $2r$ for the VeDSC method.

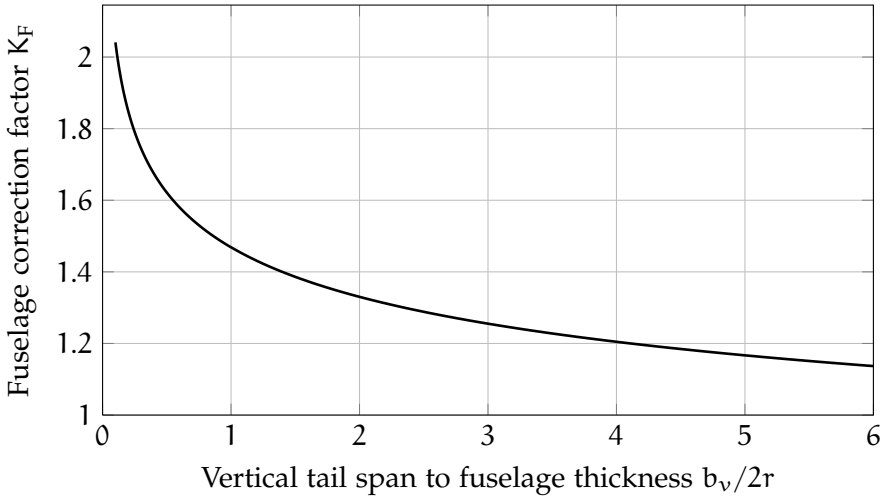

FIGURE 4.49: Fuselage correction factor.

4.4.3 Wing correction factor

The factor K_{W} is function of wing aspect ratio A and position in fuselage z_w/r_f. This parameter is defined in Figure 4.50. The curve has equation (for A close to 10)

$$K_{\mathrm{W}} = -0.0131 \left(\frac{z_w}{r_f}\right)^2 - 0.0459 \frac{z_w}{r_f} + 1.0026 \tag{4.13}$$

and it is plotted in Figure 4.51.

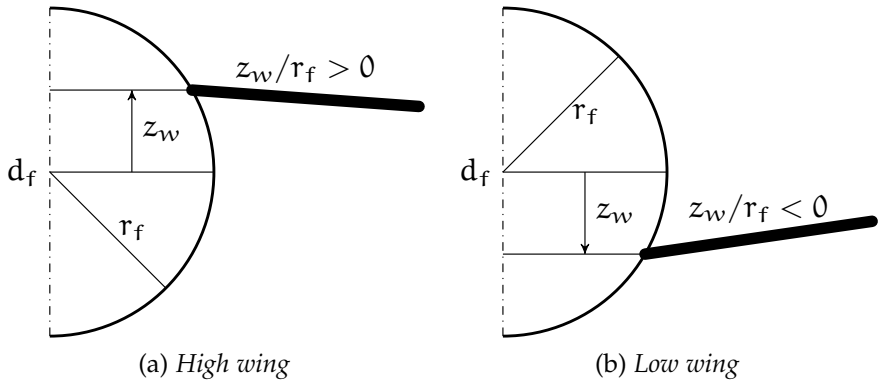

(a) *High wing* (b) *Low wing*

FIGURE 4.50: Definition of z_w/r_f for the VeDSC method. If the fuselage has a non-circular section r_f is half fuselage height.

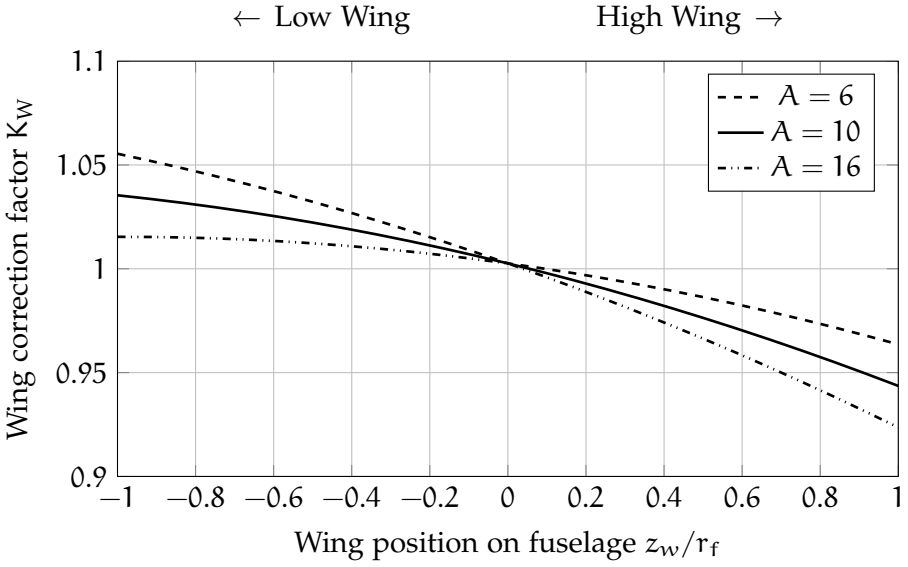

FIGURE 4.51: Wing correction factor. Between the high and low aspect ratios it is supposed a linear variation of the curve with a maximum difference of 2%.

4.4.4 Horizontal tailplane correction factor

The factor K_{H} is function of other coefficients that account for of the horizontal tailplane position K_{Hp} and size K_{Hs}, related in the following formula

$$K_{\mathrm{H}} = 1 + K_{\mathrm{Hs}} \left(K_{\mathrm{Hp}} - 1 \right) . \tag{4.14}$$

The factor K_{Hp} is function of the relative position between the horizontal and the vertical tailplanes z_H/b_{v1}, where this non-dimensional parameter is computed from the position of the tailplane in fuselage, as shown in Figure 4.52 and of the vertical tail aspect ratio A_V shown in Fig 4.47(a).

The curves have the following expressions

if $\frac{z_H}{b_{v1}} \leq 0.85$

$$K_{\mathrm{Hp}} = 0.6891 \left(\frac{z_H}{b_{v1}} \right)^2 - 0.6703 \frac{z_H}{b_{v1}} + 1.1296 \quad x/c_V = 0 \tag{4.15a}$$

$$K_{\mathrm{Hp}} = 0.6502 \left(\frac{z_H}{b_{v1}} \right)^2 - 0.5687 \frac{z_H}{b_{v1}} + 1.0714 \quad x/c_V = -0.25 \tag{4.15b}$$

$$K_{\mathrm{Hp}} = 0.6864 \left(\frac{z_H}{b_{v1}} \right)^2 - 0.6796 \frac{z_H}{b_{v1}} + 1.139 \quad x/c_V = +0.25 \tag{4.15c}$$

if $\frac{z_H}{b_{v1}} > 0.85$

$$K_{\mathrm{Hp}} = 3.255 \left(\frac{z_H}{b_{v1}} \right)^2 - 4.461 \frac{z_H}{b_{v1}} + 2.505 \qquad A_V = 1.0 \tag{4.16a}$$

$$K_{\mathrm{Hp}} = 2.089 \left(\frac{z_H}{b_{v1}} \right)^2 - 2.784 \frac{z_H}{b_{v1}} + 1.914 \qquad A_V = 1.5 \tag{4.16b}$$

$$K_{\mathrm{Hp}} = 0.6891 \left(\frac{z_H}{b_{v1}} \right)^2 - 0.6703 \frac{z_H}{b_{v1}} + 1.1296 \quad A_V = 2.0 \tag{4.16c}$$

$$\tag{4.16d}$$

and are plotted in Figure 4.53.

The factor K_{Hs} is function of the relative size of the tailplanes S_H/S_V. It has equation

$$K_{\mathrm{Hs}} = 0.9987 \left(\frac{S_H}{S_V} \right)^{0.0357} \tag{4.17}$$

and it is plotted in Figure 4.55. If the horizontal tailplane has a planform area very close to that of the vertical tailplane, the size contribution can be neglected ($K_{\mathrm{Hs}} \approx 1$ as shown in Figure 4.55), thus $K_{\mathrm{H}} \approx K_{\mathrm{Hp}}$.

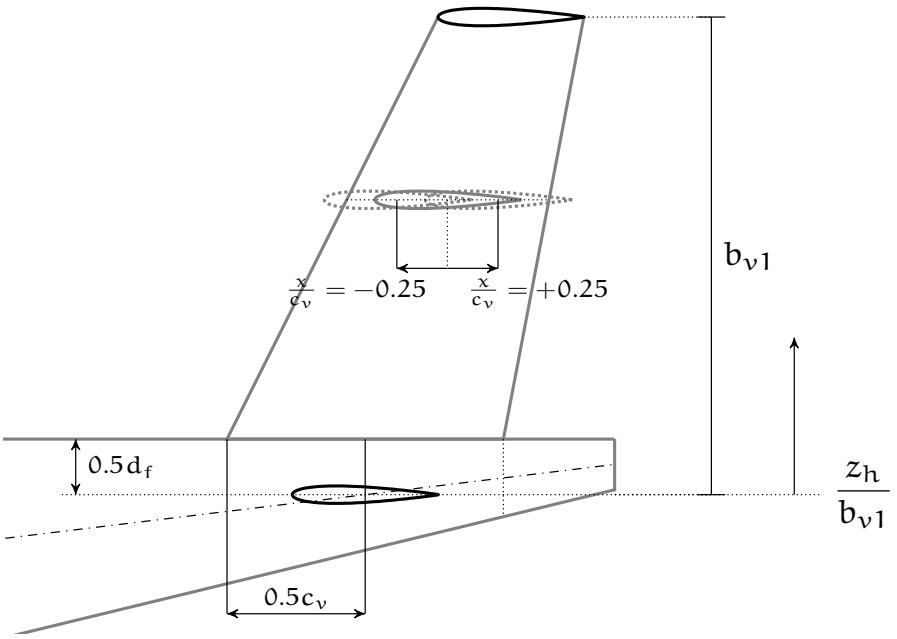

FIGURE 4.52: Definition of z_H/b_{v1} and x/c_V for the VeDSC method. The body-mounted horizontal tailplane has the mid-chord point on the fuselage centerline, coincident with the projection of the mid-chord point of the vertical tail root on the same centerline.

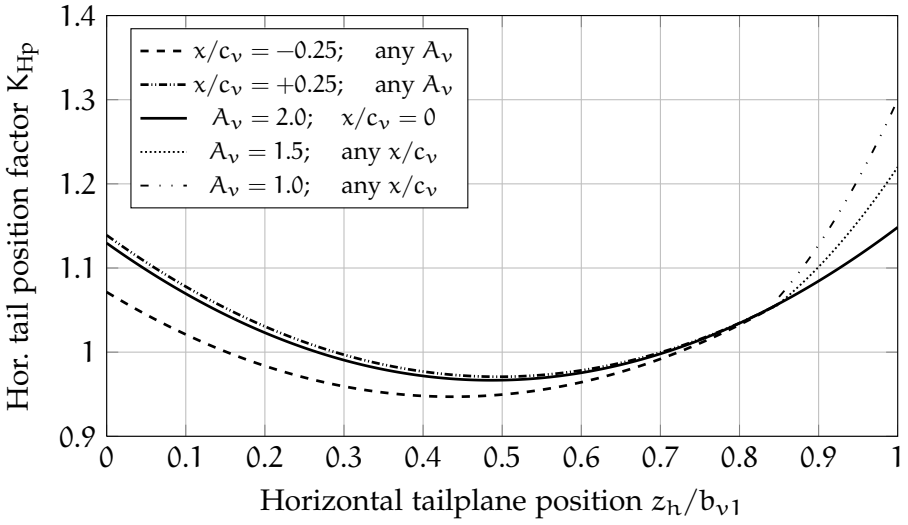

FIGURE 4.53: Horizontal tailplane position correction factor. The A_V effect must be considered starting from $\frac{z_H}{b_{v1}} > 0.85$

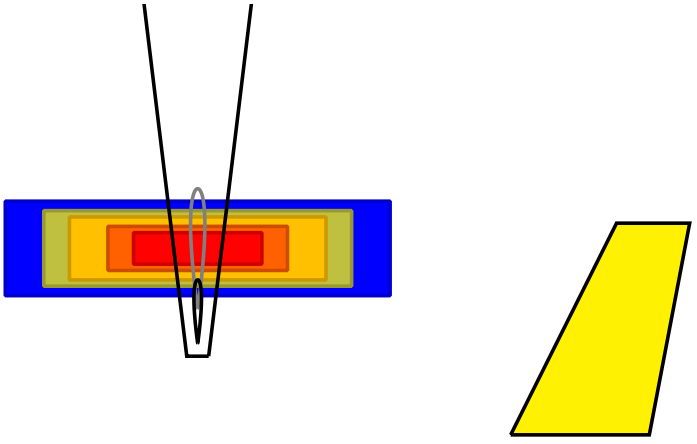

(a) *Variation of* S_h. (b) S_v *for* $A_v = 2$.

FIGURE 4.54: Definition of S_H/S_V for the VeDSC method.

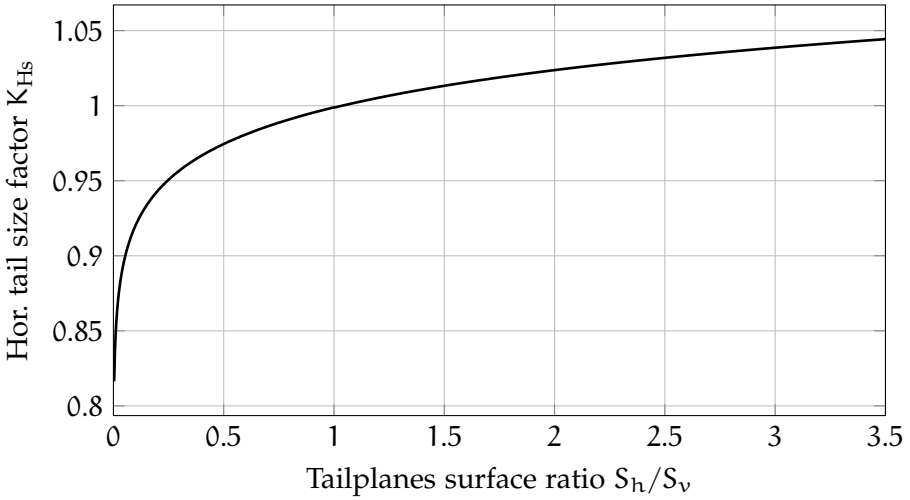

FIGURE 4.55: Horizontal tailplane size correction factor. For surface ratios close to unity it can be neglected and hence, $K_{Hp} \approx K_H$.

4.4.5 Rudder correction factor

The factor K_{δ_r} has to be computed as follows:

$$K_{\delta_r} = \left[1 + \left(\frac{K_{\mathrm{F}} - 1}{2.2}\right)\right] \cdot \begin{cases} 1.07 & \text{if horizontal tail is body mounted} \\ 1.33 - 0.09 A_V & \text{for T-tail configuration} \end{cases} \tag{4.18}$$

where K_{F} is estimated according to Sec. 4.4.2. The K_{δ_r} factor is equivalent to a fraction of the K_{F} times the effect due to the horizontal tail position.

4.5 Applications

The semi-empirical methods provided by USAF DATCOM [83] and ESDU [88] are here compared with the new VeDSC method illustrated in Sec. 4.4 on three different airplanes.

1. CFD model
2. ATR-42
3. Tecnam P2012.

1. A CFD model.
   The first comparison is about a configuration analyzed with CFD and described in Sec. 4.3.2. This application to verify the method consistent. The CFD model used is a mid wing, body-mounted tail combination with the wing in mid position on the fuselage as shown in Fig. 4.56, which data are reported in Tab. 4.18 and results in Tab 4.19. Values provided by the VeDSC method are consistent with the analyses developed to build it. The difference respect to the reference CFD analysis is about 1.9% , due to the application of Diederich formula instead to use the $C_{L_{\alpha_V}}$ computed in CFD. DATCOM and ESDU method differences are 6.5% and 11.2% respectively.
2. ATR-42
   The second application is the ATR-42 shown in Fig. 4.1, which data of interest are reported in Tab. 4.20 and results in Tab. 4.21. The three methods give almost the same value of the vertical tailplane sideforce coefficient, as also highlighted in Sec. 4.1.1.
3. Tecnam P2012
   Last example is about the Tecnam P2012 twin engine 11 seats commuter aircraft shown in Fig.4.58, which data are reported in Tab.4.22 and results in Tab.4.23.

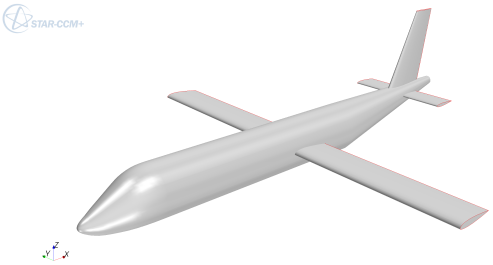

FIGURE 4.56: CFD model application.

TABLE 4.18: CFD Model data.

Wing position	Mid
Wing area S	0.225 m^2
Wing aspect ratio A	10
Vertical tail aspect ratio A_V	2.0
Vertical tail area S_V	0.047 m^2
Vertical tail span b_v	0.306 m
Horizontal tail area S_H	0.045 m^2
Horizontal tail position z_h/b_v	0
Fuselage thickness $2r$	0.08 m

TABLE 4.19: CFD Model results.

$C_{L_{\alpha_V}}$	2.600 rad^{-1}	
K_{F}	1.212	
K_{W}	1.003	
K_{Hp}	1.130	
K_{Hs}	0.997	
K_{H}	1.130	
K_{δ_r}	1.173	
$K_{\mathrm{F}}\,K_{\mathrm{W}}\,K_{\mathrm{H}}$	1.370	Δ from CFD
$C_{Y_{\beta_V}}$ VeDSC	0.737 rad^-1	1.9%
$C_{Y_{\beta_V}}$ DATCOM	0.680 rad^-1	6.5%
$C_{Y_{\beta_V}}$ ESDU	0.642 rad^-1	11.2%
$C_{Y_{\beta_V}}$ CFD	0.727 rad^-1	-

The VeDSC method has been used in preliminary design to dimension the vertical tailplane of this aircraft with particular attention on the V_{MC}, as also shown in Ref.[15]. Although experimental data are not available yet and wind-tunnel tests are still in progress, a CFD simulation on the complete airplane in clean configuration

TABLE 4.20: ATR-42 data.

Wing position	High
Wing area S	50.0 m^2
Wing aspect ratio A	12
Vertical tail aspect ratio A_V	1.6
Vertical tail area S_V	12.7 m^2
Vertical tail span b_v	4.5 m
Horizontal tail area S_H	12.7 m^2
Horizontal tail position z_h/b_v	0.82
Fuselage thickness $2r$	0.91 m

TABLE 4.21: ATR-42 results.

$C_{L_{\alpha_V}}$	2.240 rad^{-1}
K_{F}	1.168
K_{W}	0.944
K_{Hp}	1.051
K_{Hs}	0.995
K_{H}	1.051
K_{δ_r}	1.277
$K_{\mathrm{F}}\,K_{\mathrm{W}}\,K_{\mathrm{H}}$	1.159
$C_{Y_{\beta_V}}$ VeDSC	0.659 $rad^{-}1$
$C_{Y_{\beta_V}}$ DATCOM	0.669 $rad^{-}1$
$C_{Y_{\beta_V}}$ ESDU	0.642 $rad^{-}1$

was executed at DII. There is a 5% difference between the results provided by the CFD and the VeDSC procedure, although the latter is developed on regional transport aircraft geometries.

TABLE 4.22: P2012 data.

Wing position	High
Wing area S	24.92 m^2
Wing aspect ratio A	7.87
Vertical tail aspect ratio A_V	1.89
Vertical tail area S_V	3.5 m^2
Vertical tail span b_v	2.57 m
Horizontal tail area S_H	5.67 m^2
Horizontal tail position z_h/b_v	0, rear
Fuselage thickness $2r$	0.72 m

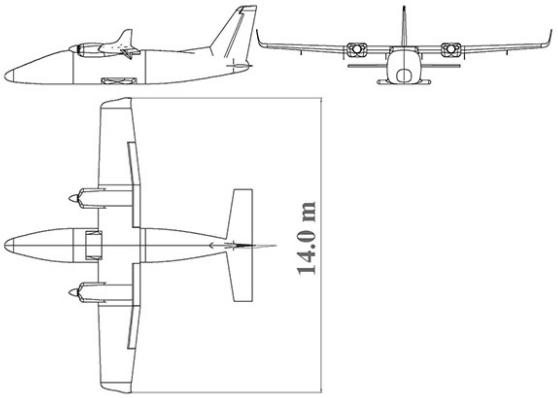

FIGURE 4.57: P2012 Geometry.

TABLE 4.23: P2012 results.

$C_{L_{\alpha_V}}$	2.160 rad^{-1}	
K_{F}	1.260	
K_{W}	0.953	
K_{Hp}	1.139	
K_{Hs}	1.022	
K_{H}	1.142	
K_{δ_r}	1.196	
$K_{\mathrm{F}}\, K_{\mathrm{W}}\, K_{\mathrm{H}}$	1.371	Δ from CFD
$C_{Y_{\beta_V}}$ VeDSC	0.362 $rad^{-}1$	4.5%
$C_{Y_{\beta_V}}$ DATCOM	0.249 $rad^{-}1$	34.0%
$C_{Y_{\beta_V}}$ ESDU	0.410 $rad^{-}1$	8.8%
$C_{Y_{\beta_V}}$ CFD	0.377 $rad^{-}1$	-

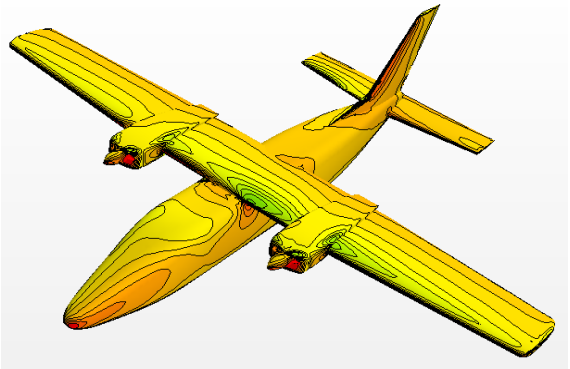

FIGURE 4.58: P2012 CFD Analysis. Navier-Stokes aerodynamic analysis performed at DII, $M = 0.1$, $Re = 1000000$, $\alpha = 0$ deg., $\beta = 10$ deg.

Chapter 5

Conclusions

The objectives reached with this research work have been to furnish useful methodologies, tools and guidelines for the aerodynamic design and optimization for future new turbopropeller and commuter aircraft with particular attention to aircraft performance.

A deep market analysis on the regional and commuter aircraft has revealed that nowadays the increase in oil price, the huge growth of air transport traffic and the increasing attention to the aircraft environmental footprint led to considerable interest of specialists in new configurations of regional and commuter transport aircraft. Also the major airlines in this segment have been demanding a replacement for many hundreds of heritage airplanes in the 20-150 seats categories currently in service around the world, as many are now coming to the end of their useful commercial life. The market challenges discussed above have constituted the motivations at the basis of this research work.

The research work has, therefore, achieved the objectives proposing the following tools and methodologies, giving aerodynamic guidelines and highlighting the effects on aircraft performance:

1. A fully embedded MATLab airfoil optimization tool, named AOT, has been carried out. Powerful and possibilities of the AOT have outlined the necessity to consider, also in a preliminary design phase, the need to use an optimization practice in the airfoil design. As a matter of fact the constrained-multi-objective optimization gives the capability to well define the operative space of an airfoil, by knowing the envelope of application. So, in the design of a typical airfoil for a regional turboprop aircraft, airfoil performance has been optimized in the entire flight envelope, subject to geometrical and aerodynamic design constraints. AOT is resulted very user friendly, tested and used also in other engineering fields applications and different users. Of course its use assumes a user knowledges of typical graduate engineer.

2. Some critical aircraft component design guidelines (aircraft nose, wing-fuselage junction, undercarriage vane) in a regional turboprop has been proposed through an aerodynamic optimization procedure, showing a zero lift drag coefficient reduction of about 4-5%. It is needful to consider these guidelines in the future preliminary design of new aircraft and, where it is possible, applied the optimization procedures to also improve aircraft performance. Maximum true airspeed or, conversely aircraft fuel consumption can be improved of about 2-3% on a typical 200 nautical miles mission. A free flight every 40 flights can be obtained through the application of the proposed optimization.

   Winglet adoption on these aircraft categories is becoming a main topic and in the author opinion is impossible give up them! An accurate design leads to performance improvements during the entire flight envelope, giving extremely improvements in climb performance. This performance is fundamental in commuter and tubopropeller aircraft for the operative and commercial success of the airplanes. Just think about a typical European route between north of Italy and south of Germany (which crosses the Alps mountain) some turbopropellers have route limitation due to their low OEI ceiling performance!

3. New more accurate Design Method for Vertical Tail Design Stability and Control, named VeDSC has been proposed.

   USAF DATCOM and ESDU, the most known semi-empirical methods, have been compared in parametric studies, giving close results for certain configurations, as the high-wing, T-tail turboprop, but results are quite different for other configurations, e.g. those providing the horizontal stabilizer mounted in fuselage, giving differences up to 20-40%. To perform with a higher level of accuracy and reliability the estimation of vertical tail contribution (including all interference effects highlighted by semi-empirical methods) several CFD analyses were planned on a modular configuration with different size and position of aircraft components. About 150 CFD analyses were executed to better understand the aerodynamic interference among aircraft components for configurations derived from a regional turboprop. Comparison between CFD results and semiempirical methods shows that both DATCOM and ESDU methodologies tend to overestimate (respect to CFD) the interference effects, especially those due to low-wing position and horizontal tailplane position.

   Therefore, the curves obtained by correlating CFD data can be considered as an accurate alternative approach respect to the classical semi-empirical procedures for the analysis and design of vertical

tailplane, especially in early conceptual design phase. The present approach can be considered particularly significant in case of general aviation or regional turboprop aircraft configurations. As a matter of fact the VeDSC method has been used in the preliminary design of the vertical tail of the new Tecnam P2012 commuter aircraft and on the preliminary design of a next generation of turboprop aircraft of 90 seats.

Future works will be focused on the experimental demonstrations of the numerical results obtained. In particular wind-tunnel investigations will be performed on a modular model to verify the aircraft components optimization and the vertical tail mehtod VeDSC.

The future large turbopropeller aircraft is necessary and the author does not view deep changes from the actual aircraft geometry. We like to see so...

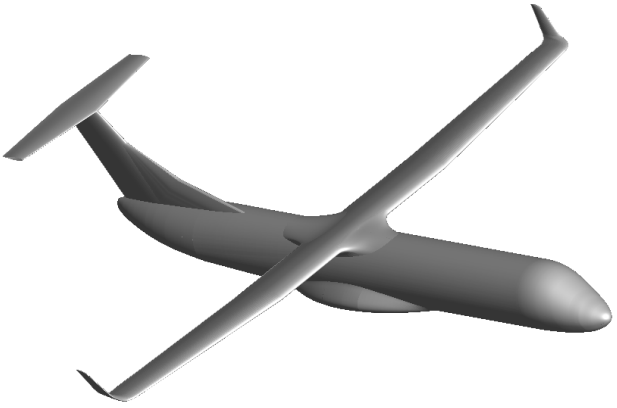

FIGURE 5.1: Future Large Turbopropeller

Appendix A

Airfoil Optimization Tool

Airfoil Optimization Tool is written in MATLab environment version 6.5 and following. In this appendix will be assumed to use AOT directly in MATLab environment, highlighting also the possibility to use the AOT as executable file with MATLab compiler runtime libraries. Airfoil Optimization Tool can be used via graphical user interface mode or via simple text files. Following sections briefly describe how to set the code to perform airfoil optimization in the above mentioned modes. AOT can be started by running the main function named Airfoil Optimization 1 0.m. Here the user has to choose if wants run an optimization via GUI or via text files by push on:

- Create Project by text file
- Create Project by GUI

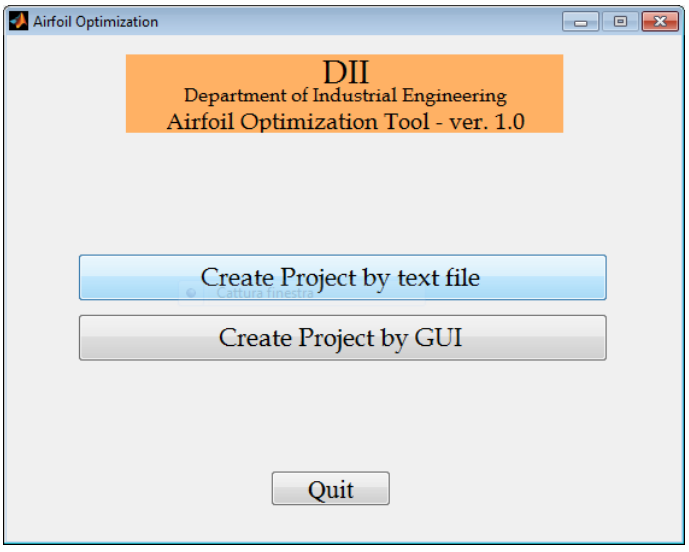

FIGURE A.1: AOT main GUI.

A.1 Input from GUI

If Create Project by GUI has been pushed in Fig. A.1, the import airfoil GUI will be open, as shown in Fig. A.2. By clicking on the Airfoil Import button, the user will choose the airfoil to optimize. The dialog

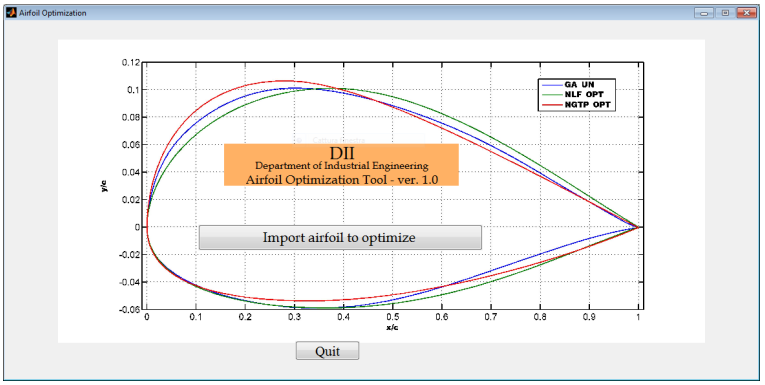

FIGURE A.2: AOT Import airfoil GUI.

window will open in the root path of the AOT code as shown in Fig. A.3, where airfoils to optimize can be previously stored. It has to be noted that airfoil to be optimized have to be written in double column, x, y coordinates, space separated without any names or string characters before coordinates as shown in Fig. A.4. Airfoil file extension have to be .txt.

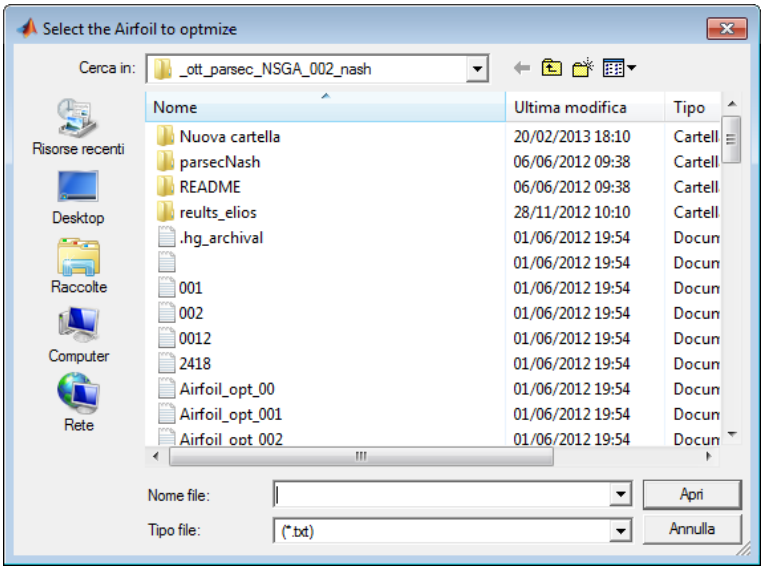

FIGURE A.3: AOT Airfoil to optimize dialog GUI.

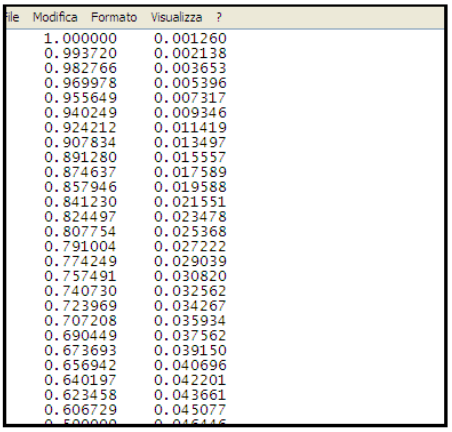

FIGURE A.4: Example of airfoil coordinates for AOT.

Once the airfoil has been choose, geometry parameterization technique have to be set as shown in Fig. A.5. Airfoil reconstruction can be chosen among:

- Bezier curves
- Legendre polynomials
- PARSEC Method

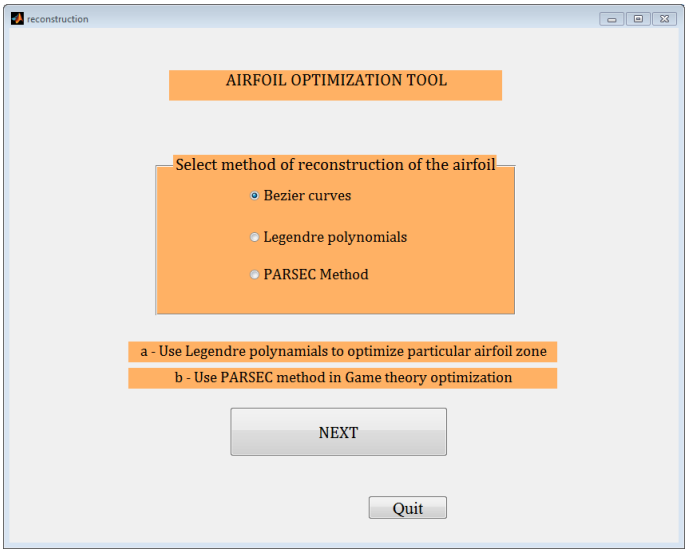

FIGURE A.5: AOT Parameterization method GUI.

Once checked the button of method of parameterization, by clicking on NEXT button AOT allows to set boundaries and constraints according to the chosen geometry parameterization. Boundaries and constraints

selections GUI are different according to the parameterization method but have the same 3 panels, as shown in Fig. A.6, Fig. A.9 and Fig. A.10:

1. airfoil graphics
2. boundaries settings
3. constraints settings

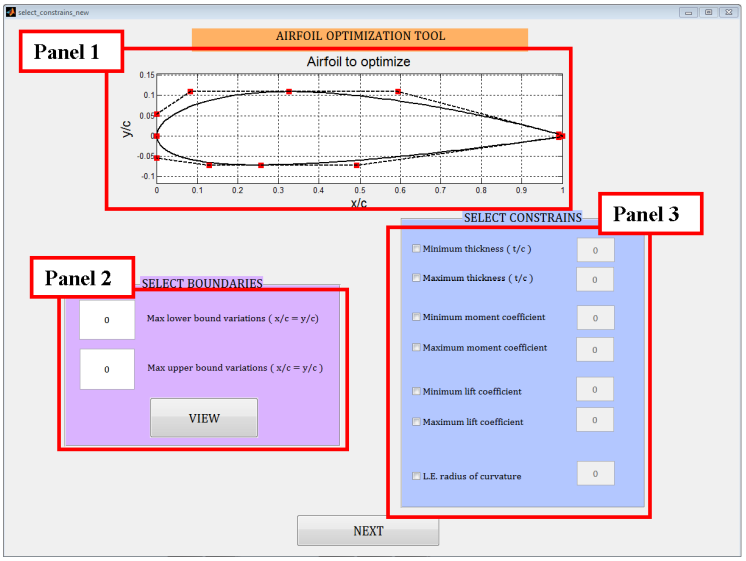

FIGURE A.6: AOT Boundaries and Constraints GUI.

In panel 1 the user can see the airfoil chosen to optimize. In panel 2 the user can select the boundaries and in panel 3 geometry and aerodynamic constraints can be settings. Panels 2 only is different among the three parameterization methods.

If Bezier curves parameterization has been chosen, the boundary conditions have to be set according to Fig. A.7 in panels 2. In particular the user has to insert:

- Max lower bound variation **with a minus sign**
- Max upper bound variation **with a plus sign**

Upper and Lower boundaries settings can then visualize (by clicking on the view button of panels 2) in the panels 1, as shown in Fig. A.7. Blue and red curves represent the maximum upper and maximum lower boundaries and the space between them is the space of geometry modifications. Unfeasible range of variation have to be avoided to not cause errors of the aerodynamic solvers. It has to noted that to avoid frequent errors in the Bezier curves parameterization technique some control points have

been blocked in one or both x and y direction and they are not visible to the user.

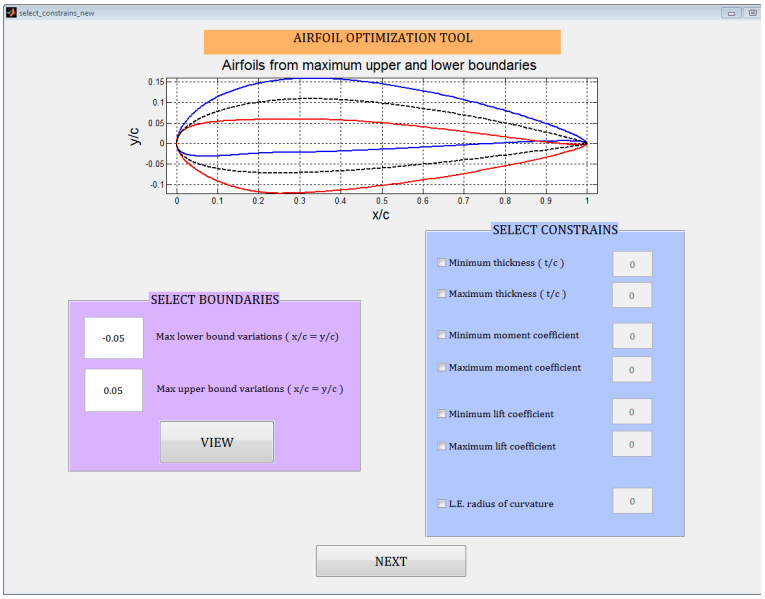

FIGURE A.7: AOT Details of Bezier boundary settings.

Panels 3 is the same for the three parameterization techniques. Here the user can or cannot choose to set the geometric and aerodynamic constraints, only one, two or all together by checking the box and then inserting the number of:

- Minimum airfoil thickness expressed as t/c
- Maximum airfoil thickness expressed as t/c
- Minimum pitching moment coefficient
- Maximum pitching moment coefficient
- Minimum lift coefficient
- Maximum lift coefficient
- Minimum leading edge radius of curvature expressed as $l.e._r/c$

Figure A.8 shows an example of two constraints enable by the user: minimum thickness and leading edge radius. The user can disable the previously enabled constraints simply removing the check in the box. It has to be noted that original airfoil leading edge radius is always calculated by the code and shown in the corresponding windows; this value can be useful as reference value if it wants to be constrained, otherwise it is not used.

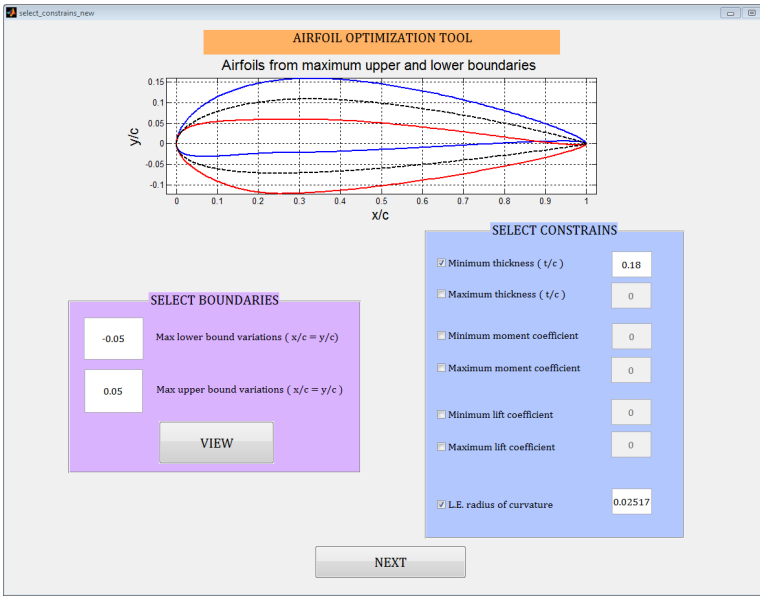

FIGURE A.8: AOT Details of constraints settings.

If Legendre polynomials parameterization has been chosen, the boundary conditions have to be set according to Fig. A.9 in panels 2. In particular the user has to insert:

- Airfoil Abscissa length to optimize **from 0.0 to 1.0**
- Max lower bound variation **with a minus sign**
- Max upper bound variation **with a plus sign**

Figure A.9 shows an example of Legendre boundary conditions settings where airfoil abscissa length optimization goes until 0.5 and lower and upper bound variations are respectively equal to -0.05 and 0.05 x/c. Panels 1 shows also the modifications range. Upper and lower boundary curves intersection has to be avoided to not cause aerodynamic solver errors.

If PARSEC parameterization has been chosen, the boundary conditions have to be set according to Fig. A.10 in panels 2. In particular the user has to insert the percentage of variation of control points that control:

- leading edge radius
- upper crest position in horizontal coordinates
- upper crest position in vertical coordinates
- upper crest curvature

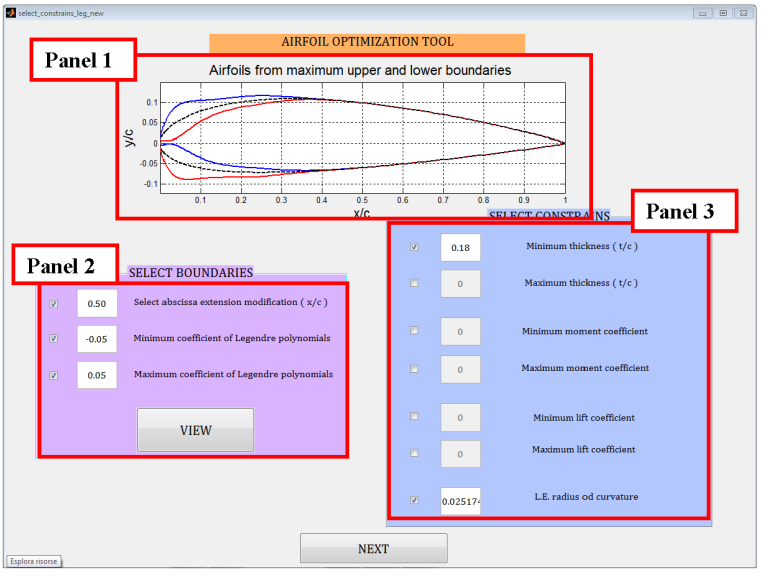

FIGURE A.9: AOT Details of Legendre boundary settings.

- lower crest position in horizontal coordinates
- lower crest position in vertical coordinates
- lower crest curvature
- trailing edge offset in vertical sense
- trailing edge thickness
- trailing edge direction
- trailing edge wedge angle

Figure A.10 shows an example of PARSEC boundary conditions settings where all the parameters have been settings to vary of 20% except for the trailing edge parameters equal to 0 to have a closed trailing edge. Panels 1 shows also the modifications range.

Once completely defined boundaries and constraints, the user has to click on NEXT button to choose the optimization algorithm as shown in Fig. A.11among

- genetic algorithm
- gradient based algorithm
- NashGA algorithm

Then click on the NEXT button to create the objective function. Objective function GUI is different between GA-GB algorithm and NashGA and they are presented in Fig. A.12 and Fig. A.13 respectively.

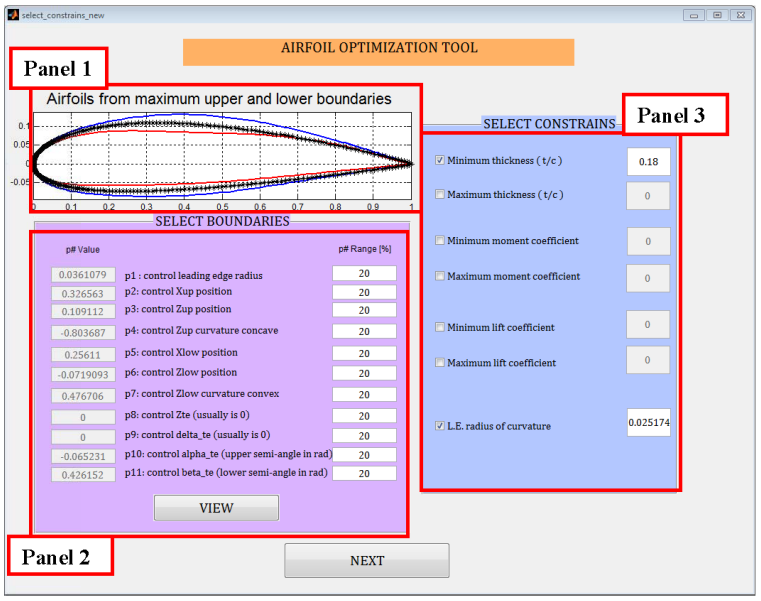

FIGURE A.10: AOT Details of PARSEC boundary settings.

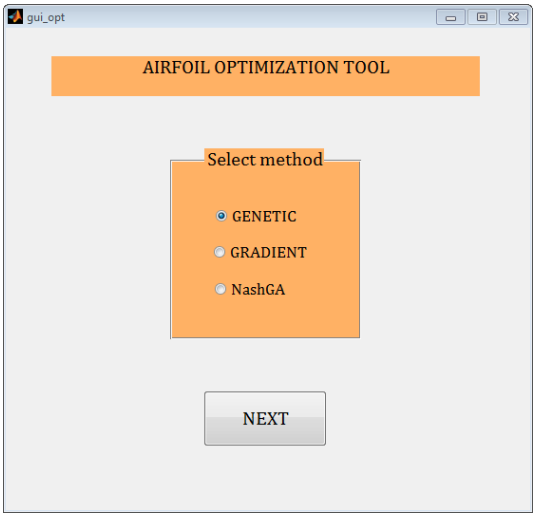

FIGURE A.11: AOT Optimization algorithm GUI.

Figure A.12 shows the objective function GUI used in multi-objective optimization with GA and GB algorithm. It is divided into 4 main sectors:

- Sector A: to set aerodynamic condition
- Sector B: to build the single objective function
- Sector C. to give the weight of the single objective function
- Sector D. to set the solver of the single objective function

For each condition to optimize the user has to complete all the 4 sectors.
In **sector A** the user has to set:

- α, angle of attack expressed in degrees
- Re, Reynolds number
- M, Mach number

In **sector B** the user has to build the single objective function by assigning the weight to:

- lift coefficient, C_l
- drag coefficient, C_d
- moment coefficient, C_m
- efficiency, C_l/C_d
- efficiency in climb, $C_l^{3/2}/C_d$
- target lift coefficient, $C_{l_{TARGET}}$
- target efficiency, E_{TARGET}

In **sector C** the user has to give the weight of the single condition. In **sector D** the user has to set the aerodynamic solver of the single condition among:

- Xfoil
- MSES
- Fluent

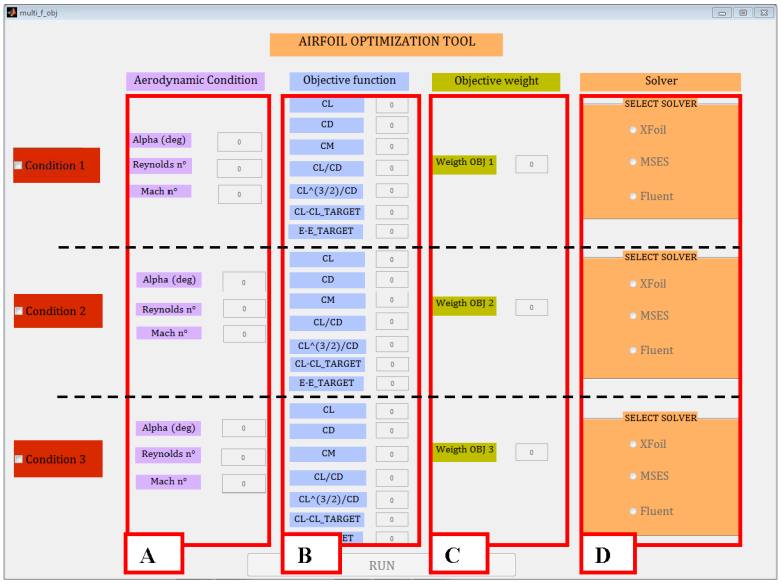

FIGURE A.12: AOT Objective function multi condition GUI for GA and GB algorithm.

Once completed the configuration of objective function through Fig. A.12, pushing on RUN button the optimization starts.

If NashGA optimization algorithm has been chosen, objective function has to be built according to Fig. A.13 GUI. In this GUI the user has to set: **sector A**

- α, angle of attack expressed in degrees
- Re, Reynolds number
- M, Mach number

sector B_1

- the objective function to assign to player 1
- the variables which can use player 1, according to parameterization

sector B_2

- the objective function to assign to player 2
- the variables which can use player 2, according to parameterization

sector C, the aerodynamic solver

- Xfoil
- MSES
- Fluent

FIGURE A.13: AOT Objective function single condition GUI for NashGA.

Finally the optimization starts, pushing on RUN button.

A.2 Input from file

AOT can be also used via batch mode by setting an input text file to avoid recursive operations necessary in the GUI mode. The file has to be properly configured, pay attention on name, space and positions. The text files allow to configure all the settings previously described in Sec. A.1. Here an example of text file is shown and following described. The text file useful to configure the AOT has to be in the same directory of the main root of the tool and its name has to be "AOT text settings.txt". Figure A.14 shows an example of text configuration file. In particular the user has to set seven text lines:

1. The name of the airfoil (NACA23015.txt).
2. The parameterization technique
   (BEZ = Bezier curves; LEG = Legendre polynomials; PAR = PARSEC Method).
3. The boundary range (Different according to parameterization).
4. The aerodynamic and geometry constraints.
5. The optimization algorithm (GE = Genetic algorithm; GR = Gradient based; NASH = NashGA algorithm).
6. The number of case/cases to optimize.
7. The flow condition, objective function and aerodynamic solver for each case. In particular the last number (3 in the example file) represents the aerodynamic solver settings (1=Xfoil; 2=Mses; 3= Fluent).

```
Airfoil coordinate:
                NACA23015.txt

Geometry parameterization:
                BEZ

Boundary:       lower   upper
                -0.01   0.01

Constraints:    min.thick max thick min.cm  max.cm min.cl max.cl l.e.radius
                0         0         0       0      0      0      0

Algorithm:
        GE

Conditions and Objectives:
objective
1

alpha Re        M   Wcl Wcd Wcm Wce Wcec Wcltg Wetg  Wobj solver
0.0   2000000   0.1 1   0   0   0   0    0     0     1    3
```

FIGURE A.14: AOT Text file configuration, example of settings.

A.3 AOT Output

The AOT output is the same for both GUI or text file mode. In particular the following files and figures will be saved:

1. Iteration results.txt.
   This is the most important file. It contains all the results for each iteration in terms of aerodynamic coefficients and airfoil.
2. original airfoil.txt
   It contains the initial airfoil coordinates used to start the optimization process.
3. optimized airfoil.txt
   It contains the optimized airfoil coordinates at the end of the optimization process.
4. Original result.txt
   It contains the Xfoil original aerodynamic results at prescribed flow condition within α range variation 0 to 10 deg.
5. Optimized result.txt
   It contains the Xfoil optimal aerodynamic results at prescribed flow condition within α range variation 0 to 10 deg.
6. Xfoil and/or Mses and or Fluet settings.txt It contains the Xfoil, Mses or Fluent settings of the analysis.
7. seven matlab figures (see Fig. A.15) which are: fitness function.fig, airfoil compare.fig, cl alpha.fig, cd alpha.fig, cm alpha .fig, cp 2deg.fig cp 5 deg.fig.

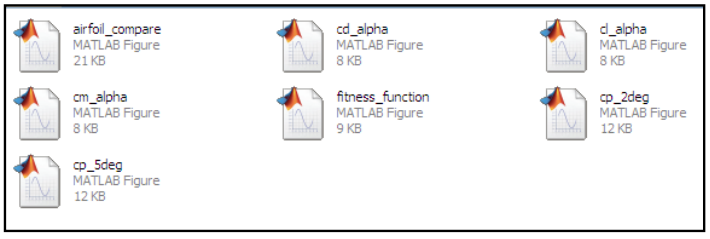

FIGURE A.15: AOT Output figures.

Appendix B

VeDSC - Tables of configurations

Unless otherwise stated, the data refers to the following conditions, for the Vertical tail plane without rudder control surface

$\alpha = 0°$

$\beta = 5°$

$M = 0$

$Re = 1000000$

$A = 10$, $A_v = 2$ (for complete airplane).

Vertical tail without rudder configurations

ID	*abbr.*	*parameters*	*notes*	C_{Y_v}
1	V	$A_v = 0.5$	CFD model	0.0073
2	V	$A_v = 1.0$	CFD model	0.0194
3	V	$A_v = 1.5$	CFD model	0.0322
4	V	$A_v = 2.0$	CFD model	0.0451
5	V	$A_v = 0.5$ $\beta = 10°$	CFD model	0.0156
6	V	$A_v = 1.0$ $\beta = 10°$	CFD model	0.0404
7	V	$A_v = 1.5$ $\beta = 10°$	CFD model	0.0667
8	V	$A_v = 2.0$ $\beta = 10°$	CFD model	0.0918
9	V	$A_v = 0.25$	Straight vertical tail	0.0030
10	V	$A_v = 0.5$	Straight vertical tail	0.0085
11	V	$A_v = 1.0$	Straight vertical tail	0.0263
12	V	$A_v = 1.5$	Straight vertical tail	0.0507
13	V	$A_v = 2.0$	Straight vertical tail	0.0796
14	V	$A_v = 2.5$	Straight vertical tail	0.1111
15	V	$A_v = 0.25$ $\beta = 10°$	Straight vertical tail	0.0065
16	V	$A_v = 0.5$ $\beta = 10°$	Straight vertical tail	0.0181
17	V	$A_v = 1.0$ $\beta = 10°$	Straight vertical tail	0.0549
18	V	$A_v = 1.5$ $\beta = 10°$	Straight vertical tail	0.1045
19	V	$A_v = 2.0$ $\beta = 10°$	Straight vertical tail	0.1625
20	V	$A_v = 2.5$ $\beta = 10°$	Straight vertical tail	0.2256

Continued...

ID	*abbr.*	*parameters*	*notes*	C_{Y_v}
21	V	$b_v = 0.05$ $\lambda_v = 0.62$	Constant taper ratio	0.0026
22	V	$b_v = 0.10$ $\lambda_v = 0.62$	Constant taper ratio	0.0077
23	V	$b_v = 0.20$ $\lambda_v = 0.62$	Constant taper ratio	0.0238
24	V	$b_v = 0.30$ $\lambda_v = 0.62$	Constant taper ratio	0.0454
25	V	$b_v = 0.40$ $\lambda_v = 0.62$	Constant taper ratio	0.0705
26	V	$b_v = 0.50$ $\lambda_v = 0.62$	Constant taper ratio	0.0979
27	V	$b_v = 0.05$ $\beta = 10^\circ$	Constant taper ratio	0.0055
28	V	$b_v = 0.10$ $\beta = 10^\circ$	Constant taper ratio	0.0163
29	V	$b_v = 0.20$ $\beta = 10^\circ$	Constant taper ratio	0.0495
30	V	$b_v = 0.30$ $\beta = 10^\circ$	Constant taper ratio	0.0932
31	V	$b_v = 0.40$ $\beta = 10^\circ$	Constant taper ratio	0.1433
32	V	$b_v = 0.50$ $\beta = 10^\circ$	Constant taper ratio	0.1975
33	BV	$A_v = 0.5$	Body-vertical, CFD model	0.0107
34	BV	$A_v = 1.0$	Body-vertical, CFD model	0.0262
35	BV	$A_v = 1.5$	Body-vertical, CFD model	0.0417
36	BV	$A_v = 2.0$	Body-vertical, CFD model	0.0564
37	BV	$A_v = 2.0$ $\beta = 10^\circ$	Body-vertical, CFD model	0.1076
38	BV	$A_v = 0.25$	Body-vertical, straight vertical tail	0.0047
39	BV	$A_v = 0.5$	Body-vertical, straight vertical tail	0.0123
40	BV	$A_v = 1.0$	Body-vertical, straight vertical tail	0.0345
41	BV	$A_v = 1.5$	Body-vertical, straight vertical tail	0.0615
42	BV	$A_v = 2.0$	Body-vertical, straight vertical tail	0.0942
43	BV	$A_v = 2.5$	Body-vertical, straight vertical tail	0.1267
44	BV	$b_v = 0.05$ $A_v = 0.40$	Body-vertical, constant taper ratio	0.0043
45	BV	$b_v = 0.10$ $A_v = 0.80$	Body-vertical, constant taper ratio	0.0115
46	BV	$b_v = 0.20$ $A_v = 1.59$	Body-vertical, constant taper ratio	0.0313
47	BV	$b_v = 0.30$ $A_v = 2.39$	Body-vertical, constant taper ratio	0.0557
48	BV	$b_v = 0.40$ $A_v = 3.19$	Body-vertical, constant taper ratio	0.0822
49	BV	$b_v = 0.50$ $A_v = 3.98$	Body-vertical, constant taper ratio	0.1123
50	WBV	$A = 6$ $A_v = 1.0$	Wing-body-vertical, high wing	0.0248
51	WBV	$A = 8$ $A_v = 1.0$	Wing-body-vertical, high wing	0.0246
52	WBV	$A = 10$ $A_v = 1.0$	Wing-body-vertical, high wing	0.0246
53	WBV	$A = 12$ $A_v = 1.0$	Wing-body-vertical, high wing	0.0242
54	WBV	$A = 14$ $A_v = 1.0$	Wing-body-vertical, high wing	0.0245

Continued...

ID	*abbr.*	*parameters*	*notes*	C_{Y_v}
55	WBV	$A = 16 \quad A_v = 1.0$	Wing-body-vertical, high wing	0.0240
56	WBV	$A = 6 \quad A_v = 2.0$	Wing-body-vertical, high wing	0.0536
57	WBV	$A = 8 \quad A_v = 2.0$	Wing-body-vertical, high wing	0.0521
58	WBV	$A = 10 \quad A_v = 2.0$	Wing-body-vertical, high wing	0.0526
59	WBV	$A = 12 \quad A_v = 2.0$	Wing-body-vertical, high wing	0.0528
60	WBV	$A = 14 \quad A_v = 2.0$	Wing-body-vertical, high wing	0.0525
61	WBV	$A = 16 \quad A_v = 2.0$	Wing-body-vertical, high wing	0.0517
62	WBV	$A = 6 \quad A_v = 1.0$	Wing-body-vertical, mid wing	0.0262
63	WBV	$A = 8 \quad A_v = 1.0$	Wing-body-vertical, mid wing	0.0263
64	WBV	$A = 10 \quad A_v = 1.0$	Wing-body-vertical, mid wing	0.0263
65	WBV	$A = 12 \quad A_v = 1.0$	Wing-body-vertical, mid wing	0.0263
66	WBV	$A = 14 \quad A_v = 1.0$	Wing-body-vertical, mid wing	0.0260
67	WBV	$A = 16 \quad A_v = 1.0$	Wing-body-vertical, mid wing	0.0261
68	WBV	$A = 6 \quad A_v = 2.0$	Wing-body-vertical, mid wing	0.0262
69	WBV	$A = 8 \quad A_v = 2.0$	Wing-body-vertical, mid wing	0.0263
70	WBV	$A = 10 \quad A_v = 2.0$	Wing-body-vertical, mid wing	0.0263
71	WBV	$A = 12 \quad A_v = 2.0$	Wing-body-vertical, mid wing	0.0263
72	WBV	$A = 14 \quad A_v = 2.0$	Wing-body-vertical, mid wing	0.0260
73	WBV	$A = 16 \quad A_v = 2.0$	Wing-body-vertical, mid wing	0.0261
74	WBV	$A = 6 \quad A_v = 1.0$	Wing-body-vertical, low wing	0.0275
75	WBV	$A = 8 \quad A_v = 1.0$	Wing-body-vertical, low wing	0.0270
76	WBV	$A = 10 \quad A_v = 1.0$	Wing-body-vertical, low wing	0.0272
77	WBV	$A = 12 \quad A_v = 1.0$	Wing-body-vertical, low wing	0.0270
78	WBV	$A = 14 \quad A_v = 1.0$	Wing-body-vertical, low wing	0.0271
79	WBV	$A = 16 \quad A_v = 1.0$	Wing-body-vertical, low wing	0.0266
80	WBV	$A = 6 \quad A_v = 2.0$	Wing-body-vertical, low wing	0.0578
81	WBV	$A = 8 \quad A_v = 2.0$	Wing-body-vertical, low wing	0.0582
82	WBV	$A = 10 \quad A_v = 2.0$	Wing-body-vertical, low wing	0.0569
83	WBV	$A = 12 \quad A_v = 2.0$	Wing-body-vertical, low wing	0.0571
84	WBV	$A = 14 \quad A_v = 2.0$	Wing-body-vertical, low wing	0.0564
85	WBV	$A = 16 \quad A_v = 2.0$	Wing-body-vertical, low wing	0.0571
86	WBV	$A = 10 \quad A_v = 2.0$	Wing-body-vertical, high wing	0.1055
87	WBV	$A = 10 \quad A_v = 2.0$	Wing-body-vertical, mid wing	0.1078
88	WBV	$A = 10 \quad A_v = 2.0$	Wing-body-vertical, low wing	0.1093
89	WBVH	$h1$	Complete, mid wing, horizontal in fuselage, centered	0.0631
90	WBVH	$h2p$	Complete, mid wing, horizontal near fuselage, centered on fin chord	0.0552
91	WBVH	$h2$	Complete, mid wing, horizontal low on fin, centered on fin chord	0.0541

Continued...

ID	*abbr.*	*parameters*	*notes*	C_{Y_v}
92	WBVH	$h3$	Complete, mid wing, horizontal middle on fin, centered on fin chord	0.0552
93	WBVH	$h4$	Complete, mid wing, horizontal high on fin, centered on fin chord	0.0577
94	WBVH	$h5$	Complete, mid wing, horizontal tip-mounted, centered on fin chord	0.0639
95	WBVH	$h1f$	Complete, mid wing, horizontal in fuselage, forward	0.0601
96	WBVH	$h2pf$	Complete, mid wing, horizontal near fuselage, forward on fin chord	0.0526
97	WBVH	$h2f$	Complete, mid wing, horizontal low on fin, forward on fin chord	0.0530
98	WBVH	$h3f$	Complete, mid wing, horizontal middle on fin, forward on fin chord	0.0548
99	WBVH	$h4f$	Complete, mid wing, horizontal high on fin, forward on fin chord	0.0577
100	WBVH	$h5f$	Complete, mid wing, horizontal tip-mounted, forward on fin chord	0.0640
101	WBVH	$h1r$	Complete, mid wing, horizontal in fuselage, rearward on fin chord	0.0632
102	WBVH	$h2pr$	Complete, mid wing, horizontal near fuselage, rearward on fin chord	0.0561
103	WBVH	$h2r$	Complete, mid wing, horizontal low on fin, rearward on fin chord	0.0549
104	WBVH	$h3r$	Complete, mid wing, horizontal middle on fin, rearward on fin chord	0.0547
105	WBVH	$h4r$	Complete, mid wing, horizontal high on fin, rearward on fin chord	0.0571
106	WBVH	$h5r$	Complete, mid wing, horizontal tip-mounted, rearward on fin chord	0.0642
107	WBVH	$h1$	Complete, high wing, horizontal body-mounted, centered on fin chord	0.0608
108	WBVH	$h1$	Complete, low wing, horizontal body-mounted, centered on fin chord	0.0638

Continued...

ID	*abbr.*	*parameters*	*notes*	C_{Y_v}
109	WBVH	$h1 \quad \beta = 10^\circ$	Complete, high wing, horizontal body-mounted, centered on fin chord	0.1198
110	WBVH	$h1 \quad \beta = 10^\circ$	Complete, low wing, horizontal body-mounted, centered on fin chord	0.1243
111	WBVH	$h5$	Complete, high wing, horizontal tip-mounted, centered on fin chord	0.0607
112	WBVH	$h5$	Complete, low wing, horizontal tip-mounted, centered on fin chord	0.0665
113	WBVH	$h5 \quad \beta = 10^\circ$	Complete, high wing, horizontal tip-mounted, centered on fin chord	0.1180
114	WBVH	$h5 \quad \beta = 10^\circ$	Complete, low wing, horizontal tip-mounted, centered on fin chord	0.1204
115	WBVH	$S_h/S_v = 0.24$	Complete, mid wing, horizontal in fuselage, centered	0.0592
116	WBVH	$S_h/S_v = 0.47$	Complete, mid wing, horizontal in fuselage, centered	0.0603
117	WBVH	$S_h/S_v = 1.39$	Complete, mid wing, horizontal in fuselage, centered	0.0638
118	WBVH	$S_h/S_v = 2.17$	Complete, mid wing, horizontal in fuselage, centered	0.0651
119	WBVH	$S_h/S_v = 0.24$	Complete, mid wing, horizontal tip-mounted, centered on fin chord	0.0615
120	WBVH	$S_h/S_v = 0.47$	Complete, mid wing, horizontal tip-mounted, centered on fin chord	0.0626
121	WBVH	$S_h/S_v = 1.39$	Complete, mid wing, horizontal tip-mounted, centered on fin chord	0.0647
122	WBVH	$S_h/S_v = 2.17$	Complete, mid wing, horizontal tip-mounted, centered on fin chord	0.0664
123	VH	$A_v = 1.0$	Vertical + Horizontal, T-tail	0.0253
124	VH	$A_v = 1.5$	Vertical + Horizontal, T-tail	0.0394
125	VH	$A_v = 2.0$	Vertical + Horizontal, T-tail	0.0521

Unless otherwise stated, the data refers to the following conditions, for the Vertical tail plane with rudder control surface

$\alpha = 0°$

$M = 0$

$Re = 1000000$

$A = 10.$

Vertical tail with rudder configurations

ID	*Config.*	*Notes*	A_v	δ_r	β	C_{Y_v}
1	V	-	2	5	0	0.0338
2	V	-	2	5	5	0.0799
3	V	-	2	5	10	0.1290
4	V	-	2	10	0	0.0682
5	V	-	2	10	5	0.1168
6	V	-	2	10	10	0.1626
7	V	-	2	15	0	0.1026
8	V	-	2	15	5	0.1529
9	V	-	2	15	10	0.2022
10	V	-	2	20	0	0.1357
11	V	-	2	20	5	0.1861
12	V	-	2	20	10	0.2342
13	BV	-	2	10	0	0.0751
14	BV	-	2	10	5	0.1310
15	BV	-	2	10	10	0.1754
16	WBV	mid wing	2	10	0	0.0750
17	WBV	mid wing	2	10	5	0.1324
18	WBV	mid wing	2	10	10	0.1789
19	WBV	high wing	2	10	0	0.0768
20	WBV	high wing	2	10	5	0.1299
21	WBV	high wing	2	10	10	0.1806
22	WBV	low wing	2	10	0	0.0758
23	WBV	low wing	2	10	5	0.1341
24	WBV	low wing	2	10	10	0.1816
25	WBVH	mid wing, body tail	2	10	0	0.0807
26	WBVH	mid wing, body tail	2	10	5	0.1436
27	WBVH	mid wing, body tail	2	10	10	0.1945
28	WBVH	high wing, body tail	2	10	0	0.0807
29	WBVH	high wing, body tail	2	10	5	0.1428
30	WBVH	high wing, body tail	2	10	10	0.1984
31	WBVH	low wing, body tail	2	10	0	0.0805

Continued...

ID	*Config.*	*Notes*	A_v	δ_r	β	C_{Y_v}
32	WBVH	low wing, body tail	2	10	5	0.1467
33	WBVH	low wing, body tail	2	10	10	0.2027
34	WBVH	mid wing, T-tail	2	10	0	0.0852
35	WBVH	mid wing, T-tail	2	10	5	0.1454
36	WBVH	mid wing, T-tail	2	10	10	0.1941
37	WBVH	high wing, T-tail	2	10	0	0.0865
38	WBVH	high wing, T-tail	2	10	5	0.1441
39	WBVH	high wing, T-tail	2	10	10	0.1917
40	WBVH	low wing, T-tail	2	10	0	0.0846
41	WBVH	low wing, T-tail	2	10	5	0.1476
42	WBVH	low wing, T-tail	2	10	10	0.1950
43	V	-	1	10	0	0.0303
44	BV	-	1	10	0	0.0348
45	WBV	mid wing	1	10	0	0.0350
46	WBV	high wing	1	10	0	0.0350
47	WBV	low wing	1	10	0	0.0352
48	WBVH	mid wing, body tail	1	10	0	0.0379
49	WBVH	high wing, body tail	1	10	0	0.0379
50	WBVH	low wing, body tail	1	10	0	0.0375
51	WBVH	mid wing, T-tail	1	10	0	0.0416
52	WBVH	high wing, T-tail	1	10	0	0.0419
53	WBVH	low wing, T-tail	1	10	0	0.0425

Bibliography

[1] Forecast International Inc. The market for regional transport aircraft. (Product code F612), 2010.

[2] Special Convention RAA News. Regional horizons. *RAA Annual Convention*, Milwaukee, Wisconsin, May 2010.

[3] Bombardier Aerospace Commercial Aircraft Market Forecast. Commercial aircraft market forecast 2012-2031. 2012. URL http://www2.bombardier.com/en/3_0/3_8/market_forecast.

[4] U.S. Energy Information Administration. International energy outlook 2011. (DOE/EIA-0484(2011)), September 2011.

[5] Bureau of Transportaion Statistics. 3rd-quarter 2011 airline financial data: Network airlines, low-cost airlines and regional airlines all report profits. BTS 11-12, March 2012.

[6] L. Lombardi. ATR, program review and market outlook. *10th EWADE Conference*, (ISBN 978-88-906484-1-0), Naples, May 2011.

[7] C. R. Frlschtak. Learning, technical progress and competitiveness in the commuter aircraft industry: an analysis of embraer. *The World Bank Industry and Energy Department, OSP*, (11195), June,15 1992.

[8] A. Zizolfi. Atr product overview. *10th EWADE Conference*, (ISBN 978-88-906484-1-0), Naples, May 2011.

[9] J. Roskam. Preliminary calculation of aerodynamic, thrust and power characteristics. *DARcoporation*, Airplane Design, Part VI(2nd Edition), Lawrence, Kansas, 2000.

[10] D. P. Raymer. Aircraft design: A conceptual approach. *AIAA Education Series*, (3rd Edition), Reston, Virginia, 1999.

[11] J. Roskam and C. T. E. Lan. Airplane aerodynamics and performance. *DARcoporation*, (ISBN 1-884885-44-6), 1st Edition Lawrence, Kansas, 1997.

[12] F. Nicolosi, A. De Marco, and P. Della Vecchia. Flight tests of a twin-engine flight aircraft: performances, stability and parameter estimation. (20th AIDAA Congress), June-July 2009.

[13] F. Nicolosi, A. De Marco, and P. Della Vecchia. Flight tests, performances, and flight certification of a twin-engine light aircraft. *Journal of Aircraft*, 48(1):177–193, January 2011.

[14] F. Nicolosi and P. Della Vecchia. Aerodynamic guidelines in the design and optimization of new regional turboprop aircraft. *3rd CEAS and 21st AIDAA Congress*, (ISBN: 9788896427187):577–587, 24-28 October 2011.

[15] F. Nicolosi, P. Della Vecchia, and S. Corcione. Aerodynamic analysis and design of a twin engine commuter aircraft. *28th ICAS Conference*, (ISBN: 9780956533319), 23-28 September 2012.

[16] E. Daniele, A. De Fenza, and P. Della Vecchia. Conceptual adaptive wing tip design for pollution reductions. *Journal of Intelligent Material Systems and Structures*, 23(11):16, DOI: 10.1177/1045389X12445030 2012.

[17] W. K. Song and A. J. Keane. A study of shape parameterisation methods for airfoil optimisation. *10th AIAA/ISSMO Multidisciplinary Analysis and Optimization Conference*, (AIAA 2004-4482), 30 August - 4 September 2004.

[18] E. K. P. Chong and S. K. Zak. An introduction to optimization. *Wiley*, 2001.

[19] P. Pedregal. Introduction to optimization. *Springer*, 2004.

[20] M. Mitchell. An introduction to genetic algorithms. *MIT Press*, 1999.

[21] J. Dreo, A. Petrowski, P. Siarry, and E. Taillard. Metaheuristics for hard optimization. *Springer*, 2006.

[22] J. A. Samareh. A survey of shape parameterization techniques. *CEAS/AIAA/ICASE/NASA Langley International Forum on Aeroelasticity and Structural Dynamics*, June 22-25 1999.

[23] R. M. Hicks and G. N. Vanderplaats. Applications of numerical optimization to the design of low-speed airfoil. *NASA TM X-3213*, March 1975.

[24] Q. Ruizhan and Z. Ziqiang. A variable fidelity optimization framework using second-order multi-point additive scaling functions applied to airfoil design. *25th ICAS Conference*, 3-8 September 2006.

[25] M. Khurana. Airfoil geometry parameterization through shape optimizer and computational fluid dynamics. *46th AIAA Aerospace Sciences Meeting and Exhibit*, 7th-10th January 2008.

[26] R. W. Derksen and T. Rogalsky. Bezier-parsec: An optimized aerofoil parameterization for design. *Advances in Engineering Software*, (41): 923–930, 2010.

[27] F. Grasso. Multi-objective numerical optimization applied to aircraft design. *PhD thesis in Aerospace Engineering, Department of Aerospace Engineering, University of Naples Federico II*, 2008.

[28] R. M. Hicks and P. A. Henne. Wing design by numerical optimization. *Journal of Aircraft*, 15(7):407–412, 1978.

[29] H. Sobieczky. Geometry generator for cfd and applied aerodynamics. *Courses and Lecture International*, 1997.

[30] H. Sobieczky. Parametric airfoils and wings. *K. Fujii, G. S. Dulikravich (Ed.), Notes on Numerical Fluid Mechanics*, 68:7–88, 1998.

[31] E. D'Amato, E. Daniele, L. Mallozzi, G. Petrone, and S. Tancredi. A hierarchical multi-modal hybrid stackelberg-nash ga for a leader with multiple followers game. *Dynamics of Information Systems: Mathematical Foundations, Springer*, (ISBN 9781461439059):267–280, 2012.

[32] E. D'Amato, E. Daniele, L. Mallozzi, and G. Petrone. Three level hierarchical decision making model with ga. *Engineering Computations. Emerald Group Publishing Limited*, 2012.

[33] S. Tancredi, E. D'Amato, E. Daniele, P. Della Vecchia, and G. Petrone. A nash equilibrium-genetic algorithm optimization code for structural problems. test case: an aluminum plate subjected to low velocity impact events. *2010 ENGINSOFT International Conference*, 21-22 October 2010.

[34] Z. Tang and J. A. Desideri. Multicriterion aerodynamic shape design optimization and inverse problems using control theory and nash games. *Journal of Otimization Theory and Applications*, (135):599–622, 2007.

[35] M. Drela. Xfoil: An analyse and design system for low reynolds number airfoils. *Low Reynolds Number Aerodynamics, Springer Verlag Lecture Notes in Engineering*, 54, 1989.

[36] M. Drela. Xfoil 6.94 user guide. *MIT Department of Aeronautics and Astronautics*, December 2001.

[37] M. Drela. A user's guide to mses 3.05. *MIT Department of Aeronautics and Astronautics*, July 2007.

[38] I. H. Abbott and A.E. Von Doenhoff. Theory of wing sections: Including a summary of airfoil data. (ISBN 978-0486605869), 1959.

[39] R. Simson. Junction flows. *Annual Review of Fluid Mechanics*, 33, 2001.

[40] S. F. Hoerner. Fluid dynamic drag. *Hoerner Fluid Dynamics*, 1965.

[41] H. Schlichting and E. Truckenbrodt. Aerodynamics of the aeroplane. *McGraw Hill*, 2nd edition 1979.

[42] S. Siegel. Comparison of design rules regarding the wing-body junction flow of a subsonic aircraft. *University of Technology Dresden*, Dep. of Aerodynamics, 30 June 2011.

[43] E. Jacobs and K. Ward. Interference of wing and fuselage from tests of 209 combinations in the naca variable-density test tunnel. *NACA Technical Report No. 540*, 1935.

[44] H. Muttray. Aerodynamic aspects of wing-fuselage
llets. *NACA Technical Memorandum No.764*, 1935.

[45] J. Fleming, R. Simpson, J. Cowling, and W. Devenport. An experimental study of a turbulent wing-body junction and wake flow. *Experiments in Fluids*, 14, 1993.

[46] S. Oelcmen and R. Simpson. Some structural features of a turbulent wing-body junction vortical flow. *Report No. VPI-AOE-238*, Virginia Polytechnic Institute and State University Blackburg, 1996.

[47] L. M. M. Boermans, F. Nicolosi, and K. Kubrynski. Aerodynamic design of high perormance sailplane wing fuselage combinations. *21st ICAS Conference*, Paper No.A98-31523(ISBN-10:1-56347-287-2), 13 -18 September 1998.

[48] J. A. White and Manley M. J. Hood. Wing-fuselage interference tail buffeting and air flow about the tail of a low wing monoplatet. *NACA Technical Report No.482*, 1933.

[49] M. Maughmer, D. Hallmann R. Ruszkowski G. Chappel, and I. Waitz. Experimental investigations of wing-fuselage integration geometries. *AIAA Journal of Aircraft*, 26(8), 1989.

[50] J. Vassber, A. Sclafani, and M. DeHaan. A wing-body fairing design for the dlr-f6 model: A dpw-iii case study. *AIAA Conference paper 2005-4730*, 2005.

[51] P. Della Vecchia and S. Serino. Aerodynamic analysis and optimization of a regional transport aircraft. *AIAA Pegasus Conference*, page 11, April 2010.

[52] A. D. Young. The calculation of total and skin friction drag of bodies of revolution at zero incidence. *ARC R-M 1874*, April 1939.

[53] L. Pascale and F. Nicolosi. Design and aerodynamic analysis of a light twin-engine propeller aircraft. *26th ICAS Conference*, Anchorage, Alaska (ISBN: 9781605607153), 14-19 September 2008.

[54] L. Piegl and W. Tiller. Curve and surface constructions using rational b-splines. *Computer-Aided Design*, 19(9):14, November 1987.

[55] L. Piegl and W. Tiller. The nurbs book. *Springer-Verlag (Berlin)*, (ISBN: 3-540-61545-8.), 2nd Edition 1997.

[56] K. J. Versprille. Computer-aided design applications of the rational b-spline approximation form. *Doctoral dissertation, Syracuse University*, Syracuse, N.Y., 1975.

[57] D. F. Rogers and J. A. Adams. Mathematical elements for computer graphics. *McGraw-Hill (New York)*, 1st ed. 1976.

[58] F. Sessa. Modellazione geometrica: principi teorici ed applicazioni all'ingegneria navale. *Tesi di dottorato in Ingegneria Navale*, (3 ciclo, BN 2002-3376T), UniversitÃ degli studi di Napoli 2002.

[59] J. D. Foley, A. van Dam, S. K. Feiner, and J. F. Hughes. Computer graphics: Principles and practice in c. *Addison-Wesley Professional*, (ISBN-10: 0-201-84840-6), 4 August 1996.

[60] G. Becker, , and M. Schafer. An advanced nurbs fitting procedure for post-processing of grid-based shape optimizations. *49th AIAA Aerospace Sciences Meeting*, 4-7 January 2011.

[61] L. Piegl. On nurbs : A survey. *IEEE, University of South Florida*, (DOI:0272-17-16/91/0100-0055-01.00), August 1991.

[62] L. M. M. Boermans and F. Nicolosi. Sailplane fuselage and wing-fuselage junction design. *XXV Ostiv Congress*, (S. Auban France), 3-11 July 1997.

[63] D. P. Coiro and F. Nicolosi. Design of natural laminar flow fuselages. *19th ICAS Conference*, (Anaheim, California), 18-23 September 1994.

[64] L. M. M. Boerman and D. C. Terleth. Wind tunnel tests of eight sailplane fuselage conbinations. *Technical Soaring*, 3(3), 1984.

[65] E. Obert. Aerodynamic design of trasport aircraft. *IOS Press TUDelft Amsterdam*, (1st ed.), 2009.

[66] B. S. De Mattos, R. Papa, and L. C. de Castro. Considerations about forward fuselage aerodynamic design of a transport aircraft. *42nd AIAA Aerospace Sciences Meeting and Exhibit, AIAA 2004-1241*, (Reno, Nevada), 5-8 January 2004.

[67] EASA. Certification specifications and acceptable means of compliance for large aeroplanes cs-25. *European Aviation Safety Agency*, (Amendment 11), 4 July 2011.

[68] G. S. Langevin and P. Overbey. Concept to reality: Winglets. *NASA Langley Research Center*, Hampton, VA 2003.

[69] V. J. Burnelli. End plating wing tips. *U.S. no 1,775,474*, 1930.

[70] W. Mangler. The lift distribution of wings with end plates. *NACA TM 856*, 1938.

[71] S. Hoerner. The aerodynamic shape of the wing tips. *Air Materiel Command, Wright-Patterson Air Force Base, Dayton, Ohio*, 1952.

[72] R.E. Bower. Opportunities for aerodynamic-drag reduction. *NASA/University Conference on Astronautics. NASA SP-372*, pages 323–352, 1975.

[73] S.G. Flechner, P.F. Jacobs, and R.T. Whithcomb. A high subsonic speed wind-tunnel investigation of winglets on a representative second-generation jet transport wing. *NASA TN D-8264*, 1976.

[74] R.T. Whithcomb. A design approach and selected wind-tunnel results at high subsonic speeds for wing-tip mounted winglets. *NASA TN D-8260*, 1976.

[75] L. FalcÃ£o, A. Gomes, and A. Suleman. Multidisciplinary design optimisation of a morphing wingtip. *2nd International Conference on Engineering Optimization, Lisbon, Portugal*, 2010.

[76] D.P. Coiro, F. Nicolosi, F. Scherillo, and U. Maisto. Single versus multiple winglets: Numerical and experimental investigation. *26th ICAS Conference*, Anchorage, Alaska(ISBN: 9781605607153), 14-19 September 2008.

[77] J. A. Jr Blackwell. Numerical method to calculate the induced drag or optimum loading for arbitrary non-planar aircraft. *NASA SP-405*, 1976.

[78] J. E. Yates and C. P. Donaldson. Fundamental study of drag and assessment of conventional drag-due-to-lift reduction devices. *NASA CR 4004*, 1986.

[79] M. D. Maughmer. The design of winglets for high-performance sailplanes. *AIAA Paper 2001-2406*, 2001.

[80] L. C. Montoya, S. G. Flechner, and P. F. Jacobs. Effects of winglets on a first generation jet trasport aircraft. ii-pressure and spanwise load distributions for a semispan model at high subsonic speeds. *NASA TN D-8474*, (Dryden Flight Research Center), July 1977.

[81] R. R. Meyer and P. F. Covell. Effects of winglets on a first generation jet trasport aircraft. vii-sideslip effect on winglets loads at subsonic speeds for a full span model. *NASA Technical paper 2619*, (Ames Research center), 1986.

[82] E. Torenbeek. Synthesis of subsonic airplane design. *Delft University Press*, (ISBN 90-298-2505-7), 1976.

[83] R. D. Finck. Usaf stability and control datcom. *AFWAL-TR-83-3048*, Wright-Patterson Air Force Base, McDonnell Douglas Corporation, Ohio 1978.

[84] R. J. Bamber and R. O. House. Wind-tunnel investigation of effect of yaw on lateralstability characteristics. ii - rectangular naca 23012 wing with a circular fuselage and a fin. *TN-730, National Advisory Committee for Aeronautics*, 1939.

[85] J. D. Brewer and J. H. Lichtenstein. Effect of horizontal tail on low-speed static lateral stability characteristics of a model having 45 deg. sweptback wing and tail surfaces. *Technical Note 2010, National Advisory Committee for Aeronautics*, 1950.

[86] R. O. House and A. R. Wallace. Wind-tunnel investigation of effect of interference on lateral-stability characteristics of four naca 23012 wings, an elliptical and circular fuselage and vertical fins. *Report 705, National Advisory Committee for Aeronautics*, 1940.

[87] W. D. Wolhart M. J. Queijo. Experimental investigation of the effect of the vertical-tail size and length and of fuselage shape and length on the static lateral stability characteristics of a model with 45 deg. sweptback wing and tail surfaces. *Report 1049, National Advisory Committee for Aeronautics*, 1950.

[88] R. W. Gilbey. Contribution of fin to sideforce, yawing moment and rolling moment derivatives due to sideslip, $(y_v)f$, $(n_v)f$, $(l_v)f$, in the presence of body, wing and tailplane. *Item 82010, Engineering Science Data Unit*, 1982.

[89] J. Weber and A. C. Hawk. Theoretical load distributions on fin-body-tailplane arrangements in a side-wind. *Reports and Memoranda No. 2992, Ministry of Supply*, (London, UK), 1954.

[90] M. Lamb, W. C. Sawyer, and J. L. Thomas. Experimental and theoretical supersonic lateral-directional stability characteristics of a simplified wing-body configuration with a series of vertical-tail arrangements. *NASA Technical Paper 1878, National Aeronautics and Space Administration*, 1981.

[91] M. Park. Determination of stability and control derivatives using computational fluid dynamics and automatic differentiation. *AIAA-99-3136*, American Institute of Aeronautics and Astronautics 1999.

[92] J. D. Anderson. Computational fluid dynamics: The basics with applications. *McGraw-Hill, New York*, (ISBN 0-07-001685-2), 1995.

[93] Charles R. O'Neill. Determination of flight stability coefficients using a finite element cfd. *Oklahoma State University, Stillwater*, 2001.

[94] R. M. Hall and R. T. Biedron. Computational methods for stability and control (comsac): the time has come. *American Institute of Aeronautics and Astronautics*, 2005.

[95] F. T. Johnson, E. N. Tinoco, and N. J. Yu. Thirty dates of development and application of cfd at boeing commercial airplanes. *American Institute of Aeronautics and Astronautics*, 2003.

[96] E. Obert. Tail design. *Report H-0-93, Fokker Aircraft B.V.*, (Amsterdam, Netherlands), 1992.

[97] F. Nicolosi, P. Della Vecchia, and D. Ciliberti. An investigation on vertical tailplane design. *Research and Education in Aircraft Design*, 17-19 October 2012.

[98] F. Nicolosi, P. Della Vecchia, and D. Ciliberti. An investigation on vertical tailplane contribution to aircraft sideforce. *Aerospace Science and Technology*, (DOI:10.1016/j.ast.2012.12.006), 2013.

[99] F. W. Diederich. A plan-form parameter for correlating certain aerodynamic characteristics of swept wings. *TN-2335, National Advisory Committee for Aeronautics*, 1951.

[100] SCoPE. *UniversitÃ degli studi di Napoli Federico II*, 2012. URL http://scope.unina.it/.

[101] A. P. Antunes, J. Luiz R. G. da Silva, and F. Azevedo. On the effects of turbulence modeling and grid refinement on high lift configuration aerodynamic simulations. *28th ICAS Conference*, (ISBN 9780956533319), 23-28 September 2012.

[102] C. L. Rumsey, M. Long, R. A. Stuever, and T. R. Wayman. Summary of the first aiaa cfd high lift prediction workshop. *AIAA-2011-839, American Institute of Aeronautics and Astronautics*, 2011.

[103] Star-CCM. *Star-CCM+ Version 6.06.017 User Guide*, CD-adapco 2011.

[104] C. D. Perkins and R. E. Hage. Airplane performance stability and control. *Wiley, New York*, (ISBN 0-471-68046-X), 1949.